EUSKAL HERRIKO UNIBERTSITATEA/
UNIVERSIDAD DEL PAÍS VASCO
Zientzia eta Teknologia Departamentua/
Facultad de Ciencia y Tecnología

Study of Li metal anode surface: interaction with atmospheric gases and impact of impurities in electrochemistry

Ane Etxebarria Dueñas

Thesis Supervisor: Dr. Miguel Ángel Muñoz Márquez

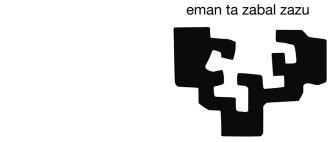

Universidad del País Vasco Euskal Herriko Unibertsitatea

February 2020

EUSKAL HERRIKO UNIBERTSITATEA/
UNIVERSIDAD DEL PAÍS VASCO
Zientzia eta Teknologia Departamentua/
Facultad de Ciencia y Tecnología

CIC ENERGIGUNE

Study of Li metal anode surface: interaction with atmospheric gases and impact of impurities in electrochemistry

A dissertation submitted to the University of the Basque Country in partial fulfillments of the requirements for the degree of Ph.D.

Ane Etxebarria Dueñas

Thesis Supervisor: Dr. Miguel Ángel Muñoz-Márquez

UPV/EHU Tutor: Dr. Francisco Javier Zúñiga Lagares

February 2020

Contents

ACKNOWLEDGEMENTS

The thesis work presented here couldn´t be done without all the support received the last four years. I would like to start thanking Basque Government for the financial support (PRE_2015_1_0376 and EP_2018_1_0004), CIC Energigune for the opportunity to perform this work at their facilities and the University of the Basque Country (Departamento de Física de la Materia Condensada), for accepting this work in their department. My sincerely gratitude goes to the supervisor of this PhD, Miguel Ángel Muñoz, for guiding me through these years and supporting every step of the process. Present and past research group members, I really appreciate all of you. Alex, thanks for your patience, there is too much one can learn from you. Jokin, eskerrik asko zure laguntzeko prestutasun itzelagatik eta hurkotasunagatik, ezinbestekoak honako lana aurrera ateratzeko. Maider, asko izan da zurekin ikasitakoa, baina are gehiago ikasi beharko nuke zutaz. Begoña, Elena, que fácil es trabajar con vosotras, muchas gracias por toda la indispensable ayuda ofrecida. Y Giorgio, gracias por preocuparte porque todo salga adelante y por los muchos y variados consejos. Por muchos años más. CIC Energiguneko teknikari zein administrazio kideei, eskerrik asko zuengatik jasotako laguntza guztiagatik. Eta, nola ez, doktoretza ikasle zein bestelako lankide baino lagun bihurtu zareten guzti horiei, esker mila lanean kalean bezain eroso sentiarazteagatik. Muxu bana Jon, Itziar, Oierx2, Jaio, Bego, Mariax3, Xabi, Guillermo eta bidean ahaztuak.

I would also like to sincerely thank all the group members from ALS beam line 9.3.2, and financial support through ALS doctoral fellowship program. It was amazing working around you all, Yifan, Moni, Don-Jen, Maxime, Pinar, Hongyang, Meiling, Kyung-Jae, Jin. And, especially Ethan Crumlin, thanks for being such an incredible supervisor and for giving me the opportunity to keep learning and growing. Cannot forget all the good friends found there outside the lab, thanks for receiving me so warmly and being so close. See you all soon.

Zer esanik ez, Gasteizko lagun maiteak, hain hurbilekoak, betikoak, betirako zuek denak, eskerrik asko kuadrilla. Eta azkenengo eskerrak, barren-barrenekoak, familiarentzako dira, bizitzan zerbaitetan benetan zorteduna izan banaiz, zuekin izan da eta. Milesker aita, ama, bro.

ABSTRACT

Gaining market share of electric vehicles is essential in order to mitigate greenhouse effects partially caused by thermal engine vehicles gas emissions. However, the technology in charge of powering electric vehicles, Li-ion batteries, is not competitive enough, it has still several limitations in terms of fast charging, autonomy, safety and lifetime. Therefore, development of Li-ion technology is vital if a full electric transport market implementation wants to be achieved. Furthermore, it will ensure the evolution of portable electronic devices market, also powered by Li-ion batteries. Among the several alternatives to improve Li-ion batteries energy density, changing the actual graphite anode by lithium metal is one of the most promising ways due to its high theoretical capacity (about ten times higher than graphite) and lowest reduction potential known (-3.040 V vs standard hydrogen electrode). Yet, the high reactivity of Li surface makes it impossible to have a stable interfaphase between the electrode and electrolyte, continuously loosing active material. Besides, lithium deposition during charge and discharge processes is not homogenous, and dendrites are grown. These ones could reach the anode causing several safety issues.

In this thesis work, the surface of metallic lithium is studied in order to gain knowledge about its instability. For that, firstly how most common dry atmospheric gases (O_2, CO_2 and N_2) modify the chemical composition and electronic properties of lithium surface is analyzed by X-ray photoelectron and ultraviolet photoelectron spectroscopic techniques. It has been concluded that most reactive gas towards metallic lithium is O_2, and that three gases reduce the work function of metallic lithium. After this study, the evolution of lithium carbonate on lithium surface has been analyzed by *in-situ* ambient pressure X-ray spectroscopic technique. This compound increases the inhomogeneity of Li deposition when it is present in the interface between the electrode and the electrolyte, thus avoiding conditions where it will be promoted is of interest. In this study, insight into the reaction mechanism and kinetic studies of Li_2CO_3 growth are provided.

Lastly, the effect commercial Li foil native surface impurities have in an electrochemical system has been studied. For that, in order to avoid these

impurities, first step has been to grow a lithium thin film, which has been characterized using a scanning electron microscope. Then, the electrochemical performance and internal resistance of a standard polymer electrolyte system with Li symmetric electrodes has been analyzed. In this study, it has been concluded that avoiding Li foil native surface impurities strongly modifies interfacial properties that determine the electrochemical performance of a system. This emphasizes the need of gaining knowledge about the initial state of metallic lithium surface used in batteries.

RESUMEN

Aumentar cuota del mercado de vehículos eléctricos es esencial si se pretenden mitigar las consecuencias del efecto invernadero causadas, entre otros factores, por las emisiones de gases de vehículos de motor térmico. Sin embargo, la tecnología que suministra energía a los vehículos eléctricos, la tecnología de Li-ion, no es suficientemente competitiva debido a sus limitaciones en carga rápida, autonomía, seguridad y durabilidad. Para que se produzca una completa implementación del transporte eléctrico en el mercado, el desarrollo de la tecnología de Li-ion es vital. Además, su avance asegurará la evolución de los aparatos electrónico portátiles, también alimentados por baterías de Li-ion. De entra las diferentes alternativas existentes para mejorar la densidad energética de las baterías de Li-ion, una de las estrategias más prometedores es el cambio del ánodo actual, grafito, por litio metálico. Esto se debe a la alta capacidad del Li (unas diez veces superior al grafito) y a que posee el menor potencial de reducción conocido (-3.040 V vs electrodo de hidrógeno estándar). Aun así, la gran reactividad de la superficie del litio imposibilita tener una superficie estable entre el ánodo y el electrolito, perdiendo continuamente material activo. Además, la deposición de litio entre los procesos de carga y descarga en el ánodo no es homogénea, y se forman y crecen dendritas. Éstas pueden llegar a alcanzar el cátodo, causando varios problemas de seguridad.

En este trabajo de tesis, la superficie del litio ha sido estudiada con el objetivo de adquirir mayor conocimiento sobre su estabilidad. Para ello, primeramente, se ha analizado cómo los gases atmosféricos secos más comunes (O_2, CO_2 y N_2) modifican la composición química y las propiedades electrónicas de la superficie del litio. Este estudio se ha realizado por medio de las técnicas espectroscópicas de fotoemisión de rayos X y de rayos ultravioleta. Se ha concluido que el gas más reactivo es el O_2, y que los tres gases reducen la función de trabajo del litio metálico. En el siguiente estudio, la evolución del carbonato de litio en la superficie del litio se ha analizado *in situ* por medio de la técnica espectroscópicas de fotoemisión de rayos X de presión ambiente. El carbonato de litio incrementa la uniformidad de la deposición del litio metálico cuando está presente en la interfase entre el electrodo y el ánodo. Por ello, es de gran interés evitar

condiciones en las que el crecimiento de este compuesto está favorecido. En este estudio, se ha obtenido información que contribuye al esclarecimiento del mecanismo de reacción, además de proporcionar estudios cinéticos del crecimiento del Li_2CO_3.

Finalmente, se ha analizado el efecto de las impurezas nativas de la superficie de una lámina de litio comercial en un sistema electroquímico. Para ello, con el fin de evitar estas impurezas, el primer paso ha sido crecer una capa fina de litio, la cual ha sido caracterizada por medio de un microscopio electrónico de barrido. A continuación, se ha analizado el rendimiento electroquímico y resistencia interna de un sistema formado por electrodos simétricos de litio y un electrolito polimérico estándar. En este estudio, se ha observado que evitar las impurezas nativas de las láminas de litio comerciales modifica notoriamente las propiedades interfaciales, las cuales determinan la ejecución electroquímica de un sistema. Esto enfatiza la necesidad de adquirir mayor conocimiento sobre el estado inicial de la superficie de litio que se utiliza en las baterías.

LABURPENA

Energia sortzeko egun erregai fosilekiko dagoen menpekotasunak ondorio zuzenak ditu ingurugiroan, bestak beste CO_2 isuriek areagotzen duten berotegi efektua dela eta. Honakoari aurre egiteko, energia berriztagarrien erabilerak eta ibilgailu elektrikoetarako jauziak berebiziko garrantzia daukate. Bi eremu hauetan, energiaren metaketarako gailu eraginkorrak beharrezkoak dira. Iturri berriztagarriek sortzen duten energia baldintza klimatologikoen araberakoa da, ez dute energia denboran iraunkorki sortzen. Hori dela eta, eskaintza eta eskariak bat egin dezaten, sortzen duten energia metatuko duen gailuen menpe daude. Bestetik, ibilgailu elektrikoak lehiakorrak izan daitezen, eskaintzen duten autonomia motore termikoko ibilgailuekiko alderagarria izan behar da. Beraz, hauek ere, energia metaketa gailu eraginkorren beharrean daude.

Energia metaketarako gailu desberdinen artean, bateriak dira arruntenetakoak. Bateria bat hainbat zelda elektrokimikoz osatua dago, eta beraietako bakoitzean energia elektrikoa energia kimiko gisa metatzen da erredox erreakzioen bitartez. Zelda elektrokimikoek honako osagai nagusiak dituzte: katodoa edo elektrodo positiboa, anodoa edo elektrodo negatiboa, elektrolitoa eta elektrodo bakoitzeko korronte kolektoreak. Katodo eta anodoen arteko erredukzio potentzial desberdintasuna erredox erreakzioen indar eragilea da. Elektrolitoaren bitartez, elektrodoek ioiak elkar trukatzen dituzten, eta prozesu honen ondorioz elektroiak kanpo zirkuitu baten bidez elektrodo batetik bestera doaz, elektrizitatea sortuz.

Anodoari erreparatuz gero, litio metalikoa teorikoko oso aukera aproposa da. Izan ere, kapazitate espezifiko teoriko altua dauka (3860 mAh/g), dentsitate baxua (0.53 g/cm) eta ezagutzen den potentzial elektrokimiko negatibo txikiena (-3.040 V hidrogeno estandarra erreferentziatzat hartuta), azken hau bateriak energia handiagoa ematearen erantzulea delarik. Hala ere, litioaren gainazal ezegonkorrak bere merkaturatzea zaildu du. Elektrolitoarekin etengabe erreakzionatzen du, material aktibo asko galduz, eta ezinezkoa du elektrodo/elektrolito gainazal arte egonkor bat lortu. Honetaz gain, karga eta deskarga artean, litioa ez da era homogeneo batean jalkitzen anodoaren gainazalean, eta dendrita antzeko mikroestrukturak sortzen dira. Hauek hazi

egiten dira eta, katodora helduz gero, zirkuitu laburrak eragin ditzakete, honek dakartzan arriskuekin.

Litioaren ezegonkortasunaren arazoari aurre egiteko, 90. hamarkadan anodo bezala Li-ioiak itzulgarriki tartekatu litezkeen matrize bat erabiltzea proposatu zen, non matrizearen eta elektrolitoaren arteko gainazal artea egonkorra izango zen. Material honen aurkikuntzak 1991. urtean Sonyk lehendabizikoz Li-ioi teknologia merkaturatzea ahalbidetu zuen. Bateria haietako anodoa petrolio jatorriko kokea izan zen, katodoa $LiCoO_2$ oxido laminarra eta elektrolitoa disolbatzaile organiko karbonikoetan disolbaturiko Li gatza. Egun, Li-ioi baterietako anodoa petrolio jatorriko kokea izatetik grafitoa izatera pasa da. Teknologia hau sortu zenetik merkatuko lehiakorrena da, energia dentsitate altua eskaintzen duelako era seguru eta eraginkor batean. Hori dela eta, merkatuko ibilgailu elektrikoek Li-ioi teknologian oinarritutako bateriak dituzte. Gailu elektroniko eramangarriek ere, hazkunde etengabean dagoen merkatuak, teknologia mota berdina erabiltzen du baterietan. Hala ere, grafitoaren kapazitate (372 mAh/g), litiorenarekin alderatuz hamar bat aldiz txikiagoa. Beraz, litio metalikoarekiko interesak bizirik jarraitzen du, eta berau egonkortzeko bide desberdinak proposatu dira azken urteetan; hala nola, gainazalaren moldatzea aurre tratamenduen bidez edo elektrolito solidoen erabilera zirkuitu laburrak ekiditeko. Hala ere, oraindik ez da aurkitu litio metalikoa egonkortuko duen epe luzerako konponbidea.

Honako tesian litioaren gainazalaren egonkortasuna aztertu da, eta litio komertzialaren berezko ezpurutasunek sistema elektrokimiko batean duten eragina neurtu da. Honetarako, lehendabizi atmosferan ugariak diren O_2, CO_2 eta N_2 gasek litioan zein ondorio dituzten aztertu da 3. kapituluan, eta Li_2CO_3 konposatuaren bilakaera jarraitu da Li gainazalean 4. kapituluan zehar. Jarraian, ezpurutasunik gabeko litio/elektrolito gainazal artea sortze bidean, litio geruza fina hazi eta karakterizatu da 5. kapituluan. Azkenik, 6. kapituluan, elektrolito polimerikoa duen sistema elektrokimiko batean litio komertzialaren ezpurutasunek elektrokimikan duten eragina ikertu da.

Litioaren gainazalean atmosferan aurkitzen diren O_2, CO_2 eta N_2 gasek sortzen dituzten aldaketak aztertzeko fotoigorpen espektroskopia teknikak erabili dira: XPS (*X-Ray Photoelectron Spectroscopy*) eta UPS (*Ultraviolet Photoelectron Spectroscopy*). CIC Energiguneko Gainazalen Azterketa Plataforman aurkitzen den teknika anitzeko ekipoan burutu dira bi

espektroskopia hauek. Lehenengo teknikaren bidez gainazalean sortzen diren konposatu kimikoak zehaztu dira. Bigarren teknikaren bidez gainazalen lan-funtzioa (w_f, *work function*) determinatu da. Parametro honek huts mailaren araberako Fermi mailaren posizioa adierazten du, eta elektroi bat gainazaletik ateratzeko beharrezko energia zenbat den adierazten du. Fotoigorpen espektroskopia teknika hauekin litioaren gainazala *ex-situ* aztertu da; hau da, litioaren gainazala moldatu ostean neurtu da huts altuko egoeran (UHV, *Ultra High Vacuum*).

Gasen eragina ikertu aurretik, lehendabizi argoi atmosferan gordetako litio xafla komertzialaren gainazala aztertu da, baterietarako anodo bezala erabiltzen dena. Xafla honen gainazaleko litio guztia oxidatua dagoela konprobatu da, Li_2O eta Li_2CO_3 konposatuetan bereziki. Hori dela eta, atmosferako gasek beragan duten eragina aztertzeko, litio gainazala Ar ioiekin bonbardatu da UHV egoeran. Metodo hau eraginkorra izan da gainazaleko ezpurutasunak kentzeko: garbituriko gainazalak %(93.6 ± 1.9) Li metalikoz osatuak daude, gainerakoa Li_2O delarik.

O_2, CO_2 eta N_2 gasen artean, oxigeno gasa da litioarekin bortitzen erreakzionatu duena. 9 L O_2 gas (non 1 L 10^{-6} Torr presiopean segundo batez eginiko dosifikazioaren baliokidea den) nahikoa dira gainazaleko 8.6 nm-tako litio guztia oxidatua izateko. O_2 gasaren presioa 10^{-4} mbar azpitik denean, erreakzio honetako produktu bakarra Li_2O izan da. Hortik gorako presioetan, Li_2O_2 ere neurtua izan da gainazalean. CO_2 gasaren interakzioari dagokionez, Li_2O, Li_2CO_3 eta bestelako karboi oinarridun produktuak identifikatu dira. Erreakzio hau askoz motelagoa da, $8{\cdot}10^8$ L CO_2 gas ere ez dira nahiko gainazaleko 8.6 nm-tako litio metaliko guztia oxidatzeko. Nitrogenoari dagokionez, litioak ez du gas honekin erreakzionatzen 10000 L-etik behera. Eta 10000 L-tan, soilik gainazalen %1.2 dago osatua nitrogeno oinarria duten konposatuekin. Li_3N lortzeko modu bakarra litio gainazala nitrogeno ioiekin bonbardatzea izan da. Modu honetan lorturiko gainazala honako konposatuez osatua dago: %68.4 Li^0, %19.8 Li_3N, %8.1 Li_2O eta %3.7 ezpurutasun.

Lan funtzioa dagokionez, hiru gasek bere balioaren txikiagotzea dakarte. Li^0-ren batez besteko lan-funtzioa 3.01 ± 0.08 eV da. 1000 L O_2-ren ondorioz, lan funtzioa 2.12 eV-ra txikitzen da, eta 1000L CO_2-ren eraginez 2.30 eV-ra murrizten da. Li_3N konposatuak era lan funtzioaren txikitzea dakar, 2.49 eV-

ra jaitsiz. Bereziki, gainazala Li_2O and Li^0 konposatuez osatua badago, lan-funtzioak Li_2O kontzentrazioaren araberako erorketa esponentziala jarraitzen duela ondorioztatu da. Beraz, hiru gas hauek moldatuko litio gainazalek litio metilkoak baina erraztasun handiagoaz galduko dute elektroi bat, anodo bezala erabiltzeko ezaugarri kaltegarritzat jo dena.

Jarraian, litio karbonatoren garapenaren azterketa egin da litio metalikoaren gainazalean. Izan ere, litio karbonatoa kaltegarritzat hartua dago litio anodo gainazalaren egonkortasunerako. Konposatu honek gainazaleko bestelako konposatu batzuekin alderatuz Li-ioi konduktibitate txikiagoa dauka, eta honek litioaren deposizio ez homogeneoa bultzatzen du. Ikerketa honetarako litio gainazalaren bilakaera neurtu da CO_2 atmosferapean APXPS (*Ambien Pressure X-Ray Photoelectron Spectroscopy*) teknikaren bidez sinkrotroi bidezko erradiazioa erabiliz. Neurketa hauek ALS (*Advanced Light Source*) azeleragailuan egin dira, LBNL (*Lawrence Berkeley National Laboratory*) laborategian. Aurretik erabilitako XPS-rekin alderatuz gero, APXPS teknikaren abantaila nagusia neurketak *in-situ* egin daitezkeela da; hau da, erreakzioa ematen den bitartean gainazalaren eboluzioa jarraitua izan daiteke. Gainera, sinkrotroiari esker, erradiazioa aldatu daiteke, sakontasun profileko neurketa ez-suntsitzaileak egitea ahalbidetuz.

Aurreko kasuan bezala, hemen ere argoi atmosferan gordetako eta garbitutako litio xaflaren hasierako egoera ikertu da, non berriro konprobatu den litioaren gainazal osoa oxidatua dagoela. Sakontasun profileko neurketek bidez Li_2CO_3 Li_2O-ren gainean kokatzen dela ikusi da. Kasu honetan, litioaren gainazala garbitzeko bestelako teknika erabili da: gainazala fisikoki urratua izan da UHV egoeran, marraza baten bidez.

Litio karbonatoaren eboluzioa aztertzerakoan, berarekin batera beste konposatu baten bilakaera ere neurtua izan da: litio oxalatoa, $Li_2C_2O_4$. Konposatu hau aurretiaz bitartekari gisa proposatua izan zen Li_2CO_3 sortzeko, baina ez zegoen bere hazkuntzaren ebidentzia esperimentalik. Beraz, oxalatoaren neurketak karbonatoa sortzeko mekanismoa argitze bidean informazio oso baliagarria eskaintzen du. Karbonatoaren hazkunde motari dagokionez, bi tarte identifikatu dira: erreakzioak kontrolaturikoa eta difusioak kontrolaturiko. Lehenengoak hazkunde lineala dauka, eta bigarrenak parabolikoa. Litioa CO_2 gasaren pean egotearen ondorioz, Li_2O konposatua ere sortzen da gainazalean. Atal honetan lorturiko informazioarekin erreakzio mekanismo bat proposatu da. CO_2 atmosferari O_2 gasa gehitzeak dituen ondorioak ere aztertu dira, non ikusi den

oxigenoak litio karbonatoaren bilakaera bultzatzen duen, oxalatoa sortzea ekidinez. Azterturiko gainazal guztiek estruktura berdina daukate: Li_2O Li metalikoaren gainean kokatzen da, eta Li_2CO_3 oxidoaren gainean oxalatoarekin batera, baldin eta oxalatoa sortzen bada.

Behin litio xafla komertziala aztertuta, litio geruza fina sortu eta karakterizatzeari ekin zaion. Honetarako, baporizazio termiko teknika erabili da. Li iturri komertzial batetik abiatuz, sortutako gainazalak elektroien mikroskopia bidez karakterizatu dira CIC Energiguneko Gainazalen Azterketa Plataforman aurkitzen den SEM (*scanning electron microscope*) erabilita. Honakoarekin iturri komertzialaren deposizioa abiadura neurtu eta geruzaren hazkuntzaren morfologia behatu dira. Iturritik 8 A-ko korrontea pasatzean, deposizio abiadura 120 – 400 nm/h-koa da eta geruzak mendixkak eta zuloak ditu. Prozesu honetan zehar substratuaren tenperatura 42.3 °C-koa da. Korrontea 10 A denean, berriz, deposizio abiadura 730 – 1400 nm/h-koa da, eta substratuaren tenperatura 51.5 °C-ra igotzen da, zeinak gainazalaren morfologia homogeneizatzen duen. Litioaren hazkundea hainbat substratutan aztertu da: Si monokristalinoa, Ti geruza, altzairu herdoilgaitza, PET (*Polyethylene terephthalate*) polimeroa eta $SrTiO_3$ monokristalinoa. Hauetatik, Si monokristalinoan ez da lortu litioa geruza moduan haztea. Horren ordez, litioak mikroestruktura ez homogenoa jarraitzen du, dendrita erakoa. Ezin izan da hazkunde mota hau silizioaren propietate jakin batekin erlazionatu.

Azkenik, litio xafla komertzialaren ezpurutasunek sistema elektrokimiko batean duten eragina aztertu da. Azterketa honetarako LiTFSI (*lithium bis(trifluoromethanesulfonyl)imide*) gatza duen PEO (*Poly(ethylene oxide)*) elektrolito solido polimeriko estandarra sintetizatu da. Polimero honekin Li/PEO:LiTFSI/Li sistema elektrokimikoaren portaera aztertu da bi kasutan, CIC Energiguneko elektrokimika karakterizazio baliabideen bidez. Lehenengo kasuan, Li xafla komertziala erabili da. Aurretik ikusi bezala, xafla honen gainazalak Li_2O eta Li_2CO_3 konposatuak ditu, beraz elektrodo/elektrolito gainazal artean ezpurutasun hauek egongo dira. Bigarren kasuan, litioa zuzenean baporatu da polimeroaren gainean UHV egoeran, gainazal arteko ezpurutasunak minimizatuz. 70 °C-tan, non elektrolito polimerikoak konduktibitate aproposa daukan, litio xaflen ezpurutasunak ekiditeak gainazal artean barneko erresistentzia %26 murriztea dakar. 45 °C-tan, oso tenperatua baxua elektrolitoaren funtzionamendu egokirako, murrizketa hau are eta nabariagoa da, %92-koa. Polarizazio galvanostatikoan ere eragina dauka ezpurutasuna ekiditeak, gain-boltaiaren

murriztea baitakar. Emaitza hauekin Li gainazalaren egoerak zelda elektrokimikoaren jardueran erantzukizun zuzena daukala konprobatu da, material honen erreaktibotasun altua ulertze bideko esperimentuen garrantzia azpimarratuz.

CHAPTER 1

Introduction

1.1 Motivation

Human progress and energy consumption are undeniably linked. According to The United Nation´s Human Development Index, energy consumption up to around 100 GJ per head is related with substantial increase in human development and well-being. However, only 20% of total world population live in developed countries where average energy consumption is above that value[1]. A scenario where all human beings will be within the 100 GJ/person energy consumption involves a dramatic rise of actual energy demand. In 2018, 80% of worldwide total primary energy demand was supplied by fossil fuels such as oil, gas and coal[2]. This extreme dependence on fossil fuels has directly impacted the continuous increase of greenhouse gases emissions in last years (see Figure 1.1 for CO_2 emission evolution), being the last four years the warmest since there are official temperature records[3].

The uncontrolled temperature increase has tremendous consequences on the world climate. A recent study predicts that, under high emissions scenarios, by 2050 340 million people will be directly affected by sea-level rise and coastal flooding, an estimation that triples the amount of people affected by previously considered models[4]. Energy demand will also be affected by climate change, as rising temperature increases hot season cooling demand and cool season heating demand in several economic sectors such as agriculture, industry, residential and commercial. In a vigorous warming scenario climate change, it will produce a 25% rise in energy demand on top of the 1.7-2.8 times increase factor due to socioeconomic developments[5]. In order to address this issue, in 2015 an agreement was draft in the United Nations Framework Convention on Climate

Change, the so-called Paris Climate Agreement. Countries signing the agreement compromised to hold the rise in temperature below 2 °C, pursuing efforts to limit it below 1.5 °C. By November 2019, 197 countries worldwide have signed it. The acquired compromise represents a tremendous challenge for the world, besides decarbonization, it has also been estimated that 640-950 Gt (Gigatonnes) of cumulative CO_2 are needed to be removed[6], which, considering atmospheric mass is 5.137×10^{18} kg, will be equivalent to 82-122 ppm (part per million).

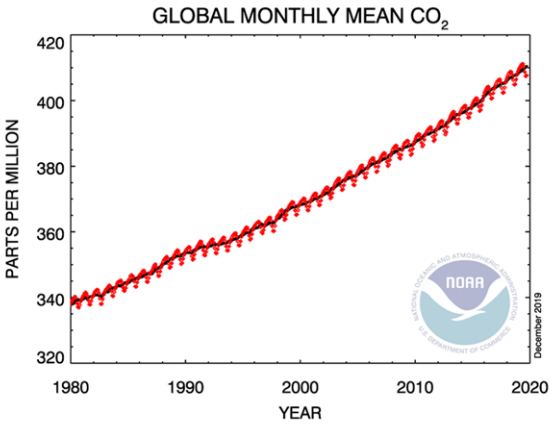

Figure 1.1. Monthly mean carbon dioxide globally averaged over marine surface sites. The dashed red line with diamond symbols represents the monthly mean values, centered on the middle of each month. The black line represents the same, after correction for the average seasonal cycle[7].

Recently, in December 2019, Madrid held the 25th United Nations Climate Change Conference where almost 200 countries negotiated to overcome the issues in implementing the Paris Climate Agreement. Unfortunately, little was achieved during this negotiation, where no rules for trading carbon emission credits and for helping developing countries with climate issues were created. Furthermore, the country that was responsible of 14.75% of total CO_2 emissions in 2018, United States of America[2], announced the withdrawn from the Paris Climate Agreement[8]. Even this careless attitude to address the consequences of climate change, worldwide alarm on this matter is a reality, as demonstrated by the dire issued in November 2019 where thousands of scientists declared a climate emergency[9]. In this regard, the European Union has started a long-term strategy to become climate-neutral by 2050 while fulfilling the Paris Climate Agreement. This strategy, presented in November 2018, is based on seven blocks: energy efficiency; deployment of renewables; clean, safe and connected mobility;

competitive industry and circular economy; smart network of infrastructure and interconnections; bioeconomy and natural carbon sinks; and tackling remaining emissions with carbon capture and storage[10]. All of them represent a giant challenge for the community, and the development of current energy storage systems is key for the success of this strategy. Energy storage could efficiently overcome the main drawback of renewable energies, i.e. the non-constant generation; and make a difference in transition from internal combustion engine vehicles to electric powered ones, since nowadays electric vehicles only represent less than 0.5% of the global vehicle fleet[11].

1.2 Li-ion technology

The technology taking whole accountability of powering electric vehicles is the same that ensures the development of portable electronic devices: Li-ion rechargeable batteries[12–17]. The urgency of the development of the first market to meet environmental standards already introduced, and the unavoidable growth of the second market related to human progress is pushing Li-ion technology to its limits in terms of cost, fast charging, energy density, safety and lifetime[18]. Following, the basic principles of Li-ion technology and current approaches to overstep its boundaries will be discussed.

1.2.1 Li-ion technology basics

A lithium-ion battery pack is composed of battery modules and various control and protection systems as a Battery Management System (BMS). Likewise, a battery module is a conjunction of electrochemical cells, the basic unit of a lithium-ion battery pack. Each cell is able to store electric energy transforming it into chemical energy by redox reactions, and it has the ability of recharge over and over.

This technology was firstly commercialized in 1991 by Sony, and the Novel price of 2019 conceded to John B. Goodenough, M. Stanley Whittingham and Akira Yoshino for their work in developing it underlined the enormous effect Li-ion technology made in our society. Figure 1.2 shows the principal parts of a Li-ion electrochemical cell.

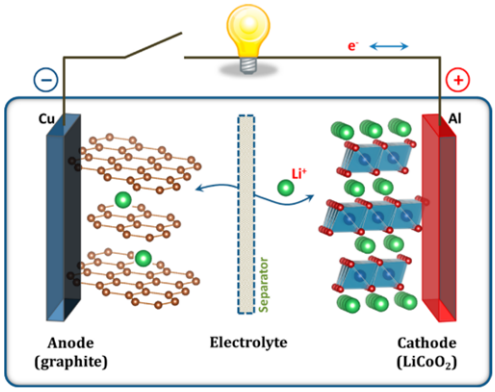

Figure 1.2. Schematic of a conventional lithium-ion cell. [Reproduction with permission from[19], Copyright (2019) Journal of the American Chemical Society].

The positive electrode (cathode) is the one with the highest reduction potential, and the negative electrode (anode) has the lowest reduction potential. When there is an ionic conductor and electronic insulator media, the electrolyte, separating the anode and the cathode, and both electrodes are electrically connected via an external circuit, the difference in reduction potential leads to half redox reaction in both electrodes. During the discharge process, anode will oxidize and cathode will reduce. In this process, Li atoms move from the anode to the cathode, while electrons move through the external circuit to maintain electronic neutrality, thus producing electricity. When charging the cell, the inverse process happens.

The difference between the electrode potentials defines the cell voltage (V_{OC}). Capacity (Q) specifies the amount of charge a cell can deliver. The stored energy density (E) depends on this voltage and the capacity of the electrodes, according to the equation:

$$E = Q \cdot V_{OC} \tag{1.1}$$

These terms are normally expressed in kWh for energy, mAh for capacity and V for cell voltage. Both energy and capacity can be normalized to weight or volume obtaining energy density or specific capacity respectively. In a full cell, weight of anode and cathode has to be balanced to match each other capacity.

Most common materials in a Li-ion battery are graphite anodes (C) and lithium metal oxide cathodes (LMO_2, M = Co, Mn, Ni) with an organic liquid electrolyte. Cell reactions will be represented as:

During charge:

$$Cathode: LiMO_2 \rightarrow Li_{1-x}MO_2 + xLi^+ + e^- \quad (1.2)$$

$$Anode: xLi^+ + xe^- + C \rightarrow Li_xC \quad (1.3)$$

During discharge:

$$Cathode: Li_{1-x}MO_2 + xLi^+ + e^- \rightarrow LiMO_2 \quad (1.4)$$

$$Anode: Li_xC \rightarrow xLi^+ + xe^- + C \quad (1.5)$$

When using Co as the transition metal material in the cathode (average redox potential of $LiCoO_2$ (LCO) is 3.8 V vs Li/Li^+), a graphitic anode (average redox potential of graphite is around 0.1 vs Li/Li^+) and an organic liquid electrolyte, the overall energy density of the battery cell lies between 150-200 Wh/kg[20]. In the next section, the reasons to choose these materials among others and the development of them with some alternative candidates are briefly introduced.

1.2.2 Li-ion battery main component materials

Conventional Li-ion batteries are based on Li^+ intercalation mechanism electrodes. First commercialized Li-ion battery **cathode** was LCO. This material has a layered structure, with three CoO_2 layers per unit cell, resulting in a two-dimensional migration channel for Li. Theoretical capacity of LCO is 274 mAh/g, but it only reaches 140 mAh/g due to physico-chemical instabilities. The origin of these instabilities relies on the overlapping between $Co^{3+}/^{4+}$:t_{2g} orbital with O^{2-}:2p, which causes phase transitions in the crystal structure at high voltages[21]. Some attempts to address the overlapping phenomena are based on replacing Co with different transition metals such as Ni and Mn. Apart from minimizing the overlapping effect, these materials are also ecologically and economically a better alternative. However, synthesis of stoichiometric $LiNiO_2$ (LNO) is challenging, and undesired phase transitions at some intercalation states have also been found. Besides, Jan teller effect happening in Ni is a major drawback because it causes the distortion of the structure upon electrochemical cycling[22]. In the case of layered structure Mn oxide cathode, it suffers from poor cycle life related to a

spinel structure phase transition[23]. In the last decades, the interest in mixed transition metal oxides combining Ni, Mn and Co (NMC) has been growing, due to the synergetic benefits of merging them. These materials can offer a capacity of 200 mAh/g when charging between 2.5 V and 4.5 V[24].

Apart from the above-mentioned cathode materials that rely on the intercalation of Li in layered oxide channels, three-dimensional structures also represent a competitive alternative: e.g. the $LiMn_2O_4$ spinel and the $LiFePO_4$ (LFP) olivine structures. The most recent advances are exploring both high voltage lithium-ion cathode materials, as the spinel $LiMn_{1.5}Ni_{0.5}O_4$ which can operate at 4.7-4.8 V, and high capacity cathodes, such as the so-called Li-rich layered oxides; denoted as $xLi_2MnO_3(1-x)LiTO_2$ (T=Mn, Ni, Co), they can reach capacities higher than 250 mAh/g[22].

Most common standard **electrolyte** in Li-ion batteries are composed by $LiPF_6$ salt in a mixture of organic carbonate solvents. Generally, the solvent includes ethylene carbonate (EC) and dialkyl carbonates[25]. The advantages of organic liquid electrolytes are the relatively high potential window at which they can operate without degradation (stable until 4.4 V) and the high ionic conductivity. However, these electrolytes are flammable, corrosive and thermally unstable, which could cause explosions and fire accidents when not used properly. Furthermore, $LiPF_6$ salts is highly toxic[26]. Despite water-based electrolytes[27] could be a suitable option to remove organic solvents, main alternative electrolytes to avoid the safety issues of organic liquids are the solid electrolytes and ionic liquids.

Solid electrolytes can be divided in two main families: polymer electrolytes and ceramic electrolytes[28]. In order to be competitive, both of them should possess high ionic conductivity (above 10^{-4} S/cm) at room temperature, have negligible electronic conductivity with high ionic transference number and remain stable in a wide electrochemical window[29]. Polymer based electrolytes are relatively easy to process at room temperature and have a good adhesion, but their conductivity at room temperature is below the desired one[30]. Among the different alternatives, polyethylene oxide-based are the most studied ones. Ceramic electrolytes have a high mechanical rigidity, they are stable at high temperature improving safety and kinetics, and possess a very high Li^+ transport number, close to one. However, cracking and delaminating due to high temperature processing constitutes a mayor problem, and still suffer from a lower ionic conductivity than

liquid electrolytes[31]. Some examples of actively researching ceramic electrolytes are NASICON type ($Na_{1+x}Zr_2Si_xP_{3-x}O_{12}$, 0<x<3) Li-ion conductors[31] and garnet type electrolytes, derivatives from the $Li_3Ln_3M_2O_{12}$ (M = T,W; Ln = Y, Pr, Nd, Sm, Eu, Gd, Tb, Dy, Ho, Tm, Yb, Lu) garnet discovered in 1968[32], among others. Currently, hybrid polymer-ceramic electrolytes are under intense study with the aim to find a solid electrolyte that will fulfil all the requirements to be integrated competitively in a Li-ion battery[33].

Ionic liquid electrolytes are also an attractive alternative to organic liquid electrolytes due to their negligible vapor pressure and almost negligible flammability, which enhanced safety of the battery[34]. Furthermore, they also show a wide electrochemical window stability (up to 6 V for certain combinations), high ion density and wide liquidus phase range. These room-temperature molten salts have asymmetrical, large and bulky anions and cations. Typical ionic liquid is comprised of a quaternary ammonium cation, such as imidazolium, pyridinium or pyrrolidinium, combined with an organic or inorganic counter anions such as BF^{4-}, PF^{6-}, $[(FSO_2)(CF_3\ SO_2)N]^-$ or $[(CF_3SO_2)(CF_3CO)N]^-$, for instance. However, issues as their lower ionic conductivity compared with organic liquid electrolytes, and some incompatibilities with common active materials still represent major challenges for their implementation in Li-ion batteries[35].

The finding of an appropriate **anode** was the main promoter of the development of Li-ion technology by Sony Energetic of Japan in 1991. Previous attempts of rechargeable batteries used Li metal as anode. Considering its lightness, high theoretical capacity (3860 mAh/g) and lowest reduction potential known (-3.040 V vs standard hydrogen electrode), it was a very attractive anode material. Indeed, in the 1960s, the concept of lithium secondary batteries was presented[36]. In the next decade, first commercial Li metal rechargeable batteries appeared[37]. However, the highly reactive nature of lithium made it impossible to have a stable interface between the anode and the electrolyte, thus metallic lithium anode rechargeable batteries were quickly discarded. More details about the problematic characteristic of cycling a metallic lithium anode are explained later in this chapter (section 1.3.2). In the 90s, the proposed solution to address the instability of lithium was the use of a material where Li ions could intercalate reversible and the interface between the anode and electrolyte could be stable. The finding of a material that met these requirements gave birth to lithium-ion rechargeable batteries. The first chosen material was petroleum coke, a soft

carbon material with a certain amount of structural disorder that enabled the commercialization of Li-ion batteries[38]. Nowadays, graphitic carbon materials that consist of graphene layers held together by weak van-der-Waals forces[39] are still used as anode due to their outstanding stability[40]. This material can intercalate Li^+ at 0.1 V vs Li/Li^+, and it has a theoretical capacity of 372 mAh/g when LiC_6 is formed.

1.2.3 Solid Electrolyte Interphase (SEI): a key parameter

Having a stable solid electrolyte interphase (SEI) over the graphite anode, a layer that was able to stabilize de interface between the anode and the organic liquid electrolyte, was determining for the development of Li-ion battery technology. The SEI forms because the chemical potential of the anode is outside the electrochemical stability window (ESW) of the electrolyte (Figure 1.3a). The organic electrolyte will reduce until the anode electrolyte reaction is blocked by the SEI layer[19], which prevents the anode from further reduction the electrolyte, providing stability to the electrochemical system (Figure 1.3b).

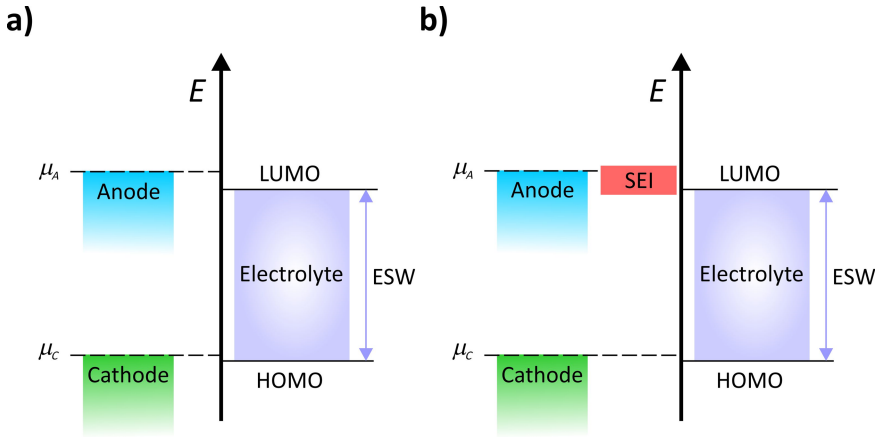

Figure 1.3. Relative energies of a liquid electrolyte and the electrodes in an electrochemical cell **a)** when anode potential lies outside the electrochemical stability window of the electrolyte and **b)** once SEI layer passivates the anode surface, stabilizing the interface between anode and the electrolyte. (μ_A: chemical potential of the anode, μ_C: chemical potential of the cathode, LUMO: lowest unoccupied molecular orbital, HOMO: highest occupied molecular orbital, ESW: electrochemical stability window).

This irreversible layer must be both ionic conductive and electronic insulating to avoid the continuous reduction of electrolyte[25], and it also needs to be adhered to the electrode and be insoluble in electrolyte, specially at high temperatures[41]. Furthermore, SEI must be both mechanically stable and flexible enough to expand and contract during cycling without breaking[42]. The composition of the SEI will vary depending on electrolyte and active material compositions. Using classical organic electrolytes and $LiPF_6$ salt, various organic and inorganic components have been identified in the SEI of graphite anodes: Li_2CO_3, LiOH, LiF, Li_2O, $ROCO_2Li$ and RCOLi, among others[43]. Same researchers that named the electrode-electrolyte interphase as SEI in 1979 proposed a heteropolymicrophase mosaic type morphology to represent the SEI layer in both graphite and lithium anodes[44] (Figure 1.4).

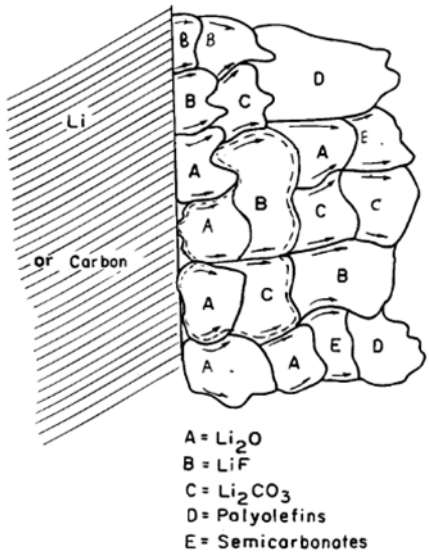

Figure 1.4. Schematic representation of a solid electrolyte interphase (SEI) formed upon graphite or lithium anode and composite solid organic electrolyte. [Reproduction with permission from[44], Copyright (2019) Journal of Electrochemical Society].

It has been proved that this mosaic model, under certain conditions, shows a bilayer structure: an inner layer dominated by inorganic compounds and an outer layer dominated by organic compounds[45]. The inner layer is assumed to be dense. The organic layer, in contrast, is assumed to be porous. However, this bilayer structure interpretation could be more complex in general, so the mosaic of micro phase model is believed to be a more appropriate model[42]. Indeed, modern

interpretations are still based on this model[46]. The estimated thickness of a standard SEI layer is assumed to be from around 20 Å to several tens of nanometers[45,47].

The SEI is directly influencing the battery performance, irreversible charge, rate capability, cyclability, and safety, as well as preventing graphite exfoliation when using this anode[43]. It has been proved that some additives enhance the battery properties, since they induce the formation of a more stable SEI[41]. A profound understanding of SEI formation, composition and evolution during cycling is essential if want to improve the performance of Li-ion battery. However, despite all the efforts to reach such level of understanding, the elucidation of the formation and evolution of SEI remains elusive[25,41].

1.3 Next generation Li metal batteries (LMB): role of Li metal

Li-ion technology, despite being the best rechargeable energy storage option so far, has an state of the art gravimetric energy density of around 260 Wh/kg[30], one order of magnitude lower than that of petrol. Moving to Li metal anode, Li metal batteries (LMB), is the only possible way to reach very high energy density systems based on Li chemistry. Li metal, as earlier mentioned, has a capacity of 3860 mAh/g, ten times larger than that of actual graphite anode, and it also operates at the lowest reduction potential known. Both parameters will increase the overall energy density of the battery according to equation (1.1). By replacing current anodes of Li-ion batteries with Li metal, this technology will be able to deliver ≈ 440 Wh/kg (Li-LMO batteries in Figure 1.5, where LMO refers to $LiMO_2$, M = Co, Mn, Ni).

Besides, emerging technologies postulated as next generation energy storage systems such as Li-air and Li-Sulfur batteries also rely on the use of Li metal as anode. With these technologies, the energy density of batteries could increase up to 650 Wh/kg for Li-S and 950 Wh/Kg for Li-air[15]. The comparison of the gravimetric and volumetric energy density delivered by these technologies is illustrated in Figure 1.5.

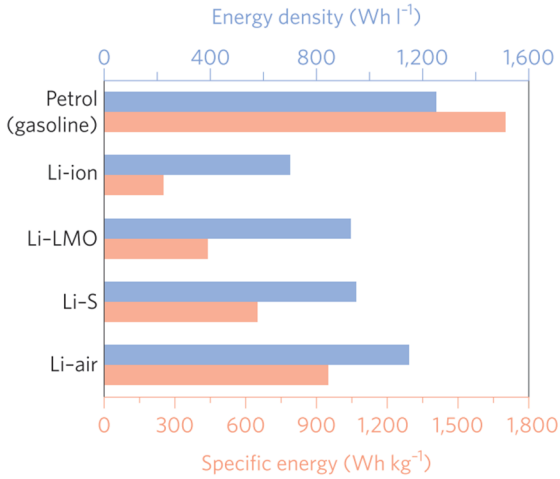

Figure 1.5. Comparison of practical specific gravimetric and volumetric energy density obtained by petrol, state of the art Li-ion batteries and next generation Li metal-based (LMB) batteries: Li metal - LMO batteries, Lithium-sulfur batteries and Lithium-air batteries. (LMO: $LiMO_2$, M = Co, Mn, Ni) [Reproduction with permission from[15], Copyright (2019) Nature Nanotechnology].

1.3.1 Li-sulfur and Li-air batteries

Both Li-sulfur and Lithium-air batteries cathodes are not based on intercalation reactions as in Li-ion batteries, but in conversion reactions. In a lithium-sulfur battery (Figure 1.6 for main components schematics of this battery), the reaction from sulfur (S) to lithium sulfide (Li_2S) incorporates two electrons per sulfur atom, which results in a cathode capacity up to 1672 mAh/g[48]. Several intermediates are formed during this reaction, summarized in Figure 1.6.

One of the biggest challenges of this technology is related to the formation of intermediate polysulfides that are soluble in the liquid electrolyte and can freely move from the cathode to the anode. This so-called shuttle effect results on the passivation of electrodes, loss of active material and self-discharge. Moreover, both Li_2S and S are insulating materials, so conductive additives need to be added to the cathodes in order to ensure electron percolation. Another problem of this technology is the volume expansion of about 80% happening when sulfur converts to Li_2S[49]. Nowadays, great efforts in research are carried out to overcome all these challenges of Li-Sulfur batteries[50,51]. Some niche technologies that use Li-S batteries can be found, as the Zephyr High Altitude Pseudo-Satellite (HAPS) Aircraft[52]. In this technology, the low cyclability of Li-S batteries is not a matter of

concern, the interest is to have high capacity during operation. However, for common applications this technology is still not competitive if compared with Li-ion batteries[53].

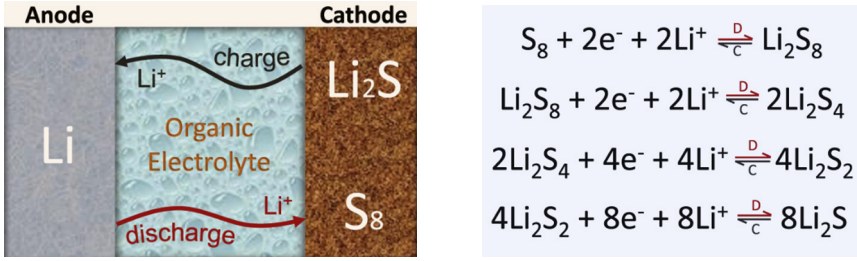

Figure 1.6. Schematic representation of a Li-sulfur battery and redox reactions occurring in the cathode during the discharge. [Reproduction with permission from[49], Copyright (2019) Journal of Power Sources].

Li-air batteries are very attractive due to their theoretical high energy density (Figure 1.5) and also due to having a freely available cathode fuel: O_2 gas, which although being a convenient gas, its filtering and handling needs to be solved. The typical product of the battery discharge in the cathode is Li_2O_2, where an oxygen reduction reaction takes place. During the charge, oxygen evolution reaction takes place in the cathode (Figure 1.7).

The cathode of this battery consists of a porous material, typically carbon with binder material such as the standard Li-ion batteries binder Polyvinylidene fluoride, or higher stability binder alternatives such as polyethylene[54]. In these cathodes special architectures with an adequate porous structure are necessary to avoid mass transport limitations. Several problems arise in these batteries, mainly related to the parasitic reactions that decompose both carbon electrode and electrolyte: rechargeability becomes poor, charge voltages high, efficiency low, and the cell ends up dying within a few cycles[55]. Finding new cathode designs to overcome these issues is becoming a big challenge due to the unresolved active reaction interface of electrochemical oxidation of lithium peroxide[56,57]. Even with all these problematics, the potential of this batteries is so high that researchers are still putting their efforts to find practical solutions[58]. What is more, the study of how to deal with the air components besides O_2 to avoid the purification of the air is being seriously considered in the development of the batteries[59].

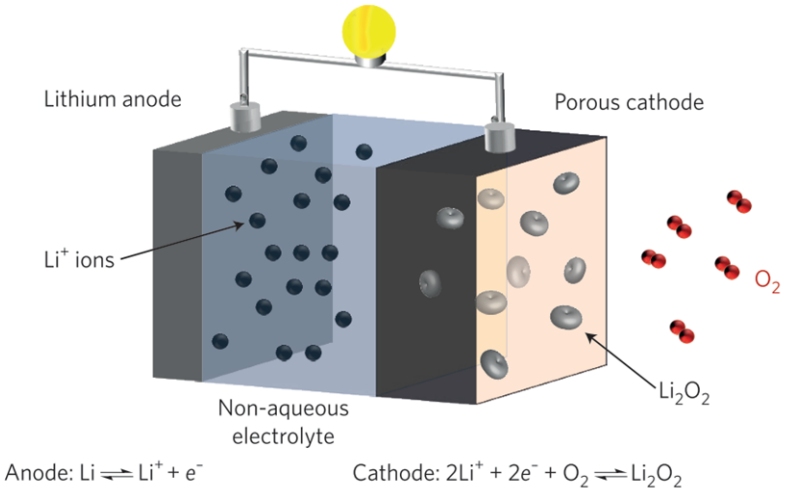

Figure 1.7. Schematic representation of a Li-air battery and the redox reaction happening during discharge and charge in both anode and cathode. [Reproduction with permission from[57], Copyright (2019) Nature Energy].

1.3.2 Li metal surface instability

In addition to the abovementioned intrinsic problems of lithium-sulfur and lithium-air batteries, another concern needs to be added to these technologies: having a Li metal anode that will result in handling and stability problems. Getting over the instability hazards arising from the high reactivity of lithium surface that hindered its commercialization back in 1980s is still one of the major drawbacks to achieve a real development of LMB.

In contrast to the current graphite anode, solid electrolyte interphase (section 1.2.3) formed on metallic lithium is not stable during the cycling of a cell, directly affecting the performance of the cell[60]. The low reduction potential of metallic lithium will reduce the electrolyte (practically any of them[61]) at the surface of the metal, forming an unstable SEI that will break during plating and stripping process due to volume changes of Li anode[15]. Fresh lithium will be then exposed to the organic electrolyte, forming a new SEI layer. The first SEI model, the mosaic one from Figure 1.4, was proposed both for carbonaceous and lithium metal anode. Analogously to the graphite anode case, for Li metal anodes two layers were also identified in this mosaic SEI: an inner compact layer close to the electrode mainly including inorganic species and an outer porous layer mainly composed by organic

material[62]. Here also, modern studies based their SEI interpretation in the mosaic model, as show in the Figure 1.8[63].

Significant surface research results summarized in a Li metal SEI review[47] have found that, using several organic solvents and salts, major inorganic compounds are Li_2O, Li_2S/Li_2S_2, LiOH, LiF, LiI, Li_3N and Li_2CO_3; whereas the organic ones are ROLi, RCOOLi, ROCOLi, $RCOO_2Li$ and $ROCO_2Li$ (R = alkyl groups).

This complex heterogeneous nature of SEI is rendering very difficult a proper quantitative characterization of SEI chemical composition, structure and mechanical properties. Still, both experimental and theoretical studies keep trying to elucidate the nature of the SEI due to the direct impact of this interphase in the performance of the cell[64,65].

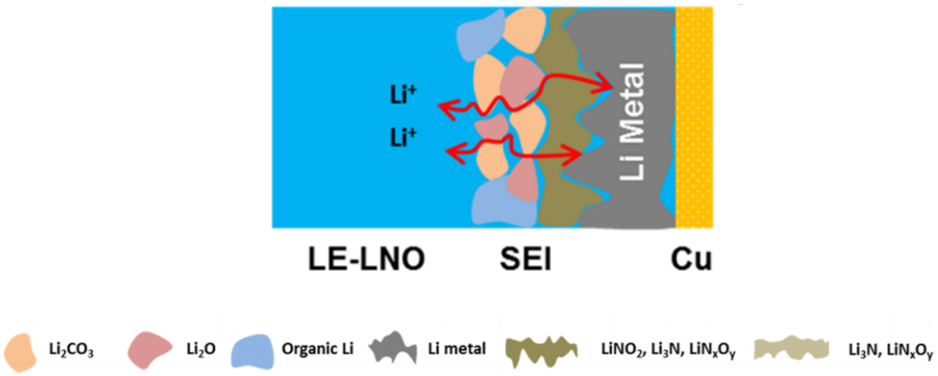

Figure 1.8. Schematic representation of Li plating and stripping effect on lithium metal surfaces based on the mosaic model for SEI interpretation, using organic carbonate liquid electrolyte (LE) with $LiNO_3$ (LNO). [Reproduction with permission from[63], Copyright (2019) Chemistry of Materials].

The other big issue related to the metallic lithium anode is the non-uniform electrodeposition of lithium in the anode during electrochemical cycling. When depositing, it grows forming whisker type structures, named as dendrites (Figure 1.9a). Although the ramified metallic electrodeposition from dilute salt solutions in high electric field was already considered an old subject in 1990[66], the difficult interfacial chemistry of lithium surface makes the explanation of dendrite growth complex. The heterogeneous SEI entails inhomogeneous nucleation due to different ion conductivity of the several compounds, and the cracks in the non-stable SEI increment the non-uniform deposition. In order to explain the self-enhanced nature of the dendritic growth several theories have been proposed.

One of them focused on the higher electric field at the tip of the bulges due to their curvature, which attracts more Li ions and thus forms further protrusions, evolving into dendrites[67]. If the dendrites grow perpendicular to the anode and pierce the separator, thermal runaway and explosion could occur due to the short circuit[68].

Another negative consequence of the dendrites is the loss of active lithium. When the dendrite detaches from the anode, it disconnects electrically. This lithium, surrounded by SEI, becomes inactive, and is usually called dead lithium (Figure 1.9b). Furthermore, the continuous accumulation of the dead Li creates tortuous diffusion pathways that affects the diffusion of Li ions[69].

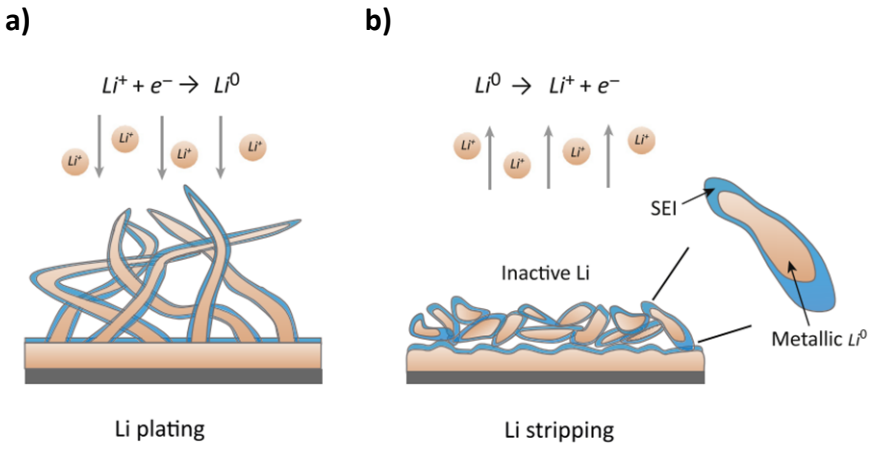

Figure 1.9. a) Dendrites formation as a consequence of non-uniform electrodeposition of lithium. **b)** Inactive dead lithium as a consequence of dendrite detaching from the anode, which decreases the amount of active material of the anode. [Reproduction with permission from[70], Copyright (2019) Cell Press].

From both SEI cracks and dead lithium that cause the loss of active material, main contributing factor to the low Coulombic efficiency is believed to be the dead lithium[71]. This parameter is defined as the ratio of the amount of charge that exits the battery during the discharge and the amount of charge that enters the battery during charge. Normally, in conventional carbonate organic electrolyte, the Coulombic efficiency is lower than 90%[70]. But even when reaching 99% of Coulombic efficiency with advanced electrolytes[72], the inefficiency remains being a problem. The goal for applicability that will allow to have more than 1000 cycles needs a Coulombic efficiency of 99.98%[73]. All these interfacial issues, besides the low coulombic efficiency, have also a direct impact in other parameters that

determine the electrochemical performance of the cell: cycle life is poor due to the loss of all active material or short circuit induced by dendrites, capacity fades related to the progressive active material loss and overpotential increases associated to the high internal resistance of the SEI[70]. Obtaining an appropriate dendrite growth model while understanding the nature of SEI are crucial to better define next strategies to design lithium metal batteries.

1.3.3 Artificial solid electrolyte interphases for Li metal anodes

When lithium deposits almost uniformly with minimal tortuosity instead of in whisker like structure and the SEI is stable and homogeneous, the loss of active lithium is mitigated and the overall performance of the cell improved[70]. In order to reach this goal, forming artificial interphases over lithium surfaces has attracted the attention of many research groups, which are focused on the growth of these layers usually called **artificial solid electrolyte interphase**. The ideal artificial SEI should satisfy same properties as the SEI, i.e., it needs to be both chemically and electronically stable with electron insulation, it is crucial also to have mechanical compliance and robustness, and a rapid and uniform Li-ion pathway is essential to avoid lithium nucleation induced by the inhomogeneous conductivity[74].

The strategies to stabilize lithium metal surface through artificial SEI layers can be categorized depending on the electrolyte type. Same electrolytes summarized in section 1.2.2 for Li-ion technology are currently being tested for LMB. If we focus on the solid and liquid electrolytes, as already explained, organic liquid electrolytes are the current choice because of their high conductivity. However, safety hazards related to their volatile and flammable nature foresee a future transition to solid electrolytes. With solid electrolytes safety is almost 100% granted, but their low ionic conductivity at room temperatures is slowing down their commercial applicability[75]. Furthermore, even the reaction with metallic lithium and solid electrolytes is less strong than with organic electrolytes, and the solid nature of them present a mechanical blocking to the dendrite growth, cell failures due to dendrites and interfacial instabilities are also found in this type of electrolytes[75,76]. Besides, the worse interfacial contact between the metal and the solid electrolyte at room temperature increases the interfacial resistance between them, so solutions when dealing with solid electrolytes need to consider adhesion issues also. Therefore, it is very convenient to separately evaluate strategies to stabilize lithium surface in liquid and solid electrolytes[77]. A summary

of several strategies used to form artificial SEI in Li metal during the last years is shown in Figure 1.10.

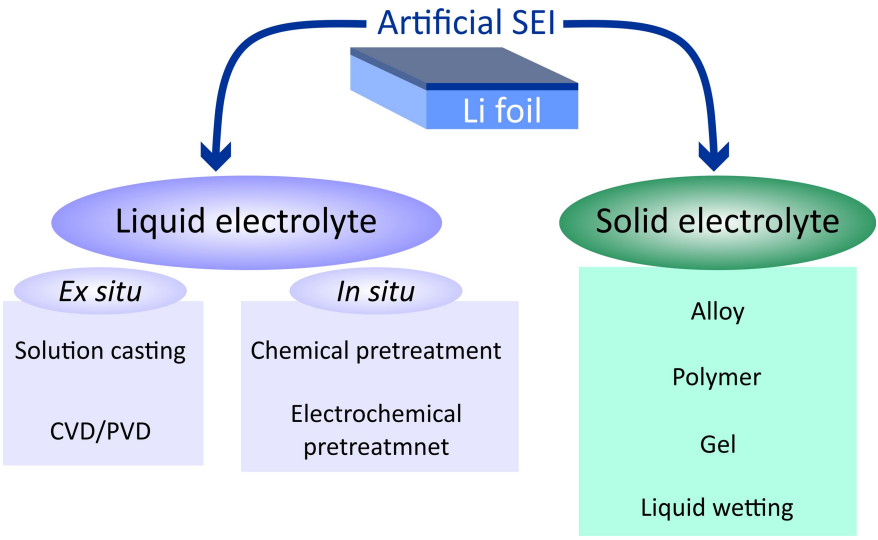

Figure 1.10. Summary of the main strategies used to form an artificial SEI that stabilizes the interface between lithium and electrolyte (CVD = chemical vapor deposition, PVD = physical vapor deposition). [Modified from[74]].

When dealing with liquid electrolytes, if the lithium metal is treated before the contact with the electrolyte, then the artificial SEI is formed *ex situ*. To form the *ex situ* artificial SEI, facile and effective solutions are the casting methods as doctor blade, spin coating, immersion and spray coating. When using more advanced approaches such as chemical vapor deposition (CVD), highly uniform and compact films in atomic-layer control can be obtained. Advantages of physical vapor deposition (PVD) are the tunable composition and control over the thickness of the layers, where widely used techniques such as magnetron sputtering can be employed. In the *in situ* formed artificial SEI, the interphase is formed when lithium gets in contact with the liquid electrolyte. Main advantage here is the enhanced contact of the interphase with the anode. However, the control of the composition and thickness is less precise than with *ex situ* methods. *In situ* artificial SEI can be achieved via chemical methods with pretreatment reagents (organic, inorganic and combination of both) or via electrochemical methods. In the last one, recycling experiments with specific parameters are used to modify

the surface of the lithium, obtaining artificial SEI with more complex structures and components[74,77].

One of the promising examples when dealing with liquid electrolytes is the hybrid silicate artificial *ex situ* SEI proposed by Liu et al[78]. This layer is made by chemical vapor deposition method under ambient conditions, with vapors of both methoxysilane and ethoxysilane catalyzed by LiOH and Li_2O on the surface of the lithium. Thanks to the hybrid nature, it has a hard-inorganic moiety to block the growth of the dendrites and enable good Li-ion conductivity and an organic moiety to enhance the flexibility (Figure 1.11). Lifetime of both Li-$LiFePO_4$ and Li-S batteries was proved to significantly improve within this protective layer with standard organic electrolyte used in commercial Li-ion batteries, 1 M $LiPF_6$ in ethylene carbonate/diethyl carbonate (v:v = 1:1).

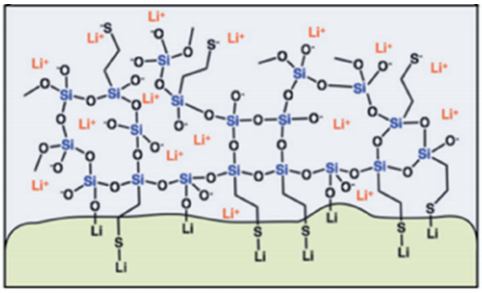

Figure 1.11. An organic-inorganic hybrid artificial *ex situ* SEI layer formed upon lithium surface by chemical vapor deposition. [Reproduction with permission from[78], Copyright (2019) Advanced Energy Materials].

In the case of the solid electrolytes, the ideal artificial SEI, besides considering the properties mentioned at the beginning of this section, it also should enhance the contact between the solid electrolyte and the anode to minimize the interfacial resistance[74]. Alloys, polymers, gels and liquid reagents are used to this purpose. Alloys are formed when depositing a coating layer on the electrolyte that reacts chemically with the lithium, generally following alloying reactions. These layers can both reduce the interfacial resistance and block side reactions between the lithium and the solid electrolyte. Polymers have better contact than ceramic electrolytes, so they can be used as buffer layers between the anode and the ceramic. The polymer-ceramic-polymer sandwich type electrolyte has been investigated since its proposal[79] as a solution to the interfacial problems. Gels,

materials that have both polymer and liquid plasticizer, deliver higher ionic conductivity than polymers. When dealing with liquid reagents, ion transfer in the interface accelerates, but the amount of it has to be well control to keep a safe system.

A very simple though effective artificial SEI to improve the interface between ceramic solid electrolyte and lithium metal is the atomic layer deposited Al_2O_3 in LLCZNO ($Li_7La_{2.75}Ca_{0.25}Zr_{1.75}Nb_{0.25}O_{12}$) electrolyte[80]. When this layer contacts the lithium anode, both Li and Al oxides are formed, improving the contact (Figure 1.12) and decreasing the interfacial resistance from 1710 Ωcm^2 to 1 Ωcm^2, effectively negligible. After the success of this pioneering research, the same approach with different interlayers has been also tested to enhance the interfacial contact with LLZO ($Li_7La_3Zr_2O_{12}$) electrolyte as Sn[81] and Au[82,83].

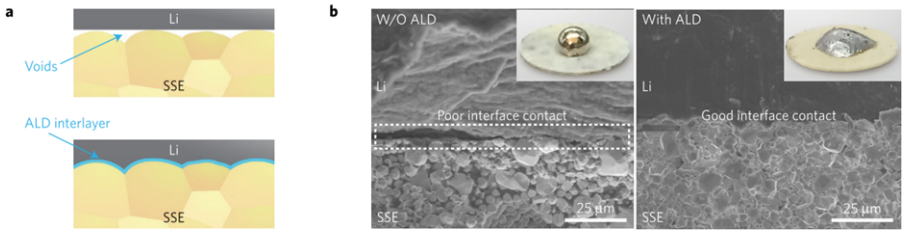

Figure 1.12. a) Schematic of the effect of adding Al_2O_3 by atomic layer deposition (ALD) between LLCZNO ($Li_7La_{2.75}Ca_{0.25}Zr_{1.75}Nb_{0.25}O_{12}$) solid state electrolyte (SSE) and lithium metal. **b)** SEM images of the interface with and without the atomic layer deposited Al_2O to prove the better interface contact with the modified interface. Inset photos with melted lithium shows the effect of having an atomic layer deposited Al_2O_3 on the wetting. [Reproduction with permission from[80], Copyright (2019) Nature Materials].

1.3.4 Considerations of Li metal-based energy demand

Lithium is used for a wide variety of purposes. In 2018, consumption of this metal in batteries was 46% of total consumption, rest of it was distributed in ceramic and glass (27%), lubricating greases (7%), polymers (5%), casting mold powders (4%), air treatment (2%) and others (9%) such as stabilizer for bipolar disorder[84]. Therefore, if an energetic transition occurs in next few years and lithium becomes the anode of choice, several considerations need to be addressed.

Main concern is related to the availability of lithium. Figure 1.13 indicates the countries which has lithium reserves. When talking about the availability of a

mineral, two terms need to be defined: resources and reserves. Resources refers to the amount of minerals that are known to exist in a deposit and their grade and quality is reasonably well defined. Reserves are the quantity of mineral that can be economically and feasibly extracted from the resources[85]. The estimated global lithium resources in 2017 was 34 Mt (Megatonnes)[86], and the value increased to 53 Mt for the estimation of resources in 2018[87]. This variation reflects the existence of an uncertainty on the quantification of the resources. Today, approximately 59% of resources are found in brines and 25% in minerals. About 50% of extraction is coming from brines, 40% from minerals and 10% form clay deposits and other resources[85].

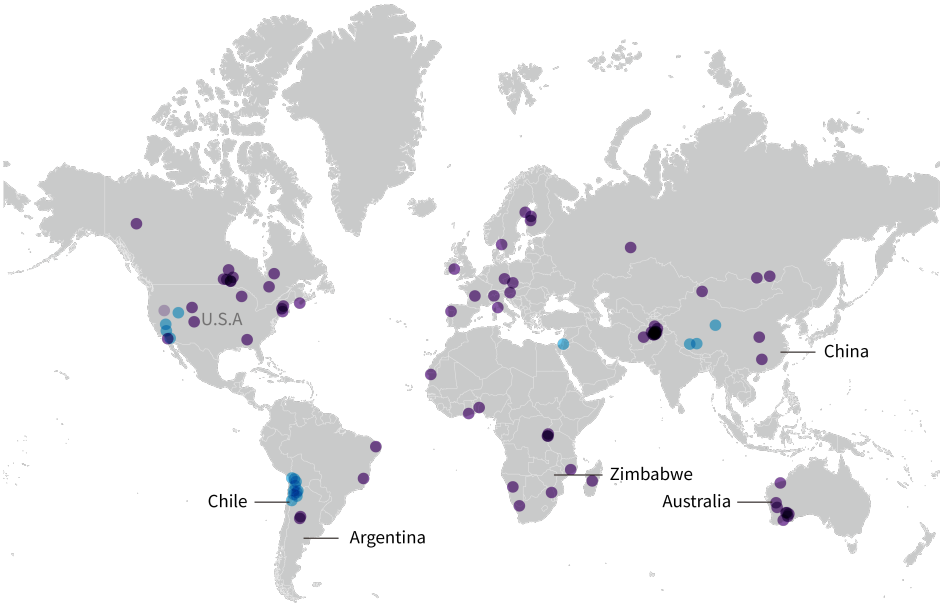

Figure 1.13. Location of known lithium reserves by 2018. Dark purple represents the mineral reserves, light purple lithium clay reserves and blue represent the brine reserves. In 2018, Chile was the country that produced more lithium, followed by Australia, Argentina, China and Zimbabwe[88].

Most abundant brines to obtain lithium are found in the Salars (brine aquifers) of the Andean mountain in South America, concentrating the 50% of global lithium reserves in three countries: Argentina, Bolivia and Chile. Both Argentina and Chile produce lithium, being Salar de Atacama in Chile the largest producer of lithium. By contrast, the country that holds, by far, the largest reserves of lithium on earth remains unmined. Estimations for the Salar de Uyuni in Bolivia predict it could hold

up 25% of world lithium reserves[85]. Regarding the minerals, the three main global suppliers are Australia, Canada and Zimbabwe, where Australia is the largest producer. Besides, Australian production is believed to increase 23% by 2020-2021 owing to several new mines[89]. A country that could play an important role is Afghanistan if its vast mineral resources are utilized and geopolitics favor this process. At present, European Union only produces the 1 to 2% of worldwide lithium in Portugal[85]. Attempts to exploit new mines are currently on going, such as the second largest European lithium deposit located in Spain[90].

Some authors believed there will not be enough lithium to meet future demands[91]. By contrast, other studies conclude there will be enough lithium to meet the demand until 2050[92,93]; and by then, lithium recycling will be already an established industrial process that will help to equilibrate offer and demand[85]. Nowadays, recycling only accounts for less than 1% of the total lithium consumption[91]. There is not enough need for incentivizing its recover due to its relative abundance and ease of extraction. But, unlike oil, lithium is relatively easy to recycle due to its low melting point (180 °C) and low solubility of several derived compounds as fluoride, carbonate and phosphate[94]. Other studies assume that mineral deposits will be offsetting any deficit in the lithium production, and the vast resources of lithium in the world, widely spread in several countries, should be enough to meet the demand[85].

The lithium supply market in 2018 was mostly controlled by four companies: Albermarle, SQM (*Sociedad Química y Minera de Chile*), Tianqui and FMC Lithium[95], recently changed to Livent Corporation[94]. Albermale acquired Rockwood Holdings in 2015, which was the owner of the two largest lithium deposits in Chile[95]. China, despite having its own resources, is importing massive amounts of lithium, controlling almost half of the world lithium production in 2017 with companies like Tianqi[85]. This oligopoly could change if countries such as Afghanistan and Bolivia start to exploit their resources. Especially Bolivia, due to its vast amount of resources, could become a determinant country for the future energetic transition. Responsibility of market dominant enterprises and countries, and respect towards their political decisions on how to mine their lithium are essential if adverse consequences are to be avoided on the development of the country and its society, as earlier happened in oil rich countries.

1.4 Scope of the thesis

In order to move to next generation lithium metal batteries, the unstable interface between lithium and electrolyte needs to be addressed. Most efforts pursuing this objective are focused on finding an appropriate artificial SEI. However, little attention has been paid so far to the influence lithium native surface exerts in the stability of the interface. The aim of this dissertation is to understand how atmospheric gases modify the surface of metallic lithium and analyze which is the real pristine surface of a battery grade commercial lithium foil to finally see to which extent the preexisting impurities are affecting the interface, which will ultimately drive the electrochemical performance of the cell. In order to do that, the interaction of lithium foil with main pure atmospheric gases (O_2, CO_2 and N_2) is studied using spectroscopic techniques, and the electrochemical performance of an impurities free surface and a standard surface is compared in a symmetric solid electrolyte system.

CHAPTER 2

Experimental techniques

In this chapter, fundaments of the experimental techniques used to develop the work presented in this thesis are introduced. Chapter is divided in four sections. Firstly, techniques employed to grow thin film are presented. In the second section, the method applied to modify surfaces is explained, and after that surface characterization techniques are detailed. Lastly, a description of the electrochemical characterization techniques can be found.

2.1 Thin film growth

Two physical vapor deposition (PVD) processes were used to grow thin films. These techniques are based on moving atoms in gas phase from the target material in solid phase to the growing film, also solid phase. The vaporization of the target atoms in this thesis has been produced either by applying heat (thermal energy) or by cathodic pulverization (sputtering).

2.1.1 Thermal evaporation

Vacuum thermal evaporation is the most basic physical vapor deposition process. The element to be evaporated is placed in a metallic crucible, which is heated by passing a current (i) through it, according to Joule effect. The amount of heat generated is then:

$$Q = i^2 r \qquad (2.1)$$

where r is the parallel resistance of the crucible and evaporant combination at the evaporation temperature.

Under perfect vacuum conditions and considering a single-component evaporant material, the maximum molar flux of substance from the solid phase to its gaseous form is expressed by the Hertz-Knudsen equation[96]:

$$J_{v,max} = \frac{P}{\sqrt{2\pi MRT}} \tag{2.2}$$

where M is the molecular weight of the evaporating compound, R is the universal gas constant, T is the absolute temperature at the evaporant surface and P is the standard vapor pressure of the evaporant, which is a function of the absolute temperature. The relationship between the evaporation flux and maximum evaporation flux is correlated by the evaporating coefficient (α_v) according to:

$$J_v = \alpha_v J_{v,max} \tag{2.3}$$

Most metals have atomic vapors and evaporating coefficient is equal to one. When evaporating an alloy, which is a solid solution or a mixture of solid phases, the evaporated flux will be richer in the more volatile element for any composition, so the melting will continue to deplete in that element as evaporation proceeds. Compounds have a very different evaporation behavior compared to alloys. In contrast with alloys, they have a specific ratio of elements, that is, they have a specific stoichiometry, and during evaporation they can evaporate as molecules, partially dissociated or dissociated completely upon evaporation. This last behavior is very practical when evaporating alkaline metals, because their low sublimation point makes them inappropriate for use in high vacuum evaporators which are usually baked out at temperatures above 100 °C. With an intermetallic compound, the very low sublimation temperature can be significantly increased by high melting intermetallic alkali compound of high enthalpy of formation[97].

One of the main problems of thermal evaporation is the contamination, both crucible material and evaporants release contaminant vapors from their surfaces and from the bulk. Much of the volatile impurity content in the evaporant can be removed before film evaporation, which includes adsorbed gases and dissolved elements of higher vapor pressure than the evaporant. For their removal, crucible is heated at a temperature below evaporation temperature of evaporant, where

the dissolved impurities will progressively deplete relative to the evaporant, purging the evaporant.

2.1.2 Magnetron sputtering

In this process, represented in Figure 2.1, a solid target is sputtered by energetic ions of inert gases (e.g., argon) from a magnetically enhanced glow discharge. The sputtered material is deposited on the substrate, which is placed opposite the target. A crosswire magnetic field incorporated over the target traps secondary electrons near the target surface. Then, electrons path length is greatly increased before they finally escape to the substrate. When the substrate is electrically insulating, radiofrequency (RF) bias instead of direct current (DC) bias must be used.

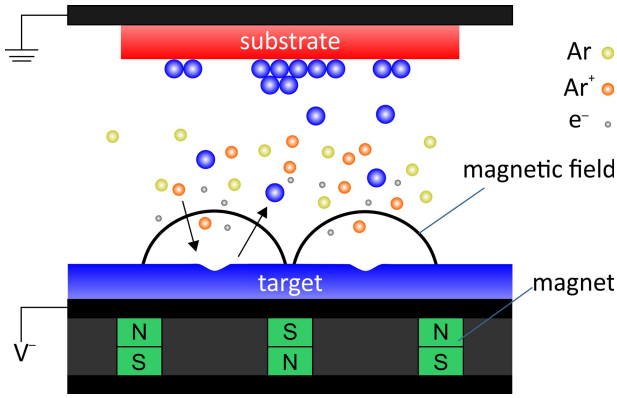

Figure 2.1. Schematic cross section representation of a magnetron sputtering process.

2.1.2.1 Sputtering instrument

The sputtering instrument used in this thesis is a Pfeiffer Classic 500 SP, which consist of a process chamber with 5 magnetron heads: 3 DC power supplies and 2 RF power supplies. The system is part of surface analysis unit of CIC Energigune and it can reach a base pressure of 10^{-8} mbar. The instrument is equipped with a fast entry chamber that allows keeping good vacuum levels. In addition, the fast entry chamber has a modification that enables the attachment of an air tight transfer system for sensitive samples.

2.2 Surface modification

In this thesis work, surfaces were modified by ion bombardment for two purposes. On one side, this technique was used to remove impurities from the surface. On the other side, surface chemistry was modified bombarding it with reactive ions.

2.2.1 Ion bombardment

The impingement of energetic ions or atoms upon a solid surface produces a variety of effects related to the high efficiency energy transfer of this process. The amount of kinetic energy transferred from the ion to the target atom is defined by:

$$T_m = \frac{4m_i m_t}{(m_i + m_t)^2} E_i = \gamma_m E_i \qquad (2.4)$$

where m_i is the mass of the impinging particle, m_t is the mass of the target atom, E_i is the kinetic energy of the impinging ions and γ_m defines the efficiency of the energy transfer process between the bombardment ions and target atoms. If the masses are within two times each other, γ_m is > 0.9.

The ways in which bombarding ions can move surface atoms can be grouped in surface and subsurface processes. Surface processes are usually in the range from few eV to tens of eV. One of the surface displacement process is very useful if the aim is to remove contaminants from the surface of our sample. During this process an inert gas is used to bombard the sample surface, and the adsorbed impurity receives enough vibrational energy to break its bond to the surface and desorbs (Figure 2.2a). Special care has to be taken with the energy of the ions, because if it is too high, the contaminant, instead of being removed, can be implanted on the subsurface (Figure 2.2b).

When the ion bombardment energy exceeds a few tens of eV, then particle penetration into the bulk material begins, and one of the most important subsurface phenomena that appears at this point is the ion implantation (Figure 2.2c). When working with an inert gas, implantation is generally undesired, main purpose is the removal of surface contamination. However, it can be used to incorporate a desired dopant or even to form a compound film if the impinging ion is reactive. This last one is called reactive implantation.

In the ion sources, gas ions are produced, focused, accelerated and emitted as a narrow and intense beam towards the sample. In all types of ion sources, the ions are generated by an electric discharge that goes through the gas at low pressure. Ions are produced by electron collision inside ionization cavity forming an electron ion plasma.

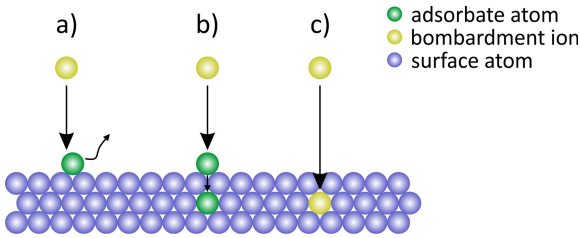

Figure 2.2. Typical surface and subsurface process generated by ion bombarding. **a)** adsorbate removal process, **b)** knock-on implantation of an impurity atom and **c)** ion implantation.

2.2.1.1 Ion source instrument

Ions sources used in this thesis are IQE 11 and IQE12/38, both from SPECS GmbH. Both sources generate and extract ions, but second type also focus and deflect the ion beam using a double lens system and deflection plates. IQE 11 is used for the reaction implantation processes and IQE12/38 to clean surfaces by Ar ion sputtering.

2.3 Surface Characterization

Several techniques were used in order to characterize the surfaces studied in this thesis. Chemical composition was determined by X-ray photoelectron spectroscopy. To study the electronic configuration, ultraviolet photoelectron spectroscopy was used. Lastly, information about the morphology and thickness of thin film samples was obtained by scanning electron microscopy.

2.3.1 X-ray photoelectron spectroscopy

X-ray photoelectron spectroscopy (XPS) is widely used to determine the chemical composition of the surface. It consists of an X-ray source that irradiates the sample under study with photons that excite electrons from the core levels of the atoms of a solid sample into the vacuum. Thus, XPS probes the electronic structure of matter with elemental sensitivity and chemical state specificity. The photon

penetrates into the sample surface and is absorbed by a core electron with a binding energy below the energy difference between the photon energy and the vacuum level. Then, electron emerges from the solid with a given kinetic energy as determined by the photoelectric effect. The kinetic energy (KE) of emitted electrons in the sample is determined by:

$$KE = h\upsilon - BE - w_{f,s} \tag{2.5}$$

where $h\upsilon$ is the photon energy, $w_{f,s}$ the work function of the sample and BE the binding energy of the excited electrons.

The kinetic energy of these electrons is measured, in our case, by a photoelectron hemispherical analyzer (HAS). Figure 2.3 shows the main parts of the HAS analyzer system. It consists of two metallic hemispherical plates concentrically arranged. A set of electrostatic lenses collects the emitted photoelectrons and focuses them onto the analyzer entrance slit. Electrons are retarded by a potential difference *R* inside the lens system until they match the electrostatic field of the hemispherical analyzer. This field is called the pass energy and it is applied between the inner and outer hemispheres of the analyzer so that trajectory of the incoming electrons is bent into a curve. A channeltron type electron multiplier (detector) is situated behind the exit slit of the analyzer and counts the emerging electrons. Therefore, by scanning *R*, spectrum of the photoelectron intensity as a function of kinetic energy can be recorded, the measured kinetic energy being the sum of *R* and pass energy. One way to increase the energy resolution of the analyzer is decreasing the pass energy; however, the collected intensity will decay. The hemispherical analyzer and transfer lenses can be operated in two modes, namely Fixed Analyzer Transmission (FAT) and Fixed Retard Ratio (FRR). In FAT mode, the pass energy is held constant, transfers lenses are in charge of retard the kinetic energy channel to the one accepted by the analyzer. In FRR, the constant value is the initial electron energy and analyzer pass energy ratio. First one is most used in XPS systems because the energy resolution is constant for the whole spectrum.

The HAS is characterized by its own work function. A contact potential exists between the sample and the analyzer when both are electrically connected, if the sample is electrically conducting, the Fermi energies of sample and analyzer are aligned. Consequently, kinetic energy (KE') of electrons collected in the analyzer is affected by the contact potential, yielding in:

$$KE' = h\upsilon - BE - w_{f,s} + \left(w_{f,s} - w_{f,a}\right) = h\upsilon - BE - w_{f,a} \tag{2.6}$$

where $w_{f,a}$ is the work function of the sample. Then, the measured kinetic energy is determined by the photon energy, the binding energy and the work function of the analyzer. A schematic of energies of core level photoelectron spectroscopy is shown in Figure 2.3.

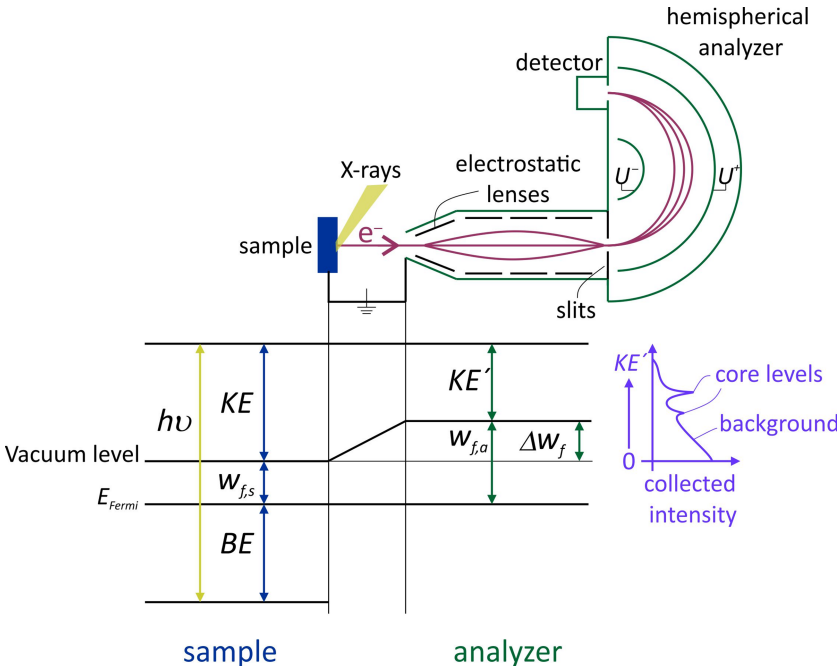

Figure 2.3. Energy level diagram of core level photoelectron spectroscopy from a solid. Energetic level terms are explained in the text. A schematic of a hemispherical analyzer is also drawn, showing the path of electrons from the sample to the detector. There is an example of a typical XPS spectrum in the right side of the figure.

The measured KE spectrum is a superposition of primary electrons and secondary continuum electrons. The primary electrons result from elastic collisions and are featured as distinct spectra (peaks), these primary electrons are the ones that contain the information about the core levels of the sample elements including their oxidation state. Secondary electrons are primary electrons that undergo inelastic collisions resulting in a reduction of their kinetic energy. They have a more or less continuous energy spectrum.

As said previously, the photoemission process relays on the interaction between one X-ray photon and one core level electron. Conventional X-ray sources are based on the bombardment of a solid target with high energy electrons. The

emission from this target consists of characteristic X-ray emission lines associated with the filling of core holes created by the incident high energy electron beam. Electron energy is generally chosen to create holes of K-shells. The ideal energy photon source should have low background and narrow characteristic line emission, the nearest to a monochromatic source. Another important feature of the target is its capacity to dissipate heat, which will facilitate the cooling down process needed because of the incident electron beam bombarding the target. Most used materials that have appropriate characteristic to fulfill the previous mentioned criteria are Mg and Al. Both of them have a dominant $K\alpha_{1,2}$ X-ray emission line, at 1253.6 eV for Mg and 1486.6 eV for Al. These emissions also have other lines associated with doubly and multiply ionized atoms. Table 2.1 shows the energies of main emission lines when using Mg as target to produce X-rays.

Table 2.1. X-ray emission line energies for a Mg source. Most pronounced characteristic line is $K\alpha_{1,2}$. Relative height of secondary lines is less than 9% of main line.

$K\alpha_{1,2}$ (eV)	$K\alpha_3$ (eV)	$K\alpha_4$ (eV)	$K\alpha_5$ (eV)	$K\alpha_6$ (eV)	K_β (eV)
1253.6	1262	1263.7	1271.2	1274.2	1302.3

One way to overcome the non-monochromatic nature of targets is adding a monochromator, which is a set of suitable crystals to create single or multiple Bragg reflections. The process leads in having just a part of the dominant $K\alpha_{1,2}$; however, this energy resolution improvement suffers from a considerable intensity loss.

2.3.1.1 XPS spectra main features

The emitted electrons are recorded according to their kinetic energy. To obtain chemical information, BE (obtained from equation (2.6)) is used to correlated the peaks with tabulated core levels of elements. Since the binding energy of a photoelectron is sensitive to the chemical surroundings of the atom: when changing the chemical environment, there will be a shift in the binding energy, which provides information to identify individual chemical state of an element. These peaks are named as nl_j, where n is the principal quantum number, l the orbital momentum quantum number and j the total angular momentum quantum number. *s* levels (l=0) give rise to a singlet peak (Figure 2.4a for Li 1s), but p, d and *f* levels (l>0) to a doublet (Figure 2.4b for Cu 2p), which arises from spin-orbit coupling (splitting) effects in the final state.

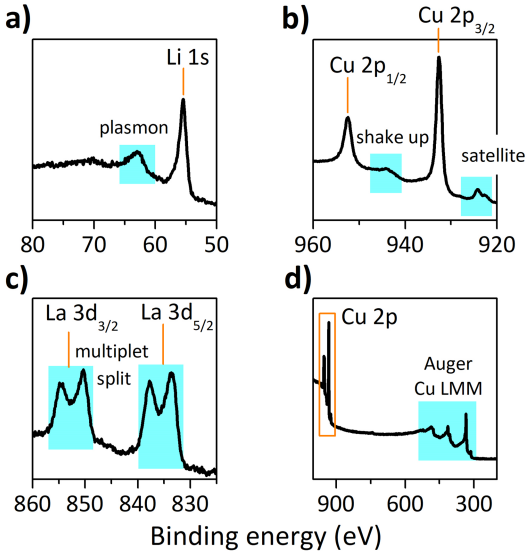

Figure 2.4. Example of different spectra features collected when measuring XPS using Mg K_{α} non-monocromatic source. Satellite from **b)** corresponds to Mg $K_{\alpha 3}$ and Mg $K_{\alpha 4}$ emission lines.

When an atom has unpaired electrons in the valence band, emission of an electron from core level arises in multiplet splitting: this is the result of coupling between the unpaired electron in the core with the unpaired electron in the outer shell, creating a number of final states which will be reflected in the measured photoelectron spectrum (Figure 2.4c)

Other important features that also appear on the spectrum are X-ray satellites, shake up lines, plasmon loss peaks and Auger electrons. X-ray satellites (Figure 2.4b) are a consequence of irradiation with a non-monochromatic X-ray source, where irradiation has not only the characteristic X-ray but also some minor components at higher photon energies, as shown in Table 2.1 for Mg. Thus, these minor components excite also core level electrons that appears at lower binding energies. Shake up peaks (Figure 2.4b) appear when the outgoing photoelectron interacts with a valence band electron and excites it to a higher energy level changing the kinetic energy of the emitted photoelectron. Shake up peaks have intensities of up to 5-10% of the main peak. The plasmon loss peak (Figure 2.4a) is a typical feature for some metals, where emitted electrons loss a specific amount of energy due to the interaction between the photoelectrons and delocalized electrons in the conduction band that are typically involved in collective oscillations, the so called plasmons.

Additional main features observed in a typical XPS spectrum are Auger electron peaks (Figure 2.4d), emitted due to relaxation process of the energetic ions left after photoemission process. The difference between Auger process and photoelectric process can be observed in Figure 2.5. In an Auger process, an outer electron falls into the inner orbital vacancy, and a second electron is emitted due to the excess energy of the process. The kinetic energy of the Auger electron is equal to the difference between the energy of the initial and final ion, which means, in contrast with the photoelectron energy, that Auger electron energy is independent from the photon energy and thus has a constant kinetic energy.

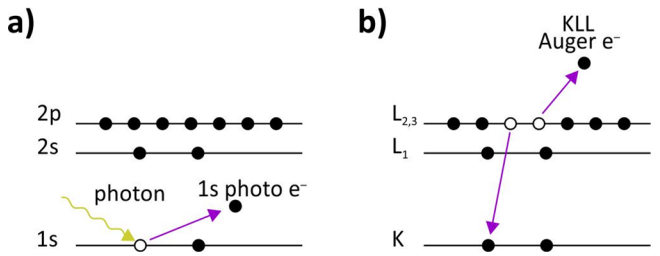

Figure 2.5. Diagram of **a)** photoelectric process and **b)** Auger process. Both processes are observed when measuring XPS spectra, but the kinetic energy of the outgoing electron depends on the photon energy only in the photoelectric process, being the Auger electron kinetic energy independent of the X-ray source.

2.3.1.2 Collected intensity and overlayer attenuation

The collected photoelectron intensity in the analyzer for the element A in a homogeneous sample is determined by physical, sample and instrument effects, all of them summarized in the following equation:

$$I^0 = TD_{eff}(A\cos\theta)\Delta\Omega F\sigma N\lambda \qquad (2.7)$$

T is the analyzer transmission function, a value that defines the collection efficiency for a specific operating mode of the spectrometer. D_{eff} is the efficiency of the detector, A is the analyzed area, θ is the emission angle of photoelectrons with respect to the surface normal, $\Delta\Omega$ is the analyzer solid acceptance angle, F is the flux of X-ray photons, N is the atomic density (number of atoms in unit volume), σ is the photoemission cross section for a given core level of element A and λ is the photoelectron inelastic mean free path. In this equation we are using the straight-line approximation for the electrons, where the photoelectron elastic scattering events are neglected[98]. Following, we are going to analyze in more

detail the parameters that are material dependent: the cross section and the inelastic mean free path (λ).

Cross section is the probability of photoionization, that is, the probability of an electron to reach the vacuum level from its initial energy level. This parameter is function of the photon energy, the element and the initial energy level of the photoelectron.

Inelastic mean free path is the average distance an electron with a given kinetic energy can travel through the material without suffering energy losses by inelastic scattering. Therefore, it provides an indication of the photoelectron escape depth. Figure 2.6 shows the inelastic mean free path of electrons at different kinetic energies for various solid materials. In the small λ values, even for the highest kinetic energies, lies the reason for XPS being a surface specific technique: only electrons from first atomic layers are able to leave the sample before being completely attenuated by inelastic collisions. As can be observed in Figure 2.6, there is a general trend for the dependency of the electrons mean free path and the kinetic energy, material dependence is weaker. An empirical universal curve was proposed for elements, inorganic compounds and organic compounds to calculate the λ based on the kinetic energy of the electrons[99]. A more accurate way to calculate the λ is using TPP-2M model, which considers also parameters from the material and is derived from fits to λ calculated for many solids from optical data[100,101].

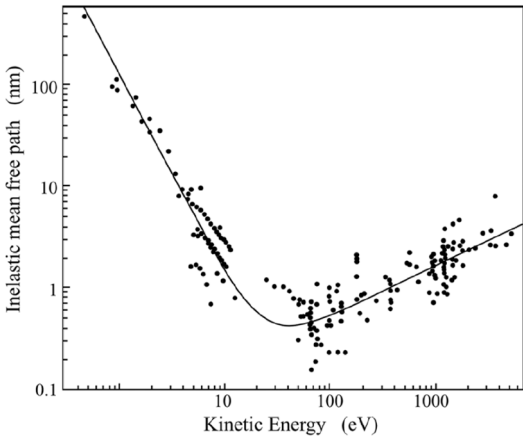

Figure 2.6. Inelastic mean free path of electrons for various materials as a function of their kinetic energy. The general trend observed is referred as the universal curve. [Reproduction with permission from[99], Copyright (2019) Surface & Interfaces Analysis].

The effect produced by an overlayer of material B in a photoelectron originated at the substrate material A is assumed to result in an exponential decay of the photoelectron intensity[102]. Then, attenuation will be defined by the following equation.

$$I_A = I_A^0 e^{-\frac{d_B}{\lambda_B \cos(\theta)}} \tag{2.8}$$

In this equation, I is the substrate photoelectron intensity after the attenuation, I^0 is the intensity that we would observe without the attenuation of the overlayer B as defined in equation (2.7), d is the thickness of the overlayer B, λ is the inelastic mean free path of the electrons when passing through the overlayer and related to the kinetic energy of electrons coming from A, and θ is the emission angle with respect to the surface normal.

The photoelectron intensity of the photoelectrons generated in the overlayer is going to be:

$$I_B = I_B^0 \left(1 - e^{-\frac{d_B}{\lambda_B \cos(\theta)}}\right) \tag{2.9}$$

Here λ is the inelastic mean free path of the electrons traveling through the overlayer B and related to the kinetic energy of electrons coming from B. If the energy of the electrons coming from the substrate and overlayer are similar we can assume that the inelastic mean free path of signal electrons in the overlayer are the same. Then, taking the ratio between the substrate photoelectron intensity (equation (2.8)) and overlayer photoelectron intensity (equation (2.9)), thickness of the overlayer can be determined:

$$d_B = \lambda_B \cos(\theta) \ln\left(1 + \frac{I_B I_A^0}{I_A I_B^0}\right) \tag{2.10}$$

If substrates and overlayer photoelectron intensities corresponds to the same element in two different chemical states, the parameters needed to calculate the photoelectron intensity ratio between the substrates and the overlayer without the attenuation, $\frac{I_A^0}{I_B^0}$, are just the atomic density and the inelastic mean free path of each element. In this situation, thickness of the overlayer can be calculated as:

$$d_B = \lambda_B \cos(\theta) \ln\left(1 + \frac{I_B N_A \lambda_A}{I_A N_B \lambda_B}\right) \quad (2.11)$$

When a new layer C is added on top of layer B and assuming again that the photoelectron intensities corresponds to same element in different chemical states, then the thickness of this top layer C is going to be:

$$d_C = \lambda_C \cos(\theta) \ln\left(1 + \left(\frac{I_C N_A \lambda_A}{I_A N_C \lambda_C}\right) e^{-\frac{d_B}{\lambda_B \cos(\theta)}}\right) \quad (2.12)$$

2.3.1.3 XPS instrument

XPS results presented in this work have been collected with a SPECS Phoibos 150 spectrometer using a non-monochromatic X-ray source and 3D-DLD detector system which combines a multichannel plate (MCP) in chevron mount followed by a two-dimensional delayline detection (DLD) array. As a result, this detector can deliver real count rates in cps with lateral resolution. The measurements were recorded with the analyzer in Fixed Analyzer Transmission mode so the resolution is the same for each measured spectrum. Mg K_α ($h\nu$ = 1253.6 eV) has been used as photon source. In this instrument configuration, the angle between the axis of the analyzer and the axis of the photon source is 55.44 °, the so-called magic angles. With this specific angle there is no need to correct the instrument angular distribution.

This instrument is located in a multitechnique surface analysis system available at CIC Energigune. It is a set of interconnected ultra-high vacuum (UHV) chambers with a base pressure of $1 \cdot 10^{-10}$ mbar where different surface analysis techniques and surface preparation methods are available (Figure 2.7).

To deal with air sensitive samples, a specific transfer tool has been used, which allows the transportation of the sample either in vacuum or in argon atmosphere. Figure 2.8 shows the transfer tool and the sample holder system used for XPS measurements. The transfer tool is coupled in the top CF port of the buffer chamber at the UHV multitechnique system.

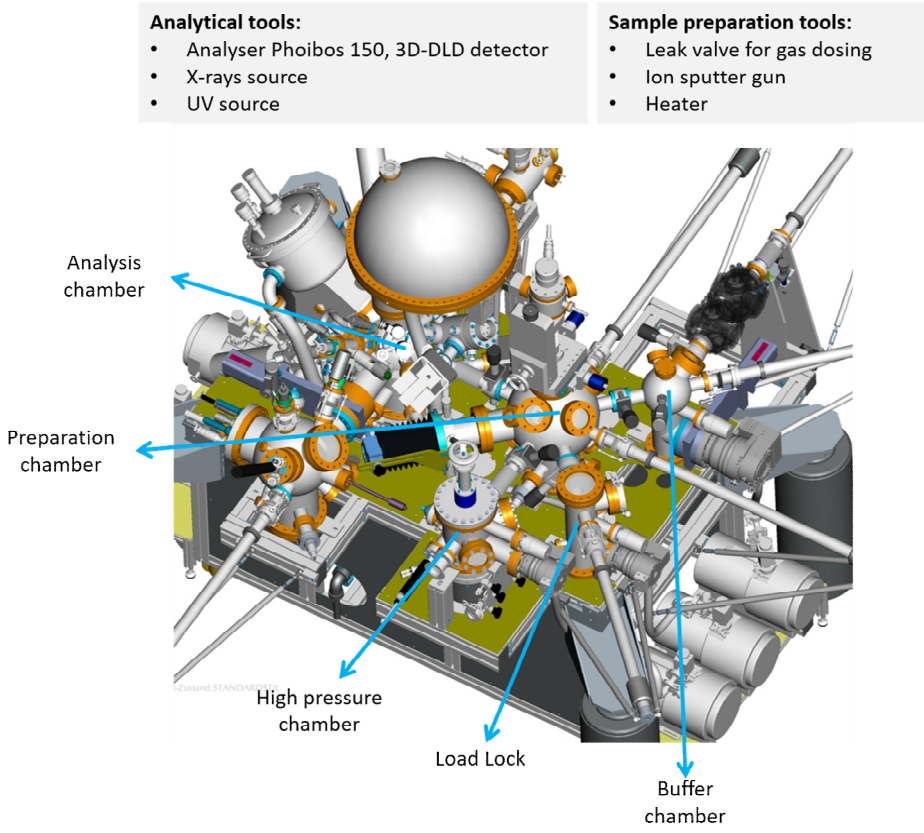

Figure 2.7. UHV multitechnique surface analysis system from CIC Energigune, where XPS measurements have been carried out.

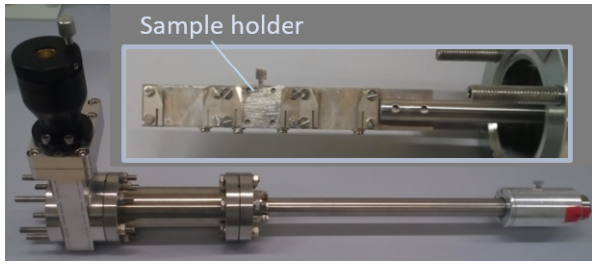

Figure 2.8. Transfer tool to move samples to and from the UHV multitechnique surface analysis system either in vacuum or argon atmosphere. The insight of the picture shows the inside of the transfer, which has three slots to move three sample holders at a time.

2.3.1.4 Spectra simulation

With the Nist Database for the Simulation of Electron Spectra for Surface Analysis (SESSA) software Auger electron and photoelectron spectra can be simualted for layered samples and for samples with selected nanomorphologies such as islands, spheres, and layered spheres[103]. The compositions and thicknesses can then be adjusted to find maximum consistency between simulated and measured spectra. To perform the spectra simulation, software contains parameters such as differential inverse inelastic mean free paths, total inelastic mean free paths, differential elastic-scattering cross sections, total elastic-scattering cross sections, photoionization cross sections, photoionization asymmetry parameters and electron-impact ionization cross sections in its database.

In this work, photoelectron spectra for layered samples have been simulated. Then, the ratio of the intensities of simulated spectra has been compared with measured spectra ratios for same elements, looking for the most appropriate surface layer thickness values. The information needed by the SESSA software are some instrument settings, those typically recorded by an experimentalist when actually performing a measurement, and an initial estimate of the sample composition and morphology.

2.3.2 Ambient pressure X-ray photoelectron spectroscopy

Despite all the useful information XPS provides about the composition of surfaces, this technique has been limited by the need to work under ultra-high vacuum conditions, where pressures are below 10^{-6} mbar. The need of ultra-high vacuum is related to the scattering electrons surfer when working at higher pressures. To overcome this issue, several instrumental developments have been added to the UHV XPS system, emerging the concept of ambient pressure XPS (APXPS) firstly introduced in 1970´s by Siegbahn and co-workers in Uppsala[104]. This technological refinement allows to follow the surface evolution under realistic conditions, positioning APXPS as one of the most powerful techniques to study surface phenomena.

Even if APXPS can be used to obtain photoemission spectra at relatively high pressures, the photoelectron detector still operates under UHV conditions, so it has to be separated from the ambient pressure conditions where the sample is placed. This separation is accomplished by adding a differential pumping system between the ambient pressure chamber and the analyzer with apertures from

which electrons and gas molecules escape. The pressure difference across this aperture depends on the size of the aperture, type of the gas, gas temperature and pumping efficiency, and it is typical of the order of 10^2 and 10^4 Torr. Small apertures spaced at large distance improve differential pumping but decrease the effective solid angle of transmitted electrons. In this kind of system, maximum operation pressure in sample environment is about 1 Torr. In order to be able to operate at higher pressures, electrostatic lenses are used to focus electrons through the apertures (Figure 2.9) allowing then the measurements of samples in environments with a pressure up to 10 Torr[105].

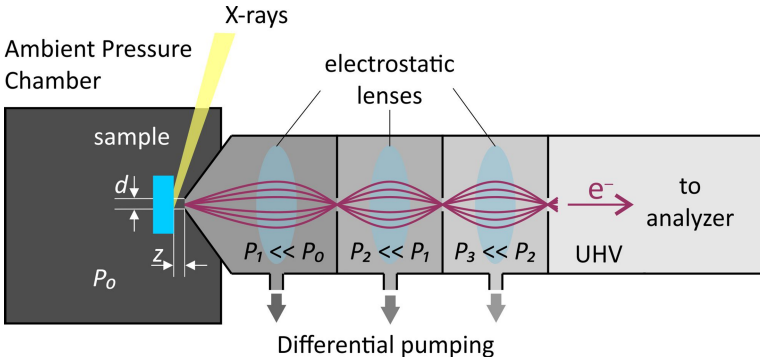

Figure 2.9. Schematic of APXPS differential pumping system. Sample is placed in a high-pressure chamber and electrons reach the analyzer under UHV conditions thanks to the differential pumping system between them. The diameter of the aperture (*d*) defines the optimal distance between surface and aperture (*z*)[105].

Similar to the attenuation produced by an overlayer mentioned in previous section (section 2.3.1.2), the attenuation of the photoelectron yield in gas environment has also an exponential decay according to:

$$I = I^0 \cdot e^{-z/\lambda_g} \tag{2.13}$$

where I is the photoelectron intensity from the material under study after the gas attenuation, I^0 is the photoelectron intensity that we would observe without the attenuation, z is the distance the electrons travel in gas atmosphere and λ_g is the mean free path of electrons in gas environment, which is defined as:

$$\lambda_g = \frac{kT}{P\sigma} \tag{2.14}$$

k is the Boltzmann constant, T the temperature of the gas, P the pressure of the gas and σ the electron scattering cross section.

Therefore, a way to decrease the attenuation of ejected photoelectrons is placing the sample near the aperture of differential pumping system. However, there is a minimum distance at which the sample should be kept in order to ensure a homogeneous pressure on the sample surface. This distance is correlated with the aperture dimension of the differential pumping system[105]. If both aperture and distance from sample to aperture are the same, then pressure at sample surface is 95% of chamber pressure and, if the distance is double that from the aperture dimension, the pressure at the surface is 98%. Therefore, the focal distance *z* at which electrons suffer less attenuation and surface pressure is same as chamber pressure is similar to the aperture dimension (Figure 2.9). Then, the smaller the aperture the more is reduced the path electrons need to travel under gas atmosphere. Standard apertures of APXPS system are less than 1 mm for the front aperture and 2 mm for the rest of apertures between differential pumping stages. With this technique it is also possible to collect the photoelectron signal from the gas phase; this is because X-ray irradiates not only the sample but also the gas.

Besides all the possibilities this technique offers to study solid gas interface, nowadays its design is being pushed to study also the solid liquid interface, using instruments that can work at pressures up to 110 Torr[106].

2.3.2.1 Synchrotron radiation

When X-ray spectroscopies use synchrotron radiation instead of laboratory-based X-ray tube as incident X-ray, more information about the surface can be obtained. Brilliance is a parameter that defines the photons generated per second divided by the light source footprint, divergence and bandwidth (BW). When comparing the brilliance obtained from each source, it is around 10^7photons/(s mm^2 mrad^2 0.1%BW) for a laboratory X-ray tube, whereas it is around 10^{22} photons/(s mm^2 mrad^2 0.1%BW) for a third-generation light source where the generated photon beam is highly collimated. Another important property of synchrotron radiation is its polarization and coherence, the emitted light is linearly polarized in the orbit plane and it can produce detectable wave-like effects. Furthermore, generated X-ray covers a wide spectrum, from microwaves to hard X-rays.

Most common synchrotron radiation sources are based on storage rings, where a beam of highly energetic electrons is stored and kept traveling on a circular path.

Relativistic accelerations on the electrons will result on the emission of an electromagnetic field, the so-called synchrotron radiation used as a light source for experiments (Figure 2.10).

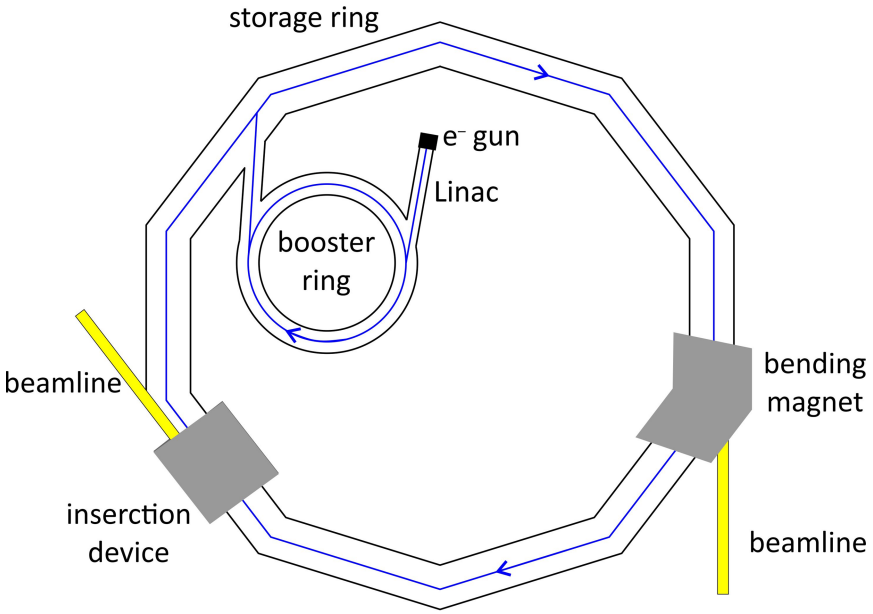

Figure 2.10. Schematic of a synchrotron radiation facility.

Electrons are produced inside the electron source and initially accelerated by a high voltage or radiofrequency field, these electrons are then feeded into the Linac (linear accelerator). The electrons are packaged in bunches and accelerated enough for injection in the booster synchrotron. This is a pre-accelerator where electrons are accelerated to their final energy in the order of GeV before being finally injected into the storage ring. The booster only works when the storage ring has to be refilled. In the storage ring, electrons travel at a constant relativistic speed. In order to recirculate the charged particles along a circular path, a magnetic field perpendicular to the horizontal orbital plane is used.

As the electrons travel around the ring, radiation is emitted whenever they are forced to deviate from a straight-line motion. Bending magnets were the first available sources to apply a magnetic field used to deviate electrons and, subsequently, generate synchrotron radiation. A way to increase the intensity of radiation generated by bending magnets is using wigglers, where a series of bending magnets are lineup enhancing the intensity simply by the number of

magnet poles. The spectrum generated by a wiggler is that of a bending magnet but with a higher brilliance, because the individual emissions of each magnet overlap and the intensity adds up. Most modern way to create synchrotron light is using undulators instead of wigglers, these are most powerful generators. They consist of a periodic arrangement of dipole magnets generating an alternating static magnetic field which deflect the electron beam sinusoidally, resulting in radiation with the wavelength of this periodic motion, differing from bending magnets and wiggles spectrum. Figure 2.11 compares the spectra brilliance of a bending magnet, wiggler and undulator of the Spring-8 synchrotron facility.

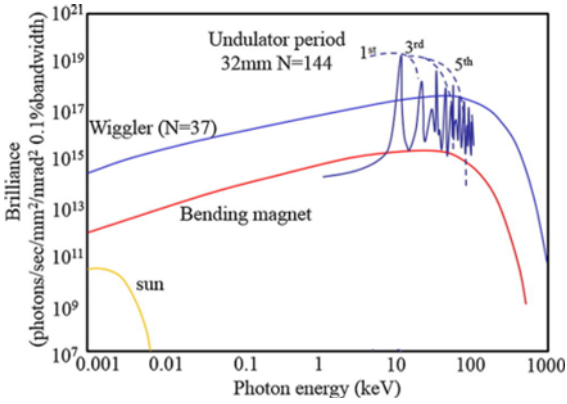

Figure 2.11. Brilliance of the SPring-8 synchrotron bending magnet, wiggler and undulator. The solid curve for the undulator shows the output at a fixed gap between top and bottom poles, the dashed lines the variation in the harmonic peaks as the gap is varied from 25 to 8 mm. Brilliance of sun has also been indicated in the figure. [Modified from[107]].

2.3.2.2 APXPS instrument

APXPS experiments present on this work were carried out using a Scienta R4000 HiPP APXPS system, which is placed at Beamline 9.3.2 Lawrence Berkeley National Laboratory's (LBNL) Advanced Light Source (ALS). This system is based on a Scienta R4000 with a two-dimensional detector consisting of two multichannel plates coupled to a phosphor screen and charge-coupled device (CCD) camera. It has four pumping stages, and the base pressure of the analyzer is low 10^{-9} Torr. The separation between the high-pressure chamber and first pumping stage is a removable Ti cone with a 0.425 mm aperture radius on the tip (Figure 2.12). The approximate focal distance of this instrument is 0.8 mm and it can record spectra above 2 Torr.

The 9.3.2 bending magnet beamline generates soft X-rays with an energy between 250 and 850 eV. A Si_3N_4 window isolates the UHV X-ray tube from the high-pressure chamber. The UHV system has also a preparation chamber which includes an ion gun for ion sputtering processes. An air sensitive transfer tool was used to move samples under argon atmosphere from an argon glove box to the load lock of the UHV system.

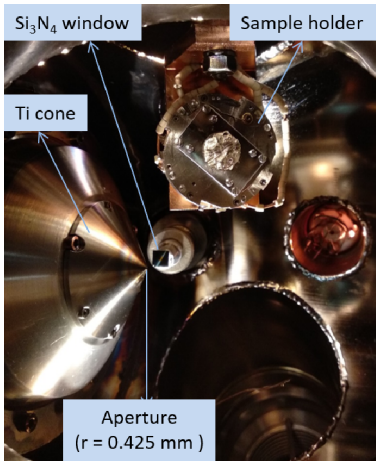

Figure 2.12. Picture of main chamber of APXPS system placed in beamline 9.3.2 at Advanced Light Source. The sample holder is a Thermionics STLC plate.

One of the main advantages of measuring APXPS spectra using synchrotron radiation, apart from the high-resolution spectra, is the capability to tune the energy of the source. When changing the photon energy, kinetic energy of ejected electrons from the same core level is also changed so photoelectrons generated at different depths in the sample surface can be measured and compared. Therefore, a nondestructive depth profile can be measured, which is essential to understand the distribution of the compounds on the surfaces under analysis. Furthermore, it is also useful to measure different core levels at the same kinetic energy for quantification reasons, because in that way we are ensuring that all electrons are coming from same depth.

2.3.3 Ultraviolet photoelectron spectroscopy

The basis of ultraviolet (UV) photoelectron spectroscopy (UPS) are the same as for XPS already explained in section 2.3.1, the difference relays on the irradiation

source: instead of using X-rays, photoelectrons are generated after excitation by ultraviolet light. Typical UV source is a He gas discharge line which can be operated to maximize the output of either He I (hν = 21.2 eV) or He II (hν = 40.8 eV). Because of this low energy, only valence levels can be probed, the ones having lower binding energies. These include the occupied band states of a clean solid surface as well as the bonding orbital states of adsorbed molecules. This technique is surface sensitive, but according to the attenuation of the low kinetic energy electrons (Figure 2.6), this attenuation is smaller than that of high kinetic energy electrons. In summary, UPS can probe deeper regions than XPS.

Apart from the study of valence band structure, another information that can be obtained by this technique is the value of the materials work function, which stands for the minimum energy required to withdraw an electron from a bound state into the vacuum level. A detailed explanation of the work function and its usefulness to study surface properties can be found in Chapter 3 section 3.1.2. The value of the work function corresponds to the difference in the photon energy and the energy of the secondary cut off (estimated with a linear fitting) related to the Fermi edge, as indicated in Figure 2.13.

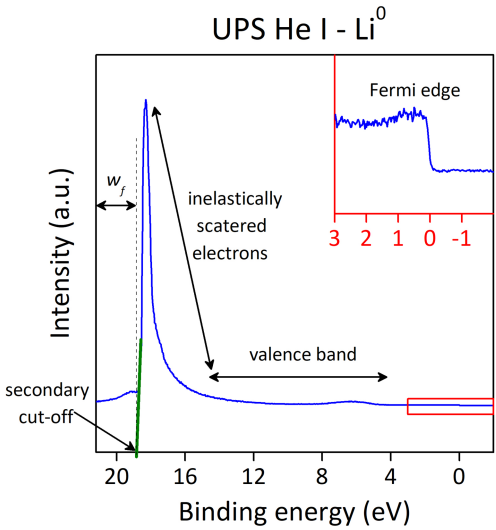

Figure 2.13. Work function (w_f) extraction from a UPS He I spectra. The UPS spectra corresponds to a clean lithium metal surface and it was obtained with the UV photons emitted by Helium gas with an energy of 21.8 eV (He I). The figure shows different regions of the spectra and how we can use it to obtain the work function of the surface. The inset is the enlarged spectra in the region of the Fermi edge. During data collection the sample was polarized -12 V to obtain a sharp secondary edge, the binding energy scale is calibrated according this polarization.

The determination of secondary edge can be tricky because electrons from sample at low kinetic energy overlap with electrons generated on the analyzer itself: these are generated when photoelectrons from the sample hit the internal surface of the analyzer which is typically coated with graphite. The analyzer electrons are not influenced by the contact potential between sample and analyzer, and they form a spectrum superimposed to the secondary edge of the sample spectrum. An easy way to avoid this overlap is applying a potential between the sample and the analyzer. Electrons from sample are going to be accelerated, separating the secondary edges. In Figure 2.13, the binding energy has been corrected, but in order to get a sharp secondary edge sample was polarized -12 V.

2.3.3.1 UPS instrument

UPS spectra were taken with a He I emission lamp (hν = 21.2 eV), SPECS UV10/35, and the same photoelectron analyzer used for XPS measurements from the UHV multitechnique surface analysis system at CIC Energigune (Figure 2.7). The helium gas used in the UPS lamp had a purity of 99.99% (Praxair). To increase the purity of the gas, the gas line was guided through a liquid nitrogen trap which acts as a cryopump reducing the amount of impurities in the gas; especially those with a condensation point above the temperature of liquid nitrogen.

2.3.4 Scanning Electron microscopy

In a scanning electron microscope (SEM) an electron beam generated by an electron gun is focused using electromagnetic lenses later accelerated onto the sample surface. UHV is needed to avoid interaction of electrons with air. When scanning the beam over the sample, secondary and backscattered electrons ejected by the incoming electron beam are collected in a specific detector for each type of electron, hence obtaining a magnified image of the surface. Secondary electrons are electrons ejected from the sample when the incident beam electrons transfer energy to the atom. Usually, their kinetic energy is lower than 50 eV. The image obtained is a magnification of the surface morphology. Backscattered electrons are electrons from the incident electron beam after interaction with sample atoms. The kinetic energy of backscattered electrons goes from 50 eV to almost the energy of the incident beam electrons[108]. Then, backscattered electrons are coming from deeper regions of the sample than secondary electrons. In contrast to the secondary electrons, backscattered electrons also contain information about the chemical differences of the surface

compounds: heavier elements can deflect incident electrons more strongly, hence those elements appear brighter in the images when compared to light elements.

When the sample is not conductive, an overcharging of the surface happens due to electron accumulation that cannot be drain to ground. Before measuring SEM, non-conductive samples are usually sputter coated with a conductive and inert metal, like Au. Enhanced spatial resolution of scanning electron microscope depend on design of the system, but they can typically achieve spatial resolutions below 1 nm owing to the shorter wavelength of electrons if compared to visible light. Hence, SEM allows to obtain higher resolution images than with an optical microscope.

2.3.4.1 SEM instrument

FEI Quanta-200FEG microscope from CIC Energigune has been used for the microscopy studies. In the field emission gun (FEG), electrons are emitted from the cathode by applying a high electric field near the filament tip. This technology generates electrons without heating of the gun which can induce problems.

An air sensitive transfer tool (Figure 2.14) with a specific coupling for the load lock of this instrument was used to deal with air sensitive samples and to move them from the inert atmosphere of a glove box to the vacuum conditions of the SEM.

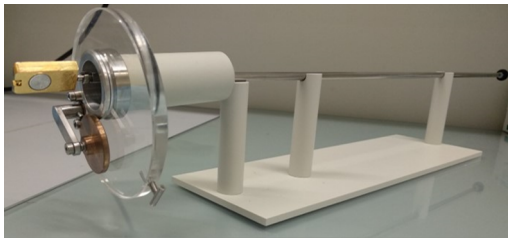

Figure 2.14. Air tight transfer tool to move samples from an inert atmosphere to the SEM microscope.

Another SEM microscope was also used for the measurements presented in this thesis work: Helios NanoLab 450S – FEI, from CIC Nanogune. The particularity of this SEM is that is has a Focused Ion beam (FIB) incorporated. The FIB is used to precisely etch or cut the sample, then the new exposed surface is measured by SEM. An advantage of this microscope is that a clearer cross section can be measured if cutting the sample by other methods presents difficulties.

2.4 Electrochemical characterization

For the electrochemical measurements, coin cells were assembled using a manual clamper in an argon atmosphere glove box. The type of coin cells used are CR2032 (20 mm diameter and 3.2 mm height). Different parts of a coin cell are specified in Figure 2.15.

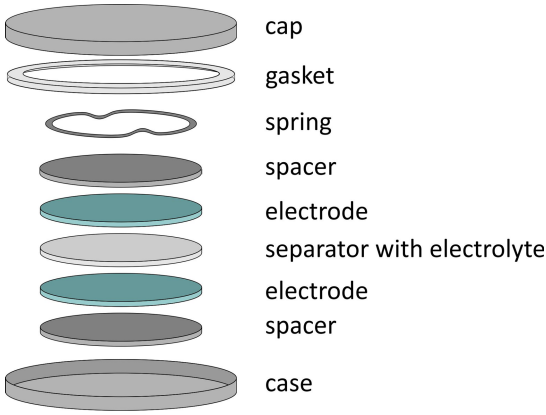

Figure 2.15. CR2032 type coin cell elements.

Case, cap, spring and spacers (current collectors) are made by 316L stainless steel, and the propylene gasket avoid the short circuit of the cell. Note that, when a solid electrolyte is used, there is no need for separator.

During this work, two types of CR2032 were assembled. In experiments involving full cells, conventional electrode configuration was used with positive and negative electrodes that deliver an open circuit voltage (OCV) which is the difference between the reduction potential of the electrodes. The second type of CR2032 assembly were symmetric cells. In this case, both electrodes are made of the same material, consequently, OCV of symmetric cells should be zero.

All the electrochemical measurements were performed using a Biologic VMP3 potentiostat tester from CIC Energigune. Following the electrochemical characterization methods used in each type of cell are explained.

2.4.1 Full cell electrochemical characterization

The electrochemical characterization techniques used in conventional two electrode systems were cyclic voltammetry (CV) and galvanostatic cycling. In a cycling voltammetry experiment, the intensity response of a working electrode

(the electrode under study) is measured while applying a voltage sweep using a constant scan rate (Figure 2.16). It provides information about the redox reactions, the voltage at which they occur and their reversibility.

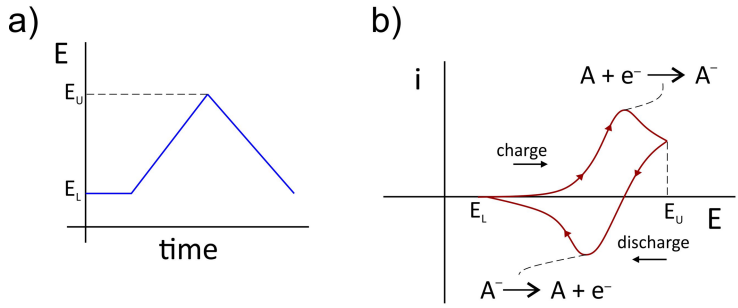

Figure 2.16. Example of a cyclic voltammetry experiment of one redox process for element A. **a)** Applied cyclic potential sweep to the working electrode and **b)** response of the working electrode resulting in a cyclic voltammetry. E_u indicates the upper limit of the voltage and E_L is the lower limit of the voltage, which corresponds to the OCV at discharged state.

In a galvanostatic cycling experiment, in contrast to the previous method, the current is controlled and held constant until reaching the upper and lower voltage window limits, and the potential becomes the dependent variable, which is followed as a function of time (Figure 2.17). Within this technique, we can also observe the voltage at which the redox reaction is happening: represented by a *plateau* in the plot.

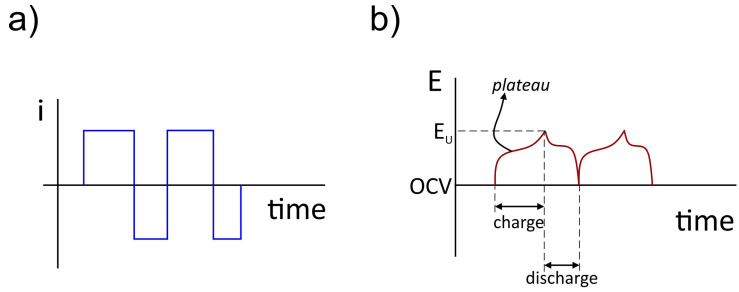

Figure 2.17. Example of a galvanostatic cycling experiment of one redox process for element A. **a)** Applied constant intensity until reaching the desired voltage in the working electrode and **b)** response of the working electrode. E_u is the upper limit of the voltage, and the plateau indicates a redox reaction process. Time needed for charge and discharge is not the same related to irreversible reactions.

Another important characteristic of this method is that it can be used to calculate the capacity of an electrode and compare it with the theoretical one. The theoretical capacity of an electrode is derived from the Faraday law according to the following equation:

$$Q = \frac{mnF}{M} \tag{2.15}$$

where m is the mass of the active material (g), n is the number of electrons involved in the electrochemical reaction per formula unit, F is the Faraday constant (96500 As/mol), and M is the molecular weight of the active material (g/mol). Units of theoretical capacity are (As), but normally the theoretical gravimetric capacity is used (mAh/g).

The time needed to reach the desired voltage at the applied intensity for the specific active material are data obtained from a galvanostatic cycling, and they can be used to calculate the capacity of the electrode and compare it with the theoretical one from equation (2.15). Another important parameter that can be obtained from this experiment is the coulombic efficiency, defined as:

$$\eta = \frac{Q_{out}}{Q_{in}} * 100 \tag{2.16}$$

where Q_{out} is the amount of charge that exists the battery during the discharge cycle, and Q_{in} is the amount of charge that enters the battery during charging cycle. This parameter indicates the capacity retention of the system.

Furthermore, the rate of the applied intensity can be changed to compare the capacity and capacity retention at different intensity rates (C-rates). Normally, the intensities used to cycle are related to the time needed to reach the theoretical capacity in one hour, which correspond to a rate of C. Then, nC rate will use an intensity n times higher than that for one hour, so it corresponds to fast charges/discharges. And C/n is related to the slower processes, where intensity will be the one needed to charge the battery n times slower than intensity of one hour.

2.4.2 Symmetric cell electrochemical characterization

The aim when studying symmetric cell performance was to analyze the stability of a cell and study the resistance of the interface. Two techniques were used for that:

galvanostatic polarization and electrochemical impedance spectroscopy (EIS). In the first technique, current is held constant and voltage is monitored. In the symmetric cells there is no redox reaction, so response of voltage should be stabilized and remained constant. Then, current is applied until certain time. The useful information obtained from the galvanostatic polarization in a symmetric cell corresponds to the number of cycles before the cells starts to perform badly and to the stability of the voltage (Figure 2.18).

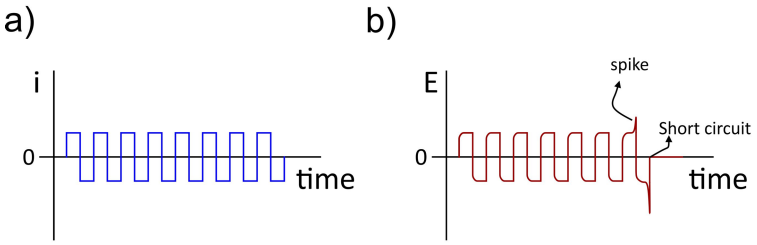

Figure 2.18. Example of a galvanostatic polarization experiment of a symmetric cell. **a)** Applied intensity and **b)** response of the working electrode. Spikes indicate a non-uniform plating/stripping and dendrite formation[109], and when cell is short circuited no more potential response is observed.

In electrochemical impedance spectroscopy (EIS), the cell is perturbed with an altering signal of a small current to observe the system response to the perturbation at steady state. An advantage of it is that measurements can be done over a wide frequency (or time) range, between 10^{-4} Hz to 10^{6} Hz.

Electrochemical impedance is usually measured by applying an alternating current (AC) potential to an electrochemical cell and measuring the current through the cell. When the excitation signal is small, the cell response is pseudo linear. Then, the current response to a sinusoidal potential will be the same frequency but shifted in phase. The excitation signal is defined as:

$$E_t = E_0 \sin(\omega t) \tag{2.17}$$

where E_t is the potential at time t, E_0 is the amplitude of the signal, and ω is the radial frequency, related to the frequency f as:

$$\omega = 2\pi f \tag{2.18}$$

In a linear signal, the I_t response of the system is shifted by ϕ phase and has I_0 amplitude:

$$I_t = I_0 \sin(\omega t + \phi) \tag{2.19}$$

The impedance is defined as,

$$Z = \frac{E_t}{I_t} = \frac{E_0 \sin(\omega t)}{I_0 \sin(\omega t + \phi)} = Z_0 \frac{\sin(\omega t)}{\sin(\omega t + \phi)} \tag{2.20}$$

It represents the ability of a circuit to resist the flow of electrical current and is expressed in terms of Z_0 magnitude and ϕ phase shift. These oscillating magnitudes can also be represented using complex numbers:

$$Z(\omega) = \frac{E}{I} = Z_0 e^{j\phi} = Z_0(cos\phi + jsin\phi) \tag{2.21}$$

If the real part of $\boldsymbol{Z}$ is plotted on the X-axis of a chart and the imaginary part on the Y-axis, a Nyquist plot is obtained. Each point of this plot is the impedance at one frequency. Analogies between the electrochemical cell and a model network of resistors and capacitors are a common way to analyze EIS data. The electrochemical model should have a basis in the physical electrochemistry system. Figure 2.19 shows an example of a Nyquist impedance plot for an electrochemical system and the equivalent circuit model of that system. At the high frequency region, first resistance (R_{bulk}) is correlated to the resistance of the electrolyte. This resistance can be used to calculate the conductivity $\boldsymbol{\sigma}$ of the electrolyte by the following definition:

$$\sigma = \frac{1}{R_{bulk}} \frac{d}{A} \tag{2.22}$$

where d is the thickness of the electrolyte and A is the area of the electrode.

At low frequencies, the interface between the electrode and the electrolyte is defining the response of the system by a semicircle which is characteristic of a single time constant element, which has a resistor and a capacitor in parallel. The resistor represents the resistance of interface and the capacitor represents the capacitance of the double layer of the interface. At the lowest frequencies, mass transfer is taking control of the process and the response of the cell can be modeled by a Warburg impedance, which represents the resistance to mass transfer.

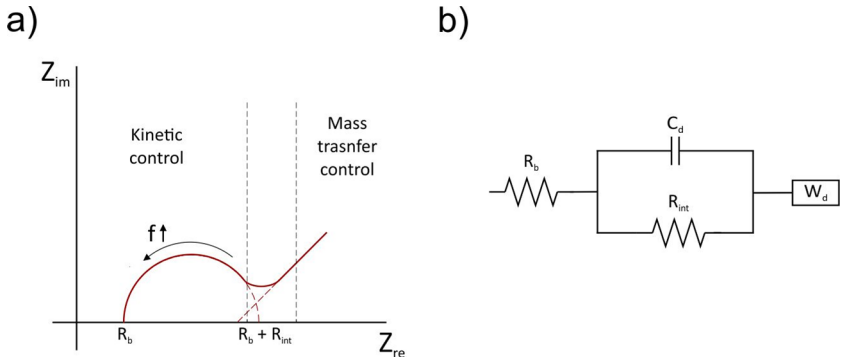

Figure 2.19. a) Nyquist impedance plot for an electrochemical system. Regions of mass-transfer and kinetic control are found at low and high frequencies, respectively. **b)** An equivalent circuit model of the electrochemical system used to analyze EIS data.

CHAPTER 3

Lithium surface interaction with pure atmospheric gases

In this chapter, the compositional and electronic structure changes induced in the lithium surface after exposition to oxygen, carbon dioxide and nitrogen gases are studied. To this end, the evolution of the lithium metal surface upon gas exposure is analyzed by means of X-ray photoelectron spectroscopy and ultraviolet photoelectron spectroscopy.

3.1 Introduction

Metallic lithium is not stable when interacting with atmospheric environment, especially with water that results in exothermic reaction, a topic that has attracted scientist since 1895[110]. One way to understand the nature of this interaction is to individually study the effect that pure atmospheric gases produce on the metal. Atmosphere composition is 78% nitrogen, 21% oxygen, 0.9% argon and 0.1% of trace gases, where carbon dioxide is the most abundant of them[111]. Water vapor concentration varies from 0 to 4% depending on the place and the time[112]. In this chapter we are going to look to the interaction of metallic lithium with the most abundant atmospheric gases that can be found in dry environments of Li-ion battery processing lines: O_2, CO_2 and N_2.

3.1.1 Literature review

Looking to the bibliography from the last five decades, we found several works that have studied the interaction between O_2, CO_2 and N_2 and the lithium metal

surface[113-141]. In these research works, surface is analyzed by one of the following surface specific techniques: auger electron spectroscopy (AES)[113–122], ultraviolet photoelectron spectroscopy (UPS)[123–127], infrared spectroscopy (IR)[128,129], X-ray photoelectron spectroscopy (XPS)[116,118,134–138,119,120,124,127,130–133], electron energy loss spectroscopy (EELS)[122,134], absorption spectroscopy(XAS)[118], metastable deexcitation spectroscopy[125], ellipsometry[121], surface X-ray diffraction (XRD)[139], density functional theory (DFT) combined with molecular dymanics (MD)[140], selected area electron diffraction[141] and energy filtered transmission electron microscopy[141]. Figure 3.1 shows the distribution of published scientific articles per decade (Figure 3.1a) and per studied gas (Figure 3.1b). We found that, after an interest decay in the first decade of the 21st century, the number of published papers in the last decade (2011-2020) increased (Figure 3.1a), this suggests there are still unsolved questions related to the interaction of metallic lithium with atmospheric gases. In following, we will discuss the effects O_2, CO_2 and N_2 produce on the lithium surface as reported in the works from Figure 3.1 agreed on, in addition, we will also emphasize the controversial issues that entail us to further investigate the gas-lithium interaction.

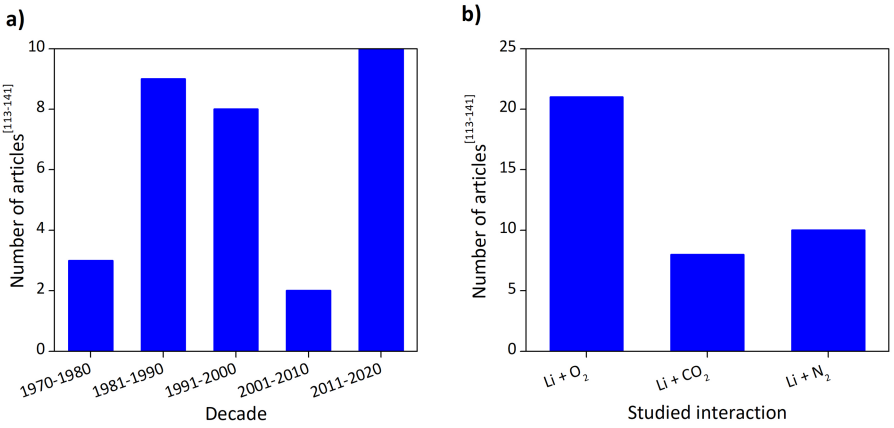

Figure 3.1. Distribution of the number of published articles that analyze the interaction of O_2, CO_2 and N_2 with the surface of metallic lithium; **a)** per decade and **b)** per studied gas, from references[113-141].

According to our literature review (Figure 3.1b), the most studied reaction is the one between metallic lithium and oxygen gas. All studies, without exception, corroborate that lithium surface is very reactive to oxygen, being Li_2O the reaction product. Most of the authors agree that this reaction does not create a stable passivation layer on the lithium surface. Indeed, the oxidation reaction continues into the bulk of the metal. Zavadil et al.[134] explained this phenomenon as a

consequence of a combination of relative thermodynamic stabilities, the solubility of zero valent lithium in its own oxide and the fact that lithium is a highly viscous liquid at room temperature that allows for a continuous structural rearrangement. However, besides thermodynamical and solubility considerations, lithium has a melting point of 180.5 °C and the only metal that is considered liquid at 1 atm and room temperature is mercury[142], then it is more appropriate to say that lithium is a soft metal rather than a highly viscous liquid. An alternative explanation provided some years later attribute the continuous oxidation process to the difference in the atomic density of Li and Li_2O: being four times larger for Li_2O than for metallic lithium[121]. It was claimed that the density difference produces a contraction of the surface where fresh metallic lithium will be continuously in contact with the atmosphere. By means of ellipsometry, it was concluded that Li_2O layer is porous, so it has free pathways for oxygen to reach metallic lithium. In contrast, a recent study suggests that pure oxygen will form a passivation layer if the gas has no traces of moisture and only after certain exposure time[141]; this nm-thick layer blocks the diffusion of oxygen molecules preventing further oxidation of the underlying lithium.

The reaction between lithium and CO_2 gas was comprehensively studied by Zhuang et al.[137], where the reaction mechanism was investigated by combining XPS, UPS and Ab initio Hartree-Fock self-consistent calculations. These authors concluded that the reaction of CO_2 gas with clean lithium leads to a mixture of CO_3^{2-} with O^{2-}.

Out of the three interactions, the one with nitrogen gas is of special interest due to the reported strategies based on nitride materials chemistry to stabilize lithium metal anode[143]. Despite its importance, we find some controversial results reported in the literature. Some authors believe nitrogen gas is, together with oxygen and water, the most reactive residual gas for metallic lithium in UHV systems[123]. Indeed, several times, it has been reported the formation of Li_3N by direct chemical reaction between the metal and nitrogen gas with the aim of creating a passivation layer that protects lithium upon electrochemical cycling[139,144–146]. In contrast, theoretical studies by Koch et al.[140] reported that direct exposure of N_2 to a clean lithium surface does not favor the dissociation of N_2 gas. At the same time, some other investigations that analyze the reaction between metallic lithium and nitrogen gas claim that the reaction is not

spontaneous[131,132], hence contradicting all the studies that confirm Li_3N formation.

3.1.2 Work function to monitor lithium surface stability

In this chapter lithium surface work function (w_f) evolution is monitored in order to evaluate the stability of lithium surface as a result of treatment with different gases. To define the work function, we have to look at the different energetic levels of the surface of a metal as illustrated in Figure 3.2. The Fermi energy E_F level refers to the energy when the electron occupation probability equals to 0.5 in the electronic energy. As the electron distribution can be represented by a step function, it can be approximately considered that electrons mainly fill the energy levels below Fermi energy level at the finite temperature, while levels above are unoccupied[147]. This term is defined in relation to the average electrostatic potential energy of an electron of the conduction band, V_i, deep inside the metal: $V_i(-\infty)$. V_i becomes constant again at a large enough distance from the surface, $V_i(+\infty)$. However, to define the vacuum level we also need to consider the dipole layer defined by the Galvani potential (φ) in which all electrostatic interactions, not included in V_i, are included. The difference in the absence of excess electric charge on the surface is the surface potential χ:

$$\varphi(-\infty) - \varphi(+\infty) = \chi \tag{3.1}$$

The chemical potential μ_e of the electron is defined by

$$\mu_e = E_F - V_i(+\infty) \tag{3.2}$$

And consequently, we obtain the work function

$$w_f = -\mu_e + q\chi \tag{3.3}$$

where q is the charge of an electron. The two terms of equation (3.3) represent the following: one part ($q\chi$) describes the electrical work for the electron to go through the intrinsic surface dipole layer and the other ($-\mu_e$) is equivalent to the chemical potential. According to this definition, the work function in vacuum corresponds to the minimum work needed to extract one electron from the surface to the vacuum level, being free of excess electric charge.

When the condition of absence of any excess surface charge, i.e. equation (3.1) is fulfilled, the relation between the Fermi energy and the work function is

$$w_f = -E_F \tag{3.4}$$

Then, the work function in a metal is equivalent to the position of the Fermi level with respect to the vacuum level[148]. It depends on the surface structure and is affected by the outermost layer of the sample.

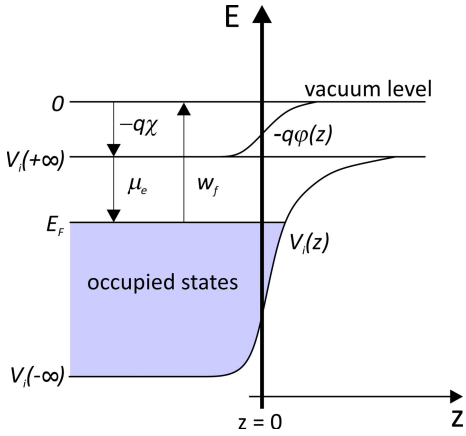

Figure 3.2. Characteristic electronic energies at the metal/vacuum contact in the absence of excess surface charge. Symbols and terms are explained in the text. Adapted from[148].

In order to correlate the work function of the lithium surface with its stability, in a first approach we could consider the relationship between Fermi energy and the chemical potential of a system. When temperature is zero Kelvin, both terms are equivalent[149]. In turn, open circuit potential (V_{OC}) of an electrochemical cell is defined by the chemical potentials of electrodes[19]:

$$V_{OC} = (\mu_{anode} - \mu_{cathode})/q \tag{3.5}$$

Then, at zero Kelvin we should have the following equivalence:

$$\mu_{anode} = E_F = w_f \tag{3.6}$$

However, considering that our lithium is at room temperature, if the electric potential differences of each interface in an electrochemical system is considered, together with the surface potential of the electrolyte, the cell potential difference

can be expressed as the difference of absolute electrode potentials $E_{electrode}(abs)$ which is related to the electrode work function

$$E_{electrode}(abs) = \frac{w_f}{F} + \Delta_{electrolyte}^{electrode}\psi \quad (3.7)$$

as described by Trasatti[150], where F is the Faraday constant and $\Delta_{electrolyte}^{electrode}\psi$ is the contact (Volta) potential of the electrode-electrolyte system. With this definition, we observe that work function changes on the lithium surface are indicatives of electrode absolute potential modifications, which will affect its stability against the electrolyte.

Then, at a first approximation, an increase in the work function will make the surface less energetically favorable transfer an electron, thus more stable against the electrolyte. In this line, a modified lithium metal anode with a higher work function than bare metallic lithium will help to gain stability in the electrode-electrolyte interface.

3.2 Spectra measuring conditions and data analysis guidelines

Lithium surface reactions with O_2, CO_2 and N_2 gases were characterized with two surface sensitive techniques: XPS and UPS. The first one is used to determine the composition of the Li surface. The second surface characterization technique is used to determine work function, and it also gave information about the valence band structure. Both spectroscopies (XPS and UPS) were carried out in the multitechnique surface analysis system available at CIC Energigune (Figure 2.7), using instruments explained in sections 2.3.1.3 and 2.3.3.1.

XPS measurements were recorded with a non-monochromatic Mg K_α photon source (hν = 1253.6 eV). The pass energy was set to 90 eV for survey spectra acquisition and 40 eV for the detailed regions of each element. UPS spectra were taken with a He I emission lamp (hν = 21.2 eV), using a pass energy of 1 eV and polarizing the sample -12 V.

3.2.1 XPS and UPS data analysis guidelines

XPS spectra is analyzed with CasaXPS version 2.3.16dev52 (Casa Software Ltd, Teighmouth, UK). The binding energy zero is calibrated in every spectrum prior to

fitting the photoelectron lines for each element. A survey spectrum is recorded for every sample to ensure the surface is free from any contaminants. The binding energy calibration, in the case of the O_2 interaction, is done using the metallic lithium component in the Li 1s region and lithium oxide component in the O 1s region. For the CO_2 interaction, the binding energy calibration is based on the position of metallic lithium component in the Li 1s region and lithium carbonate component in the C 1s region. For the last gas studied, N_2, the binding energy is calibrated with respect to the position of metallic lithium in Li 1s region and position of lithium oxide in the O 1s region.

The peak background is simulated by a Shirley function. A Voigt profile (30%-70%, Lorentzian-Gaussian distributions) is used as peak lineshape to fit all components except for metallic lithium. The lineshape of this last one is a pseudo-Voigt function (LF(1.5,2,5,50)) which takes into account the asymmetric tail in the higher binding energy side of the metallic peak; caused by the small kinetic energy losses originated by the interaction of the core level electrons with the conduction band of the metal. This shape is equivalent to the asymptotic form of theoretical Doniach-Sunjic asymmetric lineshape. First two parameters of LF(1.5,2,5,50) define the asymmetry of the lineshape, third one is the Gaussian contribution and fourth the damping parameter to force the tail to reduce towards the limits of the integration limits[151].

The assignment of the compounds has been done based on reported binding energies (BE) in works where the studied system is similar to our case[127,133,137,152]. With these references, and considering a BE uncertainty of ± 0.1 eV, we are able to clearly identify the following compounds: Li^0, Li_2O, Li_2O_2, Li_2CO_3 and Li_3N. The maximum FWHM (full width at half maximum) for these compounds is variable depending on the element. Table 3.1 summarizes the BE and FWHM constrains used to fit the data. Any other compound that is not in the table will be discussed in its section.

To quantify the surface composition, the concentration of each compound is calculated from equation (2.7). The area of every fitted photoelectron line is corrected with the corresponding sensitivity factor (σ) of each element and orbital based on Scofield cross sections together with a transmission function (T) specific for this photoelectron analyzer. An exponential factor is also used to correct for the different photoelectron escape depths. This correction is needed because all core levels are measured using same photon energy, so photoelectrons emitted

from each of these levels will have a different inelastic mean free path (λ). With these corrections, the atomic concentration (N) for each compound can be obtained from (2.7).

Table 3.1. Fitting parameters used to identify the compounds formed on the lithium metal surface; based on reported BE[127,133,137,152] and experimental evidence.

Compound	Fitting constrains (eV)	Li 1s	O 1s	C 1s	N 1s
Li^0	BE	54.90-55.10			
	FWHM	1-1.3			
Li_2O	BE	56.30-56.50	531.10-531.30*		
	FWHM	1.6-1.8	1.4-1.6		
Li_2O_2	BE	57.40-57.60	534.05-534.25		
	FWHM	1.8-2	1.8-2		
Li_2CO_3	BE	57.90-58.10	534.60-534.80	292.60-292.80	
	FWHM	1.6-1.8	undefined	1.5-1.7	
Li_3N	BE	54.70-54.50			395.20-395.40
	FWHM	1.4-1.6			1.2-1.4

*the residual amount of oxide we find after cleaning the lithium has a smaller BE, around 530.8 eV, as previously reported[133] and in agreement with suboxide formation due to the ion assisted cleaning process.

The work function is calculated from the minimum kinetic energy measured in the photoelectron spectrum (secondary electron cut-off), the maximum kinetic energy measured for a photoelectron emitted from the Fermi level and the photon energy, as explained in chapter 2 section 2.3.3 (Figure 2.13). The secondary electron cut-off is obtained with a linear fitting to the low kinetic energy side of the photoelectron spectrum, whilst the Fermi edge is obtained by fitting a step function that will define the zero for the binding energy.

3.3 Li foil surface cleaning

The starting point of this study is a commercial lithium foil (Rockwood Lithium, Battery Grade), which was stored in an argon filled Glove Box (MBRAUN) where O_2 and H_2O levels were below 0.1 ppm. After being mounted in the photoemission sample holders, the foils were transported to the UHV system with a specific transfer tool (Figure 2.8) that prevented air exposure

This foil has a purity of 99.8%. Even so, the XPS spectra of the Li foil stored in the glove box, represented in Figure 3.3, reveals a completely oxidized lithium surface. Binding energy of its main Li 1s peak is around 57 eV, which can be assigned to a mixture of lithium oxide and lithium carbonate according to Table 3.1. To be able to analyze the interaction of metallic lithium and the selected gases, Ar ion sputtering at 5 keV was performed, at $4 \cdot 10^{-7}$ mbar for at least 5 hours. With this method, previously used in literature[127,133,152,153] we got a surface composed by (93.6 ± 1.9)% of pure metallic lithium, where the rest of the surface is lithium oxide. The Li 1s photoelectron peak of a cleaned foil (Figure 3.3) reveals some plasmon loss structures that correspond to surface plasmons of metallic lithium[154]. These features can be used as an indicative of clean metallic lithium[135]. Another indicative of having a clean lithium surface is the value of the work function measured by UPS, which is 3.01 ± 0.08 eV, in agreement with reported values for metallic lithium surfaces[155].

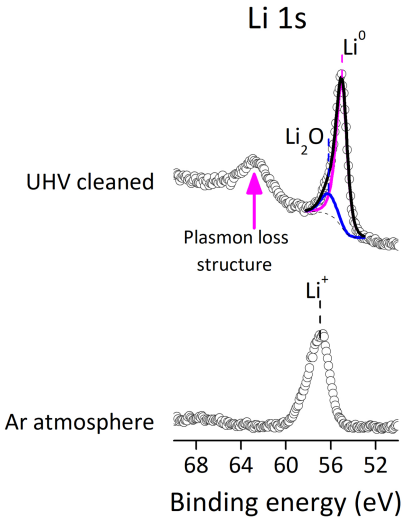

Figure 3.3. Comparison of Li 1s XSP spectra of a lithium foil stored in argon atmosphere and after cleaning the surface in UHV by Ar^+ sputtering. Whit the cleaning procedure, its binding energy of the main photoelectron peak shifts down to the binding energy of metallic lithium, and it also shows plasmon loss structures (highlighted with an arrow), indicative of metallic lithium[135].

3.4 O_2, CO_2 and N_2 gases effects on clean lithium surfaces

We dosed O_2 (Praxair, 99.9%), CO_2 (Laborgase, 99.995%) and N_2 (Praxair, 99.9%) gases in three dose ranges: 1-2-3-4-5-6-7-8-9-10 L as low dose range, 1-10-100-1000 L as medium dose range, and higher doses up to the order to $1 \cdot 10^8$ L. Langmuir (L) unit corresponds to a dose of 10^{-6} Torr of a given gas during one second. Every dosing sequence was deployed starting from a UHV cleaned lithium. The specific partial pressures we use in each dose are detailed in the analysis of the interaction with each gas.

3.4.1 Oxygen interaction

Interaction of a clean lithium surface with oxygen gas was studied at the conditions summarized in Table 3.2. Figure 3.4 shows the evolution of XPS spectra, analyzed with the parameters from Table 3.1. The first compound growing on the lithium metal surface is lithium oxide, Li_2O. The oxygen dose that leads to a full coverage of Li surface by lithium oxide has been estimated from the peak area evolution of the Li_2O component in the Li 1s photoelectron line. According to the slope change measured in Figure 3.5a, the full surface coverage dose is around 3 – 4 L of O_2, which is in agreement with the disappearance of plasmon loss structure and evolution of Li_2O energy loss peaks assigned to surface excitons of Li_2O[134,156], represented in Figure 3.5b.

Table 3.2. Pressures used for each studied dose in the analysis of the interaction of lithium metal surface with O_2 gas.

Range	Dose (L)	Pressure range (mbar)
Low dose	1,2,3,4,5,6,7,8,9,10	10^{-8}
Medium dose	1	10^{-8}
	10	10^{-7}
	100	10^{-6}
	1000	10^{-5}
High dose	$5000,1 \cdot 10^4$	10^{-4}
	$5 \cdot 10^8$	10^1

Besides Li_2O, there is no other compound evolving on the surface until we get to the high dose range, when a new peak at higher binding energy of O 1s and Li 1s XPS spectra appears, as shown in Figure 3.4 for 10^4L to $5 \cdot 10^8$ L O_2 doses. Looking

to reported binding energies[133], that peak can be assigned to Li_2O_2. In order to confirm the assignment of this new compound, we compared the O 1s XPS and O 2p UPS spectra in Figure 3.6. Li_2O and Li_2O_2 positions have been identified in O 2p region according to literature values[127]. The increase of Li_2O_2 concentration with the oxygen dose is confirmed from both spectra.

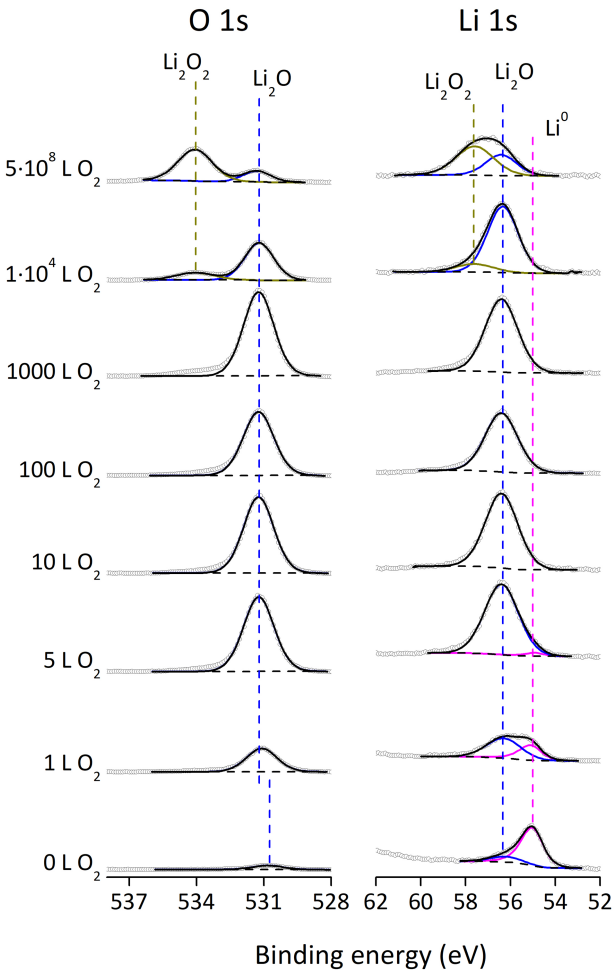

Figure 3.4. Fitting of the XPS photoelectron peaks from a lithium surface exposed to oxygen gas at selected low (1 L, 5 L, 10 L), medium (100 L, 1000 L) and high ($1{\cdot}10^4$ L to $5{\cdot}10^8$ L) dose ranges. The compounds that form in the surface are shown by the deconvolution of the 1s photoelectron peaks of oxygen (left panel) and lithium (right panel). In the spectra, the fitted curve (black line) follows experimental data (dots), and background is represented by a dash line.

From previous works that analyze the same Li-O_2 interaction, there is just one case where Li_2O_2 formation is also reported[137]. However, they only observed the formation of this compound at 130 K, and it could not be detected when rising temperature up to 300 K. As already mentioned, in our experiments Li_2O_2 is only formed at the highest O_2 doses, which are also done at the highest O_2 gas pressures (Table 3.2). The reason for observing Li_2O_2 can then be explained by the thermodynamical change that takes place when increasing O_2 pressure[157], favoring reaction pathways that leads in Li_2O_2 formation. This also explains why none of the previous studies observe Li_2O_2 as a consequence of lithium interaction with O_2; most works are carried out in pressures near UHV conditions.

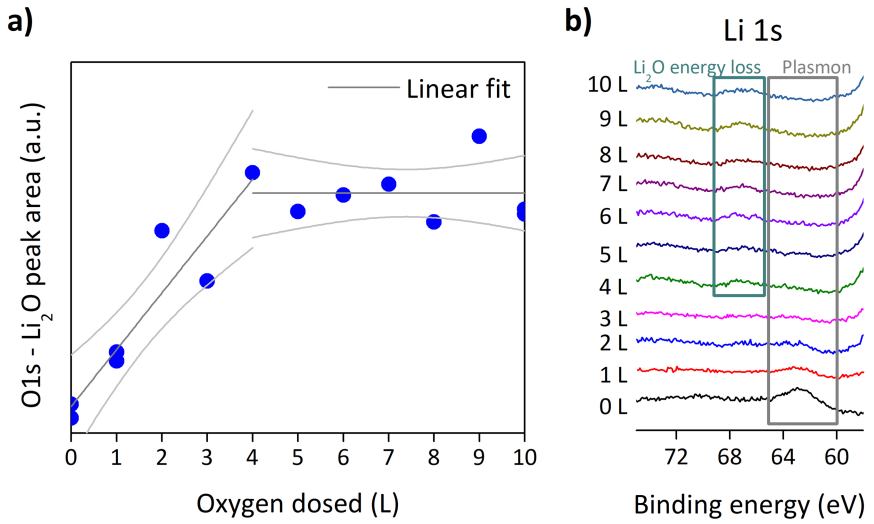

Figure 3.5. a) Li_2O peak area (blue points) measured from O 1s XPS spectra as a function of gas dose, where the intersection, slope change, of both linear fits (dark grey) corresponds to the oxygen dose needed to fully cover the lithium metal surface which is around 4 L. 95% confidence bands of the fitting are shown in light grey. **b)** the disappearance of metallic plasmon loss structure from Li 1s XPS spectra and appearance of Li_2O energy loss peaks that agree with the measured slope change in the left panel figure.

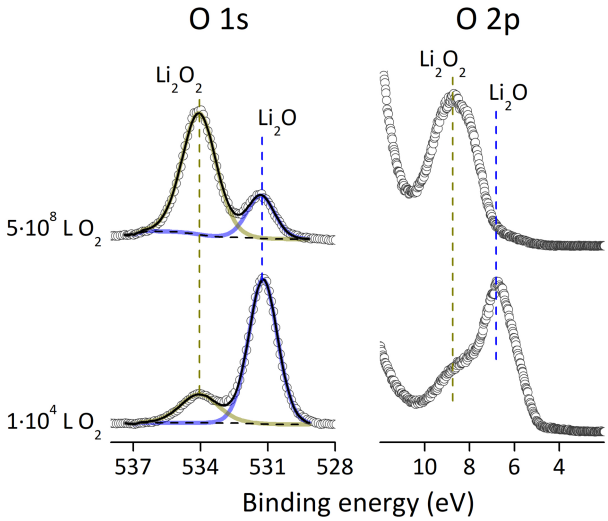

Figure 3.6. XPS O1 s and UPS O 2p spectra of a clean lithium surface exposed to $1{\cdot}10^4$ L and to $5{\cdot}10^8$ L O_2. In both spectra Li_2O_2 formation is observed. In the XPS spectra, experimental data (dots) follows the fitted curve (black line) and background is represented by a dashed line.

Figure 3.7 represents how the composition of the surface changes and how the work function evolves for the three dose ranges described in Table 3.2. The composition evolution has been estimated by the quantification of XPS peak area components and correcting these areas as explained earlier at the section 3.2. The photoelectron peaks considered for the quantification are Li^0 form Li 1s, and both Li_2O and Li_2O_2 from O 1s.

In the introduction we have mentioned that most of the authors agreed on. Looking to Figure 3.7, we observe a continuous oxidation of metallic lithium when interacting with O_2 gas, in agreement with previous studies. However, from these experimental data, we cannot conclude if this reaction propagates into the bulk or not due to surface sensitivity limitations of XPS and UPS. This oxidation process results in full oxidation of the detectable lithium surface at a dose of 9 L, as can be seen in Figure 3.7a. Considering the Li 1s photoelectrons kinetic energy (1197.2 eV) and the TPP2m formula from the QUASES-IMFP software, the inelastic mean free path (λ) for the Li 1s photoelectrons is 28.61 Å. Therefore, since the probing depth of the XPS can be estimated as 3 times λ, the oxide layer is, at least, 85.8 Å (8.6 nm) thick.

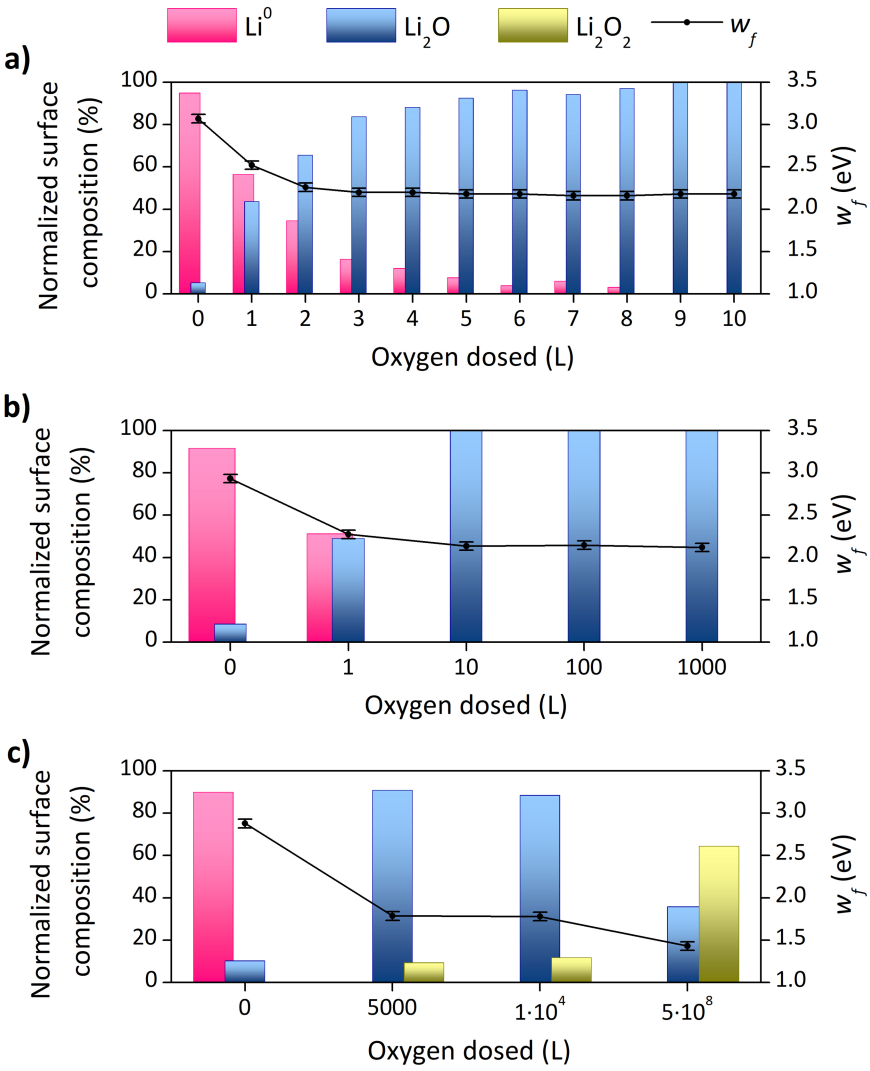

Figure 3.7. Normalized surface composition (left vertical axis) and work function evolution (right vertical axis) of a clean metallic lithium foil exposed to different doses of O_2 **a)** low dose range **b)** medium dose range and **c)** high dose range. The lithium surface is oxidized by the gas and this results in a decrease of the work function.

This oxidation process results on a decrease of the work function as the lithium oxide covers the Li surface, an evolution that is represented in Figure 3.7. A theoretical study that analyzed this same interaction by DFT geometry optimization and molecular dynamics calculations predict a decrease in the work

function for doses that will form between 0.25 and 1 monolayer (ML) of Li_2O[140]. The calculations have been done at 0 K and at room temperatures, getting in both situations a decrease in the work function. Then, although at a first view this decrease of the work function could be quite surprising taking into consideration the electronegative condition of oxygen, which even leads to suggest an increase of it upon lithium oxidation[127], theoretical studies confirm the behavior we observe. In fact, a decrease of the w_f was already experimentally observed in the 90´s by the group of Nobel laureate G. Ertl[125,126,158] which elavorated an explanation based on non-adiabatic events where the emissions of exoelectron and of O^- ions are related to the formation of Li_2O in the first oxidation state. However, there is a substantial discrepancy between the work reported in the 90's and this one: Ertl and coworkers only observed a decrease of the w_f up to O_2 exposures of 2 L, while for higher doses an increase of w_f was reported. In our case, however, we observe that for O_2 doses above 2 L the w_f does not increase (Figure 3.7).

In all the dosed samples shown in Figure 3.7 the w_f value decreases when the main compound of the surface changes, and it is kept constant whenever the surface composition is stable, which is clearly observed in Figure 3.7 c, where the two steps in w_f decrease agree with the formation of Li_2O in the first step down and Li_2O_2 in the second one. Considering the relation of the normalized amount of Li_2O in the low and medium doses and the evolution of the work function, an exponential correlation can be established (Figure 3.8):

$$w_f = 2.09 + 1.11e^{-0.03n} \quad \textbf{(3.8)}$$

where n is the Li_2O percentage of normalized surface composition. When the formation of lithium oxide starts on the surface, there is a pronounced decrease of the w_f, but when oxide quantity is higher than the metallic lithium, the w_f value converges to a constant value. This indicates that the outermost Li_2O layer is the one completely dominating the electronic response of the surface, which significantly differs from Li^0 response. Another important feature of equation (3.8) relies on the possibility to estimate the w_f of the surface just from the lithium oxide concentration, when surface compounds are Li^0 and Li_2O.

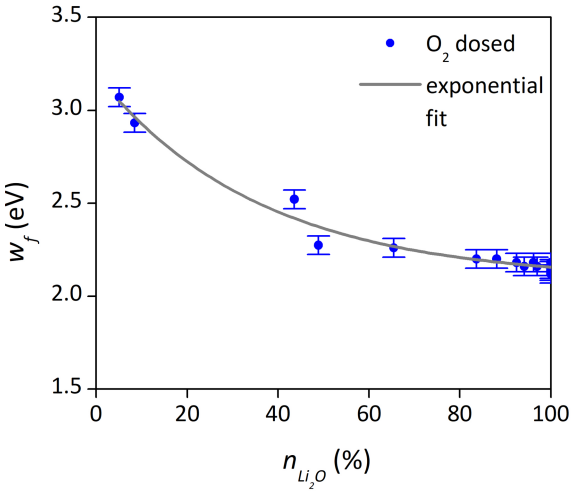

Figure 3.8. Correlation of the w_f and the lithium oxide normalized surface percentage. The work function of surfaces exposed to O_2 gas is determined by the ammount of lithium oxide when the main compounds of the surface are metallic lithium or lithium oxide. This relation is shown in the plot as an exponential correlation.

3.4.2 Carbon dioxide interaction

CO_2 gas exposures carried out for each dose range to study the interaction of CO_2 with the lithium metal surface are specified in Table 3.3. In order to determine the evolution of the surface compounds, we first evaluated how to fit XPS C 1s spectra consistently. The reason arises from the difficulty to identify all the components forming this peak. In this core level, there are two compounds that are easily identified: one is lithium carbonate which has a well reported binding energy (Table 3.1), and the other one is CH/CC, a typical contribution from adventitious carbon widely studied[159]. The struggle comes when trying to identify rest of the compounds that lie in the spectra between lithium carbonate and CH/CC, because there are several compounds with a similar binding energy[160]. These compounds are formed by C and O atoms, and will be named as CO species. In this chapter, the main objective of this evaluation is to identify the minimum number of CO species present on the surface. A full identification of carbon-based compounds created as a consequence of lithium interaction with CO_2 gas can be found in next chapter, where experimental data is more appropriate to obtain this information. The two possibilities evaluated are: fitting A, where two components are considered to fit the CO species region; and fitting B, where only one component

is used. The corresponding constrains for both fits are included in Table 3.4, and an example of each fitting for the case of 10 L CO_2 gas dose is illustrated in Figure 3.9.

Table 3.3. Pressures used for each studied dose in the analysis of the interaction of metallic lithium with CO_2 gas.

Range	Dose (L)	Pressure range (mbar)
Low dose	1,2,3,4,5,6,7,8,9,10	10^{-8}
Medium dose	1	10^{-8}
	10	10^{-7}
	100	10^{-6}
	1000	10^{-5}
High dose	$1{\cdot}10^{4}$	10^{-4}
	$8{\cdot}10^{8}$	10^{1}

Table 3.4. Constrains for two types of fitting of CO species to check which is the minimum CO species we have on lithium surface after dosing it with CO_2 gas.

	Fitting A		Fitting B
Compound	(CO)a	(CO)b	CO
Binding energy (eV)	287.3 - 287.5	289.3 - 289.5	288.2 - 288.4
FWHM (eV)	2.8 - 3	2.8 - 3	2.8 - 5

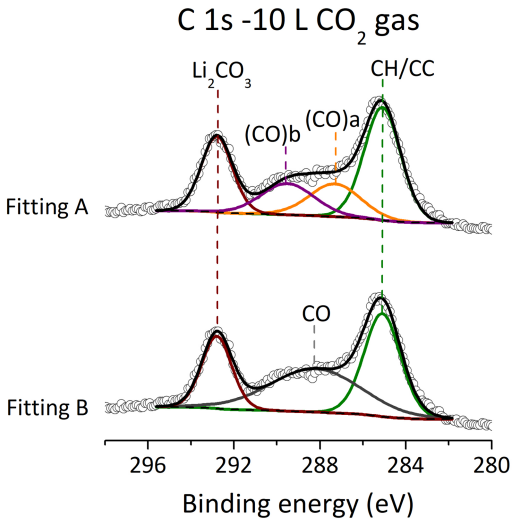

Figure 3.9. To check which is the minimum CO species we have on the surface we compare two ways of fitting in C 1s XPS spectra of a lithium foil dosed by 10 L CO_2 gas: with two CO species (Fitting A) and with just one CO specie (Fitting B).

To validate which is the most adequate fitting for our data we compare the residual standard error of both situations (calculated by CasaXPS version 2.3.19PR1.0). If we look to the residual standard deviation of the fitted spectra with respect to data, fitting with one or two components will result in very similar values, between 0.85 and 1.35 (Figure 3.10a). However, when comparing the resulting error estimates when using fitting A or fitting B methods, the residual standard deviation of the compounds is notably reduced when two components are used (Figure 3.10b).

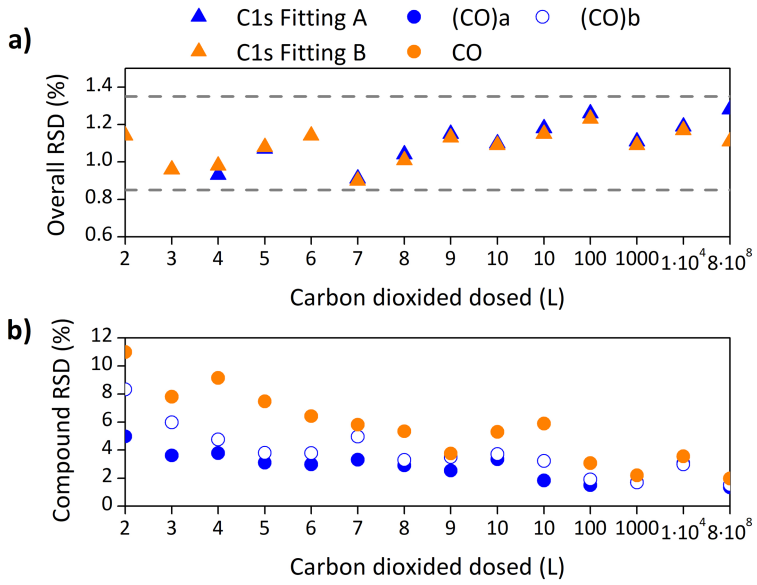

Figure 3.10. Comparison between the residual standard deviation (RSD) of two types of fitting of CO species in C 1s XPS spectra, where **a)** represents the RSD of the fitting spectra and **b)** represents the RSD of each compound.

The calculation of the standard deviation of the compounds is based on Monte Carlo analysis where the error estimates are an indicator of how stable a peak model is with respect to noise. One of the advantages of using this error analysis is that it highlights when a quantification parameter is poorly determined by the combination of model and optimization procedure. To be able to apply it, we need to have Poisson noise distribution in the spectra. To validate if we have Poisson noise distribution, a region absent of core-level excitations can be analyzed by a linear regression. If the standard deviation given by CasaXPS is around 1 then we

assume a Poisson noise distribution, which in our case is between 0.8 – 1.15, hence in good agreement with a Poisson noise distribution[161].

Using this approach, we can confirm that at least we have two compounds that form the CO species, which will be referred as (CO)a and (CO)b. Figure 3.11 shows the evolution of O 1s, C 1s and Li 1s spectra when exposing the clean lithium surface to CO_2 gas, where C 1s spectra have been analyzed using fitting A (Table 3.4) and rest of compounds have been identified according to the fitting parameters included in Table 3.1. In the figure we observe that compounds created on the surface as a consequence of Li-CO_2 interaction are Li_2O, Li_2CO_3 and CO species. If we look to the Li 1s peak evolution at the lowest doses, we detect that Li_2O is formed on the Li surface at 1 L CO_2, prior to the formation of lithium carbonate. We also see that, for low and medium doses, Li_2O is growing the most if compared with the rest of compounds. For this reason, we calculated the CO_2 dose needed to cover all the surface metallic lithium by the saturation of Li_2O area from O 1s spectra, represented in Figure 3.12a. According to this, the needed dose to reach a monolayer coverage is 8 L, which also agrees with the disappearance of plasmon loss feature represented in Figure 3.12b. In this last figure energy loss peaks corresponding to Li_2O are not present, in contrast with the results after O_2 dosing, suggesting that carbon-based compounds are growing on top of Li_2O and prevent the detection of lithium oxide energy loss features.

O 1s spectra from Figure 3.11 cannot be used to identify the contributions from CO species and Li_2CO_3, which are overlapped above 534 eV. This core level, after forming both CO species and lithium carbonate (Figure 3.11, O 1s spectra after 5 L), presents two main peaks. The one at the lower binding energy (531.20 ± 0.1 eV) corresponds to Li_2O as defined in the literature[127,133,137], and its FWHM (1.4-1.6 eV) does not increase in agreement with the observed FWHM behavior for O_2-treated surfaces. This suggests that there are no compounds related to carbon-based species in low binding energy side. Therefore, the CO species are going to be somewhere in the high binding energy side, along with lithium carbonate which has a well-defined binding energy at 534.70 ± 0.1 eV[133]. However, as we cannot assign any exact binding energy to the CO species in this peak, we use a broad peak which contains both lithium carbonate and CO species contributions.

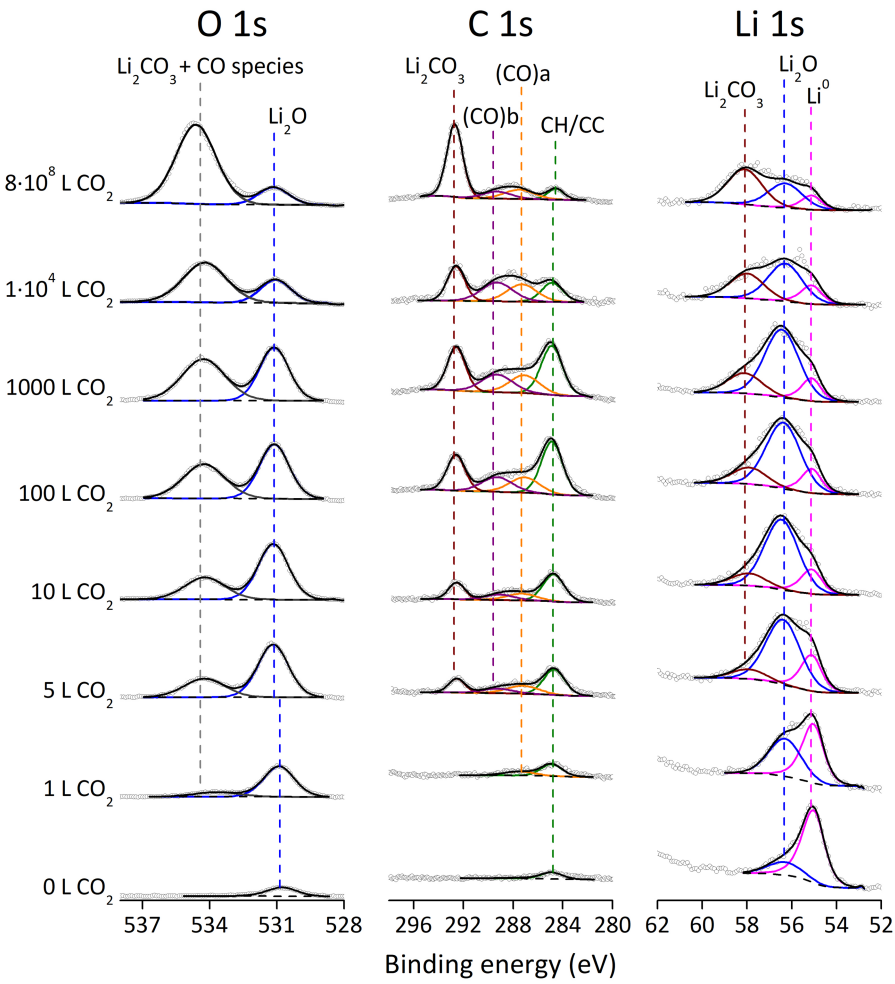

Figure 3.11. Fitting of the XPS photoelectron peaks of a lithium surface expose to carbon dioxide gas at selected low (1 L, 5 L, 10 L), medium (100 L, 1000 L) and high ($1{\cdot}10^4$ L, $8{\cdot}10^8$ L) dose ranges. The compounds that form the surface are shown by the deconvolution of the peaks of oxygen, carbon and lithium. In the spectras, experimental data (dots) follows the fitted curve (black line) and background is represented by a dashed line.

As it can be observed in C 1s spectra evolution from Figure 3.11, binding energy of CH/CC presents a lower value (0.5 eV lower) at the highest dose. This compound, related to adventitious carbon, is widely used as a reference to calibrate the spectra in XPS. However, a recent paper observes that the binding energy of the CH/CC related to adventitious carbon can vary as much as 1.44 eV, and they find a correlation between the changes in the sample work function and

the biding energy of CH/CC[159]. This observation could explain the variation we observe in the binding energy of CH/CC.

The evolution of the normalized composition and work function variation in the Li-CO_2 system is shown in Figure 3.13. For the normalized surface composition, we considered the Li^0 from Li 1s, Li_2O from O 1s, and CH/CC, Li_2CO_3 and (CO)a and (CO)b species from C 1s regions. In this case, the evolution of the work function is only represented for the low dose range and medium dose range, because some technical problems prevented to measure the work function at the high dose range.

If the reaction of lithium metal surface with O_2 gas and CO_2 gas is compared, it is observed that the oxidation process is slower in the case of the CO_2 gas, where even after the highest CO_2 dose is applied, metallic lithium can still be detected on the surface (Figure 3.11 and Figure 3.13). Then, overlayer thickness should be below 10 nm to allow Li 1s photoelectrons from subsurface Li^0 to escape and to be detected. A possible explanation for the slower kinetics of the oxidation reaction is that there is a layer slowing down the lithium oxidation, probably Li_2CO_3, the predominant one at the highest dose.

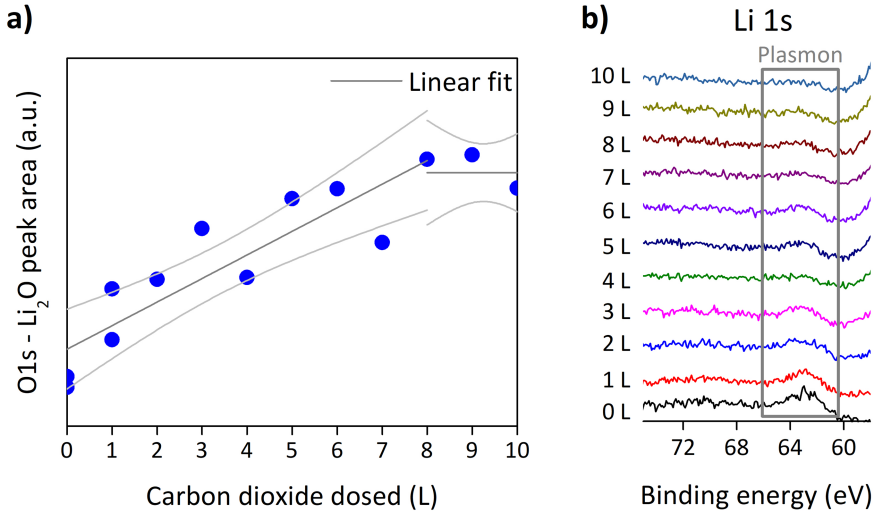

Figure 3.12. a) Li_2O peak area (blue points) measured from O 1s XPS spectra as a function of gas dose, where the intersection, slope change, of both linear fits (dark grey) corresponds to the CO_2 dose needed to fully cover the lithium metal surface which is around 8 L. 95% confidence bands of the fitting are shown in light grey. **b)** the disappearance of metallic plasmon loss structure from Li 1s XPS spectra around 63 eV agrees with the measured slope change in the left panel figure.

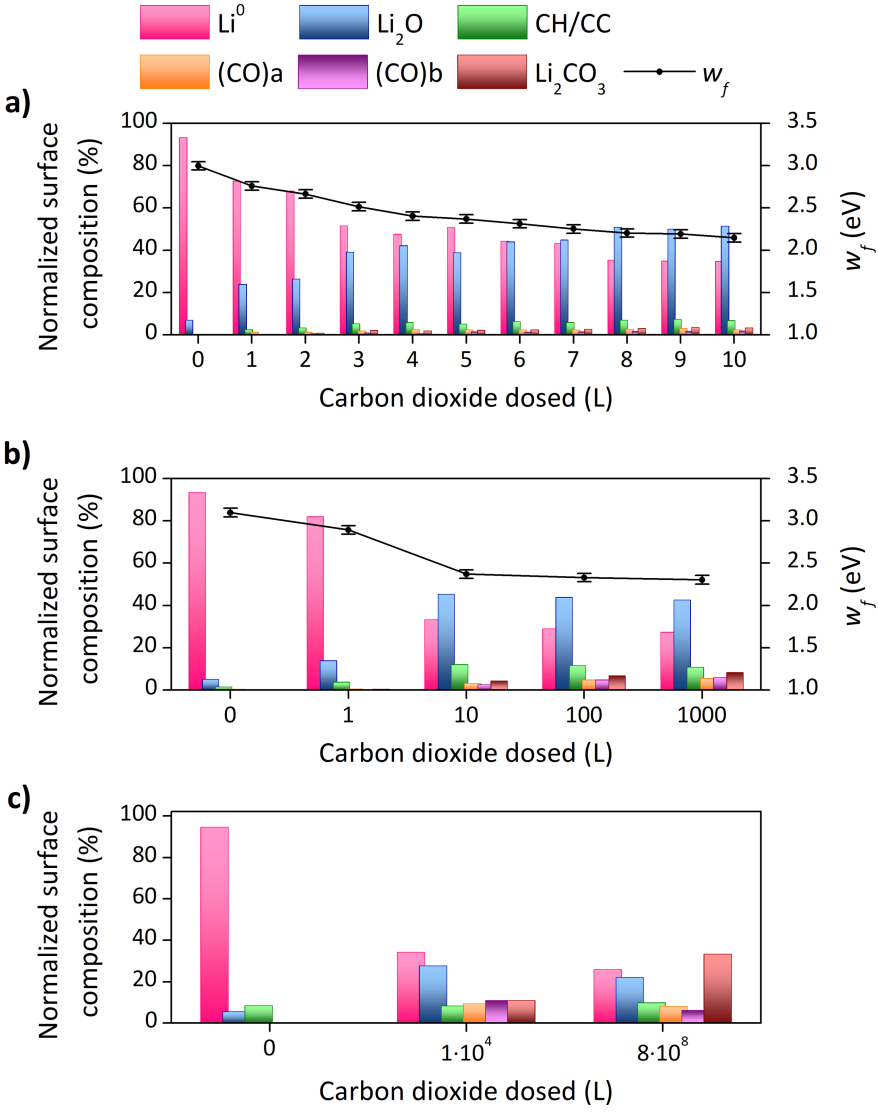

Figure 3.13. Compositional and work function evolution of a clean metallic lithium foil exposed to carbon dioxide gas for **a)** low dose range **b)** medium dose range and **c)** high dose range. In all the cases, the surface has a large amount of metallic lithium. Here, as happens with the O_2 gas, the work function decreases because of the reaction of the surface.

The work function evolution for low dose and medium dose of CO_2 follows a decreasing trend (Figure 3.13a and b) likewise it happens when dosing with O_2. This is also in agreement with the DFT geometry optimization and molecular dynamics calculations performed by Koch et al.[140] up to one monolayer coverage.

As earlier mentioned, for the low and medium dose ranges the compound that is growing most on the surface is lithium oxide. Then, it is more than plausible that the work function is going to be dominated by Li_2O. Figure 3.14 shows that, in fact, w_f evolution in the Li-CO_2 system adjusts also to the same correlation previously obtained for the oxidation of lithium with O_2 from equation (3.8). The deviations of the w_f exponential decay for O_2 and CO_2 dosed lithium surfaces can be explained by the effect that carbon-based compounds have on it.

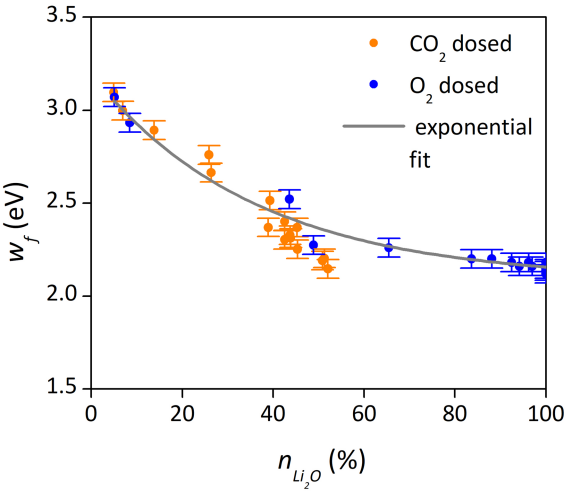

Figure 3.14. Correlation of the w_f and the lithium oxide normalized surface percentage. The exponentail fit corresponds to the lithium dosed by O_2 gas (blue dots) already shown in Figure 3.8. If we add to this plot the data from the Li-CO_2 system in the low and medium dose ranges (orange dots), we observe they follow the same exponential tendency, suggesting that in this range the work function is manly determined by the ammount of lithium oxide on the surface.

3.4.3 Nitrogen interaction

The evolution of the lithium metal surface after N_2 exposure, according to N_2 doses of Table 3.1Table 3.5 is represented in Figure 3.15, where spectra have been analyzed according to fitting parameters shown in Table 3.1. The normalized

surface composition and work function evolution are shown in Figure 3.16. For the quantification, we consider the Li^0 from Li 1s, Li_2O and Li_2O_2 from O 1s and nitrogen-based compounds from N 1s. As occurred for the Li-CO_2 system, we were not able to measure the evolution of the work function at high dose range.

Table 3.5. Pressures used for each studied dose in the analysis of the interaction of metallic lithium with N_2 gas.

Range	Dose (L)	Pressure range (mbar)
Low dose	1,2,3,4,5,6,7,8,9,10	10^{-8}
Medium dose	1	10^{-8}
	10	10^{-7}
	100	10^{-6}
	1000	10^{-5}
High dose	$1{\cdot}10^4$	10^{-4}
	$1{\cdot}10^8$	10^1

For both low and medium dose ranges we do not detect any interaction between metallic lithium and nitrogen gas. The surface composition, and consequently the work function (Figure 3.16), remain almost constant throughout exposure to N_2 doses between 1 and 1000 L. When going up to higher doses, we see some nitrogen-based compounds at $1{\cdot}10^4$ L N_2 gas (Figure 3.15). However, this surface is still dominated by metallic lithium, the total amount of nitrogen-based compounds is less than 1.2% (Figure 3.16c). Furthermore, Li_3N is just the 0.28% of the surface. Because of this low amount of Li_3N, we could not fit a component to account fo it in Li 1s spectra. We name the other nitrogen-based compounds shown in Figure 3.15 at $1{\cdot}10^4$ L as N1 (binding energy of 397.3 eV) and N2 (binding energy of 399.9 eV). Looking to literature and comparing reported binding energies with ours, we can discard that any of these two compounds is LiN_3[162] or $LiNO_3$[163]. Both of them could be related to carbon-based compounds. N1 binding energy corresponds to a poly(aniline)[164,165], and N2 could be pyrrolic-N[166] or carbon nitride[167]. If this would be the case, we should see the corresponding contribution in the C 1s spectra. However, the resolution of the C 1s spectra we have is not enough to determine whether this is the case or not. The relative sensitive factor of C 1s in our system is 1, smaller than that of N 1s (1.77), and we already observe a small amount of N compounds (Figure 3.16c, each N1 and N2 contributions are less than 0.8 % of normalized surface composition). It is fair to mention that possible reaction pathways to produce poly(aniline) or pyrrolic-N just from nitrogen gas is rather unlikely. Also, reported carbon nitride[167] was produced using a magnetron sputtering, then adding more energy to the system

than that we have just with nitrogen gas at room temperature. In order to confirm the assignment of these peaks we would need further studies with reference materials, for this reason we keep naming them as N1 and N2.

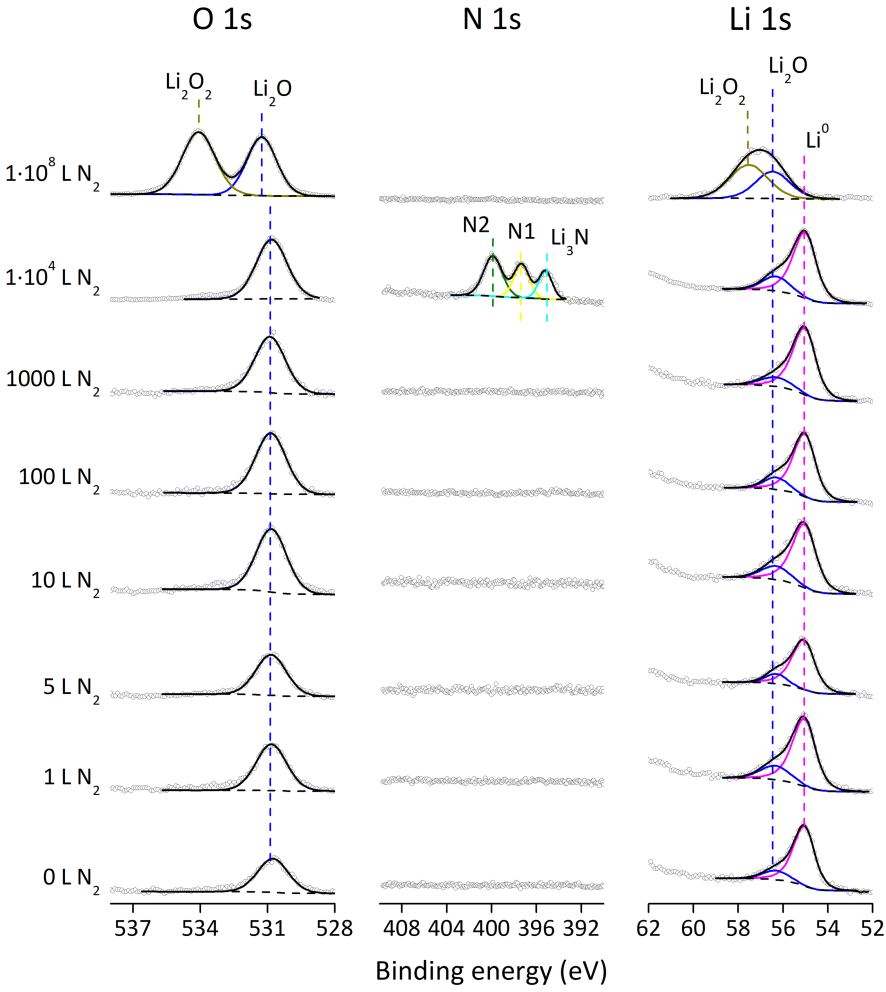

Figure 3.15. Fitting of the XPS photoelectron peaks of a lithium surface exposed to nitrogen gas at selected low (1 L, 5 L, 10 L), medium (100 L, 1000 L) and high ($1{\cdot}10^4$ L, $1{\cdot}10^8$ L) dose ranges. The compounds that form the surface are shown by the deconvolution of the peaks of oxygen, nitrogen and lithium 1s. The fitted curve (black line) follows experimental data (dots) and background is represented by a dashed line.

When treating the surface at the highest dose ($1{\cdot}10^8$ L N_2), the surface is completely oxidized, but what we observe is lithium peroxide and none of the expected nitrogen-based compounds. This result at high doses is compatible with the traces of oxygen impurities present in the nitrogen gas line. We also observe here that nitrogen-based compounds formed after a dose of $1{\cdot}10^4$ L N_2 are not strong enough to passivate the lithium surface and prevent its oxidation, and that lithium surface is much more likely to react with oxygen than with nitrogen gas.

As mentioned earlier, we could not measure the work function of this high doses because of some technical problems in the UPS system. But we could assume that the work function of the dose of $1{\cdot}10^4$ L is going to be very similar to clean lithium surface, and the last one is going to have a smaller work function expected from the interaction of lithium and oxygen (section 3.4.1).

In order to analyze the effect of lithium nitride formation on the electronic structure of lithium, a different approach based on the work done by Ishitama et al.[132] was used to obtain Li_3N: reactive ion implantation, using an ion source that generates a N^+ beam with an energy of 0.5 keV at a pressure of $4{\cdot}10^{-6}$ mbar for 5 minutes. This method allowed to prepare a surface mainly composed by lithium metal and lithium nitride, as determined by XPS analysis of Li 1s, O 1s and N 1s shown in Figure 3.17. The normalized surface composition calculated from Figure 3.17 spectra results on a surface composed by 68.4% Li^0, 19.8 Li_3N, 8.1% Li_2O and 3.7% being small amounts of impurities.

The formation of Li_3N leads to a change on the w_f value as determined by UPS, from 3.01 eV of Li^0 to 2.49 eV in the Li_3N-contaninig surface. Considering that the final surface also contains 8.1% of Li_2O, one could think that the w_f decrease is due to lithium oxide formation. However, according to the correlation obtained for O_2 and CO_2 dosing in equation (3.8), such amount of surface Li_2O should result in w_f = 2.97 eV far above the 2.49 eV measured. So, lithium nitride formation also reduces the work function of the lithium metal surface.

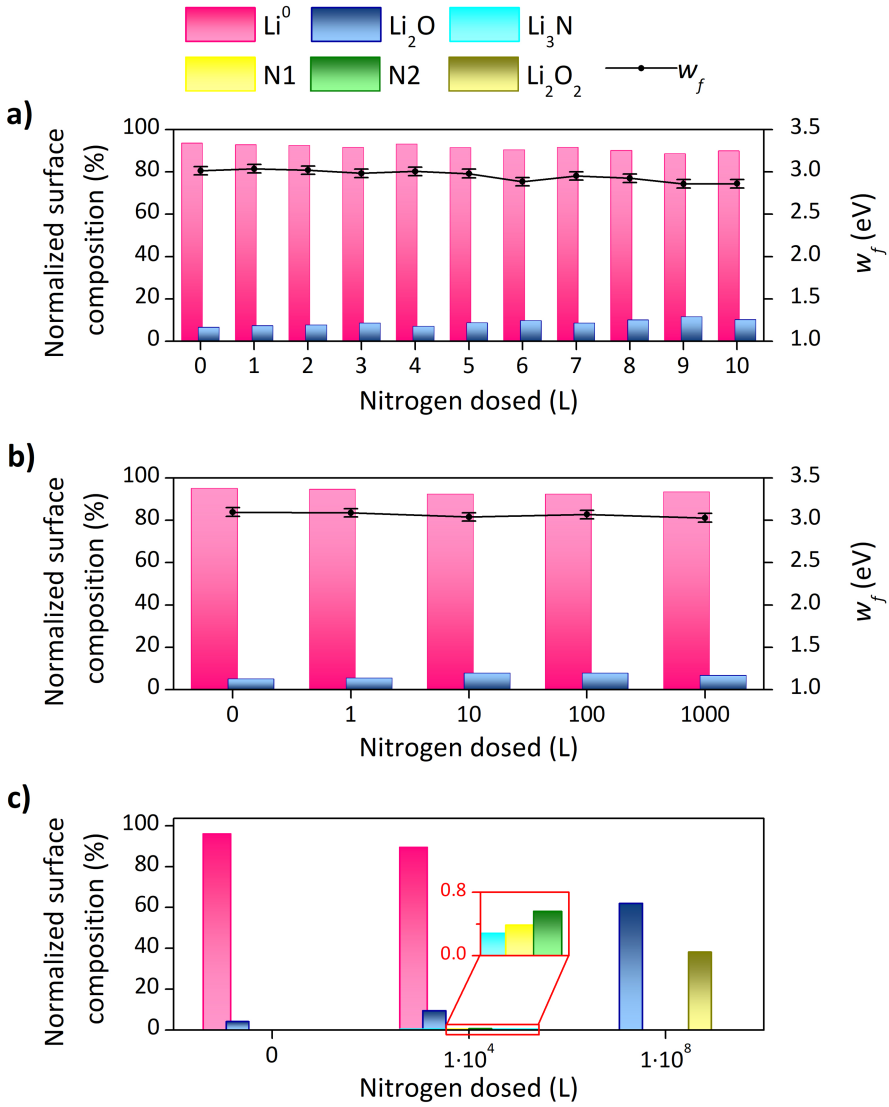

Figure 3.16. Compositional and work function evolution of a clean metallic lithium foil exposed to nitrogen gas for **a)** low dose range **b)** medium dose range and **c)** high dose range. There is no reaction between metallic lithium and nitrogen gas for low and medium dose ranges. For high dose range, a small amount of nitrogen based compunds is detected, represemted by the inset. We could not collect the work function for the high dose range.

As mentioned in the introduction, there are several studies where Li_3N is obtained just by direct reaction between lithium and nitrogen gas[139,144–146]. All these studies use atmospheric pressures, considering how sensitive is lithium to both

oxygen and carbon dioxide gases, even pressures of $1 \cdot 10^{-8}$ mbar modify the surface, it would be reasonable to think that studies at atmospheric pressure are conditioned by the traces of impurities that will have a major impact on the surface reactions of the starting surface, hence determining the evolution of the surface compounds. In other words, clean metallic lithium surface out of UHV conditions, or untreated Li metal surfaces are going to have a significant contamination overlayer even if exposed to pure gases. Then, the formation of Li_3N observed in other works could be related to the existence of native surface impurities such as lithium oxide that already reduce the surface work function enhancing the needed energy drive to catalyze the lithium nitride formation.

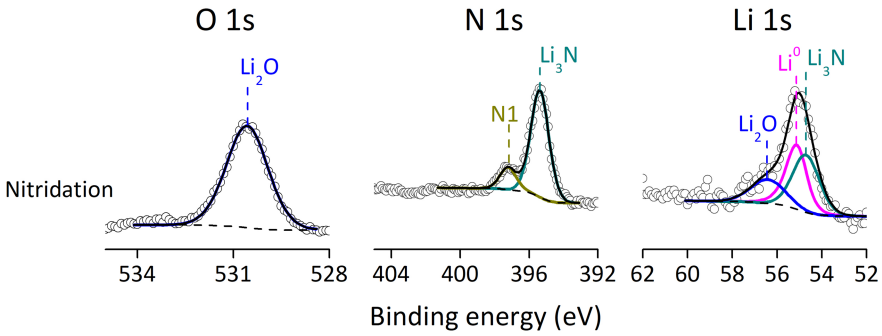

Figure 3.17. Fitting of the XPS photoelectron peaks of a lithium foil after nitrogen ion implantation. In the spectra, experimental data (dots) follows the fitted curve (black line) and background is represented by a dashed line.

3.5 Conclusions

Each of the studied gases has a singularity when they interact with the surface of clean metallic lithium. Oxygen leads to a dramatic oxidation of the lithium where there are no traces of metallic lithium on the first 8.6 nm of the surface after 9 L O_2, which lead to a surface fully covered by Li_2O. When increasing the pressure of O_2 up to 10^{-4} mbar, a new specie is also formed: lithium peroxide, Li_2O_2 that grows into the subsurface region keeping Li_2O in the outermost surface region. In the interaction of lithium with CO_2 gas, Li_2O, Li_2CO_3 and CO species are formed. Oxidation process of the Li surface is slower for this second gas, even after the highest dose of $8 \cdot 10^8$ L CO_2, metallic lithium can be detected on the first 10 nm of

the surface. This suggests that carbon-based compounds are able to slow down the reaction, being lithium carbonate the most important compound.

With the last interaction analyzed in the Li-N_2 system, no reaction between metallic lithium and nitrogen gas for low and medium dose ranges has been observed. Only a hint of a possible interaction has been detected in the high dose range. However, this at high doses is going to be rapidly masked by the reaction of the Li surface with oxygen impurities present on the nitrogen line. From the first system studied, we know that oxygen is much more reactive to lithium than nitrogen. The only way to obtain lithium nitride has been by reactive ion implantation.

Lithium surfaces treated with O_2 , CO_2 and N^+ ions present a lower work function compared to that of bare metallic lithium, a behavior summarized in Figure 3.18. We also found that, when surface compounds are Li^0 and Li_2O, independently of the dosed gas, work function follows an exponential decay defined by the amount of Li_2O on the surface.

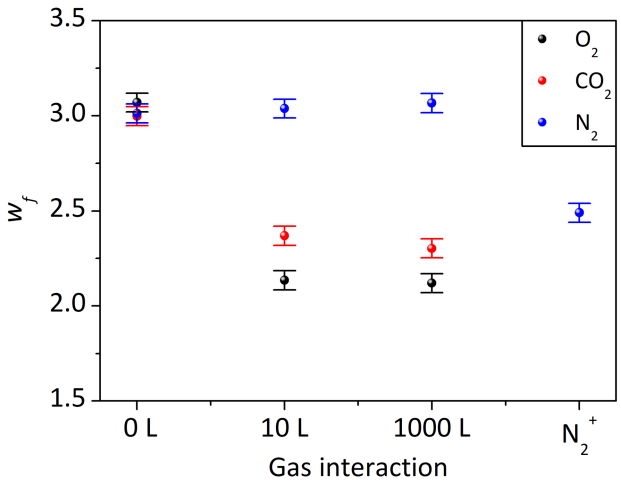

Figure 3.18. Evolution of lithium surface work function when it interacts with O_2, CO_2 and N_2 gases. Data of the work function after N^+ implantation are also included in the right hand side of the graph.

As explained in the introduction (3.1.2), we expect that a decrease in the work function will make the lithium surface less stable against the electrolyte. Then, the interaction of lithium with most common dry atmospheric gases is detrimental for

it to be used as anode in terms of electronic properties, especially the interaction with oxygen gas, the one that reduces the most the work function.

CHAPTER 4

Study of Li carbonate evolution on Li metal surface

In this chapter, insights into reaction mechanism and kinetics of Li_2CO_3 evolution on lithium surface are provided. To this purpose, CO_2 gas reduction on Li metal is studied by synchrotron radiation ambient pressure X-ray photoelectron spectroscopy.

4.1 Introduction

In previous chapter, it has been concluded that the reduction of carbon dioxide gas on pure lithium metal surface generates a mixture of lithium carbonate, lithium oxide and other carbon-based species. Among these compounds, studying the evolution of lithium carbonate is of special interest due to its adverse impact in the stability of the solid electrolyte interphase (SEI). This results from the low Li ionic conductivity of Li_2CO_3 compare to that of other species also part of the solid electrolyte interphase layer, such as Li_2O. Li_2CO_3 retards Li^+ transport through the SEI layer, promoting inhomogeneous Li deposition; thus, dendrite formation[168]. In order to shed some light on the reaction pathway that leads to Li_2CO_3 and detect atmospheric conditions that promotes its growth, in this chapter evolution of Li_2CO_3 on Li surface as a consequence of the interaction of the metal with CO_2 gas is studied.

Looking to literature, one of the few studies that analyze the mechanism behind Li_2CO_3 evolution was done in 1998[137]. Zhuang and co-workers used X-ray

photoelectron spectroscopy (XPS), ultraviolet photoelectron spectroscopy (UPS) and ab initio self-consistent Hartree–Fock theoretical calculations to propose the following reaction mechanisms:

$$CO_2 \rightarrow [CO_2]_{ads} \quad (4.1)$$

$$2[CO_2]_{ads} \rightarrow {CO_3}^{2-} + CO_{ads} \quad (4.2)$$

Probably via an oxalate $[C_2O_4]_{ads}$ intermediate, and:

$$CO_{ads} \rightarrow C + O^{2-} \quad (4.3)$$

$$CO_2 + O^{2-} \rightarrow {CO_3}^{2-} \quad (4.4)$$

However, both spectroscopic techniques used to study this reaction are limited by ultra-high vacuum (UHV) conditions, which means reaction was only studied in *ex situ* conditions. In this chapter, we propose to overcome this drawback studying surface evolution with Ambient Pressure XPS (APXPS), where reaction can be followed *in situ* (chapter 2 section 2.3.2 for more information about the technique). With it, we can further explore the reaction mechanism that leads to the formation of Li_2CO_3 by looking to the evolution of lithium surface in CO_2 gas.

APXPS has been already proved to be successful in clarifying several reaction mechanisms[169–171]. In fact, CO_2 reduction on metals such as silver, copper and nickel is actively studied by APXPS due to the role these metals play as catalyst to produce low-carbon fuels[172,173]. The aim of this studies is to be able to reduce levels of atmospheric CO_2 gas that produces greenhouse effect[160]. However, high reactivity of alkaline metals and instability in electrochemical systems make them undesirable for CO_2 reduction if the aim is the recycling of CO_2[174]. To our knowledge, the reaction mechanism of CO_2 interaction with alkaline metals is unexplored by APXPS.

4.2 Spectra measuring conditions and data analysis guidelines

APXPS spectra were collected using the system detailed in chapter 2 section 2.3.2.2. As explained there, this system is in a synchrotron radiation facility, which

generates soft X-rays that can be tuned from 250 to 850 eV and spectra can be measured from UHV conditions to pressures of 2 Torr.

4.2.1 Data analysis guidelines

APXPS data is analyzed with the CasaXPS version 2.3.19PR1.0 (Casa Software Ltd, Teighmouth, UK). Calibration is made based on Li^0 binding energy in Li 1s spectra and lithium carbonate binding energy in C 1s spectra. Fitting conditions are summarized in Table 4.1.

Table 4.1. Fitting parameters used to identify different compounds on metallic lithium surface, based on literature and experimental evidence[124,127,133,152].

Compound	Fitting parameters (eV)		Li 1s	O 1s	C 1s
Li^0	Binding energy		54.90-55.10		
	FWHM				
	hv =	280	0.4-0.6		
	hv =	510	0.6-0.8		
	hv =	600	0.7-0.9		
	hv =	750	1-1.2		
Li_2O	Binding energy		56.30-56.50	531.10-531.30	
	FWHM				
	hv =	280	1.2-1.4		
	hv =	510	1.3-1.5		
	hv =	600	1.3-1.5	1.2-1.4	
	hv =	750	1.4-1.6	1.4-1.6	
Li_2CO_3	Binding energy		57.90-58.10	534.55-534.75	292.60-292.80
	FWHM				
	hv =	280	1.2-1.4		
	hv =	510	1.3-1.5		1.1-1.3
	hv =	600	1.3-1.5	1.3-1.5	1.1-1.3
	hv =	750	1.4-1.6	1.5-1.7	1.4-1.6

FWHM varies depending on physical parameters of the measurements and equipment, so it changes with the studied photon energy. Lineshape of fitting peaks is GL(30) (30% Lorentzian and 70% Gaussian convolution) for all the compounds except for metallic lithium, which has an asymmetric pseudo voight function as lineshape. This asymmetric lineshape, defined as LF(α,β,m,w), takes into account the asymmetric tail in the higher binding energy side of the metallic peak that is caused by the small kinetic energy losses originated by the interaction of the core level electrons with the conduction band of the metal, as explained in chapter 3 section 3.2. α and β define the asymmetry of the lineshape, m is the

contribution of the gaussian function and *w* is a damping parameter to force the tail to reduce towards the limits of the integration limits[151]. This Li^0 asymmetric lineshape is, for photon energies of 510 eV, 600 eV and 750 eV, LF(1,2,20,100). For photon energy of 280 eV is LF(1,5,20,100). Other species that are not in the table are explained later in their corresponding section.

Three of the studied photon energies (280 eV, 510 eV and 750 eV) are chosen to be able to measure the different core levels of the surface at same kinetic energy. In this way, the only data needed to calculate the atomic concentration of the surface elements is the cross section of the elements at each specific photon energy and the flux of electrons, according to equation (2.7). In this chapter, overlayer attenuation method (section 2.3.1.2) is used to calculate thickness of surface layers, using data from Li 1s core level at different photon energies. Physical parameters needed to calculate both the atomic concentrations and thicknesses calculations are summarized in Table 4.2, Table 4.2 and Table 4.4.

Table 4.2. Physical parameters used to quantify surface atomic concentration and to calculate thickness of surface layers later in the chapter.

Photon energy (eV)	Photon Flux[I]	Core level	Kinetic energy (eV)	Cross section[II] (Mbarn)
280	0.231	Li 1s	~222	0.1103
510	0.705	C 1s	~222	0.2563
		Li 1s	~452	0.0199
750	0.47	O 1s	~222	0.2931
		Li1s	~542	0.0063

[I] normalized value of photon flux (photons/s mA μm), experimental parameter measured in beamline 9.3.2 of Advanced Light Source.
[II] from database[175]

Table 4.3. Atomic density of surface compounds used to calculate thickness of surface layers later in the chapter.

Compounds	Atomic density of Li (10^{-22} atom/cm^3)
Li^0	4.6
Li_2O	8.1
Li_2CO_3	3.4
$Li_2C_2O_4$	2.5

Table 4.4. Inelastic mean free path of electrons from Li 1s spectra used to calculate thickness of the overlayers. Data obtained from the software *QUASES-IMFP calculation by TPP2m formula.*

PE (eV)	Electrons originated in	Kinetic energy (eV)	λ through Li^0 layer (Å)	λ through Li_2O layer (Å)	λ through Li_2CO_3 layer (Å)	λ through $Li_2C_2O_4$ layer (Å)
280	Li^0	225.0	10.68			
	Li_2O	223.6		8.67		
	Li_2CO_3	222.0			9.15	
	$Li_2C_2O_4$	222.2				9.50
510	Li^0	455.0	18.2			
	Li_2O	453.6		13.78		
	Li_2CO_3	452.0			14.41	
	$Li_2C_2O_4$	452.2				14.87
600	Li^0	545.0	20.96			
	Li_2O	543.6		15.69		
	Li_2CO_3	542.0			16.38	
	$Li_2C_2O_4$	542.2				16.90
750	Li^0	695.0	25.43			
	Li_2O	693.6		18.79		
	Li_2CO_3	692.0			19.59	
	$Li_2C_2O_4$	692.2				19.67

4.3 Li foil surface cleaning

Lithium foil used in this study is a commercial foil from *Alfa Aesar* (99.9% purity, metal basis, 1.5 mm thick). This foil has been characterized in two situations: after scraping it in Ar atmosphere and after scraping it in UHV conditions.

4.3.1 Characterization of Li foil surface cleaned in Ar atmosphere

Commercial lithium foil was stored in an argon atmosphere glove box, where H_2O and O_2 gas levels were below 0.1 ppm. Surface was scraped using a UHV cleaned blade in the glove box, a standard procedure in battery community before using the lithium as an anode. Sample was then transferred from the glove box to the load lock of APXPS instrument, preventing surface exposure to atmospheric air. Figure 4.1 represents the APXPS spectra of the Li foil measured with a high photon energy (835 eV) in order to broaden range of measured binding energies. Detected surface elements of this foil are oxygen, carbon and lithium.

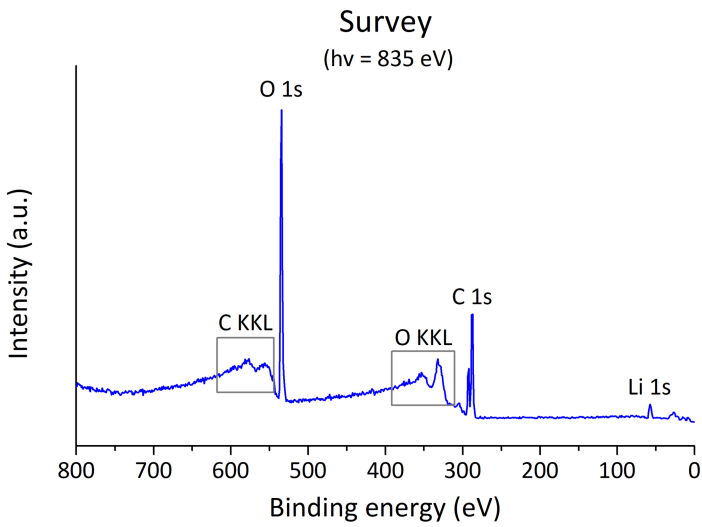

Figure 4.1. APXPS survey spectra collected in UHV of a lithium foil scraped in argon atmosphere glove box. Detected surface elements are lithium, oxygen and carbon.

Figure 4.2 shows the in-depth distribution of surface compounds. According to it, there is no clear evidence of having metallic lithium on the surface even at the highest photon energy, 750 eV. This photon energy has an estimated probing depth of 8 nm, which corresponds to 3 times the inelastic mean free path (λ) of electrons. Indeed, considering binding energies of Table 4.1, we can easily identify lithium carbonate and lithium oxide. Adventitious carbon contamination is also detected on the surface (CH/CC). A deeper analysis of the nature and binding energy of it can be found later in this chapter. It is also worth mentioning that species such as LiOH and Li_2O_2 could also be present on the surface. However, aim of this section is to have a general view of the effectiveness of cleaning the lithium in argon atmosphere condition more than conducting a detailed analysis of surface composition, so we are only going to consider the dominant compounds of surface.

When comparing O 1s and Li 1s spectra at different photon energies in Figure 4.2, the more surface sensitive (smaller photon energies), the more carbonate there is on the surface, as signal of carbonate increases while signal of Li_2O decreases. Then, in a commercial lithium foil cleaned in argon atmosphere, lithium-based compounds in the first 8 nm of the surface are Li_2O and Li_2CO_3, where the carbonate lies on top of the oxide.

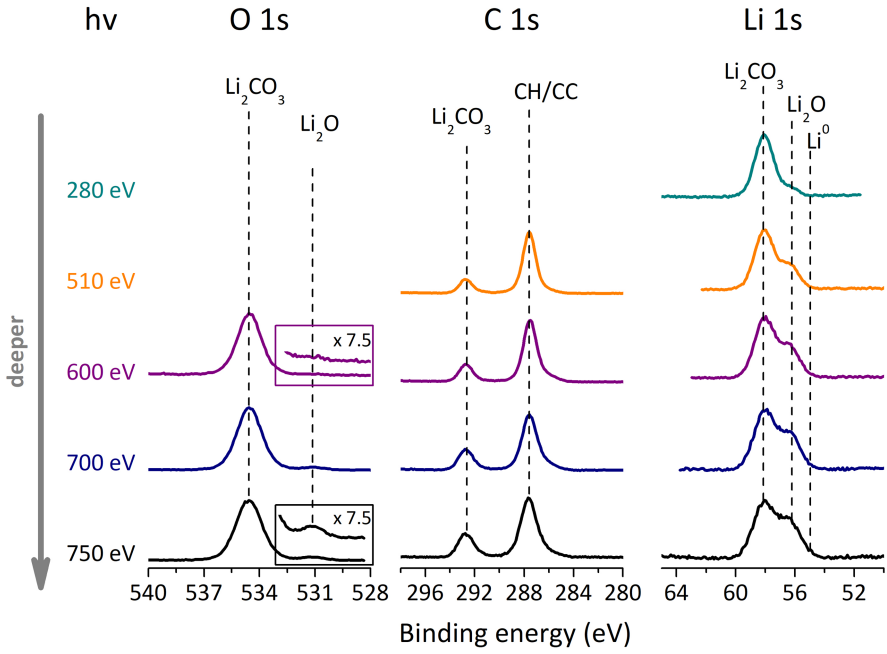

Figure 4.2. APXPS spectra showing depth profiling of a commercial lithium foil which has been scraped in argon atmosphere glove box.

Looking to the amount of carbonate this Li foil surface presents, one can think the commercial foil has already been exposed to CO_2 gas. In order to check it, 400 mTorr CO_2 gas were added to the surface. Figure 4.3 shows that surface is not changing after treating it with the gas. However, in the previous chapter we learnt that even a low dose of 10^{-8} mbar ($7.5 \cdot 10^{-5}$ mTorr) of CO_2 gas is modifying a clean metallic lithium surface. This difference suggests that, as was speculated, lithium surface stored in an inert gas has already been exposed to an atmosphere that contains CO_2 gas, which could be happening in the glove box. Although glove boxes typically have sensors for both O_2 and H_2O, they neither monitor nor control for potential CO_2 gas contamination.

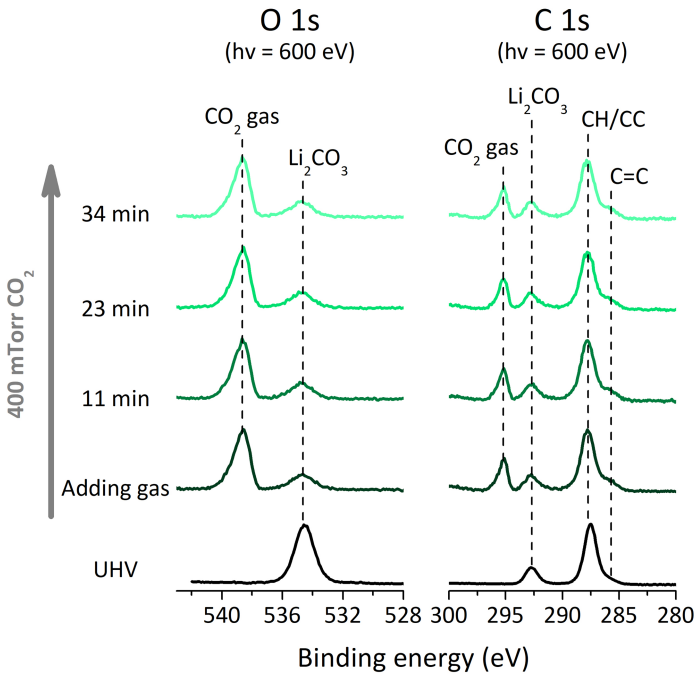

Figure 4.3. Evolution of C 1s APXPS spectra of a commercial lithium foil measured at a photon energy of 600 eV while dosing 400 mTorr of CO_2 gas.

4.3.2 Characterization of Li foil surface cleaned in UHV

As in previous chapter, in this one Li foil also needs to be cleaned in UHV conditions in order to be able to study the interaction of Li^0 with CO_2 gas. The way chosen to clean the surface of lithium foil is different from previous chapter. Here, instead of using argon ion bombardment, Li surface was cleaned by scraping it in UHV conditions. For that, a wobble stick that has both linear and 22° angle motions with a blade at the edge was assembled on a CF port of the load lock of APXPS UHV system. With this tool lithium samples were scraped in UHV conditions, with a base pressure in the range of $1 \cdot 10^{-8}$ Torr. Figure 4.4 shows the difference between scraped and non-scraped surfaces.

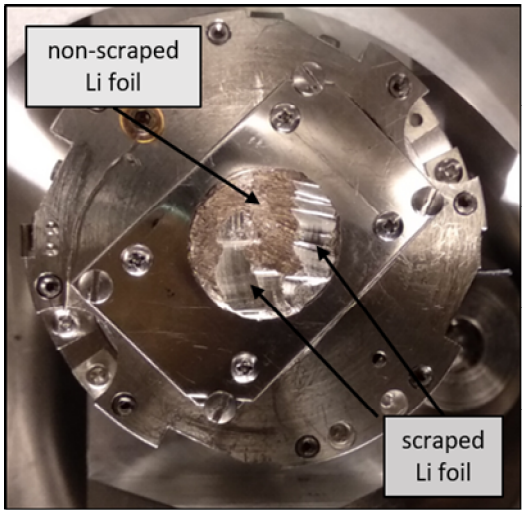

Figure 4.4. There is a clear difference in color and shine of a Li foil coming from argon atmosphere between the UHV scraped and non-UHV scraped sides.

Figure 4.5a shows the APXPS spectra of the UHV scraped side of the foil, where presence of Li^0 in the surface is clear. The three core levels from Figure 4.5a have the same kinetic energy, so the areas of that photoelectron peaks can be used to quantify the concentration of the compounds from the surface, using equation (2.7) and Table 4.2 parameters. This quantification is shown in Figure 4.5b. In Figure 4.5a, Li^0 and Li_2O have been identified with the constrains from Table 4.1. The presence of Li^0 is also corroborated by the plasmon loss structures representative of metallic lithium[135] indicated in Li 1s spectra. About LiOH, it has been identified with the position of the highest binding energy peak of O 1s, which corresponds to that of LiOH according to literature[133]. Both Li_2O and LiOH are fitted using just one peak in Li 1s spectra, called Li^+. Carbon contamination has contribution from aliphatic carbon C-H/C-C and a higher binding energy carbon that can be correlated to C-O bond[176], both typical from adventitious carbon[159]. A small amount of graphitic carbon (C=C) appears also at lower binding energies than adventitious carbon[177]. According to the surface compounds quantification represented in Figure 4.5b, if 1 oxygen atom is assigned to each C-O species from C contamination, C-O based oxygen only represent 1.1% of total oxygen atoms. Due to this, we neglect its contribution in O 1s spectra.

Binding energy of aliphatic carbon (around 288 eV, Figure 4.5a) is higher than that from previous chapter (285 eV, Figure 3.11). A study that focuses on the correct assignment of binding energies in lithium foil mentions the existence of two types of CH/CC: one from the bulk around 285 eV, and another one at 3 eV higher than that one, which comes from the surface[178]. Then, CH/CC measured in this chapter will correspond to surface CH/CC, which agrees with the higher surface sensitivity photon energies of this chapter. To confirm that the proposed binding energy based on Li^0 position is feasible, we measured the Fermi edge region of this same sample by APXPS. Figure 4.6 shows that the Fermi edge lies at 0 eV, as expected for metallic samples. Then, we can assume calibration based on Li^0 is adequate.

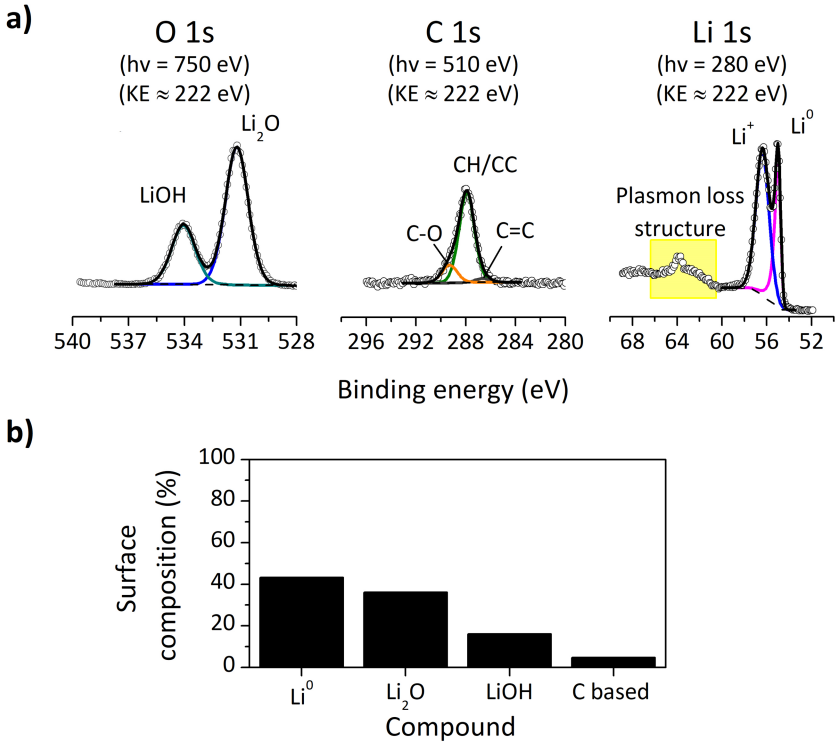

Figure 4.5. a) APXPS spectra of Li 1s, O 1s, and C 1s core levels of a UHV scraped lithium foil measured at same kinetic energy, which allows to use the areas of the photoelectron peak to quantify the surface composition. In the spectra, the fitted curve (black line) follows experimental data (dots), and background is represented by a dashed line. **b)** First 3 nm surface composition of a UHV cleaned commercial lithium foil.

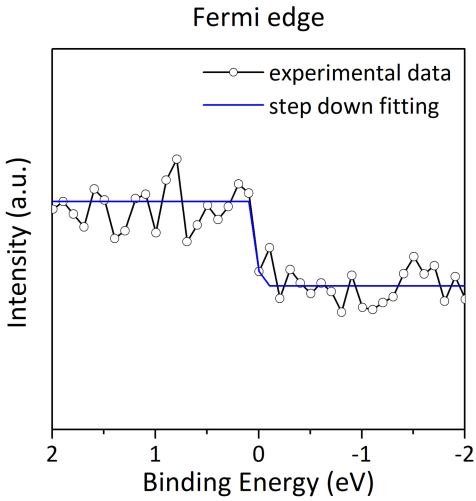

Figure 4.6. APXPS spectra of fermi edge region on a UHV scraped lithium foil measured at a photon energy of 280 eV. The position of the fermi edge is at 0 eV, as should be for a metallic sample.

According to the surface compounds quantification represented in Figure 4.5b, surface is dominated by Li^0 and Li_2O. This quantification corresponds to the first 3 nm of the surface, since probing depth can be estimated as 3 times inelastic mean free path (λ) of electrons. In order to obtain the in-depth distribution of Li species in the surface, we measured Li 1s spectrum at several photon energies. Figure 4.7 shows that when surface is measured at the highest photon energies, oxidized lithium intensity decreases compare to that of Li^0, meaning oxidized layer is on top of Li^0 substrate. In this same figure, probing depth of each photon energy is also indicated.

To have an estimation of the thickness of oxidized overlayer, SESSA (*NIST Database for the Simulation of Electron Spectra for Surface Analysis*) software was used. Considering a photon energy of 600 eV and instrument settings of the spectrometer from beamline 9.3.2 at the Advance Light Source synchrotron, several Li 1s spectra were simulated for the following system: Li_2O layer on top of a Li^0 substrate, where the variable is the thickness of Li_2O overlayer. With these spectra a correlation was obtained between the intensities of Li^0 and Li_2O measured at a photon energy of 600 eV, from Li 1s core level. This correlation is illustrated in Figure 4.8 and represented in the following equation:

$$d_{Li_2O} = 59.9 - 13.1 \ln\left(I_{Li_2O} \Big/ I_{Li_2O} + I_{Li^0}\right) \tag{4.5}$$

where d is the thickness of Li_2O overlayer (Å) and I are the intensities of Li_2O and Li^0 peaks from Li 1s measured at a photon energy of 600 eV. With this equation we can directly obtain the thickness of the overlayer, using the intensities of Li 1s Li^0 and Li_2O measured at 600 eV.

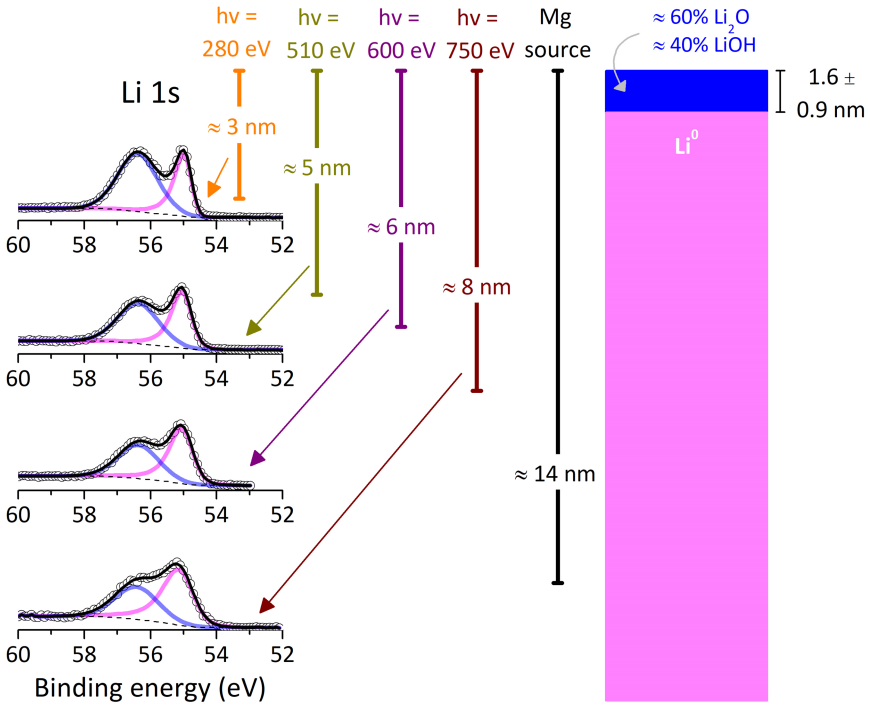

Figure 4.7. Li 1s APXPS spectra collected in UHV at different photon energies to illustrate the depth profiling of a clean Li surface. In the spectra, the fitted curve (black line) follows experimental data (dots), and background is represented by a dashed line. The approximated probing depth (3 times the inelastic mean free path) of each measured photon energy and that of Mg source are indicated in the figure. The mean oxide layer thickness present on UHV cleaned lithium surfaces is also specified in the right side of the figure.

The oxide layer on top of Li 1s of our UHV cleaned lithium foil is formed by both Li_2O and LiOH, as shown in Figure 4.5. If we want to use the above-mentioned equation to calculate the thickness of the overlayer that is attenuating Li^0 intensity in Li 1s core level, we are assuming that all Li^+ is related to Li_2O. However, according to Figure 4.5b, Li_2O accounts for the 60% of oxidized lithium. Furthermore, if we compare the λ of electrons coming from Li^0 measured at a photon energy of 600 eV, λ of electrons through Li_2O layer is 15.72 Å, and through

LiOH layer is 16.28 Å. This similar λ makes the attenuation that both compounds produce on Li metal surface electrons comparable. Then, we consider the use of equation (4.5) to calculate the thickness of the oxidized layer on top of lithium metal is adequate. The calculated average thickness of oxidized layer of the several clean surfaces studied on this chapter is 1.6 ± 0.9 nm, which is indicated in Figure 4.7.

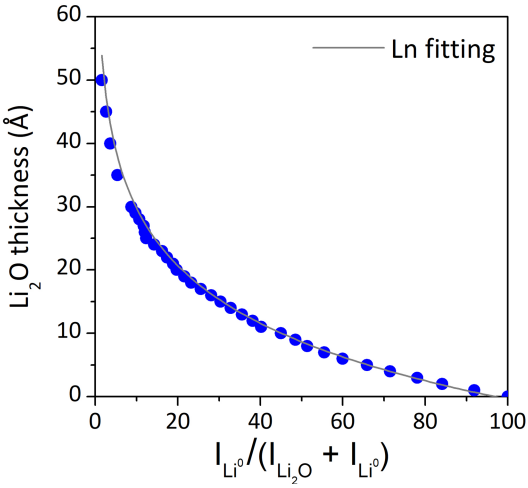

Figure 4.8. Relation between the Li^0 and Li_2O compound intensities of Li 1s and the thickness of Li_2O overlayer, calculated by SESSA software. Simulation considers a photon energy of 600 eV and instrument settings of beam line 9.3.2 from the Advanced Light Source.

4.4 Li_2CO_3 evolution on Li metal surface

For the study of Li_2CO_3 growth on Li metal, three CO_2 gas (5.0 research purity from *Praxair*) pressures were considered: 0.1 mTorr, 10 mTorr and 400 mTorr. Gas was dosed for around one hour at each pressure. Every gas pressure dose started with a UHV cleaned Li foil.

4.4.1 Evolution of carbon-based compounds

In order to study the evolution of carbon while treating Li with CO_2 gas, first of all, the compounds present on C 1s spectrum need to be defined. In this spectrum, binding energy of lithium carbonate is clearly defined at 292.70 eV (Table 4.1). Binding energy of CH/CC from adventitious carbon has also been already found to

be at 287.9 eV in this chapter (section 4.3.2). However, as in previous chapter, identifying the compounds with binding energy between carbonate and CH/CC is more complex, considering the amount of different surface compounds that can be formed[160]. In the previous chapter, while studying this same interaction with XPS, the minimum number of species besides carbonate and CH/CC were identified. Two more species were found, defined in Table 3.4. However, the higher resolution of this set of experiments and the higher surface sensitivity of the measurements allow a more detailed analysis of C 1s spectrum compared to the analysis from previous chapter.

In order to find the most appropriate fitting that would help to clarify how many species are on the surface, the residual standard deviation of selected fittings in C 1s spectrum of the final surface of 10 mTorr CO_2 gas treatment is compared, measured at 600 eV photon energy in UHV conditions. We assign same FWHM to all the components that form C 1s spectra. The starting point of the fitting has the known CH/CC and carbonate compounds, and also C-O observed in clean lithium (Figure 4.5a). Then, we add extra components until we get a reasonable simulation of the measured spectra. Looking to the residual standard deviation and representation of measured spectra illustrated in Figure 4.9, we conclude that there are two more carbon-based compounds on the surface, named as C1 and C2, which are represented in Fitting C from the figure. Finally, to refine more the spectra, we add the graphitic carbon (Fitting D, Figure 4.9) already seen in clean lithium (Figure 4.5a).

Main purpose of this chapter is the study of the evolution of lithium carbonate; then, we are looking for the most consistent fitting parameters to obtain the most trustful Li_2CO_3 area evolution. For that, we refine the FWHM of C 1s components of Fitting D. This refinement is based on the concept that FWHM of the same component should be constant, so we should have same FWHM before and after treating the surface with the gas. If we consider that all the components from C 1s have the same FWHM (Fitting D_1, Figure 4.10a), average FWHM of all the samples analyzed in this chapter is not constant, after treatment it gets smaller (Figure 4.10b). However, if we consider Li_2CO_3 FWHM is different from the rest (Fitting D_2, Figure 4.10a), now each FWHM is constant (Figure 4.10b). Then, having a different FWHM for carbonate is more consistent than having same FWHM in all C 1s components.

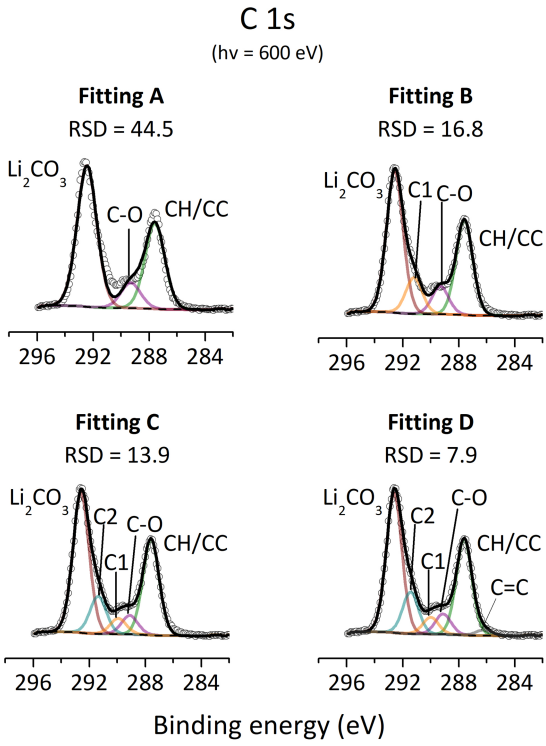

Figure 4.9. APXPS C 1s spectra of a lithium foil after 10 mTorr CO_2 gas treatment for about one hour, deconvoluted with several fittings and measured at a photon energy of 600 eV and in UHV condition. The smallest residual standard deviation corresponds to fitting D, which has two more carbon-based components besides C=C, CH/CC, C-O and Li_2CO_3. In the spectra, the fitted curve (black line) follows experimental data (dots), and background is represented by a dashed line.

According to reported binding energy difference with respect to CH/CC, C1 could be related to C=O carbonyl functional group[43,179]. The component that is representing C2 is found considering its binding energy and the evolution of carbon components of a clean lithium surface when dosing 0.1mTorr, 10 mTorr and 400 mTorr CO_2. How the C 1s spectrum evolves is represented in Figure 4.11, and how area of each compound grows is represented in Figure 4.12. All the areas are normalized to the maximum area of Li_2CO_3. In the dose of 400 mTorr CO_2, photoelectrons are attenuated by CO_2 gas, as can be seen by the gas peak measured at this pressure in Figure 4.11. In order to be able to compare the areas with the other two pressures, areas at 400 mTorr CO_2 gas represented in Figure 4.12 are corrected not to consider the attenuation effect.

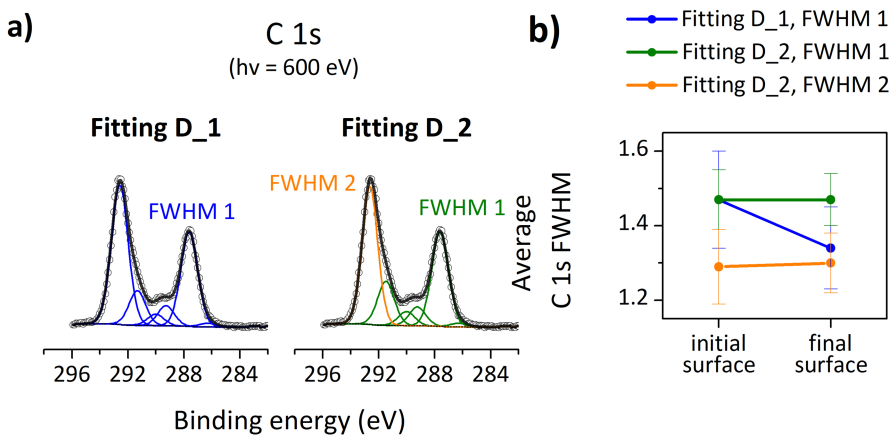

Figure 4.10. a) APXPS C 1s spectra of a lithium foil after 10 mTorr CO_2 gas treatment for about one hour, deconvoluted with two types of fittings. Data was collected at a photon energy of 600 eV in UHV conditions. In the spectra, the fitted curve (black line) follows experimental data (dots), and background is represented by a dashed line. **b)** Comparison of the evolution of average FWHM of the two refinements of fitting D. Data is from all the samples used in this chapter when Li foil surface is UHV cleaned (initial surface) and after CO_2 gas has been dosed (final surface).

When looking to the evolution of the areas in Figure 4.12, the compounds that clearly grow are Li_2CO_3, C2 and CH/CC. Considering C2 binding energy relative to carbonate, it can be related to an alkyl lithium carbonate ($ROCO_2Li$) compound[43,180–183]. In a $ROCO_2Li$ structure, there are three types of carbons which should present different binding energies: the one from carbonate ($RO\underline{\mathbf{C}}O_2Li$), another one bonded to oxygen and carbon (R-$\underline{\mathbf{C}}$-OCO_2Li) and the one from the alkyl group ($\underline{\mathbf{C}}$-C). If C2 were carbonate from $RO\mathbf{C}O_2Li$, the other two types of carbons should be evolving at least same as it. R-$\underline{\mathbf{C}}$-OCO_2Li could be related to C-O ether bond present on the surface[184]. About $\underline{\mathbf{C}}$-C, it should be represented by the component CH/CC of C 1s. When looking to the evolution of them represented in Figure 4.13, there is no evidence to support C2 is part of $ROCO_2Li$. In this evolution, the initial amounts of CH/CC and C-O have been subtracted to compare their evolution with respect to C2. C-O is evolving less than C2 at the three pressures, and CH/CC evolution is function of the pressure. Furthermore, $ROCO_2Li$ has been reported as a consequence of decomposition of organic electrolytes[182]. With all this information, we can exclude that C2 corresponds to $ROCO_2Li$.

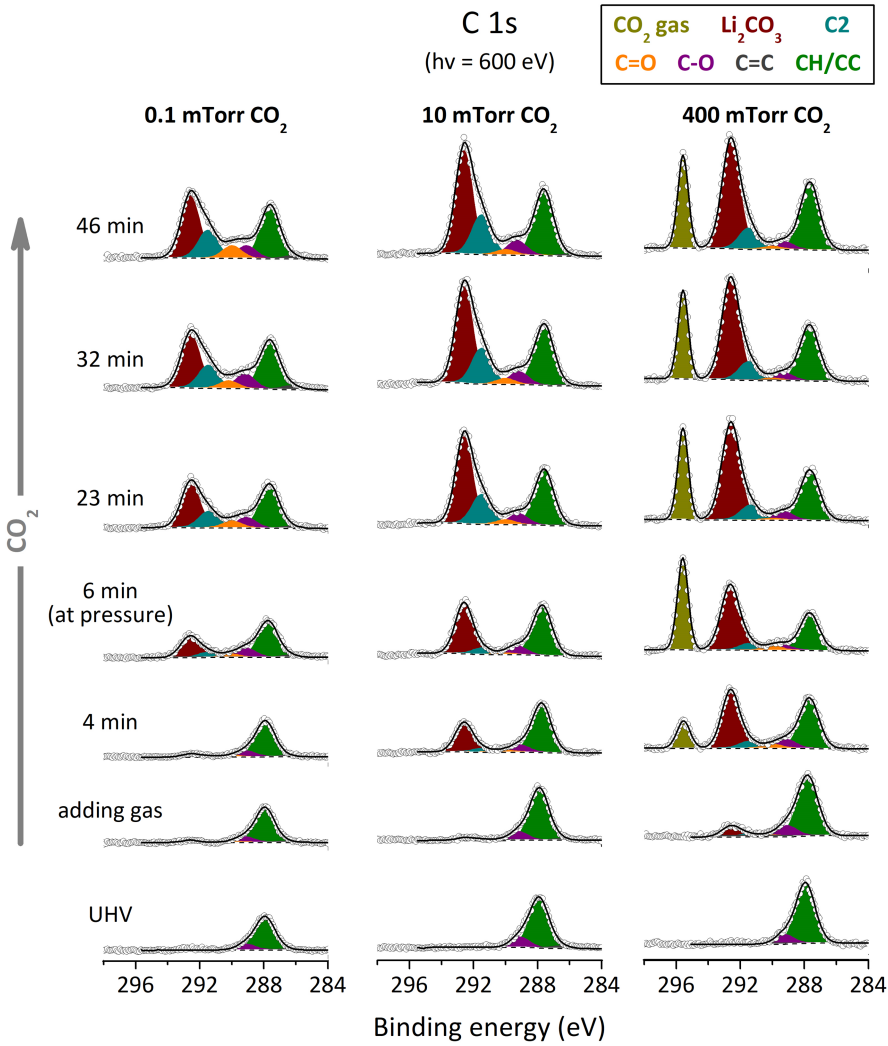

Figure 4.11. Evolution of C 1s APXPS spectra of a lithium foil surface measured while dosing CO_2 gas at 0.1 mTorr, 10 mTorr and 400 mTorr pressures. Data was collected using a photon energy of 600 eV. For the highest pressure, CO_2 gas attenuates C 1s spectra. In the spectra, the fitted curve (black line) follows experimental data (dots), and background is represented by a dashed line.

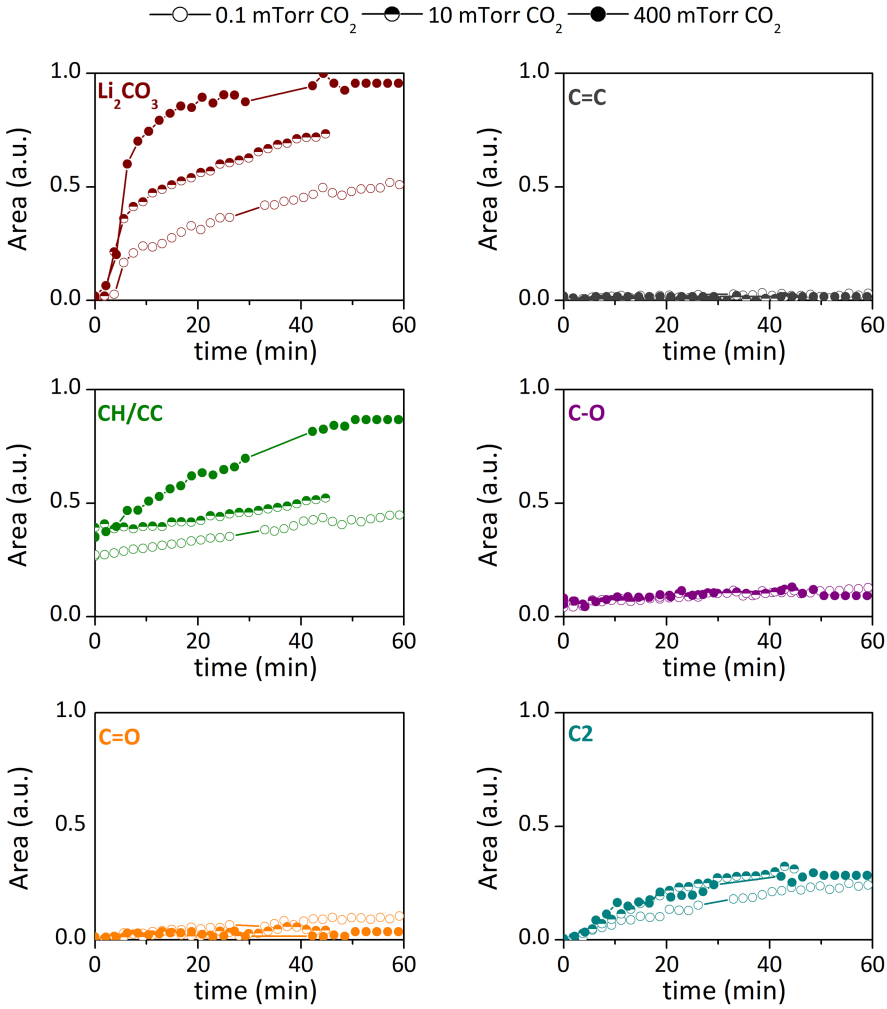

Figure 4.12. Evolution of the areas of C 1s APXPS compounds of a lithium foil surface measured while dosing CO_2 gas at 0.1 mTorr, 10 mTorr and 400 mTorr pressures. Data was collected using a photon energy of 600 eV. Areas are normalized to the maximum area of Li_2CO_3, and areas for the dose of 400 mTorr CO_2 areas are corrected not to consider the attenuation produced by CO_2 gas.

Another alternative to $ROCO_2Li$, if we consider again the binding energy difference between the carbonate and C2, is lithium-bound oxalate, $Li_2C_2O_4$[160,185]. Oxalate as a consequence of CO_2 reduction has been observed in several substrates with alkali metal coverages such as Na and K[186–188]. It was also measured by infrared spectroscopy when evaporated lithium interacts with CO_2 gas[128]. Furthermore,

$Li_2C_2O_4$ explains the independent evolution of C2 with respect to the rest of carbon-based species from Figure 4.13. Therefore, from now on, we are going to consider C2 represents $Li_2C_2O_4$.

The final refined fitting option, used to fit all C 1s at 600 eV, is summarized in Table 4.5. Here, the binding energy of CH/CC and C=C compounds is less constrained. This is due to an observed shift in the binding energy of them while dosing CO_2. Both move to lower binding energy, a behavior already discussed in previous chapter (section 3.4.2). Figure 4.14 shows the carbon spectrum of 10 mTorr CO_2 at UHV conditions, where all carbon-based compounds are identified.

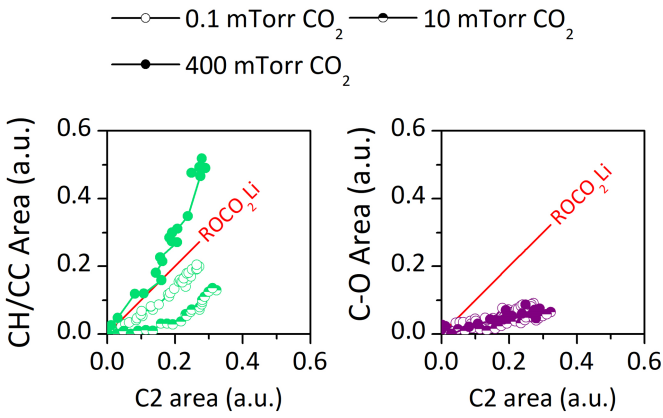

Figure 4.13. Relationship between the evolution of the C 1s XPS area of C2 with respect to C-O and CH/CC compounds of a lithium foil surface while dosing CO_2 gas at 0.1 mTorr, 10 mTorr and 400 mTorr pressures. Data was collected at a photon energy of 600 eV. Areas are normalized to the maximum area of lithium carbonate, and the initial area of each compound has been subtracted to observe the evolution. Red line indicates the relationship compound areas should follow if C2 would correspond to RO**C**O_2Li, (1:1).

Table 4.5. Final fitting parameters of C 1s spectra measured at a photon energy of 600 eV.

Fitting constrains (eV)	C=C	CH/CC	C-O	C=O	$Li_2C_2O_4$	Li_2CO_3
BE	286.20-286.50	287.50-287.90	289.10-289.30	290.00-290.20	291.30-291.50	292.60-292.80
FWHM	A	1.4-1.6 = A	A	A	A	1.2-1.4

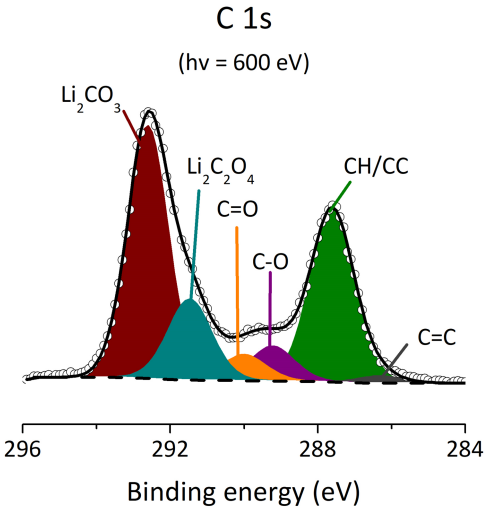

Figure 4.14. APXPS C 1s spectra of a lithium foil after 10 mTorr CO_2 gas treatment for about one hour, deconvoluted with two types of fittings. Measurement was done at a photon energy of 600 eV in UHV condition. All carbon-based compounds have been identified. In the spectrum, the fitted curve (black line) follows experimental data (dots), and background is represented by a dashed line.

4.4.2 Li_2CO_3 growth kinetics

When analyzing in more detail the evolution of Li_2CO_3 represented in Figure 4.15, we can observe that Li_2CO_3 growth is linear-parabolic, resembling Deal Groove oxide thick growth model[189]. In this type of growth two regimes are distinguished: a reaction limited regime and a diffusion limited regime, where the layer formed in the initial region is responsible for the diffusion limitation. The linear regime is defined by the following growth rate:

$$d - d_0 = k_L t \tag{4.6}$$

And the parabolic regime is:

$$d^2 - {d_0}^2 = k_P t \tag{4.7}$$

where d is the thickness of the layer at time t, d_0 the initial thickness of the layer, and k_L and k_P are the linear and parabolic reaction rate constant respectively.

Both reaction rate constants at each pressure are calculated based on the Li_2CO_3 area of normalized C 1s spectra measured at a photon energy of 600 eV, which is related to the thickness of the layer. Figure 4.16 shows that, in the linear regime,

pressure plays a noticeable role in the reaction rate. However, in the case of parabolic regime, the reaction rate at 10 mTorr CO_2 and 400 mT CO_2 is very similar. This indicates that diffusion throuhg the layer of Li_2CO_3 formed at the linear regimes of these pressures is limiting the reaction more than the incoming CO_2 molecules.

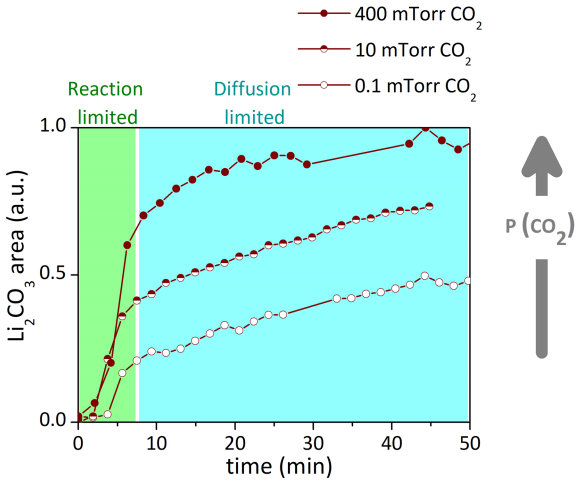

Figure 4.15. In the Li_2CO_3 area evolution (from C 1s APXPS spectra measured at 600 eV) of a lithium foil dosed by three pressures of CO_2 gas, two regimes with different reaction rates can be distinguished.

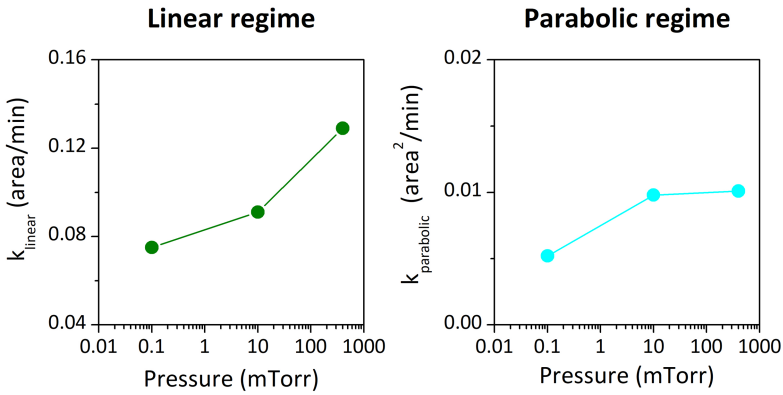

Figure 4.16. Reaction rate constant of Li_2CO_3 growth on Li metal in linear and parabolic regime at three pressures. Reaction rates have been calculated from the areas of Li_2CO_3 in C 1s APXPS spectra, measured at a photon energy of 600 eV.

4.4.3 Depth profiling of lithium-based compounds

An important advantage of performing APXPS measurements in a synchrotron radiation facility is the ability to perform non-destructive depth profiling experiments. To obtain the information of compounds distribution along the surface depth, same surface is measured using several photon energies. Figure 4.17 shows the final surface of Li foil treated at three CO_2 gas pressures, measured at three different photon energies.

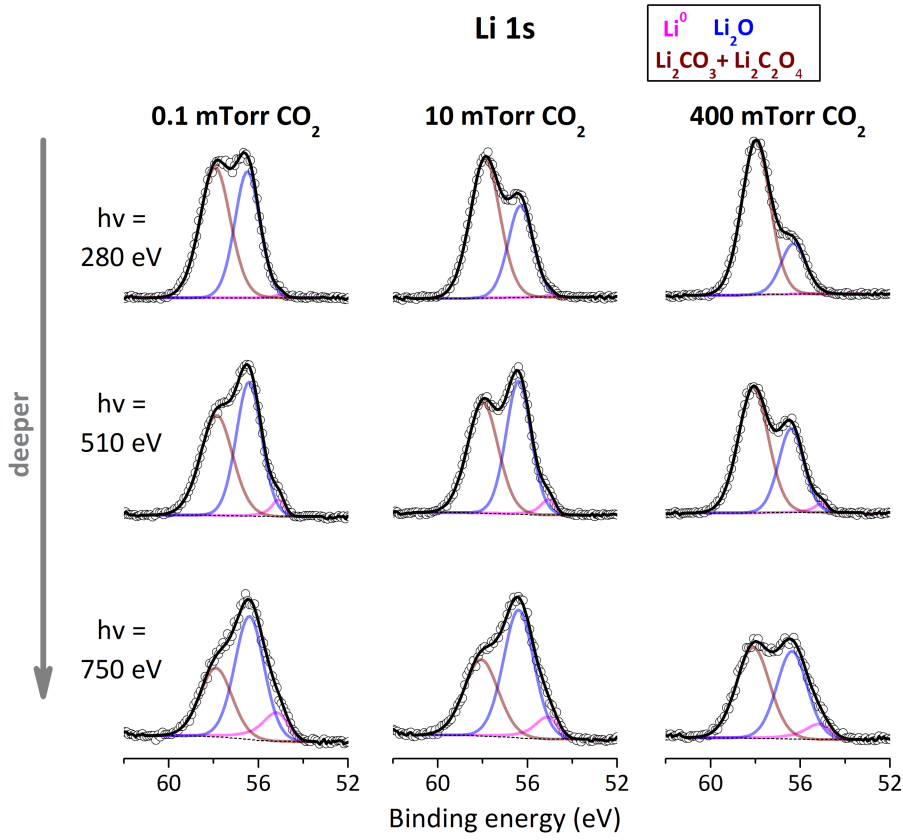

Figure 4.17. APXPS Li 1s spectra showing depth profiling of lithium foil treated with three pressures of CO_2 gas, measured at UHV condition. In the spectra, the fitted curve (black line) follows experimental data (dots), and background is represented by a dashed line.

According to Table 4.1, Li^0, Li_2O and Li_2CO_3 compounds are easily identified in lithium 1s spectra. But, as just concluded analyzing C 1s spectra evolution, $Li_2C_2O_4$ is also present on the surface. We couldn´t find any XPS binding energy reference for $Li_2C_2O_4$ in Li 1s spectra. However, reported binding energies of $ROCO_2Li$ and $Li_2C_2O_4$ in C 1s core level spectra are very similar[180,185]. Then, we consider that both Li 1s from $Li_2C_2O_4$ and $ROCO_2Li$ will also have similar binding energies. That of Li 1s in $ROCO_2Li$ is 0.2 eV lower than Li_2CO_3[180]. Because of the small difference between both binding energies, we fit the spectra coupling contributions of Li_2CO_3 and $Li_2C_2O_4$ in one peak. Binding energy of this peak lies between 58.1-57.7 eV. FWHM constrains will be 0.2 eV higher than that of Li_2CO of Li 1s from Table 4.1 to account for the two types of Li with slightly different binding energies.

Looking to Figure 4.17, the higher the photon energy (higher probing depth), the higher the intensity of Li_2O. This behavior is the same for the three pressures, suggesting that the layered surface structure is: Li^0 on the bottom, an intermediate Li_2O layer, and a topmost surface layer with both Li_2CO_3 and $Li_2C_2O_4$. In order to check whether actually electrons from Li_2O layer are being attenuated by an overlayer, we analyze the attenuation of Li_2O photoelectron intensity for the same sample measured at different photon energies. According to equation (2.8), if an overlayer is covering a substrate, intensity should obey an exponential decay when substrate electrons have lower inelastic mean free path, which happens at different photon energies. To be able to compare the intensities measured at different photon energies, according to equation (2.7), intensity has to be corrected by the photon flux (Table 4.2), cross section (Table 4.2) and the inelastic mean free path, (Table 4.4). Figure 4.18 shows Li_2O photoelectron intensity is attenuated following an exponential decay at all three pressures, confirming Li_2O is covered by an overlayer.

The fitting equations for each pressure are the followings:

$$0.1\ mTorr\ CO_2 \rightarrow \frac{I_{Li_2O}}{F\sigma\lambda} = 3.5 \cdot 10^6 e^{-11.1/\lambda} \tag{4.8}$$

$$0\ mTorr\ CO_2 \rightarrow \frac{I_{Li_2O}}{F\sigma\lambda} = 4.9 \cdot 10^6 e^{-16.8/\lambda} \tag{4.9}$$

$$400\ mTorr\ CO_2 \rightarrow \frac{I_{Li_2O}}{F\sigma\lambda} = 4.0 \cdot 10^6 e^{-20.6/\lambda} \tag{4.10}$$

where *I* indicates the corrected intensity of Li_2O photoelectron peak form Li 1s core level, λ is the inelastic mean free path of Li_2O electrons passing through the overlayer of Li_2CO_3 and $Li_2C_2O_4$, and 11.1, 16.8 and 20.6 parameters are the overlayer thickness (Å) of Li foil dosed for about one hour at 0.1, 10 and 400 mtorr CO_2, respectively.

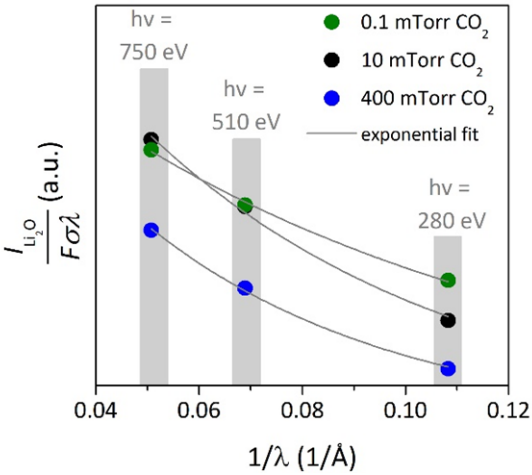

Figure 4.18. Evolution of the corrected intensities of Li 1s Li_2O photoelectron peak spectra measured at three photon energies: 280 eV, 510 eV and 750 eV. Electrons have a different inelastic mean free path (λ) in each photon energy.

Considering this sequence and the intensities of the compounds from Figure 4.17, thicknesses of surface layers are calculated using equations (2.11) and (2.12) and the parameters from Table 4.3 and Table 4.4. For the carbonaceous layer attenuating Li_2O intensity, atomic density and inelastic mean free path are calculated accounting each contribution of Li_2CO_3 and $Li_2C_2O_4$. This contribution is given by the area ratios of them in C 1s spectra of dosed surfaces, measured at a photon energy of 600 eV in UHV condition. Figure 4.19 shows layered sketches of final lithium surface, where contribution of each lithium carbonaceous compounds is also indicated. Thickness values are average thickness calculated by each photon energy, and the deviation between the photon energies is indicated by error bars. Obtained Li_2CO_3/$Li_2C_2O_4$ layer thicknesses represented in Figure 4.19 are in good agreement with that ones from equations (4.8), (4.9) and (4.10).

In Figure 4.19, we observe the higher the gas pressure the larger the Li_2CO_3 and $Li_2C_2O_4$ thickness. Li_2O also evolves considering initial clean Li surface has an oxidized layer of 16 ± 9 Å thickness, according to Figure 4.7. Li_2O as a consequence of this interaction was already observed in previous chapter (section 3.4.2). However, Li_2O layer thickness is almost the same for the three pressures, so the gas pressure is not playing a role in the growth of Li_2O.

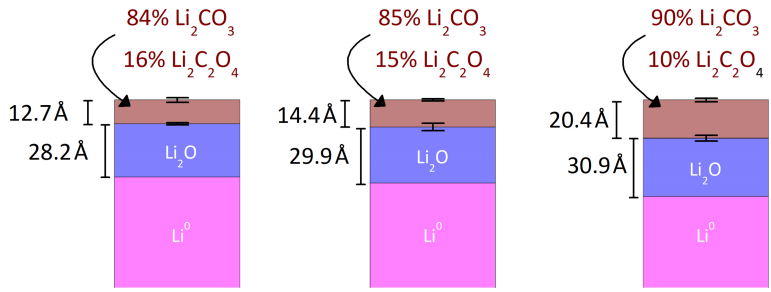

Figure 4.19. Layered sketches of lithium surfaces after exposing them to CO_2 gas at three pressures for about an hour. Estimated thicknesses of the overlayers and composition of each layer are indicated in the figure for the first 100 Å of the surface.

It is worth mentioning that in the layered model we are not considering CH/CC, C-O and C=O contributions. These compounds will produce an extra attenuation in Li 1s electrons. But we assume this attenuation to be the same for all Li 1s compounds, so the ratios between Li 1s compounds should not be affected by them.

4.4.4 Insights into the reaction mechanism

So far, our analysis reveals that carbonate, oxalate, CH/CC and Li_2O evolve on the surface upon Li interacting with CO_2 gas. Furthermore, we observe that Li_2O lies between Li^0 and carbonaceous compounds. In order to explain this surface evolution, and based on proposed reaction mechanisms[137,187], we suggest a possible reaction pathway, represented in Figure 4.20.

According to this mechanism, CO_2 reaction of Li^0 sites leads to Li_2O and CO. Depending on the availability, this CO could be adsorbed in both Li^0 and Li_2O sites. In the first case (pathway A in Figure 4.20), the reaction pathway followed to form carbonate will be the one postulated by Zhuang et al.[137], where more Li_2O will be created on the surface, and the oxide will then react with CO_2 to form carbonate. In the second case (pathway B in Figure 4.20), oxalate will be formed, which will

act as an intermediate to create carbonate and more CO, as claimed earlier[186]. This second pathway is a self-recycling process due to the continuous CO evolution. Of the two possible reaction pathways, we think B is favored. Our reasoning relies on the small C increase, compared to that of carbonate, that occurs on the surface, inferred from Figure 4.12 when we compare Li_2CO_3 and CH/CC evolutions. Another conclusion that we can draw from the reaction mechanism is that pathway B requires metallic lithium to be accessible on the surface to create the required CO for the formation of oxalate. In other words, if the surface were completely oxidized, no oxalate would evolve, and carbonate would dominate the surface.

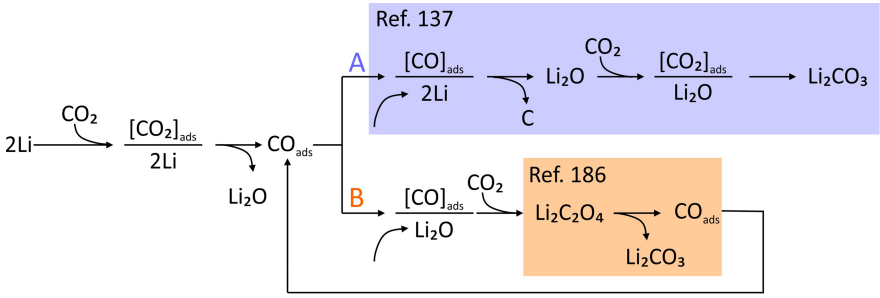

Figure 4.20. Lithium carbonate growth reaction mechanism.

4.4.5 O_2 gas effect on Li_2CO_3 growth

To further explore the system, CO_2 gas was codosed with O_2 gas (5.0 research purity from *Praxair*). Starting from a UHV cleaned Li foil, we first added 0.1 mTorr CO_2 gas and after 10 minutes, O_2 gas was also added to the system for one hour. When doing so, Li_2CO_3 growth is promoted, changing the growth rate of the reaction if it is compared with a pure CO_2 reduction, as shown in Figure 4.21.

To further study the effect of the oxygen, we repeated the codose experiment but inversing the order of adding the gases. In this second codose, first we added O_2 gas, and then CO_2 gas. If we compare the final C 1s spectra and the evolution of $Li_2C_2O_4$ for both co doses (Figure 4.22), when O_2 gas is added first, no $Li_2C_2O_4$ is evolved, and the final surface is pure carbonate without even adventitious carbon. In Figure 4.22 we also clearly see how the addition of O_2 gas is changing the mechanism to form Li_2CO_3 in the first co-dose studied, where $Li_2C_2O_4$ stops evolving.

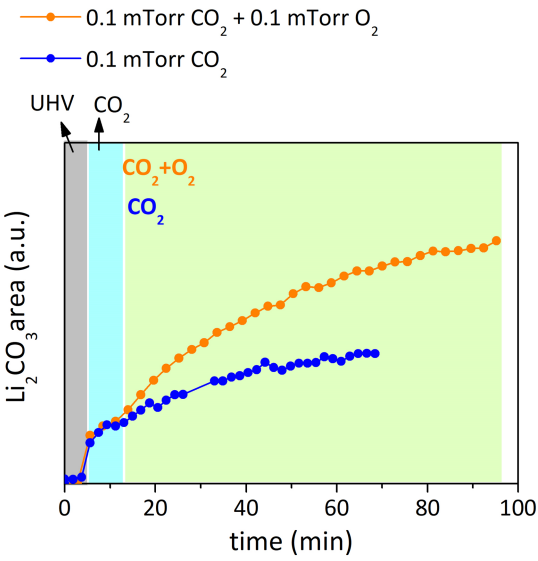

Figure 4.21. Evolution of raw area of Li_2CO_3 from C 1s APXPS spectra, measured at a photon energy of 600 eV and at two different dose conditions.

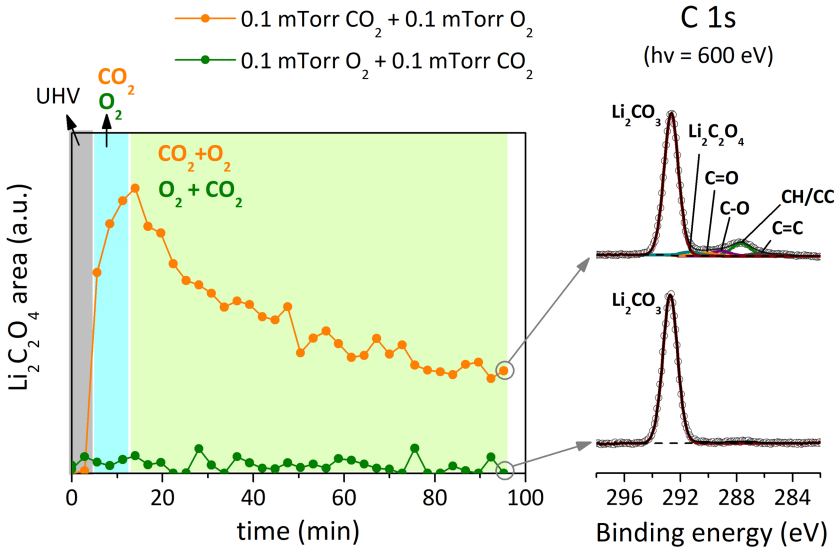

Figure 4.22. Evolution of raw areas of $Li_2C_2O_4$ from C 1s spectra measured at a photon energy of 600 eV, at two CO_2 and O_2 gas codoses experiments. In the first codose CO_2 gas is added first (orange) and in the second co dose O_2 gas is added first (green). Final C 1s spectra are also indicated in the right side of the figure for each co dose. In the spectra, the fitted curve (black line) follows experimental data (dots), and background is represented by a dashed line.

This behavior indicates that the reaction mechanism to create lithium carbonate is bypassed when the atmosphere is comprised of both CO_2 and O_2; this has been schematically represented in Figure 4.23. Due to the interaction of oxygen with lithium, lithium oxide is created on the surface, and there is no metallic lithium accessible to react with CO_2, thus no oxalate evolves on the surface, further supporting the proposed reaction mechanism of Figure 4.20.

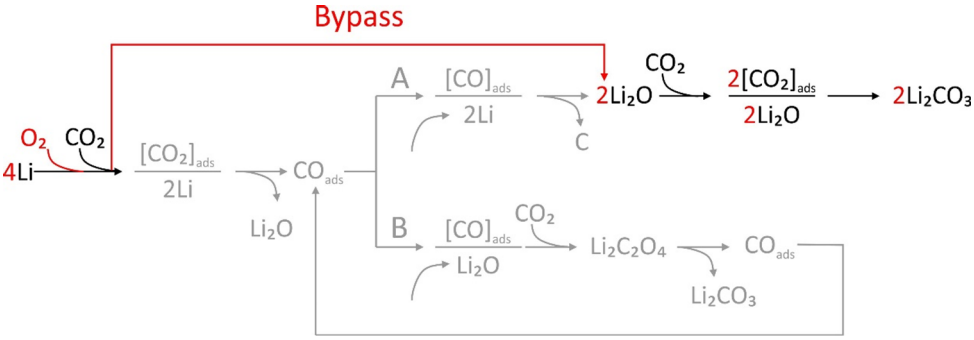

Figure 4.23. Effect of O_2 gas in lithium carbonate growth reaction mechanism.

Another consequence of adding the gases in a different order is the rate of lithium oxidation, as can be inferred from Figure 4.24 by the fast disappearance of surface Li when adding first O_2.

It is worth mentioning that oxalate contribution has not been taken into account considering its small contribution compare to that of Li_2CO_3 (Figure 4.22). The faster oxidation of the surface with O_2 agrees with the conclusion obtained in previous chapter: O_2 gas oxidation rate is higher than that of CO_2 gas (section 3.4). This behavior implies that, if lithium is pretreated with CO_2 and then O_2 gas is added, oxidation is slower and more metallic lithium will be available near the surface region, as shows Figure 4.24.

We calculate the evolution of the thickness of Li_2O and Li_2CO_3 for the first co dose, the one started with CO_2 gas. For that, Li 1s 600 eV function of time spectra compounds intensities, equations (2.11) and (2.12) and parameters from Table 4.3 and Table 4.4 are used. Results are summarized in Figure 4.25. There, we observe that, when CO_2 gas contacts Li^0 surface, both Li_2CO_3 and Li_2O are formed with a high reaction rate. When adding O_2 gas to the system (green region in Figure 4.25), Li_2O keeps constant, meaning all O_2 is used to form Li_2CO_3, further affirming bypassed reaction represented in Figure 4.23.

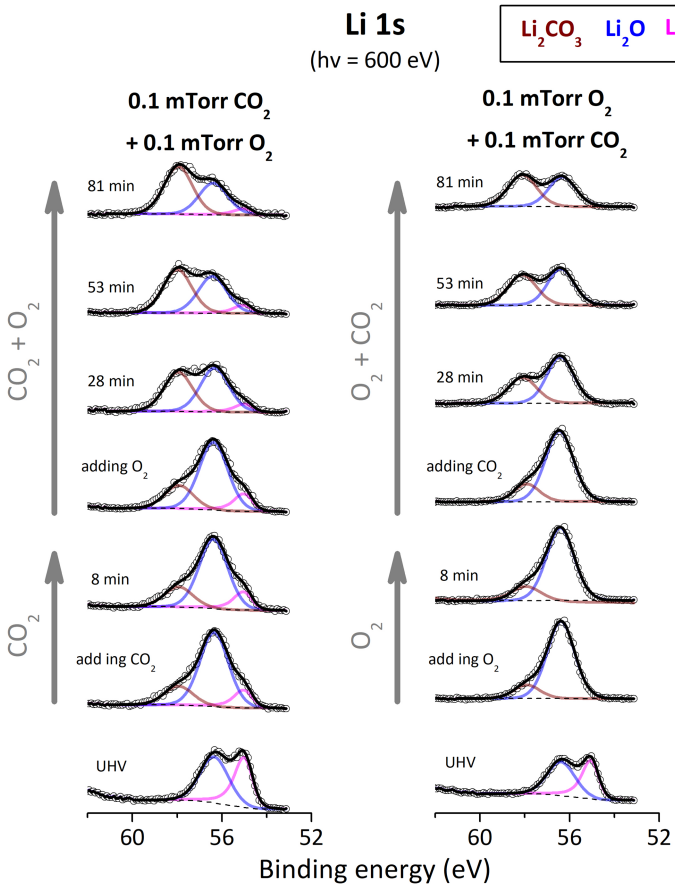

Figure 4.24. APXPS Li 1s spectra evolution while codosing a lithium surface with CO_2 and O_2 gases, changing the order of adding the gases. Spectra is measured at a photon energy of 600 eV. In the spectra, the fitted curve (black line) follows experimental data (dots), and background is represented by a dashed line.

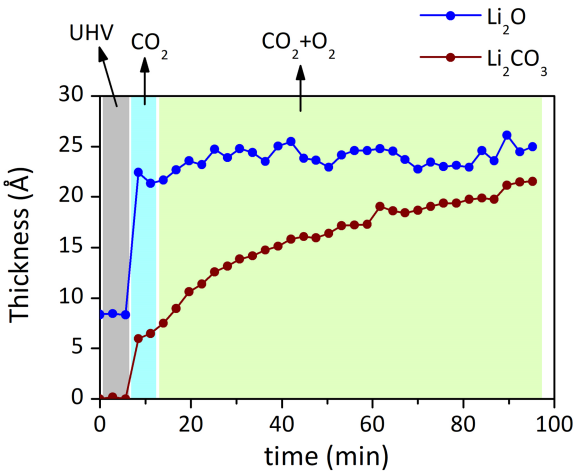

Figure 4.25. Thickness evolution of Li_2O and Li_2CO_3 layers growing on top of metallic lithium when codosing 0.1 mTorr CO_2 and 0.1 mTorr O_2, starting the codose with CO_2 gas. Calculation has been done using data from Li 1s APXPS spectra measured at a photon energy of 600 eV.

In this experiment, Li_2O grows up to 25 Å, and we know it grows at the beginning of the reaction, when just CO_2 is added to the surface. In section 4.4.2, when studying Li metal interaction with CO_2 gas at different pressures, obtained Li_2O thicknesses are around 30 Å (Figure 4.19). It leads us to think that most Li_2O is formed at the very beginning of the interaction, which could be explained by the first step of the mechanism proposed in Figure 4.20, where CO_2 interaction with Li^0 leads to Li_2O. This same behavior was observed in previous chapter, where Li_2O increases when adding CO_2 while a monolayer was forming. After that, Li_2O stops growing and carbonate starts to evolve more strongly (Figure 3.13).

The final surfaces of the codoses also have a layered sequence where Li_2CO_3 grows on top of Li_2O, as shown by the spectra and surface sketches in Figure 4.26. Both final surfaces have a similar carbonate layer, the difference lies on the metallic lithium available below the carbonate, as already mentioned.

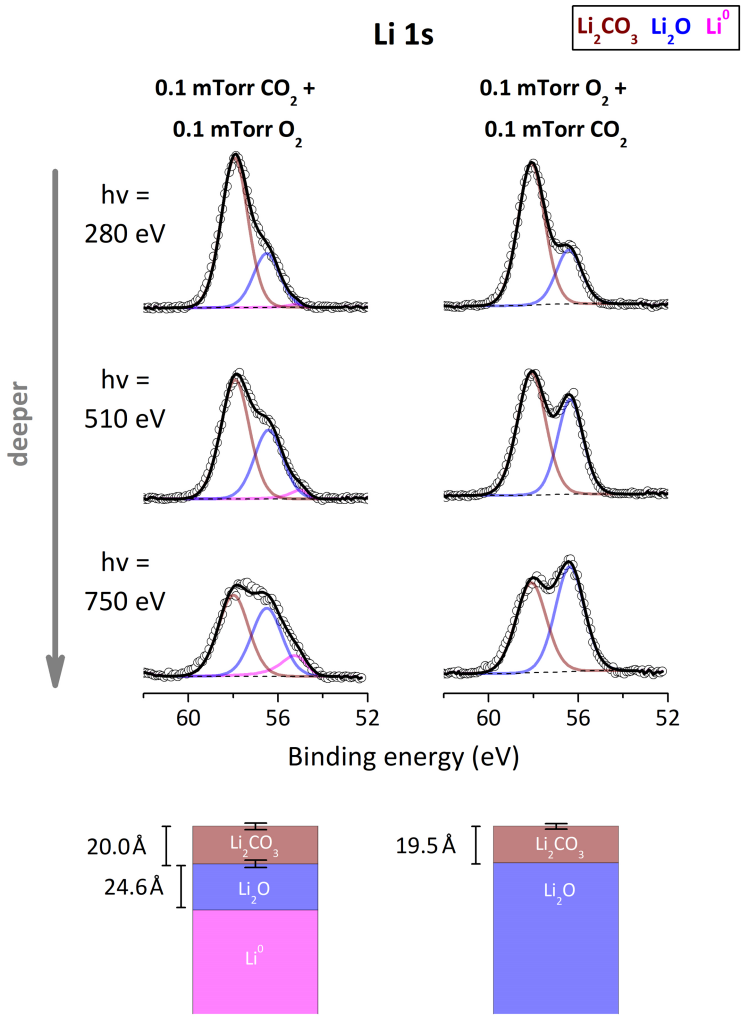

Figure 4.26. APXPS Li 1s spectra showing depth profiling of lithium foil after codosing it with CO_2 and O_2 gases, following two sequences. In the spectra, the fitted curve (black line) follows experimental data (dots), and background is represented by a dashed line. Estimated thickness of the overlayers is illustrated in the bottom of the figure for the first 100 Å of the surface.

4.5 Conclusions

Lithium foil scraped in argon atmosphere glove box presents no metallic lithium in the first 8 nm. In fact, Li_2O and Li_2CO_3 are main lithium-based compounds of the surface. A standard solid electrolyte interphase formed with an organic liquid electrolyte has an estimated thickness of 20 nm and includes various organic and inorganic compounds, where Li_2O and Li_2CO_3 has been identified[44,47]. According to our results, these two compounds could not be a consequence of the contact of the metal with the electrolyte, but part of preexisting surface contamination. Finding the real effect and origin of these compounds on the SEI layer could help to better understand the instability of the interface that is preventing the evolution of Li metal anode rechargeable batteries.

Main conclusions of the chapter are related to Li_2CO_3 growth mechanism on Li metal surface as a consequence of the interaction of it with CO_2 gas. In this reaction, apart from the expected Li_2CO_3 growth, the evolution of another carbon-based compound bonded to lithium has been observed, which has been identified as lithium oxalate, $Li_2C_2O_4$. Oxalate was previously reported as a possible intermediate in the reaction mechanism to form Li_2CO_3[137], but there was no experimental evidence of its evolution before this work. Evolution of aliphatic carbon related to C-H/C-C chemical bonds is also observed in this reaction, and three other compounds which do not show an evolution during the reaction complete the carbon-based species, which represent graphitic carbon (C=C), C-O chemical state and carbonyl (C=O) functional group. Apart from carbon-based compounds, Li_2O also grows at the very first interaction with a high reaction rate. Depth profiling experiments show that surface has the following layered structure: Li^0 on the bottom, an intermediate Li_2O layer, and a topmost surface layer with both Li_2CO_3 and $Li_2C_2O_4$. Considering this surface evolution and based on reported reaction pathways in literature, a reaction mechanism has been proposed, which is summarized in Figure 4.20.

Kinetic studies reveal that growth of carbonate presents two regimes: a reaction-controlled regime with linear growth rate and a diffusion-controlled regime with parabolic growth rate. The reaction rate constant of linear regime is more dependent on pressure than that of parabolic regime. Surface formed in linear regime is acting as a diffusion barrier in the parabolic regime, reducing the rate of the reaction.

The mechanism of Li_2CO_3 growth changes when O_2 gas is present in the atmosphere together with CO_2 gas. At this new situation, no $Li_2C_2O_4$ grows and all O_2 gas reacts to form Li_2CO_3, so Li_2CO_3 is promoted and lithium has pure Li_2CO_3 surface. Then, in an atmosphere where both CO_2 and O_2 are present, rather than to Li_2O surface evolves to Li_2CO_3. We also observe that how lithium is exposed to the surrounding gases will define its final surface composition: if lithium is first exposed to O_2 gas and then CO_2 gas is added to the atmosphere, it will be more oxidized than if the reverse happens.

CHAPTER 5

Li thin film growth

In this chapter a Li thin film is grown by thermal evaporation. Its thickness and morphology are studied by means of scanning electron microscope. Effects of the substrate type and of the temperature on the structural development of the thin film are analyzed, and the electrochemical activity of the lithium thin film is verified.

5.1 Introduction

In previous chapters we have learnt that commercial Li foil stored in inert (argon) atmosphere has a completely oxidized surface. Furthermore, no cleaning process out of ultra-high vacuum (UHV) condition will prevent its fast oxidation. Then, when using this commercial foil as anode, its surface native contaminants will become part of the solid electrolyte interphase (SEI). One way to have a SEI free of lithium surface impurities is growing a lithium thin film directly in a solid electrolyte in UHV conditions. In this chapter, the growth of a lithium thin film from a commercial lithium source is explored. Next chapter presents the consequences of avoiding lithium surface contaminants in an electrochemical system.

Looking to literature, we can find several techniques employed to grow a lithium thin film, as thermal evaporation[190], electrodeposition[191], or a method that combines evaporation and sputtering processes[192]. Among them, thermal evaporation has been chosen for this study, the most common one to grow a thin film for anode applications[190].

The process of growing a thin film by deposition has six steps: first the arriving atoms have to adsorb on the surface, then they diffuse some distance, after that a reaction of the adsorbed species with each other and with the surface occurs to form the bonds of the film. The fourth step is the nucleation, the initial aggregation of the film material, and then the structure develops. Finally, diffusional interactions occur with the bulk of the film and with the substrate[193]. Following, we are going to summarize the possible structural development morphologies, which will be useful to compare with the morphologies obtained experimentally later in the chapter.

5.1.1 Structure Development of a thin film

There are three basic structural zones that depends on the ratio between the substrate temperature (T_s) and the melting point of the film (T_m), all of them illustrated in Figure 5.1. Z1 occurs when T_s/T_m is so low that surface diffusion is negligible. Columns of Z1 have poor or none crystallinity and are separated by voids. In Z2, when T_s/T_m is higher than Z1, surface diffusion is significant and the structure consist of columns having tight grain boundaries between them. Crystalline columns are less defected than Z1 and are often facetted at surface. In Z3, due to the higher temperature of the substrate compared to previous zones, we can consider bulk annealing of the film is taking place during deposition. This is characterized by more isotropic or equiaxed crystallite shape. There is an extra zone between Z1 and Z2 called the transitional zone (ZT), which contains similar columns to those of Z1 but voids and domes are absent, and is usually associated with energy enhanced processes as sputter deposition. Sometimes, anomalous structure forms occur, in particular the whiskers, illustrated also in Figure 5.1.

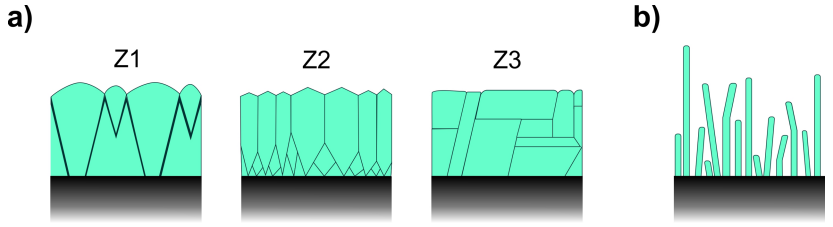

Figure 5.1 a) Characteristic cross section of the three basic structure zones when developing a thin film. Ratio of substrate temperature to film melting option increases from left to right. **b)** Whiskers anomalous structure formation. Adapted from[193].

5.2 Experimental procedure

Figure 5.2 shows the UHV chamber system designed to evaporate Li. Load lock of the system is compatible with the air sensitive portable transfer arm from Figure 2.8, thus air exposure of the samples is prevented. Base pressure of the system is low 10^{-8} – high 10^{-9} mbar.

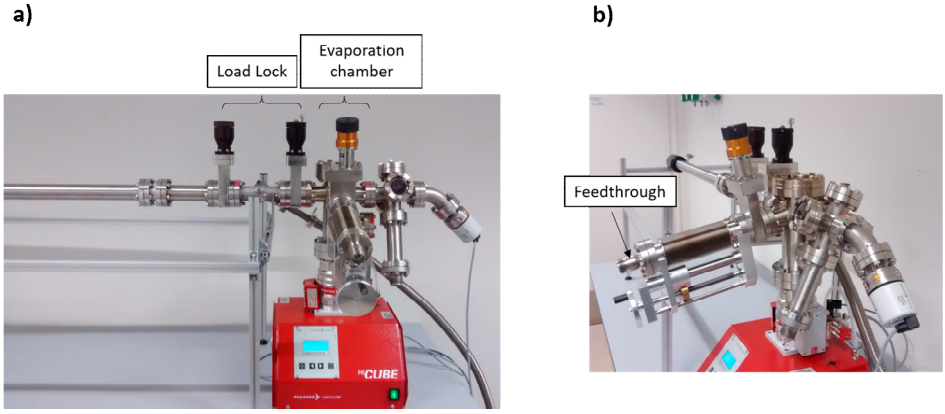

Figure 5.2. a) Front view and **b)** side view of the UHV chamber system where Li evaporations were performed.

Li sources used in this study are commercially available chromate-free metal vapor sources (alvasources, from alvatec[97]). They contain an intermetallic compound in argon atmosphere inside a small stainless-steel tube, sealed with indium, as shown in Figure 5.3. Capacity of the sources is 190 mg and diameter of the tube 5 mm.

Lithium metal is thermally evaporated from the intermetallic compound when passing a current through the contacting flaps. To do that, the contacting flaps were welded to two conductive rods connected to the feedthrough of Figure 5.2b. Fundaments of thermal evaporation are explained in chapter 2 section 2.1.1 section.

In the **activation** of the sources, indium seal is removed in UHV conditions. According to the information provided by the supplier, indium melts from 1.5 A to 4 A, which causes the release of the argon, increasing the pressure of the chamber. Experimentally, we observed this release at an intensity of 5.3 A. Besides, in order

to remove all the In from the source, we kept it at a higher intensity for about 3 hours. Once the source was activated, we never exposed it to air atmosphere.

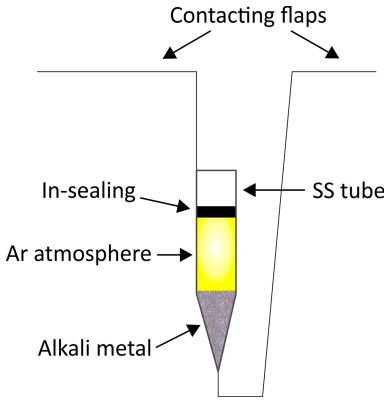

Figure 5.3. Configuration of a typical alkaline source from alvatec. Adapted from[97].

Steps followed to perform an **evaporation** were:

1) Substrate cleaning step. This step was performed in an ultrasonic bath, with the following sequence: first acetone, then ethanol and finally water, 10 minutes in each one. After that, substrate was dried in an oven at 80 °C overnight.
2) Substrate loading step. Substrate was load in the load lock and left in vacuum at least 12 hours. During this step, a titanium sublimation pump was run to help recover the base pressure of the chamber.
3) Removal of impurities step. In this step, explained in section 2.1.1, volatile impurities were removed. For that, sample was isolated from the Li source closing the corresponding gate valve, and intensity was increased up to 3 A and kept it for half an hour.
4) Li source stability step. Intensity passing through the source was increased up to the evaporating value, which will be higher than 5 A for our commercial sources according to supplier's manual[97]. We kept that intensity until pressure was stable. Pressure should be in the range of 10^{-7}–10^{-8} mbar.
5) Evaporation step. Substrate was moved to the front of the lithium source, opening the corresponding gate valve. Sample was kept there the desired evaporation time.

5.3 Study of lithium thin film deposition

5.3.1 Li source deposition rate calculation at 8 A

The deposition rate of the Li thin film is defined by the intensity applied to the Li source, so each intensity will have a specific deposition rate. Aim of this section is to determine the deposition rate at an intensity of 8 A.

Thickness of thin films were estimated by scanning electron microscope (SEM), using the instrument detailed in section 2.3.4.1, and measuring secondary electrons at 30 kV. Evaporated samples were cut in the glove box using a diamond scribe and transferred to the SEM with the air sensitive transfer arm from the SEM system (Figure 2.14). There, measuring a cross section, thickness of the deposited layer was obtained, and the top view images provided information about the morphology of the lithium.

In order to measure the thickness from a cross section image, a substrate which will be easy to cut and will produce a sharp edge is needed, as silicon wafer is, common substrate for thin film depositions. We then started the study with a silicon monocrystalline wafer (<100>, Bo additive, ρ > 1 Ω·cm, *Virginia semiconductors*). When characterizing the evaporation of lithium in Si wafer some singularities were found, which led us to study the evaporation process in several layer sequences, all of them indicated in Table 5.1. Following we are going to explain the conclusions obtained in each sequence.

Table 5.1. Sequences used to study the evaporation and growth morphology of lithium. Lithium layers are evaporated at the current and times specified in the table and Ti is sputtered using a magnetron sputtering.

Sequence	Substrate	Layer 1	Layer 2	Layer 3
A	Si wafer[I]	Li		
		8 A, 12 h		
B	Si wafer[I]	Li		
		8 A, 6 h		
C	Si wafer[I]	Li	Ti	
		8 A, 23 h	340 nm	
D	Stainless steel[II]	Li	Ti	
		8 A, 23 h	340 nm	
E	Si wafer[I]	Ti	Li	Ti
		255 nm	8 A, 24 hours	680 nm

[I] Si wafer <100>, Bo additive, ρ > 1 Ω·cm

[II] Stainless steel from the sample holder

In order to make sure that the source is evaporating lithium, first evaporation (sequence A from Table 5.1) was characterized using X-ray photoelectron spectroscopy instrument explained in section 2.3.1.3. Figure 5.4 shows that, after an evaporation of 8 A for 12 hours in a Si wafer, the surface is covered by a layer that contains mainly lithium and oxygen.

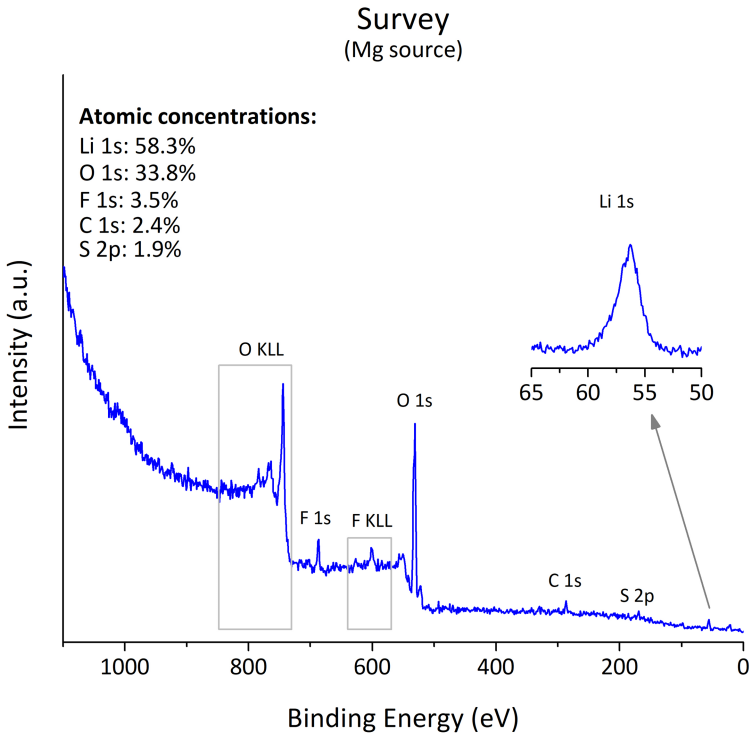

Figure 5.4. XPS survey spectra measured by Mg source of a silicon wafer after lithium evaporation, following sequence A from Table 5.2. The normalized surface atomic concentration is indicated also in the figure. The inset represents Li 1s region measured at higher resolution with same photon source.

Apart from the expected adventitious carbon impurity, there is also a small amount of fluorine and sulfur on the surface. These elements are a cross contamination because of some impurity we had at that time in the XPS instrument, and both represents around 5.5% of the normalized atomic concentration from the surface. For the calculation of this concentration we considered the areas of the peak of the elements from the survey of Figure 5.4. Areas were corrected with the corresponding relative sensitive factor of each element based on Scofield cross sections and a transmission function correction

specific for this equipment. An exponential factor was also used to correct the difference in the inelastic mean free path of electrons. With this measurement, it was confirmed that source evaporated just Li. Figure 5.5 shows the cross section and top view of this sample, where the expected thin film is not observed. Indeed, the surface is full of microstructured features, as large as 3 micrometers.

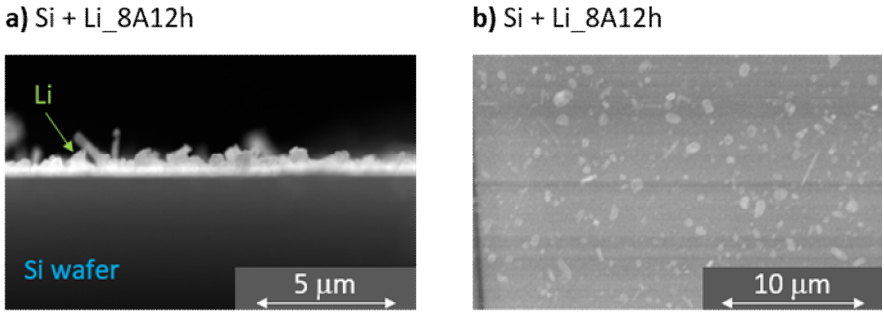

Figure 5.5. Air sensitive SEM **a)** cross section and **b)** top view of a lithium evaporation on a monocrystalline Si wafer following sequence A from Table 5.1.

Looking to the weird Li deposition obtained on Si, the state of Si wafer used in this study was checked. Figure 5.6a shows that the cut made to measure cross section using a diamond scribe was not responsible of the microstructured features. In Figure 5.6b it can be observed that initial Si wafer surface was flat, so Li morphology was not induced by an inhomogeneous substrate.

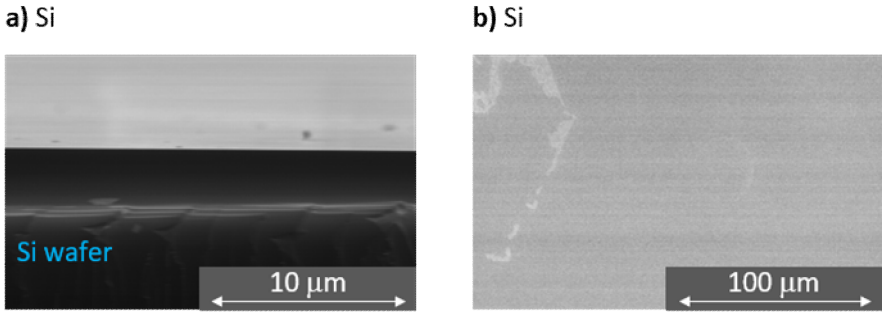

Figure 5.6. SEM images of the **a)** cross section and **b)** top view of the monocrystalline silicon wafer used to evaporate lithium.

Then, to have a better understanding of how the lithium was growing on the silicon wafer, a new Li evaporation was performed, shorten the evaporation time

(sequence B from Table 5.1). Surface of sequence B, represented in Figure 5.7, shows the same non-uniform surface got in previous evaporation. In addition, when trying to get images of the lithium surface structures at higher magnification than the ones from Figure 5.5, Li was degraded. This degradation, a consequence of the interaction of Li metal with SEM electron gun, took place when measuring with magnifications that show a scale equal or smaller to 2 µm (magnification of x50000). Figure 5.7b clearly shows how the area where SEM images are taken is completely different from the rest of the surface. Figure 5.7c also confirms this behavior, showing the disappearance of a lithium feature from the surface just by trying to focus the area with SEM microscope. Time between each image is the one needed to save the picture, around 5 seconds.

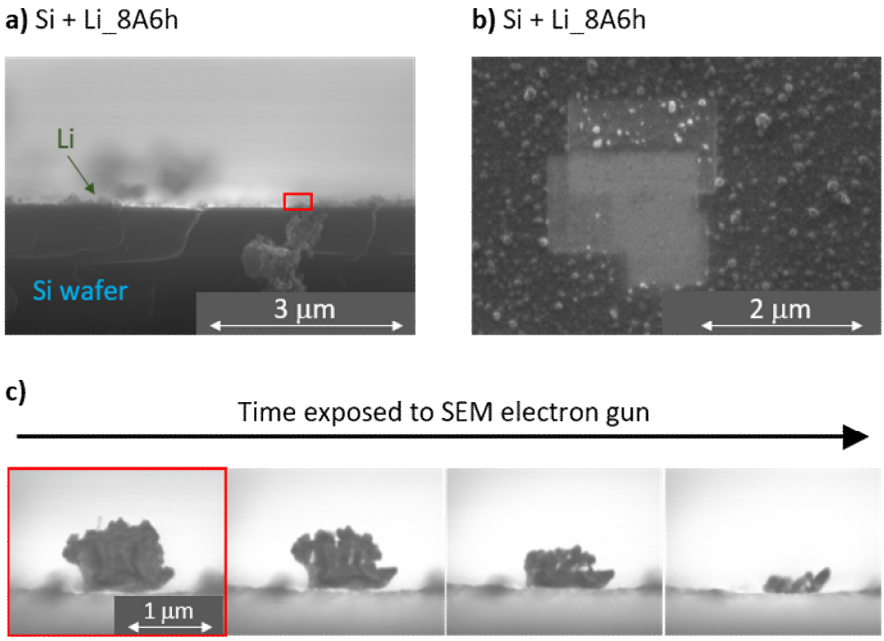

Figure 5.7. Air sensitive SEM **a)** cross section and **b)** top view of a lithium evaporation on a monocrystalline Si wafer following sequence B from Table 5.1. **c)** Evolution of a surface Li feature from the cross section exposed to SEM electron gun. Time between each picture is around 5 seconds, the one needed to save the images.

To avoid the problem of lithium degradation, in the following deposition (sequence C from Table 5.1) evaporated Li was covered with a Ti layer, deposited by magnetron sputtering. Details about the technique and equipment can be found in chapter 2 section 2.1.2. Optimal sputtering conditions and deposition

rates of Ti were obtained by other researchers of the Advanced Interface Analysis group from CIC Energigune. The same air sensitive transfer arm used to move samples from Li evaporation UHV chamber system is compatible with the sputtering system, preventing sample air exposure.

Li evaporation time in the sequence C was higher (24 hours) than previous cases in order to have better sense of the structural development of the lithium. When measuring the cross section and top view of sequence C, represented in Figure 5.8, we clearly observe that lithium was not depositing as a uniform layer.

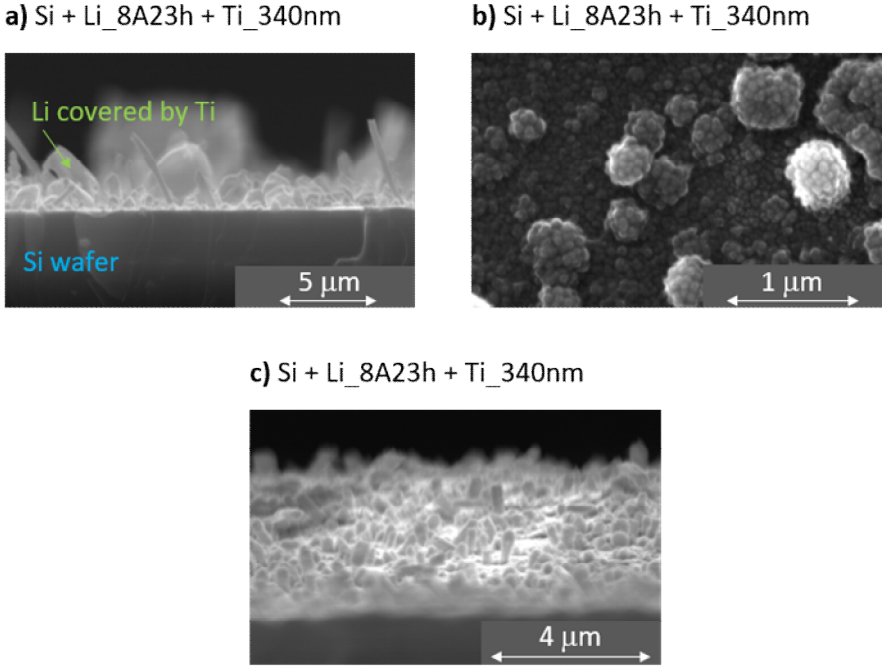

Figure 5.8. Air sensitive SEM **a)** cross section, **b)** top view and **c)** tilted view of a lithium evaporation following sequence C from Table 5.1, where a Ti layer is added to the lithium evaporated on Si wafer.

This type of structural development does not correspond to any of the basic zones explained in Figure 5.1a. In fact, this is an anomalous type growth, similar to the whiskers of Figure 5.1b, that sometimes happens when trying to obtain a thin film[194]. About the effect of covering Li with Ti to prevent its degradation, it was been effective. In this sample we were able to go to high magnifications without damaging the surface, which can be seen if Figure 5.7b and Figure 5.8b are compared

Because of the configuration of the evaporation system, we were also evaporating lithium and titanium on the holder, not just on the Si substrate. This holder is made of stainless steel, so we have a new deposition sequence here, the one called sequence D in Table 5.1. Figure 5.9 shows the comparisons of the surface morphology of lithium deposited on the Si and Li deposited on the stainless-steel (SS) holder. There, it can be concluded that whisker type growth is related to the nature of the substrate. For this reason, in next evaporation a Ti layer was added between the Li and Si wafer, a metal considered a good bonding material[193]. This deposition, called sequence E, is summarized in Table 5.1.

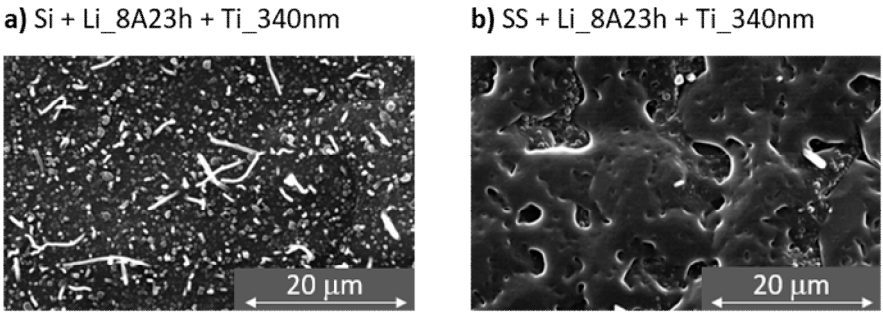

Figure 5.9. Air sensitive top view SEM of **a)** sequence C and **b)** sequence D from Table 5.1, where the difference between the sequences relies on the substrate, Si wafer and stainless steel (SS) respectively.

Figure 5.10 shows the surface morphology of several steps from sequence E. The morphology of the deposited Ti (Figure 5.10a, b) is very similar to that one from literature for similar deposition conditions[195]. About the morphology of the evaporated lithium into Ti surface (Figure 5.10c), it is more similar to the evaporated lithium into stainless steel (Figure 5.9b) than to the evaporated lithium into Si wafer (Figure 5.9a). Here, according to Figure 5.10e, we also observe that the evaporation of Ti on top of lithium is not changing the morphology of lithium.

When analyzing the morphology of the evaporated Li from Figure 5.10b, we can observe some voids on the surface. This kind of morphology corresponds to a Z1 structural development, explained in the introduction section and schematically represented in Figure 5.1a. In this type of development surface diffusion is neglected.

In the cross section images of sequence E, represented in Figure 5.11, the layer of lithium and the two Ti layers can easily be identified. With this information, the deposition rate of Li source at 8 A was estimated to be in the range of 120 – 400 nm/h.

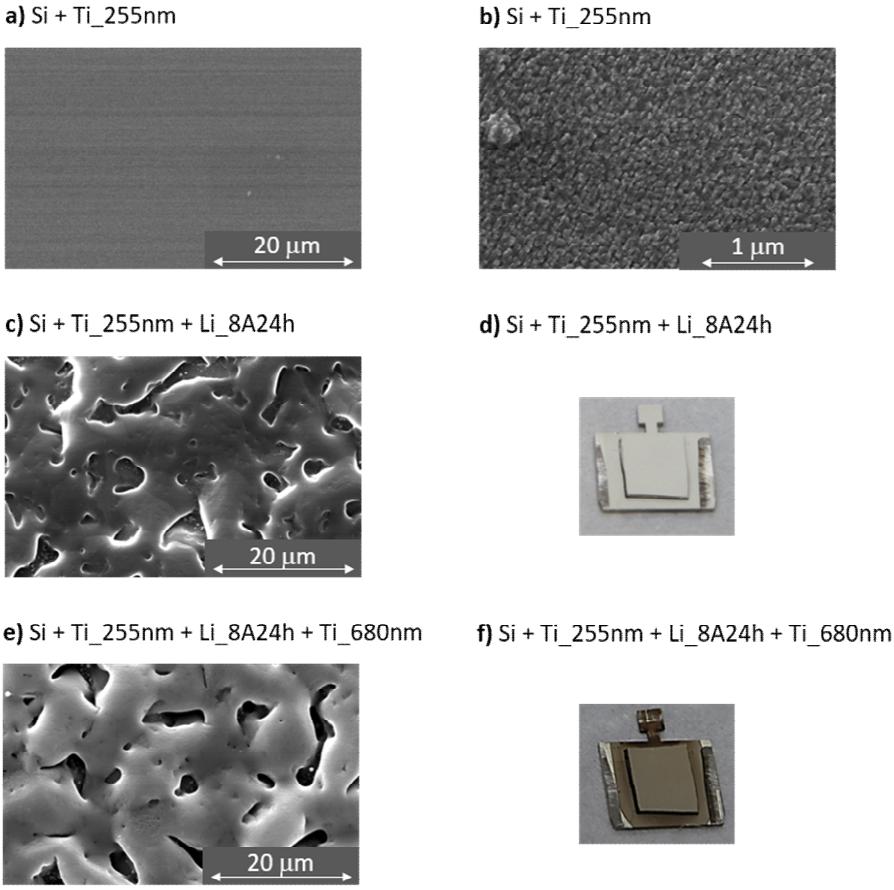

Figure 5.10. Air sensitive top view SEM images and pictures of the surfaces made while following sequence E: **a)** sputtered Ti on Si wafer, **b)** same as a) with higher magnification, **c)** evaporated lithium on Ti, **d)** photo of evaporated lithium on Ti, **e)** sputtered Ti on the evaporated Li and **f)** photo of sputtered Ti on the evaporated Li.

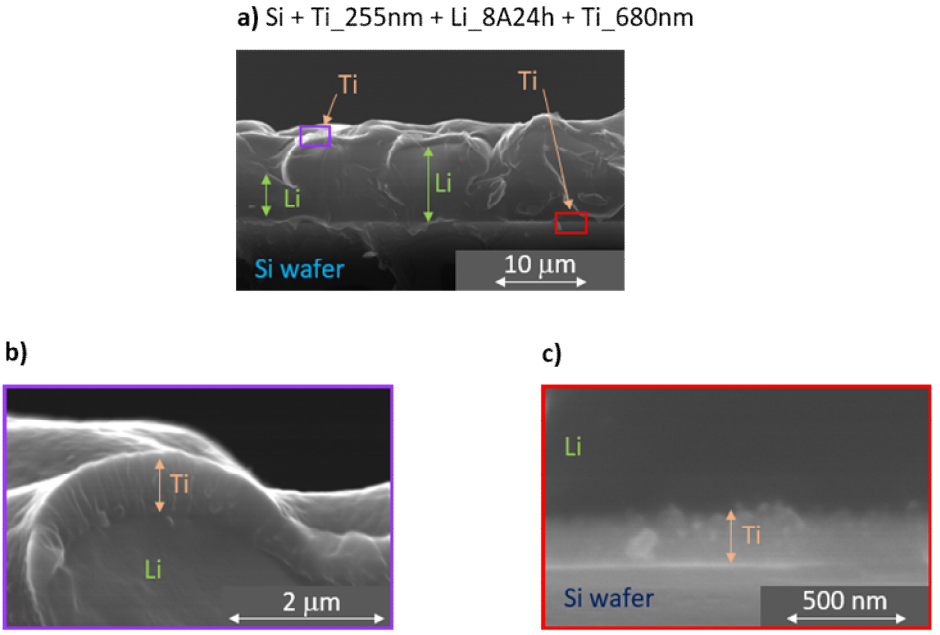

Figure 5.11. Air sensitive SEM images of final surface from sequence E, where **a)** shows the thickness of lithium layer in a cross section, and **c)** and **d)** show both top and bottom Ti layers of the sequence E indicated in a) image.

5.3.2 Substrate and temperature effect on lithium structural development

The deposition of lithium is very different in the substrates studied so far: in silicon wafer a whisker like structure develops, whereas in titanium and stainless-steel the deposition grows as a layer with a Z1 structure. In order to find a possible pattern that will predict which kind of substrate could induce the undesirable whisker growth type, different deposition sequences were tried, indicated in Table 5.2.

A typical case of having undesirable non uniform deposition is when depositing a metal in a non-metal substrate[193]. Then, first thing tried was a deposition on a polyethylene terephthalate (PET) polymer substrate (sequence F from Table 5.2). For this sample we couldn´t measure a cross section because of the degradation of polymer while measuring it with SEM. **Error! Reference source not found.** shows the top view of the same Li deposition on PET polymer (sequence F from Table 5.2) and on Ti (sequence E from Table 5.1). Both surfaces look very similar,

indicating whisker type growth observed on Si substrates cannot be explained just by the non-metal nature of Si.

Table 5.2. Sequences used to study the effect of the electronic and structural properties of the substrates. Lithium layers are evaporated at the current and times specified in the table and Ti is sputtered using a magnetron sputtering.

Sequence	Substrate	Layer 1	Layer 2
F	PET Polymer	Li	Ti
		8 A, 23 h	315 nm
G	$SrTiO4^{I}$	Li	Ti
		10 A, 24 h	500 nm
H	Stainless steel [II]	Li	Ti
		10 A, 24 h	500 nm
I	Si wafer Low resistivity[III]	Li 8 A, 22 h	Ti 315 nm

[I] $SrTiO_3$, 1.4at% Nb, <111>

[II] Stainless steel from the holder

[III] Si wafer <100>, Bo additive, ρ < 0.001 Ω·cm

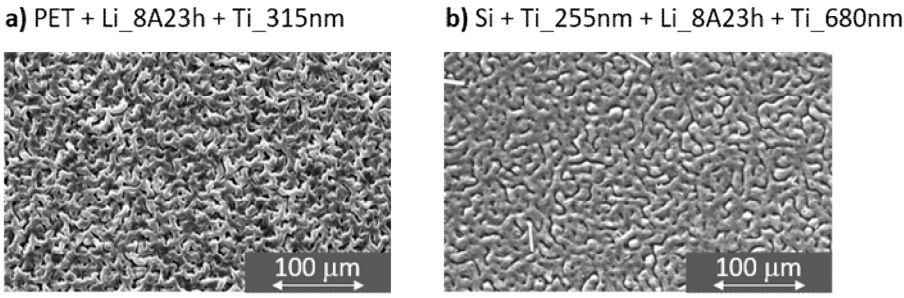

Figure 5.12. Air sensitive SEM top view images of **a)** Li evaporated onto a PET polymer (sequence F from Table 5.2) and **b)** Li evaporated onto Si wafer covered by a Ti layer (sequence E from Table 5.1).

Another main difference between all the studied substrates is the structural configuration: Si is the only monocrystalline substrate. Then, the evaporation onto another monocrystalline material was studied: $SrTiO_3$, which has a crystal orientation <111>. For this deposition, intensity was increased to 10 A (sequence G from Table 5.2). When looking to the top view in Figure 5.13a, the surface looks more uniform than any deposition done before. We also obtain the same type of surface morphology if we look to the holder area of this same deposition (Figure 5.13b), which will be sequence H from Table 5.2. This type of structural development, where no voids are observed on the surface, is related to Z2. As explained in section 5.1.1, moving from Z1 to Z2 structural development indicates

an increase in the T_s/T_m ratio, where T_m is the melting point of the film and T_s the substrate temperature. This implies the temperature of the substrate in this last deposition at 10 A is higher than in previous depositions made at a current of 8 A. To explain this phenomenon, we first have to consider that when increasing the current passing through the source, the temperature of the source will increase according to equation (2.1). Then, thermal energy will be transferred from the source to the substrate by radiation.

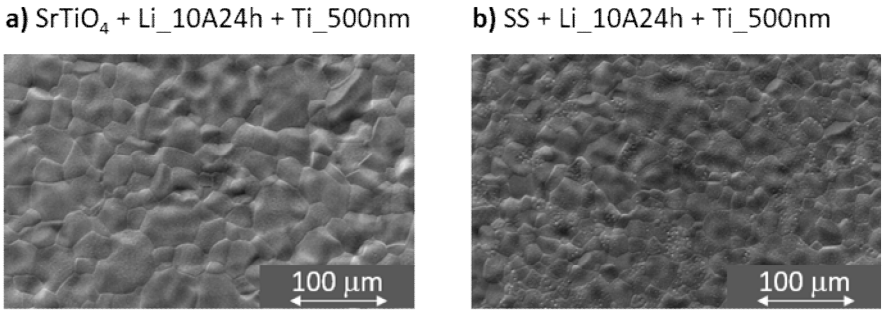

Figure 5.13. Air sensitive SEM top view images of **a)** Li evaporated onto $SrTiO_3$ monocrystalline surface (sequence G from Table 5.2) and **b)** same evaporation looking to the stainless-steel holder substrate (sequence H from Table 5.2).

In order to check which was the T_s at each current condition, a thermocouple was attached to the holder where substrates were mounted, which allowed to record the temperature while evaporating Li. Temperature reached steady state at 42.3 °C when current was 8 A, and at 51.5 °C when current was 10 A. Then, the substrate temperature transition for lithium to grow from Z1 to Z2 structure is between 42.3 °C and 51.5 °C.

In the cross section of sequence G from Table 5.2, represented in Figure 5.14, layers of lithium and Ti can be identified. With this information the deposition rate of the source at 10 A was determined, which was inside the range of 730 - 1400 nm/h. In this last deposition it is concluded that just the monocrystalline nature of the substrate material is not a sufficient reason to explain the whisker type growth of lithium in Si wafer.

Lastly, whether the effect of changing the electronic properties of the Si wafer will induce a layered growth was analyzed. The silicon wafer used so far has a resistivity higher than 1 Ω·cm, which is considered as a semiconductor, and the Si wafer used for sequence I from Table 5.2 has a resistivity in the order of

conductive materials (ρ > 0.001 Ω·cm). Figure 5.15 shows that a non-uniform deposition is obtained again, with similar whisker type microstructured surface morphology to that of semiconductor Si wafer, compared in Figure 5.16. Then, changing the electronic properties of the Si wafer does not help to obtain a layered growth on the Si <100>.

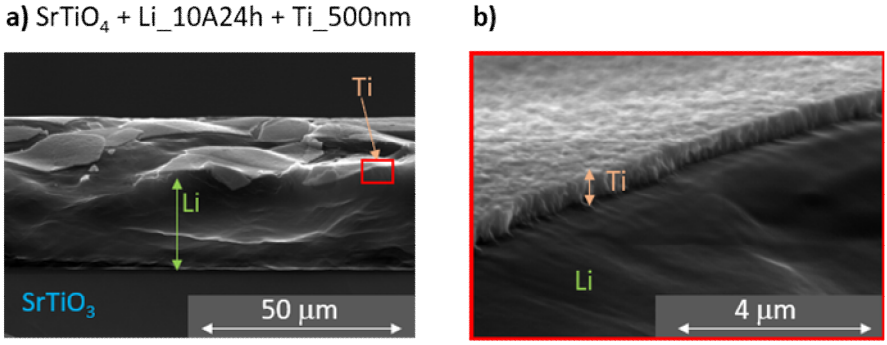

Figure 5.14. Air sensitive SEM images cross section of final surface of sequence G from Table 5.2, where **a)** shows the thickness of lithium layer evaporated onto a $SrTiO_3$ substrate and **b)** shows the top Ti layer of the sequence H indicated in a) image.

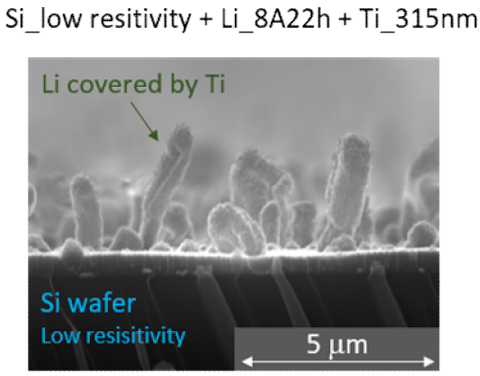

Figure 5.15. Air sensitive SEM cross section of a low resistivity Si wafer surface after evaporation of lithium sequence I from Table 5.2.

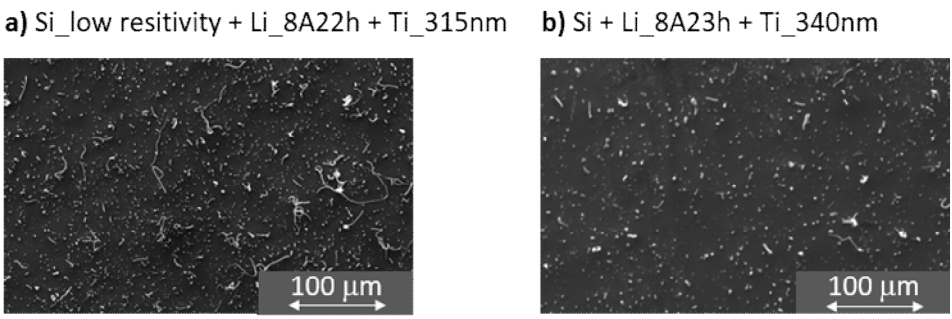

Figure 5.16. Air sensitive SEM top view images of **a)** Li evaporated onto a low resistivity Si wafer with a Ti layer on top (sequence I from Table 5.2) and **b)** Li evaporated onto a high resistivity Si wafer with a Ti layer on top (sequence C from Table 5.1).

5.3.3 Checking electrochemical activity of lithium thin film

Once lithium thin film growth was characterized, electrochemical performance of the lithium thin film was checked in the framework of MONBASA project. MONBASA was a H2020 European project (Monolithic Batteries for Spaceship Applications, grant agreement ID: 687561), which had the aim to develop an energy storage system for small satellites that could be integrated with MEMS (Micro-Electro-Mechanical Systems) technology[196]. The project was coordinated by CIC Energigune. The chosen materials to produce the solid-state battery were: lithium metal for the anode, LLZO ($Li_7Zr_2La_3O_{12}$ ceramic material) as a solid electrolyte and LMNO ($LiMn_{1.5}Ni_{0.5}O_4$) the cathode. LMNO, as mentioned in chapter 1 section 1.2.2, is one of the most promising high voltage cathode due to the large reversible capacity, high thermal stability, low cost and null content of the toxic, high cost and pollutant cobalt that most used cathodes have[197]. The use of LLZO solid electrolyte is very convenient for spaceship applications because of the vacuum conditions the battery is going to be exposed to. Besides, there are some studies suggesting the compatibility of LLZO with Li anode[198]. Then, in principle, Li/LLZO/LMNO system fulfil the requirements of the battery for MONBASA project.

First step of this battery production sequence was to sputter the LMNO cathode using a magnetron sputtering in a stainless-steel current collector. Then, with the same technique, LLZO electrolyte was deposited on the LMNO. Finally, Li was evaporated on top of the electrolyte. A mask system attached to the holder with different diameters was used during the deposition of the layers. Figure 5.17 shows the thin film battery obtained following this procedure. CIC Energigune was

in charge of the production of both electrolyte and anode, and the cathode was made and characterized in collaboration between the project partners CIC Energigune and Tecnalia.

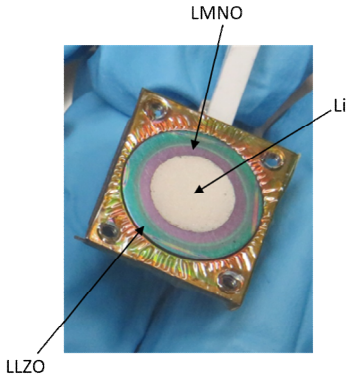

Figure 5.17. Full cells made in the framework of MONBASA project. Different layers can be identified in relation to the diameter of the masks used to deposit them.

The growth and electrochemical characterization of LMNO cathode was successfully achieved by the researchers involved in the project[199]. However, even all the efforts made, sputtering an ionic conductive LLZO was not reached. Even so, some solid-state full cells were characterized. Figure 5.18 shows the cross section of a MONBASA full battery. This cross section was taken in an SEM which has a Focused Ion Beam (FIB) to etch the sample, specified in chapter 2 section 2.3.4.1. Measurements were carried out by the responsible of electron microscope platform from CIC Energigune.

In Figure 5.18 each layer from the full cell can be identified. Some cracks in the interface between the electrolyte and the lithium anode are also observed. However, it is worth mentioning that, to be able to measure FIB-SEM, sample was exposed to air. Furthermore, Li could be interacting with the ions used to etch the sample. Therefore, the observed cracks could be a consequence of the manipulation of the sample to obtain the cross section image.

In order to check the performance of the lithium metal thin film anode with the sputtered LMNO cathode, a CR2032 type cell was assembled changing the LLZO solid electrolyte with the standard LP30 liquid electrolyte. This electrolyte has 1.0 M of $LiPF_6$ salt in ethylene carbonate (EC) and dimethyl carbonate (DMC) solution, 1:1 in volume. The separator used in the system was glass fiber. Lithium was

evaporated onto Cu coins, which is a common current collector in lithium metal anode batteries[200]. Furthermore, it has already been used as substrate for lithium thin films made by thermal evaporation[123,132,201–205]. Estimated thickness of Li anode was 720 nm - 2400 nm.

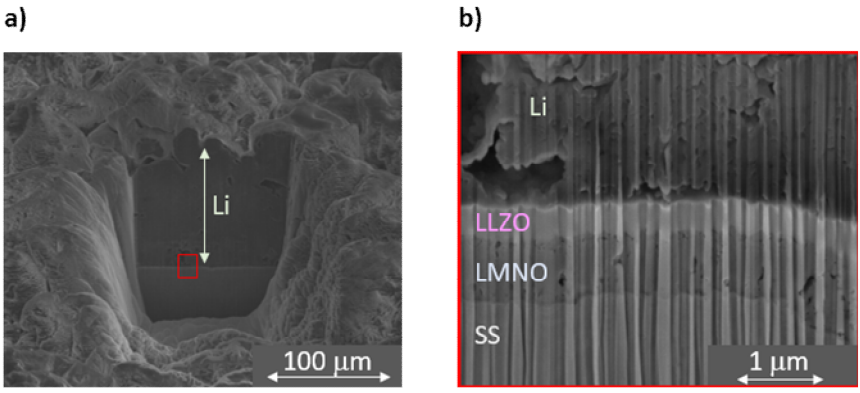

Figure 5.18. FIB SEM cross section image of a **a)** full cell fabricated in the framework of MONBASA, and **b)** magnification of the red rectangle highlighted in image a).

We performed two consecutive types of electrochemical measurements in a Biologic VMP3 potentiostat tester: a cyclic voltammetry followed by a galvanostatic cycling, both explained in chapter 2 section 2.4.1. Cycling voltammetry was measured with a rate of 0.05 mV/s, and in the galvanostatic cycling we tried different rates, where 1C equals to the current required to discharge the full electrode capacity in 1 hour. The initial configuration of LMNO is lithiated, so the first step was always to charge the cell and then back to discharge.

Figure 5.19 shows the cyclic voltammetry, where the main peaks of the electrochemical reactions of this system can be observed: $Ni^{2+} \rightarrow Ni^{3+}$ at 4.7 V and $Ni^{3+} \rightarrow Ni^{4+}$ at 4.77 V, better defined after the first cycle[206]. These two peaks can be observed in both charge and discharge of the cell, with a voltage hysteresis of 0.05 V. Within this reaction the electrochemical activity of both electrodes is proved. Apart from the expected redox reactions, there are other redox process in the system. The one around 4.2 V, according to literature, is related to oxidation of Mn^{3+} traces present in the cathode[206,207]. The oxidation of Mn^{3+} is irreversible, as we do not see any peak related to it when discharging the cell. The other one around 4.5 V can be correlated to parasitic reactions upon cycling the commercial carbon-based electrolyte above 4.5 V vs Li[197,208].

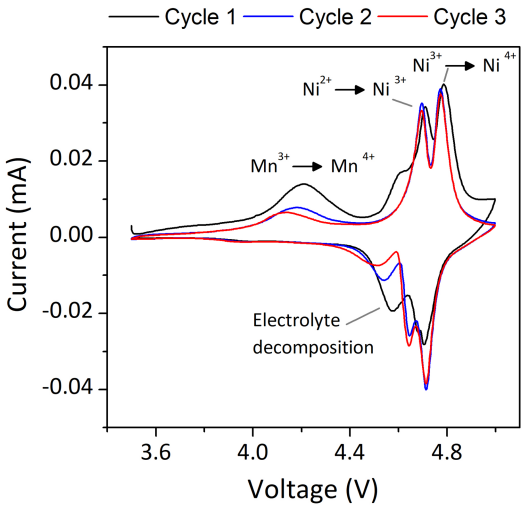

Figure 5.19. First three cycles of a cycling voltammetry of a full cell with evaporated lithium metal anode, sputtered LMNO cathode and LP30 liquid electrolyte. The scan rate is 0.05 mV/s.

In the galvanostatic cycling study shown in Figure 5.20, the obtained discharge capacities are lower than the theoretical one[206] (146.7 mAh/g), in the best case it reaches only 79.5% of the theoretical capacity. Besides, the capacity decreases abruptly while increasing the current rate, and when going back to the lowest rate, the initial capacity is not recovered. Remaining capacity is only 20.7% of the theoretical capacity. About the capacity retention, the higher the reaction rate the better the capacity retention, which is due to less time for the parasitic reactions to occur. First capacity retention of each current rate should not be considered, they are directly affected by the previous state of the cell related to previous current rate.

We attribute this bad performance to the use of a liquid electrolyte. On one side, we have the problems of its stability window at voltages higher than 4.2 V previously mentioned. And, on the other hand, as explained in chapter 1 section 1.3.2, the interface between organic liquid electrolytes and lithium metal is not stable, so the continuous reaction between them will consume the thin film. This effect is not as obvious if we were using a lithium foil, where the reservoir of lithium is much higher so the loss of surface lithium is not that important. Furthermore, the thickness of lithium is not homogeneous, which could also be affecting to the fast degradation of the battery. Yet, within these tests the electrochemical activity of both anode and cathode are proved.

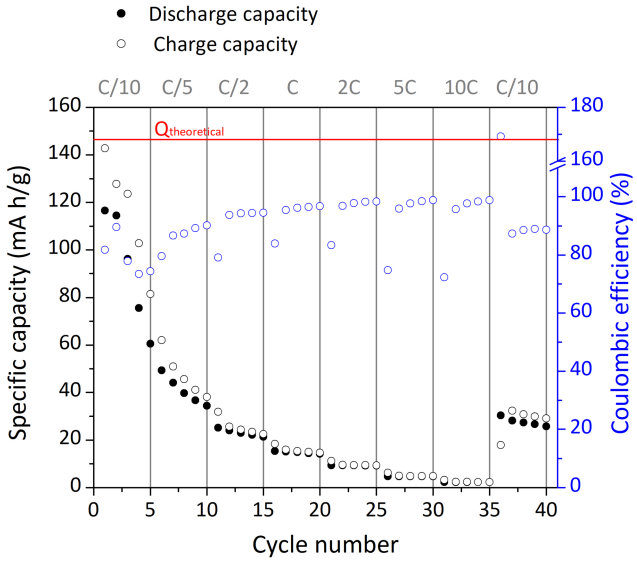

Figure 5.20. Galvanostatic cycling of a cell with evaporated lithium metal anode, sputtered LMNO cathode and LP30 liquid electrolyte.

5.4 Conclusions

In this chapter, the deposition rate of a commercial lithium source (alvasource, capacity of 190 mg) have been determined at two conditions. When passing a current of 8 A through the source, deposition rate is 120 – 400 nm/h; and at 10 A, deposition rate is 730 - 1400 nm/h. Increasing the intensity applied to the source also modifies the structural development of the lithium due to an increase in the substrate temperature. With a current of 8 A, the structure of the deposited layer is type Z1: lithium has dolmens and voids on the surface. However, when current is 10 A, the morphology is Z2 type, where lithium grows as column with tight grain boundaries between them. Substrate temperature transition for lithium to grow from Z1 to Z2 structure is between 42.3 °C and 51.5 °C. The obtained deposition rates are specific for our evaporation chamber configuration.

From all the substrates where structure development was studied (monocrystalline Si wafer, Ti layer, stainless steel, PET polymer, monocrystalline $SrTiO_3$), there is one case where lithium did not grow as a layer but in whisker like

structure: Si <100>. We couldn´t find a parameter to predict when lithium will be growing in whisker like structure.

The electrochemical activity of the evaporated lithium layer was confirmed when cycling a cell with LMNO thin film high voltage cathode and LP30 organic electrolyte.

CHAPTER 6

Li surface contaminants influence on a Li metal-polymer electrolyte system

In this chapter, the role surface contaminants have on the electrochemical performance of Li anode is reported. To this purpose, two types of Li/Li symmetric cells with solid polymer electrolyte were assembled: in one case, commercial Li foil stored in glove box was used, in the second Li was directly deposited on the electrolyte by means of thermal evaporation in ultra-high vacuum condition, guaranteeing to minimize interface contaminants.

6.1 Introduction

Most common electrolytes of Li-ion batteries are organic liquid carbonates due to their high electrochemical performance, as explained in chapter 1 section 1.2.2. However, these flammable liquids present several safety issues which could be solved moving to solid electrolytes. This kind of electrolyte also offers an improvement in terms of mechanical properties, which implies a higher resistance against dendrite growth[209,210]. Among solid electrolytes, one of the most promising candidates are polymers. In addition to mentioned characteristics, their flexibility make them appropriate to be used in the field of stretchable energy storage systems, which includes applications in medical implants, flexible electronics and textiles[211].

Solid polymer electrolytes are formed by a macromolecule polymer matrix with dissolved lithium salt. Their ionic conductivity is a result of the ions moving through the polymer chain. Contrary to what happens with liquid electrolytes, this movement is not free, it depends on the mobility of chains and the dissociative ability of the polymer[212]. Thus, the main drawback of polymer electrolytes is their low ionic conductivity at room temperature. If the temperature is raised, ionic conductivity increases exponentially[213], achieving reasonable values above realistic application temperatures[214]. Besides, at high temperature, their mechanical properties are degraded, and they lose the capability to block dendrite growth. As a consequence short circuit can occur, especially when working at high current densities[215,216].

Poly(ethylene oxide) (PEO) polymer has been widely studied as an adequate candidate for electrochemical devices since M. Armand discovered its ionic conductivity in 1984[217]. Figure 6.1 shows how the polymer dissolves lithium by binding interactions between the lithium ions and the ether oxygens.

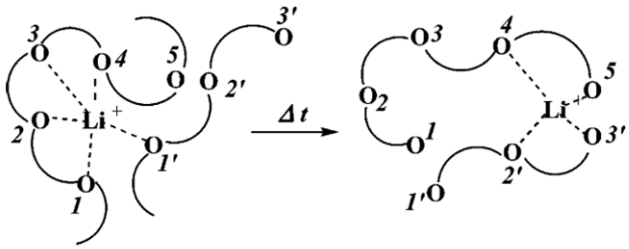

Figure 6.1. Schematic of Li ion conduction in PEO based electrolyte. [Reproduction with permission from[61], Copyright (2019) American Chemical Society].

Conductivity obtained in this way is in the rage of 10^{-8}-10^{-4} S/cm[209], whereas the conductivity for practical applications should be at least around 10^{-3} S/cm[214]. This is related to PEO being a semicrystalline polymer at room temperature, and conductivity in polymers is believed to be mainly a consequence of the amorphous phase[218], thus above the melting temperature, above 65 °C. Among several Li salts studied with PEO, Lithium bis(trifluoromethanesulfonyl)imide (LiTFSI) presents a higher ionic conductivity[209].

The aim of this chapter is to use this well characterized standard PEO:LITFSI solid polymer electrolyte and compare the effect lithium surface contaminants have on its electrochemical performance. Both polymer and salt chemical structures are

illustrated in Figure 6.2. For that purpose, PEO:LITFSI polymer membrane is synthesized and Li/PEO:LiTFSI/Li symmetric cells are assembled. To check which is the lithium surface contaminants effect in the electrochemical performance, two types of electrodes are compared. First one is commercial lithium foil stored in an argon atmosphere glove box, which, according to both chapter 3 and chapter 4 conclusions (sections 3.5 and 4.5), has a completely oxidized surface, mainly by Li_2CO_3 and Li_2O species. Second type of electrode is evaporated lithium thin film. Growing and characterization of Li thin film was explained in chapter 5. In this chapter, evaporation is performed directly on the polymer electrolyte in UHV conditions. Because of this, we can assume that the interface is essentially free of impurities.

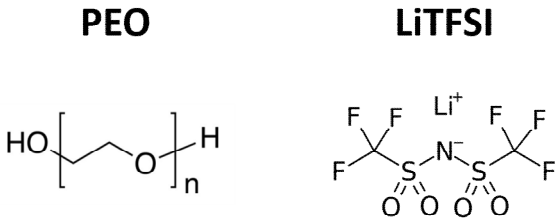

Figure 6.2. Chemical structure of PEO polymer and LiTFSI salt, both constituents of the solid polymer electrolyte used in this chapter.

6.2 Experimental section

6.2.1 Synthesis of PEO:LiTFSI polymer electrolyte

Materials to synthesize the polymer electrolyte are commercially available: poly(ethylene oxide) (PEO, Mw = $5{\cdot}10^6$ g/mol), from Sigma-Aldrich; Acentonitrile (ACN, HPLL grade), from Scharlab; and battery grade lithium bis (trifuloromethanesulfanyl) imide (LiTFSI), supplied by Solvionic. Electrolyte was prepared using the solvent casting method, schematically represented in Figure 6.3.

First, polymer and salt were mixed with the ACN solvent at 50 °C for 24 hours with a rotation speed of 500 rpm using a magnetic stirrer (Figure 6.3a). Ratios for mixing were PEO:LiTFSI 21:1 (mol) and PEO:ACN 1:50 (masa). After the mixing, dissolution was casted in a teflon disk (Figure 6.3b) and placed in a desiccator.

Once solvent was evaporated and we had a self-standing membrane (Figure 6.3c), polymer was pressed using a hot press, which allows to adjust temperature and pressure to obtain the desired thickness. Polymer electrolyte was pressed at 2 tons for 3 minutes at 70 °C, resulting in 80 μm thick membranes. In addition, this step ensures all dissolvent was evaporated. After hot pressing, electrolyte was punched and dried under dynamic vacuum at 50 °C for 12 hours to remove any trace of water it could contain. Finally, the electrolytes were moved to an argon atmosphere glove box (MBraun, O_2 and H_2O < 0.1ppm) preventing air exposure.

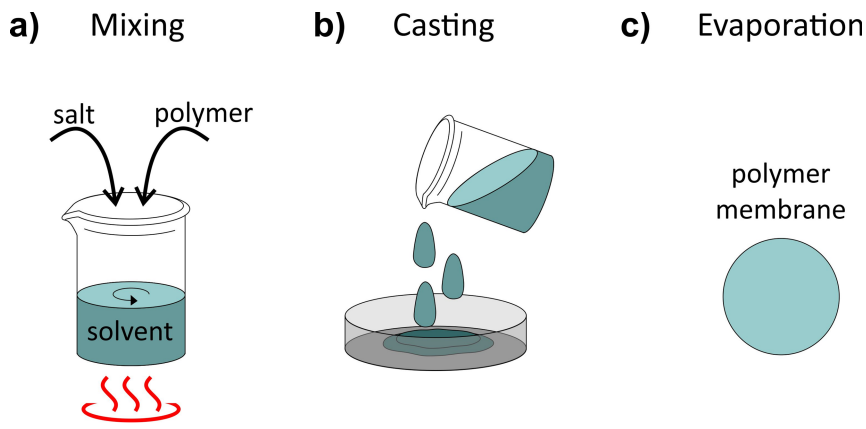

Figure 6.3. Solvent casting method used to synthesize PEO:LiTFSI solid polymer electrolyte. Process has three steps: **a)** mixing of the salt and polymer with the solvent, **b)** casting of the mixture and **c)** evaporation of the solvent to obtain a self-standing membrane.

6.2.2 Li foil (Li_F) and Li thin film (Li_TF) symmetric cell assembly

As mentioned in the introduction, two types of lithium symmetric cells using PEO:LiTFSI solid polymer electrolyte were fabricated. Symmetric cells which have commercial lithium foil electrodes will be referred as Li_F/PEO/Li_F, where F denotes lithium is a foil. Second type of cell, in which lithium was evaporated in UHV conditions, will be named as Li_TF/PEO/Li_TF. Here TF refers to thin film.

For the assembly of **Li_F/PEO/Li_F** cells, Li foil (Rockwood Lithium, Lithium metal, Battery Grade) was punched in 8 mm electrodes. Then, CR2032 (Figure 2.15) cells were built using 16 mm polymer electrolyte membranes.

First step to make **Li_TF/PEO/Li_TF** cells was to mount a 10 mm diameter polymer membrane in the glove box in a special holder designed for Li evaporation, represented in Figure 6.4a.

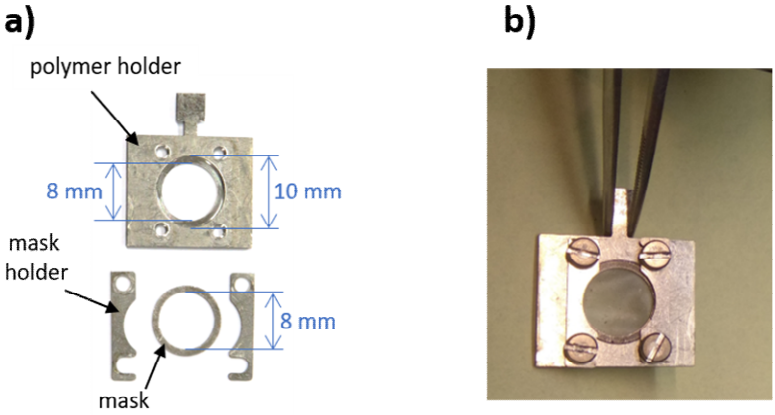

Figure 6.4. a) Stainless-steel polymer holder with a mask system to mount a 10 mm diameter polymer electrolyte and evaporate lithium in both sides of the polymer, making 8 mm diameter Li thin film electrodes. **b)** Polymer membrane mounted in the holder.

This stainless-steel holder has an 8 mm through hole. On one of the sides, a 10 mm diameter down step allows to place the polymer. An 8 mm inner diameter mask is used to hold the polymer, which, in turn, is held by two pieces that are screwed to the holder. With this configuration, Li can be evaporated on both sides of the polymer, creating 8 mm diameter Li thin film symmetric electrodes. Polymer membrane mounted in the holder (Figure 6.4b) was transferred to the lithium evaporated system (Figure 5.2) using the air sensitive transfer from Figure 2.8 to avoid air atmosphere exposure. Evaporation on each side of the membrane was done according to Li thin film characterization presented in chapter 5: using a current of 10 A during 20 hours with a commercial source (alvosource), which creates 21.3 ± 6.7 μm electrodes. Figure 6.5 shows both sides of the polymer electrolyte after Li evaporation The holder with Li_TF/PEO/Li_TF was moved back to the glove box in same air sensitive transfer arm and CR2032 cells were assembled. For this second type of cells, two extra spacers were added to compensate the thickness of Li thin film and have a similar pressure on both type of cells.

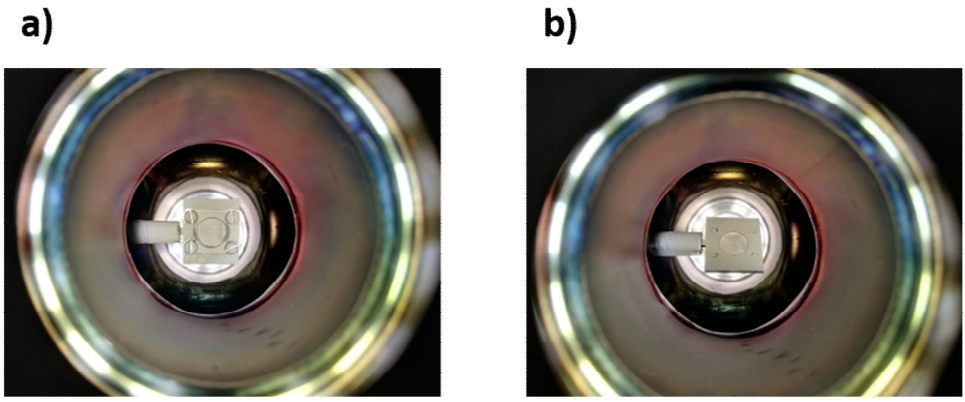

Figure 6.5. a) Front side and **b)** back side of the polymer membrane after Li evaporation.

6.2.3 Electrochemical measurement protocol

The electrochemical performance of both symmetric cells was analyzed using two electrochemical measurements explained in section 2.4.2: electrochemical impedance spectroscopy (EIS) and galvanostatic polarization. EIS gives information about the interface resistance of the cell, while the galvanostatic polarization was performed to see the effect several lithium platting and stripping processes have in the voltage of the cell. A last EIS was also measured to get information about the evolution and stability of the interface resistance after the platting and stripping process. Table 6.1 indicates the conditions of each of the measurements performed in a Biologic VMP3 potentiostat tester. The chosen conditions of the galvanostatic polarization from Table 6.1 are equivalent to a thickness variation of 121 nm in each cycle, considering the theoretical capacity of Li metal (3860 mAh/g) and the density of Li (0.534 g/cm^3). This calculation assumes a flat lithium surface and a homogenous platting and stripping process. One has to take care that this thickness is smaller than the thickness of Li electrodes, not to deplete all lithium when working with thin films. In our case, the variation represents the 0.8% of electrode thickness for the minimum thickness of thin films. Then, even if the real variation will be higher than 121 nm, there is enough lithium to be removed from the thin film electrodes.

As mentioned in the introduction section, PEO:LiTFSI polymer presents an adequate ionic conductivity at temperatures above 65 °C, its melting point, when the polymer is amorphous. We decided to explore the behavior of both Li_F/PEO/Li_F and Li_TF/PEO/Li_TF symmetric cells at two temperatures. At 70 °C,

where we are ensuring a good performance of the electrolyte, and at 45 °C, a temperature where the polymer is semicrystalline. This second temperature will be useful to observe the role surface contaminants play in very unfavorable electrochemical conditions for the electrolyte. Besides, 45 °C is nearer than 70 °C to room temperature, so it is a more interesting condition than 70 °C in terms of applicability. Climatic chambers where used to set the temperatures for the electrochemical measurements.

In Li_F/PEO/Li_F cells, interfacial contact between the electrodes and electrolyte will be defined by the pressure applied during cell assembly. However, in Li_TF/PEO/Li_TF cells, direct evaporation of lithium in the electrolyte ensures a good interfacial contact. In order to avoid any difference in the quality of the interfacial contact between the two types of cells that could affect electrochemistry, they were pretreated at 70 °C for 12 hours before the electrochemical measurements.

Table 6.1. Electrochemical protocol used to check the performance of Li_F/PEO/Li_F and Li_TF/PEO/Li_TF symmetric cells. Protocol was done in two temperatures, 70 °C and 45 °C.

Step	Conditions	Aim
1. Pretreatment	12 hours at 70 °C	Ensure good interfacial contact
2. EIS	from 101 kHz to 5 mHz	Initial interface resistance
3. Rest	10 minutes	Back to OCV
4. Galvanostatic polarization	50 cycles at 0.05mA/cm^2, 30 minutes each platting/stripping	Stability and overpotential study
5. Rest	10 minutes	Back to OCV
6. EIS	from 101 kHz to 5 mHz	Evolution of interface resistance

The impedance measurement results have been analyzed using EC-Lab view software. Within it, Nyquist plots obtained from EIS measurements have been fitted to an equivalent circuit model, a usual way to interpret EIS data, as explained in chapter 2 section 2.4.2. Figure 6.6 shows the two equivalent circuit models used to study EIS data. There, instead of using capacitors to represent double layers capacitance, constant phase elements (CPE) have been used to mimic a non-ideal capacitor. Model A considers the following electrochemical processes, all of them present in Li/polymer/Li symmetric cells according to literature[219]. First, at high frequencies it represents the resistance of the polymer electrolyte (R_b), which has

been used to calculate the ionic conductivity of the polymer according to equation (2.22). Then, the solid electrolyte interphase (SEI) is considered by a parallel combination of SEI resistance (R_{SEI}) and a double layer capacitance (CPE). At medium frequencies, the charge transfer reaction is taken into account, again with a parallel combination of its corresponding resistance (R_{CT}) and double layer capacitance (CPE). Finally, at low frequencies, the diffusion process of lithium in the polymer electrolyte is represented with a semi-infinite Warburg impedance element[220]. The model B from Figure 6.6 is a simplification of the previous model, where both charge transfer and SEI contributions are represented in one resistor (R_{int}) and one CPE in combined in parallel. R_{int} represents the total resistance of the interface, which for the model A is the sum of R_{SEI} and R_{CT}.

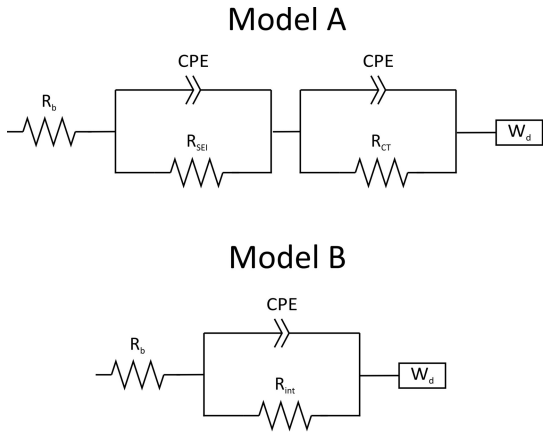

Figure 6.6. Equivalent circuit models used to analyze Nyquist plots obtained by EIS measurements.

6.3 Impact of contaminants on the electrochemical response

6.3.1 Validation of Li evaporation on polymer electrolyte

During thermal evaporation of lithium, as analyzed in chapter 5, the temperature reached by the holder increases. Particularly, evaporation conditions used to make Li_TF/PEO/Li_TF type cells increase the holder temperature up to 51.5 °C. In order to check if this temperature rise induces a lithium diffusion through the electrolyte to the other side of it, polymer surface was analyzed by X ray Photoelectron Spectrocopy (XPS). Firstly, bare PEO:LiTFSI membrane was

measured, which, as shown in Figure 6.7a, does not present lithium signal on the surface. Then, sample was transferred to the evaporation chamber with the air sensitive transfer arm and lithium was evaporated on just one side of the polymer. After that, membrane was moved back to the XPS chamber and both sides of the polymer were measured. As can be observed in Figure 6.7b, XPS only detects lithium in the evaporated side, confirming that lithium does not diffuse through the PEO during evaporation.

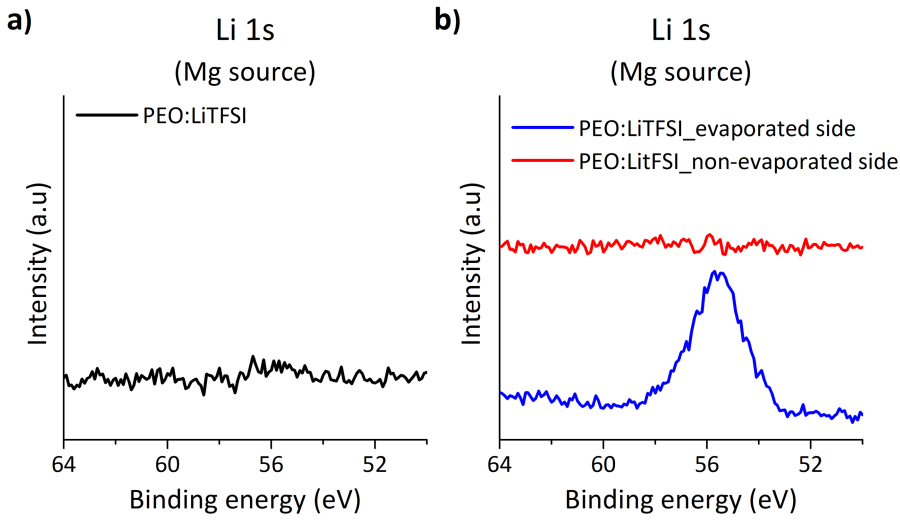

Figure 6.7. a) XPS spectra measured with Mg source in Li 1s region for **a)** PEO:LITFSI bare polymer membrane and **b)** same polymer membrane after lithium evaporation on one side of the polymer.

6.3.2 Electrochemical performance comparison of Li_TF/PEO/Li_TF and Li_F/PEO/Li_F symmetric cells

Results of galvanostatic polarization measurements of Li_TF/PEO/Li_TF and Li_F/PEO/Li_F symmetric cells at 70 °C and 45 °C are represented in Figure 6.8. In Figure 6.9 the overpotential of the cells is represented in detail, where two cells for each condition are indicated, confirming the reproducibility of the experiment. As observed in the figures, at 70 °C both cells are able to reach steady voltages. However, when polarization at 45 °C, 30 minutes is not enough for the cells to have a stable voltage, which is expected considering PEO:LiTFSI electrolyte at that temperature is semicrystalline.

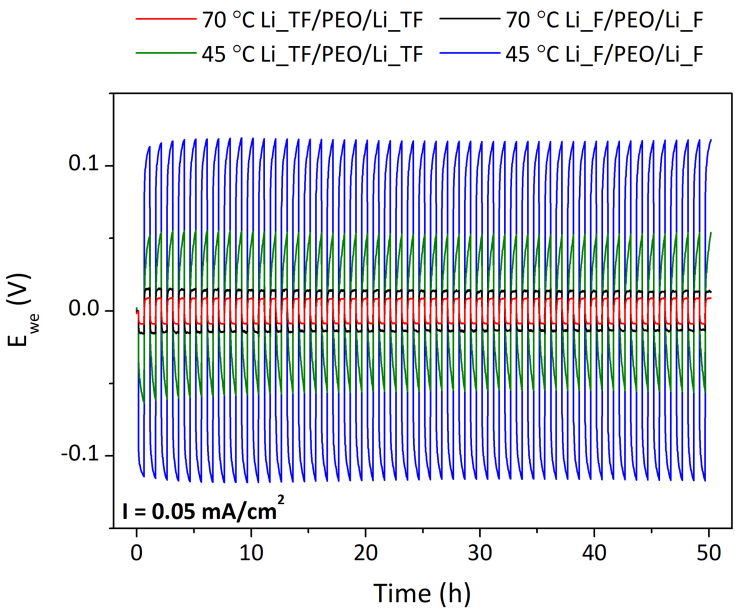

Figure 6.8. Galvanostatic polarization of Li_TF/PEO/Li_TF and Li_F/PEO/Li_F symmetric cells at two temperatures, 70 °C and 45 °C, using a current of 0.05 mA/cm^2.

If we compare the response of Li_TF/PEO/Li_TF and Li_F/PEO/Li_F cells, in both temperatures overpotential voltage is lower for Li_TF/PEO/Li_TF cells. Thus, if we avoid Li foil surface contaminants, Li ion suffers a smaller resistance to travel from one electrode to the other. This effect is more significant at 45 °C than at 70 °C. At 45 °C, overvoltage of Li_TF/PEO/Li_TF is around half of that of Li_F/PEO/Li_F. From this information, it can be concluded that SEI purity degree is strongly modifying the electrochemical response of Li anode when the cycling is limited by a very poor conductivity of the solid polymer electrolyte.

The Nyquist plots obtained by EIS measurements and fittings using equivalent circuits are shown in Figure 6.10. Error of the fittings is also indicated in the figure in terms of χ^2. This error is higher for measurements at 45 °C, according to the very noisy data due to the low conductivity of the electrolyte. Nyquist plots of Li_TF/PEO/Li_TF and of Li_F/PEO/Li_F have been analyzed using model A and B from Figure 6.6, respectively. The reason relies on the difficulty to differentiate the contribution of the charge transfer and SEI in these second cells, a usual problem when fitting EIS measurements with model A in Li polymer symmetric cells[219,220]. In this study, main purpose to measure the impedance is to obtain and

compare the internal resistance between the cells. For this reason, spectra are not fitted at the lowest frequencies as can be seen in Figure 6.10, and diffusion phenomenon that takes place there will not be analyzed

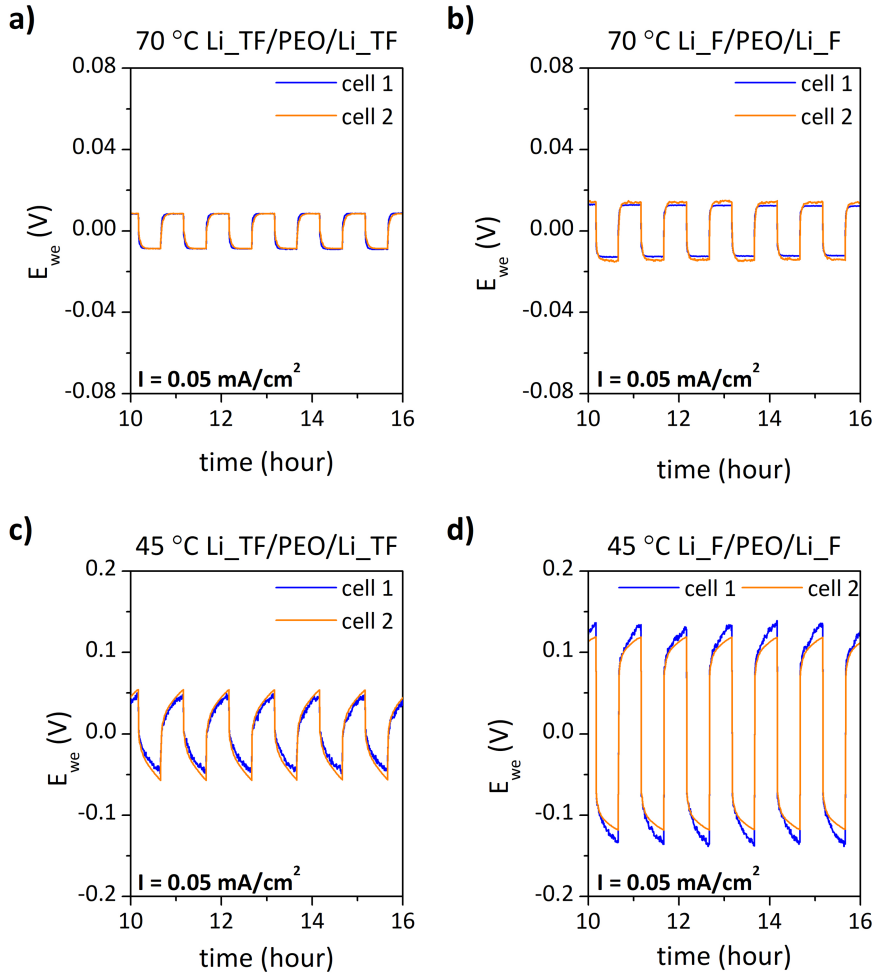

Figure 6.9. Galvanostatic polarization of **a)** Li_TF/PEO/Li_TF at 70 °C, **b)** Li_F/PEO/Li_F at 70 °C, **c)** Li_TF/PEO/Li_TF at 45 °C **d)** Li_F/PEO/Li_F at 45 °C. Two cells are represented at each condition to check the reproducibility of the experiment.

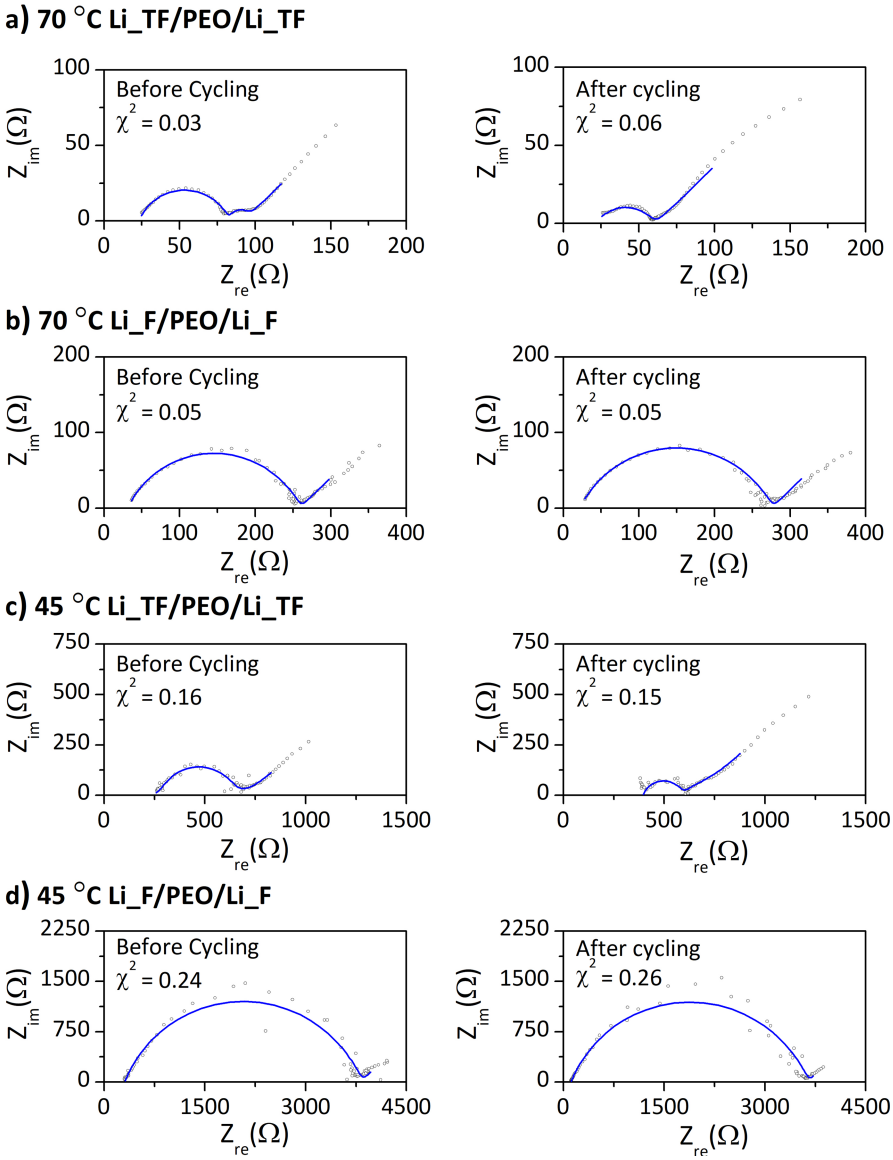

Figure 6.10. Nyquist plots of Li/PEO:LiTFSI/Li symmetric cells before and after the galvanostatic polarization and fitting of the data using equivalent circuits for **a)** Li_TF/PEO/Li_TF at 70 °C, **b)** Li_F/PEO/Li_F at 70 °C, **c)** Li_TF/PEO/Li_TF at 45 °C and **d)** Li_F/PEO/Li_F at 45 °C. a) and c) has been analyzed using equivalent circuit model A from Figure 6.6, and b) and d) equivalent circuit model B from Figure 6.6.

Considering the bulk resistance obtained from the equivalent circuit fittings and equation (2.22), conductivity of the electrolyte has been calculated. At 70 °C, conductivity is $(6.2 \pm 1.1)\cdot10^{-4}$ S/cm, and at 45 °C it is $(7.3 \pm 3.6)\cdot10^{-5}$ S/cm, which are in the order of reported values[221]. Within this conductivity values we confirm that, effectively, at 45 °C the capability of the polymers to conduce Li ions is much lower than that at 70 °C, which affects the galvanostatic overpotential response observed in Figure 6.8.

Figure 6.11 shows the internal resistance obtained from the fitting of impedance spectra from Figure 6.10. At both temperatures, internal resistance of Li_TF/PEO/Li_TF cells is smaller than that of Li_F/PEO/Li_F cells. At 70 °C, Li_TF/PEO/Li_TF internal resistance is equivalent to the 26% of Li_F/PEO/Li_F internal resistance. This percentage decreases to 8% when cycling at 45 °C. In fact, the internal resistance of Li_TF/PEO/Li_TF at 45 °C is comparable to that of Li_F/PEO/Li_F at 70 °C. With this comparison, we are directly observing the huge effect of lithium surface contaminants in the solid electrolyte interphase, which is more pronounced at the unfavored condition of the electrolyte.

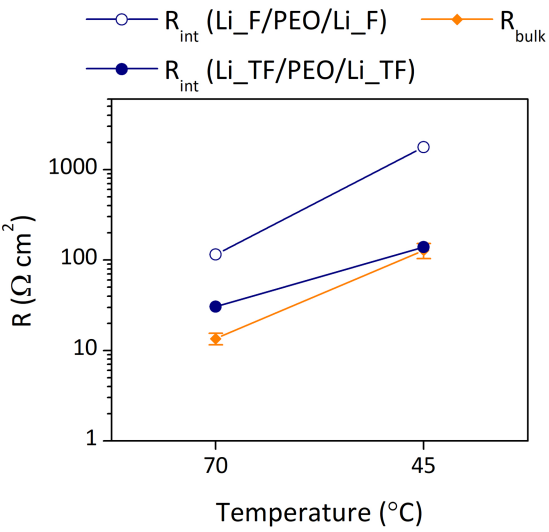

Figure 6.11. Temperature effect on interface resistance (R_{int}) and bulk resistance (R_{bulk}) of Li_F/PEO/Li_F and Li_TF/PEO/Li_TF symmetric cells before the galvanostatic polarization.

Figure 6.11 also shows the mean bulk resistance of the cells. In the case of Li_F/PEO/Li_F cells, the fact that interface resistance is higher than that of bulk resistance implies ion transport through the interface is more difficult relative to

ion transfer across the polymer. Therefore, limiting resistance factor will be the interface rather than the conductivity of the electrolyte. By contrast, for Li_TF/PEO/Li_TF cells, both bulk and interface resistance are very similar.

The effect galvanostatic polarization has on the internal resistance of the cells can be inferred from Figure 6.12. For Li_F/PEO/Li_F there is a small increase in both temperatures after platting and stripping process, indicating SEI keeps growing during the cycling process. However, the opposite happens with Li_TF/PEO/Li_TF, here internal resistance decreases after galvanostatic polarization. This implies that the interface between Li thin film and the electrolyte is not stable during platting and stripping process. This dissimilar behavior further confirms the different nature of both interfaces.

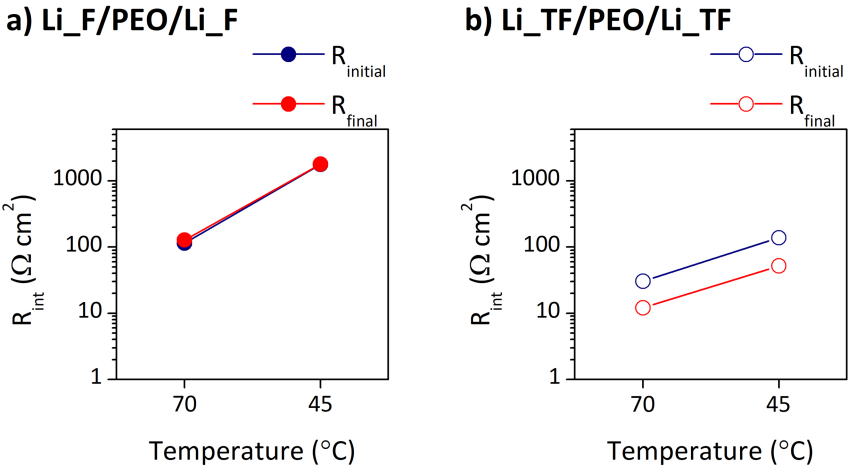

Figure 6.12. Evolution of the internal resistance (R_{int}) after galvanostatic polarization **a)** Li_F/PEO/Li_F and **b)** Li_TF/PEO/Li_TF cells. $R_{initial}$ indicates the internal resistance before the galvanostatic polarization, and R_{final} is the internal resistance after that.

The cells that were studied at 70 °C, when finishing the electrochemical protocol from Table 6.1, were further cycled at same galvanostatic polarization conditions of step 4, which has been represented in Figure 6.13. Plating and stripping potential keeps constant in both cells for 13 days, meaning cells were stable during all that time. But after that, the overpotential of Li_TF/PEO/Li_TF cell rise abruptly. The origin of the rise in voltage in a symmetric lithium cell is related to the full removal of the lithium from the electrode[73]. The fact there is no more lithium to perform the electrodeposition is related to the non-uniform deposition of the lithium and the reaction of it with the electrolyte. Then, the further stability of the

Li foil is due to the higher loading of Li in the electrodes instead of having a more stable system. This last conclusion indicates systems which have thin film electrodes where maximum loading is limited are more appropriate than standard Li foil electrodes (typically around 1.5 mm thick) to elucidate key interfacial phenomena which are determining the electrochemical performance of the cells. In fact, it has been suggested that thickness of lithium in this type of studies should be smaller than 30 μm, if one wants to have a proper understanding of the performance improvements and short circuit detection[73].

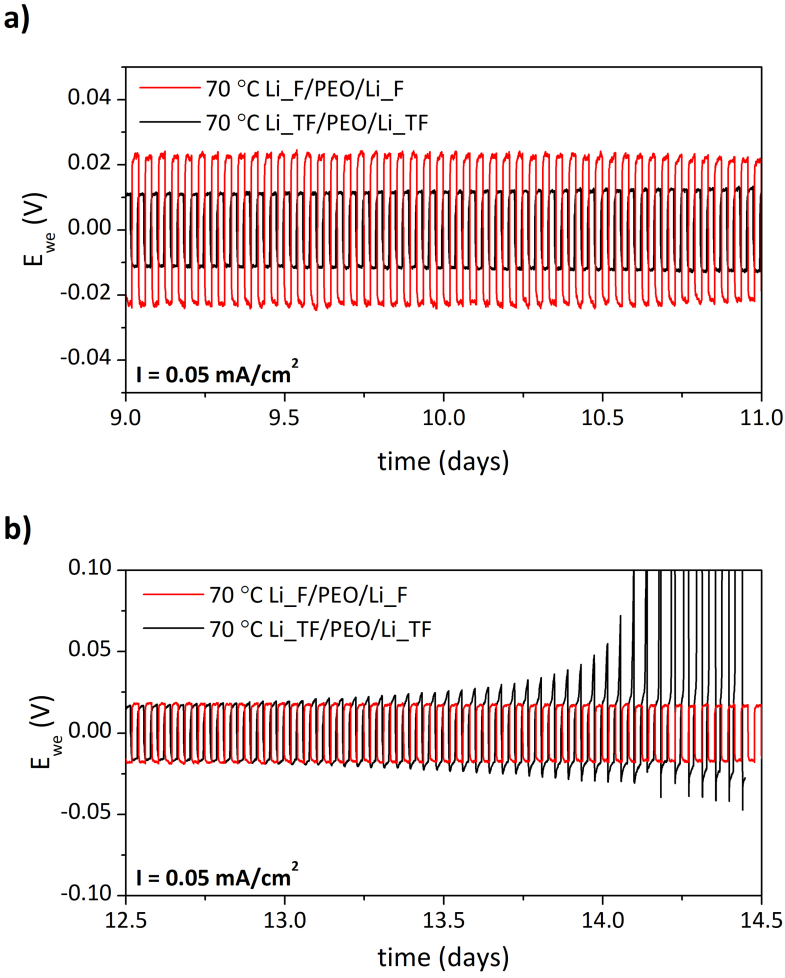

Figure 6.13. Galvanostatic polarization of Li_F/PEO/Li_F and Li_TF/PEO/Li_TF symmetric cells at 70 °C using a current of 0.05 mA/cm^2, where **a)** represents the evolution of the voltage during the day 9 and 11 and **b)** represents same evolution after 12 days and a half.

6.4 Conclusions

In this chapter we can conclude that surface impurities play a key role in the interfacial phenomena that determine the electrochemical performance of Li/PEO:LiTFSI/Li cell. When the SEI layer is free of Li foil native surface impurities, its internal resistance decreases 26% at 70 °C, a temperature where the electrolyte presents an adequate ionic conductivity, $(6.2 \pm 1.1)\cdot10^{-4}$ S/cm. At 45 °C, a condition where conductivity of electrolyte decreases down to $(7.3 \pm 3.6)\cdot10^{-5}$ S/cm, the reduction of the internal resistance is even higher, 92%. Galvanostatic polarization also shows the effect of native lithium surface impurities. Avoiding them, overpotential decreases, especially when working at 45 °C, reducing to around half. Thus, the effect of lithium surface contaminants is more pronounced when the cell is cycled at 45 °C than when it is cycled at 70 °C. This implies that when working at unfavored temperatures for the electrolyte with the aim of reaching practical application temperatures, knowing lithium anode initial surface composition becomes highly important. Furthermore, working with thin film electrodes has been proved to be more appropriate than with standard Li foil to investigate the effect of the interfacial phenomena due to the controlled reservoir of lithium. Excessive loading capacity of the electrodes, as is the case of some lithium foils, can hinder interfacial effects that otherwise will limit cyclability.

The model system chosen to study the effect of lithium surface impurities in this chapter has been a standard solid polymer electrolyte symmetric cell. In consideration of the results obtained, we can generalize that surface contaminants will affect rest of electrochemical systems where other electrolytes are used. Awareness of the native lithium surface chemical composition is essential in order to get conclusions about the stability of systems that rely on metallic lithium electrodes.

CHAPTER 7

General conclusions and perspectives

7.1 General conclusions

Next generation batteries based on metallic lithium anodes suffer from instability problems that arise in the high reactivity of the anode surface. In this thesis, how dry atmospheric gases affect the stability of the lithium surface is analyzed by looking to the changes in the chemical composition and electronic properties, where particular attention has been payed to lithium carbonate evolution. In the same line, influence of the lithium surface native impurities on the internal resistance and performance of an electrochemical system is reported.

Initial state of a commercial lithium foil stored and scraped in argon atmosphere has a completely oxidized surface, where there is no metallic lithium in the first 8 nm of the surface. Indeed, according to non-destructive depth profiling synchrotron radiation APXPS measurements, Li-based surface main compounds are Li_2O and Li_2CO_3, where the last one lies above the oxide. Thus, performing a UHV cleaning process is essential if the aim is to analyze the evolution of a metallic lithium surface. Two methods have been proved to be effective for that purpose: Ar ions sputtering and surface scraping in UHV.

When analyzing the interaction of metallic lithium with O_2, CO_2 and N_2 atmospheric gases, XPS results reveal oxygen gas is the most reactive one towards metallic lithium, where 9 L are enough to oxidize the first 8.6 nm of the surface. Li_2O is the only product of this interaction at O_2 gas pressures lower than 10^{-4} mbar. Above that, Li_2O_2 has also been detected on the surface. In the case of CO_2

gas, carbonaceous layer of the surface slows down the oxidation of lithium. Even after a dose of $8 \cdot 10^8$ L, metallic Li can be detected on the first 10 nm of the surface. Main products of this interaction are Li_2O, Li_2CO_3 and some other carbon-based species. About nitrogen gas, its interaction has surprisingly been the less reactive one. Juts some nitrogen-based compounds have been detected at $1 \cdot 10^4$ L, which represent less than 1.2% of the surface normalized composition. Furthermore, when going up to higher doses, surface reveals that O_2 impurity gas from nitrogen gas line is more reactive towards lithium than nitrogen itself. Only way to obtain Li_3N on surface has been by reactive ion implantation of nitrogen gas.

Modified surfaces with O_2, CO_2 and N_2 present a lower work function than bare metallic lithium, corroborated by UPS results. In particular, when surface compounds are Li_2O and Li^0, work function follows an exponential decay determined by the surface concentration of Li_2O. Decrease in the work function implies lithium modified by the most common dry atmospheric gases has a surface more energetically favorable to loss an electron than bare lithium, which is undesirable for anode applications.

In situ synchrotron radiation APXPS experiments, where Li_2CO_3 evolution on Li metal surface exposed to CO_2 gas has been studied at three CO_2 gas pressures (0.1 mTorr, 10 mTorr and 400 mtorr), reveal $Li_2C_2O_4$ also evolve on the surface. Oxalate was earlier postulated as an intermediate for Li_2CO_3[137], but this is the first time $Li_2C_2O_4$ is experimentally detected, providing an important clue in the way to elucidate the reaction mechanism. Kinetic studies show that carbonate growth presents two regimes: a reaction-controlled regime with linear growth rate and a diffusion-controlled regime with parabolic growth rate. According to our results, Li_2O growth observed when CO_2 gas interacts with Li metal takes place mainly in the very beginning of the interaction. Non-destructive depth profiling experiments show that, in all the studied situations, surface has a layered structure with the following sequence: Li^0 in the bottom, an intermediate Li_2O layer, and a topmost surface layer with both Li_2CO_3 and $Li_2C_2O_4$. With all this information, a reaction mechanism for the interaction of Li with CO_2 gas has been proposed. When looking to the effect of adding O_2 gas to CO_2 atmosphere, Li_2CO_3 promotion is observed rather than Li_2O promotion, and no $Li_2C_2O_4$ evolves, bypassing the proposed mechanism and leading into a surface comprised of pure carbonate.

Lithium thermal evaporation in UHV conditions has been performed onto a solid electrolyte to avoid native lithium surface impurities in the SEI. When

characterizing the evaporation of a commercial Li source, it has been observed that, using a current of 8 A, deposition rate is 120 – 400 nm/h and thin film lithium layer has dolmens and voids. When increasing the current up to 10 A, deposition rate is 730 - 1400 nm/h and lithium layer grows as columns with tight grain boundaries between them. This difference in the structural development has been related to the substrate temperate, which is 42.3 °C at 8 A and 51.5 °C at 10 A. From all the substrates where structure development has been studied (monocrystalline Si wafer, Ti layer, stainless steel, PET polymer, monocrystalline $SrTiO_3$), there is one case where lithium is not growing as a layer but in whisker like structure: Si <100>. We couldn´t find a parameter to predict when lithium will be growing in whisker like structure.

Final conclusions are related to the effect Li foil native impurities have on a lithium symmetric cell which has a standard polymer electrolyte: Li/PEO:LiTFSI/Li. When the SEI layer is free of Li foil native surface impurities, its internal resistance decreases 26% at 70 °C, a temperature where the electrolyte presents an adequate ionic conductivity. At 45 °C, a condition very unfavorable for the electrolyte performance, the reduction of the internal resistance if even higher, 92%. Avoiding lithium surface native impurities also affects the galvanostatic polarization, where overpotential decreases at both 70 °C and 45 °C, reducing to around half at last temperature. With these results we ensure Li foil surface impurities strongly affect the interfacial phenomena that will ultimately determine the performance of an electrochemical system.

In summary, all along this thesis work fundamental aspects of how most common dry atmospheric gases affect lithium surface are provided. Furthermore, considering the observed notorious effect of avoiding surface impurities in an electrochemical system, the need of more fundamental studies focused on the reaction of Li metal with surrounding gases are essential if the lithium high reactivity surface is to be successfully addressed. Gaining knowledge on this matter will help finding the appropriate conditions where Li surface would be best suited as next generation anode.

7.2 Perspectives

Among the several pathways one can follow to keep studying lithium surface reactivity and stability, two will be emphasizes as the most promising ones.

First pathway is focused on the analysis of the specific effect each gas has on the electrochemical performance. In order to do that, we have started to design a UHV chamber where it would be possible to clean a lithium surface, modify it with gases and perform electrochemical measurements using a solid electrolyte in UHV conditions. This system will allow us to study how each gas affects the internal resistance and the cyclability of the cell. With this information, we could better correlate the new chemistries and electronic configurations of Li surface with the stability of Li anode. Furthermore, if this prove to be an effective design, we could expand the scope of the study and move from atmospheric gases to other gases that could ultimately stabilize the surface of metallic lithium.

The second pathway to keep understanding lithium surface stability is to directly analyze the interface between lithium surface and an organic liquid electrolyte. For that, we need to move from the *in situ* study of solid gas interface to the one of solid liquid interface. Some recent attempts already prove the viability of ambient pressure X-ray photoelectron spectroscopy technique to reveal the interface between a lithium anode and a liquid electrolyte drop[222]. If we were able to further explore this interface while applying a voltage to the system, we then could study how the electrochemical double layer behaves in Li metal anode.

REFERENCES

[1] BP Energy Outlook: **2019** Edition.

[2] International Energy Outlook, U.S Energy Information Administration, EIA. https://www.iea.org/data-and-statistics (acceded November 2019)

[3] Climate central. https://www.climatecentral.org/gallery/graphics/national-graphs-of-global-temps-by-month (acceded November 2019)

[4] J. van Ruijven, B..; De Cian, E.; Sue Wing, I. Amplification of Future Energy Demand Growth Due to Climate Change. *Nat. Commun.* **2019**, *10*, 2762.

[5] B. J. van Ruijven, E. De Cian, I. Sue Wing, *Nat. Commun.* **2019**, *10*, 2762.

[6] G. Luderer, Z. Vrontisi, C. Bertram, O. Y. Edelenbosch, R. C. Pietzcker, J. Rogelj, H. S. De Boer, L. Drouet, J. Emmerling, O. Fricko, S. Fujimori, P. Havlík, G. Iyer, K. Keramidas, A. Kitous, M. Pehl, V. Krey, K. Riahi, B. Saveyn, M. Tavoni, D. P. Van Vuuren, E. Kriegler, *Nat. Clim. Chang.* **2018**, *8*, 626.

[7] Earth System research Laboratory. Global Monitoring Division. https://www.esrl.noaa.gov/gmd/ccgg/trends/global.html (acceded January 2020)

[8] BBC News. https://www.bbc.com/news/world-us-canada-50297029 (acceded November 2019)

[9] Ripple, W. J.; Wolf, C.; Newsome, T. M. World Scientists' Warning of a Climate Emergency. *Biosci.* **2019**, *70*(1), 8–12.

[10] European Commission. Going Climate-Neutral by 2050. **2018** https://ec.europa.eu/clima/sites/clima/files/long_term_strategy_brochure_en.pdf (acceded November 2019)

[11] Electric Vehivle Outlook 2019. Bloomberg NEF https://bnef.turtl.co/story/evo2019/ (acceded November 2019)

[12] Cano, Z. P.; Banham, D.; Ye, S.; Hintennach, A.; Lu, J.; Fowler, M.; Chen, Z. Batteries and Fuel Cells for Emerging Electric Vehicle Markets. *Nat. Energy* **2018**, *3* (4), 279–289.

[13] Yang, F.; Xie, Y.; Deng, Y.; Yuan, C. Predictive Modeling of Battery Degradation and Greenhouse Gas Emissions from U.S. State-Level Electric Vehicle Operation. *Nat. Commun.* **2018**, *9*, 2429.

[14] Lee, A.; Vörös, M.; Dose, W. M.; Niklas, J.; Poluektov, O.; Schaller, R. D.; Iddir, H.; Maroni, V. A.; Lee, E.; Ingram, B.; et al. Photo-Accelerated Fast Charging of Lithium-Ion Batteries. *Nat. Commun.* **2019**, *10*, 4946.

[15] Lin, D.; Liu, Y.; Cui, Y. Reviving the Lithium Metal Anode for High-Energy Batteries. *Nanotech.* **2017**, *12* (3), 194–206.

[16] Zhao, J.; Liao, L.; Shi, F.; Lei, T.; Chen, G.; Pei, A.; Sun, J.; Yan, K.; Zhou, G.; Xie, J.; et al. Surface Fluorination of Reactive Battery Anode Materials for Enhanced Stability. *J. Am. Chem. Soc.* **2017**, *139* (33), 11550–11558.

[17] Ramasubramanian, A.; Yurkiv, V.; Foroozan, T.; Ragone, M.; Shahbazian-Yassar, R.; Mashayek, F. Lithium Diffusion Mechanism through Solid-Electrolyte Interphase in Rechargeable Lithium Batteries. *J. Phys. Chem. C* **2019**, *123* (16), 10237–10245.

[18] Henschel, J.; Horsthemke, F.; Philipp, Y.; Evertz, M.; Wiemers-meyer, S.; Girod, S.; Lürenbaum, C.; Kristina, K.; Winter, M.; Nowak, S. Lithium Ion Battery Electrolyte Degradation of Field-Tested Electric Vehicle Battery Cells – A Comprehensive Analytical Study. *J. Power Sources* **2020**, *447*, 227370.

[19] Goodenough, J. B.; Park, K. S. The Li-ion Rechargeable Battery: A Perspective. *J. Am. Chem. Soc.* **2013**, *135* (4), 1167–1176.

[20] Battery University
https://batteryuniversity.com/Learn/Article/Types_of_lithium_ion
(acceded November 2019)

[21] Ohzuku, T.; Ueda, A. Solid-State Redox Reactions of $LiCoO_2$($R\bar{3}m$) for 4 Volt Secondary Lithium Cells. *J. Electrochem. Soc.* **1994**, *141* (11), 2972–2977.

[22] Kim, T.; Song, W.; Son, D. Y.; Ono, L. K.; Qi, Y. Lithium-Ion Batteries: Outlook on Present, Future, and Hybridized Technologies. *J. Mater. Chem. A* **2019**, *7* (7), 2942–2964.

[23] Reed, J.; Ceder, G.; Van Der Ven, A. Layered-to-Spinel Phase Transition in Li_xMnO_2. *Electrochem. Solid-State Lett.* **2001**, *4* (6), 78–81.

[24] Nitta, N.; Wu, F.; Lee, J. T.; Yushin, G. Li-ion Battery Materials: Present and Future. *Mater. Today* **2015**, *18* (5), 252–264.

[25] Heiskanen, S. K.; Kim, J.; Lucht, B. L. Generation and Evolution of the Solid Electrolyte Interphase of Lithium-Ion Batteries. *Joule* **2019**, *3* (10), 2322–2333.

[26] A. Hammami, N. Raymond, M. A. Runaway Risk of Forming Toxic Compounds. *Nature* **2003**, *424*, 635–636.

[27] Suo, L.; Borodin, O.; Gao, T.; Olguin, M.; Ho, J.; Fan, X.; Luo, C.; Wang, C.; Xu, K. "Water-in-Salt" Electrolyte Enables High-Voltage Aqueous Lithium-Ion Chemistries. *ChemInform* **2016**, *350* (6263), 938–943.

[28] Manthiram, A.; Yu, X.; Wang, S. Lithium Battery Chemistries Enabled by Solid-State Electrolytes. *Nat. Rev. Mater.* **2017**, *2* (4), 1–16.

[29] Chen, C. H.; Xie, S.; Sperling, E.; Yang, A. S.; Henriksen, G.; Amine, K. Stable Lithium-ion Conducting Perovskite Lithium-Strontium-Tantalum-Zirconium-Oxide System. *Solid State Ionics* **2004**, *167*, 263–272.

[30] Janek, J.; Zeier, W. G. A Solid Future for Battery Development. *Nat. Energy* **2016**, *1*, 16141.

[31] Bonizzoni, S.; Ferrara, C.; Berbenni, V.; Anselmi-Tamburini, U.; Mustarelli, P.; Tealdi, C. NASICON-Type Polymer-in-Ceramic Composite Electrolytes for Lithium Batteries. *Phys. Chem. Chem. Phys.* **2019**, *21* (11), 6142–6149.

[32] Zheng, F.; Kotobuki, M.; Song, S.; Lai, M. O.; Lu, L. Review on Solid Electrolytes for All-Solid-State Lithium-Ion Batteries. *J. Power Sources* **2018**, *389*, 198–213.

[33] Liu, X.; Li, X.; Li, H.; Wu, H. Bin. Recent Progress of Hybrid Solid-State Electrolytes for Lithium Batteries. *Chem. Eur. J.* **2018**, *24* (69), 18293–18306.

[34] Lewandowski, A.; Świderska-Mocek, A. Ionic Liquids as Electrolytes for Li-ion Batteries-An Overview of Electrochemical Studies. *J. Power Sources* **2009**, *194* (2), 601–609.

[35] Kalhoff, J.; Eshetu, G. G.; Bresser, D.; Passerini, S. Safer Electrolytes for Lithium-Ion Batteries: State of the Art and Perspectives. *ChemSusChem* **2015**, *8* (13), 2154–2175.

[36] Bauman, H.G.; Chilton, J.E.; Cook, G. . New Cathode-Anode Couples Using Nonaqueous Electrolyte. *Lockheed Missiles Sp. Co., Inc. Palo Alto, CA, USA,* **1963**.

[37] Dunning, J. S.; Tiedemann, W. H.; Hsueh, L.; Bennion, D. N. A Secondary,

Nonaqueous Solvent Battery. *J. Electrochem. Soc.* **1971**, *118* (12), 1886–1890.

[38] Winter, M.; Barnett, B.; Xu, K. Before Li Ion Batteries. *Chem. Rev.* **2018**, *118* (23), 11433–11456.

[39] Winter, M.; Moeller, K. -C.; Besenhard, J. O. Carbonaceous and Graphitic Anodes. Carbonaceous and Graphitic Anodes. *I*n: Nazri GA., Pistoia G. (eds) Lithium Batteries. Springer, Boston, MA, **2009**.

[40] Roselin, L. S.; Juang, R. S.; Hsieh, C. Te; Sagadevan, S.; Umar, A.; Selvin, R.; Hegazy, H. H. Recent Advances and Perspectives of Carbon-Based Nanostructures as Anode Materials for Li-ion Batteries. *Materials* **2019**, *12*, 1229.

[41] Hamidah, N. L.; Wang, F. M.; Nugroho, G. The Understanding of Solid Electrolyte Interface (SEI) Formation and Mechanism as the Effect of Flouro-o-Phenylenedimaleimaide (F-MI) Additive on Lithium-Ion Battery. *Surf. Interface Anal.* **2019**, *51* (3), 345–352.

[42] Peled, E.; Menkin, S. Review - SEI: Past, Present and Future. *J. Electrochem. Soc.* **2017**, *164* (7), A1703–A1719.

[43] Verma, P.; Maire, P.; Novák, P. A Review of the Features and Analyses of the Solid Electrolyte Interphase in Li-ion Batteries. *Electrochim. Acta* **2010**, *55* (22), 6332–6341.

[44] Peled, E.; Ardel, G. Advanced Model for Solid Electrolyte Interphase Electrodes in Liquid and Polymer Electrolytes. *J. Electrochem. Soc.* **1997**, *144* (8), 208–210.

[45] Edström, K.; Herstedt, M.; Abraham, D. P. A New Look at the Solid Electrolyte Interphase on Graphite Anodes in Li-ion Batteries. *J. Power Sources* **2006**, *153* (2), 380–384.

[46] Hou, Z.; Zhang, J.; Wang, W.; Chen, Q.; Li, B.; Li, C. Towards High-Performance Lithium Metal Anodes via the Modification of Solid Electrolyte Interphases. *J. Energy Chem.* **2019**, *45*, 7–17.

[47] Cheng, X.-B.; Zhang, R.; Zhao, C.-Z.; Wei, F.; Zhang, J.-G.; Zhang, Q. A Review of Solid Electrolyte Interphases on Lithium Metal Anode. *Adv. Sci.* **2016**, *3*, 1500213.

[48] Manthiram, A.; Fu, Y.; Chung, S.; Zu, C.; Su, Y. Rechargeable Lithium − Sulfur Batteries. *Chem. Rev.* **2014**, *114*, 11751–11787.

[49] Yan, B.; Li, X.; Bai, Z.; Song, X.; Xiong, D.; Zhao, M.; Li, D.; Lu, S. A Review of Atomic Layer Deposition Providing High Performance Lithium Sulfur Batteries. *J. Power Sources* **2017**, *338*, 34–48.

[50] Li, X.; Banis, M.; Lushington, A.; Yang, X.; Sun, Q.; Zhao, Y.; Liu, C.; Li, Q.; Wang, B.; Xiao, W.; et al. A High-Energy Sulfur Cathode in Carbonate Electrolyte by Eliminating Polysulfides via Solid-Phase Lithium-Sulfur Transformation. *Nat. Commun.* **2018**, *9*, 4509.

[51] Qi, W.; Jiang, W.; Xu, F.; Jia, J.; Yang, C.; Cao, B. Improving Confinement and Redox Kinetics of Polysufides through Hollow NC@CeO2 Nanospheres for High-Performance Lithium-Sulfur Batteries. *Chem. Eng. J.* **2020**, *382*, 122852.

[52] Drone Universities. https://www.droneuniversities.com/Drones/the-Zephyr-High-Altitude-Pseudo-Satellite-Haps-Aircraft-Gets-Lithium-Sulfur-Li-s-Batteries/ (acceded November 2019)

[53] Zhu, W.; Zhang, Z.; Wei, J.; Jing, Y.; Guo, W.; Xie, Z.; Qu, D.; Liu, D.; Tang, H.; Li, J. A Synergistic Modification of Polypropylene Separator toward Stable Lithium–Sulfur Battery. *J. Memb. Sci.* **2019**, 117646.

[54] Nasybulin, E.; Xu, W.; Engelhard, M. H.; Nie, Z.; Li, X. S.; Zhang, J. G. Stability of Polymer Binders in Li-O_2 Batteries. *J. Power Sources* **2013**, *243*, 899–907.

[55] Mahne, N.; Schafzahl, B.; Leypold, C.; Leypold, M.; Grumm, S.; Leitgeb, A.; Strohmeier, G. A.; Wilkening, M.; Fontaine, O.; Kramer, D.; et al. Singlet Oxygen Generation as a Major Cause for Parasitic Reactions during Cycling of Aprotic Lithium-Oxygen Batteries. *Nat. Energy* **2017**, *2* (5), 1–9.

[56] Wang, Y.; Lu, Y. C. Isotopic Labeling Reveals Active Reaction Interfaces for Electrochemical Oxidation of Lithium Peroxide. *Angew. Chemie - Int. Ed.* **2019**, *58* (21), 6962–6966.

[57] Aurbach, D.; McCloskey, B. D.; Nazar, L. F.; Bruce, P. G. Advances in Understanding Mechanisms Underpinning Lithium-Air Batteries. *Nat. Energy* **2016**, *1*, 16128.

[58] Wang, C.; Xie, Z.; Zhou, Z. Lithium-Air Batteries: Challenges Coexist with Opportunities. *APL Mater.* **2019**, *7*, 040701.

[59] Asadi, M.; Sayahpour, B.; Abbasi, P.; Ngo, A. T.; Karis, K.; Jokisaari, J. R.; Liu, C.; Narayanan, B.; Gerard, M.; Yasaei, P.; et al. A Lithium-Oxygen Battery with a Long Cycle Life in an Air-like Atmosphere. *Nature* **2018**, *555* (7697), 502–506.

[60] Xu, W.; Wang, J.; Ding, F.; Chen, X.; Nasybulin, E.; Zhang, Y.; Zhang, J. G. Lithium Metal Anodes for Rechargeable Batteries. *Energy Environ. Sci.* **2014**, *7* (2), 513–537.

[61] Xu, K. Nonaqueous Liquid Electrolytes for Lithium-Based Rechargeable Batteries. *Chem. Rev.* **2004**, *104* (10), 4303–4417.

[62] Aurbach, D. Review of Selected Electrode-Solution Interactions which Determine the Performance of Li and Li Ion Batteries. *J. Power Sources* **2000**, *89* (2), 206–218.

[63] Liu, M.; Cheng, Z.; Qian, K.; Verhallen, T.; Wang, C.; Wagemaker, M. Efficient Li-Metal Plating/Stripping in Carbonate Electrolytes Using a $LiNO_3$-Gel Polymer Electrolyte, Monitored by Operando Neutron Depth Profiling. *Chem. Mater.* **2019**, *31* (12), 4564–4574.

[64] Wang, M. J.; Choudhury, R.; Sakamoto, J. Characterizing the Li-Solid-Electrolyte Interface Dynamics as a Function of Stack Pressure and Current Density. *Joule* **2019**, *3* (9), 2165–2178.

[65] Bertolini, S.; Balbuena, P. B. Buildup of the Solid Electrolyte Interphase on Lithium-Metal Anodes: Reactive Molecular Dynamics Study. *J. Phys. Chem. C* **2018**, *122* (20), 10783–10791.

[66] Chazalviel, J. N. Electrochemical Aspects of the Generation of Ramified Metallic Electrodeposits. *Phys. Rev. A* **1990**, *42* (12), 7355–7367.

[67] Ding, F.; Xu, W.; Gra, G. L.; Zhang, J.; Sushko, M. L.; Chen, X.; Shao, Y.; Engelhard, M. H.; Nie, Z.; Xiao, J.; et al. Dendrite-Free Lithium Deposition via Self-Healing Electrostatic Shield Mechanism. *J. Am. Chem. Soc.* **2013**, *468*, 4450−4456.

[68] Tarascon, J.-M.; Armand, M. Issues and Challenges Facing Rechargeable Lithium Batteries. *Nature* **2001**, *414* (1), 359–367.

[69] Chen, K.-H.; Wood, K. N.; Kazyak, E.; LePage, W. S.; Davis, A. L.; Sanchez, A. J.; Dasgupta, N. P. Dead Lithium: Mass Transport Effects on Voltage, Capacity, and Failure of Lithium Metal Anodes. *J. Mater. Chem. A* **2017**, *5* (23), 11671–11681.

[70] Fang, C.; Wang, X.; Meng, Y. S. Key Issues Hindering a Practical Lithium-Metal Anode. *Trends Chem.* **2019**, *1* (2), 152–158.

[71] Fang, C.; Li, J.; Zhang, M.; Zhang, Y.; Yang, F.; Lee, J. Z.; Lee, M.-H.; Alvarado, J.; Schroeder, M. A.; Yang, Y.; et al. Quantifying Inactive Lithium in Lithium Metal Batteries. *Nature* **2019**, *572* (7770), 511–515.

[72] Yang, Y.; Davies, D. M.; Yin, Y.; Borodin, O.; Lee, J. Z.; Fang, C.; Olguin, M.; Zhang, Y.; Sablina, E. S.; Wang, X.; et al. High-Efficiency Lithium-Metal Anode Enabled by Liquefied Gas Electrolytes. *Joule* **2019**, *3* (8), 2050–2052.

[73] Albertus, P.; Babinec, S.; Litzelman, S.; Newman, A. Status and Challenges in Enabling the Lithium Metal Electrode for High-Energy and Low-Cost Rechargeable Batteries. *Nat. Energy* **2017**, *3*, 16–21.

[74] Xu, R.; Cheng, X.-B.; Yan, C.; Zhang, X.-Q.; Xiao, Y.; Zhao, C.-Z.; Huang, J.-Q.; Zhang, Q. Artificial Interphases for Highly Stable Lithium Metal Anode. *Matter* **2019**, *1* (2), 317–344.

[75] Tan, S.-J.; Zeng, X.-X.; Ma, Q.; Wu, X.-W.; Guo, Y.-G. Recent Advancements in Polymer-Based Composite Electrolytes for Rechargeable Lithium Batteries. *Electrochem. Energy Rev.* **2018**, *1* (2), 113–138.

[76] Xie, D., Chen, S., Zhang, Z., Ren, J., Yao, L., Wu, L., Yao, X., and Xu, X. High Ion Conductive Sb_2O_5-Doped β-Li_3PS_4 with Excellent Stability against Li for All-Solid-State Lithium Batteries. *J. Power Sources* **2018**, *389*, 140–147.

[77] Zhang, X. Q.; Cheng, X. B.; Zhang, Q. Advances in Interfaces between Li Metal Anode and Electrolyte. *Adv. Mater. Interfaces* **2018**, *5* (2), 1–19.

[78] Liu, F.; Xiao, Q.; Wu, H. Bin; Shen, L.; Xu, D.; Cai, M.; Lu, Y. Fabrication of Hybrid Silicate Coatings by a Simple Vapor Deposition Method for Lithium Metal Anodes. *Adv. Energy Mater.* **2018**, *8* (6), 1701744.

[79] Zhou, W.; Wang, S.; Li, Y.; Xin, S.; Manthiram, A.; Goodenough, J. B. Plating a Dendrite-Free Lithium Anode with a Polymer/Ceramic/Polymer Sandwich Electrolyte. *J. Am. Chem. Soc.* **2016**, *138* (30), 9385–9388.

[80] Han, X.; Gong, Y.; Fu, K. (Kelvin); He, X.; Hitz, G. T.; Dai, J.; Pearse, A.; Liu, B.; Wang, H.; Rubloff, G.; et al. Negating Interfacial Impedance in Garnet-Based Solid-State Li Metal Batteries. *Nat. Mater.* **2016**, *16*, 572–579.

[81] He, M.; Cui, Z.; Chen, C.; Li, Y.; Guo, X. Formation of Self-Limited, Stable and Conductive Interfaces between Garnet Electrolytes and Lithium Anodes for Reversible Lithium Cycling in Solid-State Batteries. *J. Mater. Chem. A* **2018**, *6* (24), 11463–11470.

[82] Fu, K. K.; Gong, Y.; Liu, B.; Zhu, Y.; Xu, S.; Yao, Y.; Luo, W.; Wang, C.; Lacey, S. D.; Dai, J.; et al. Toward Garnet Electrolyte–Based Li Metal Batteries: An Ultrathin, Highly Effective, Artificial Solid-State Electrolyte/Metallic Li Interface. *Sci. Adv.* **2017**, *3* (4), 1–12.

[83] Lu, Y.; Huang, X.; Song, Z.; Rui, K.; Wang, Q.; Gu, S.; Yang, J.; Xiu, T.; Badding,

M. E.; Wen, Z. Highly Stable Garnet Solid Electrolyte Based Li-S Battery with Modified Anodic and Cathodic Interfaces. *Energy Storage Mater.* **2018**, *15*, 282–290.

[84] Statista. Distribution of lithium consumption worldwide in 2018 by end use https://www.statista.com/statistics/658332/lithium-uses-worldwide/ (acceded November 2019)

[85] Kavanagh, L.; Keohane, J.; Cabellos, G. G.; Lloyd, A.; Cleary, J. Global Lithium Sources-Industrial Use and Future in the Electric Vehicle Industry: A Review. *Resources* **2018**, *7* (57).

[86] Martin, G.; Rentsch, L.; Höck, M.; Bertau, M. Lithium Market Research - Global Supply, Future Demand and Price Development. *Energy Storage Mater.* **2017**, *6*, 171–179.

[87] Ober, J. A. Mineral Commodity Summaries. *S Geol. Surv. Reston, VA, USA,* **2018**.

[88] Reuters Graphics https://graphics.reuters.com/ELECTRIC-VEHICLES-METALS/010092JB38P/ (acceded November 2019)

[89] Department of Industry Innovation and Science. Resources and Energy Quarterly. Australian government, **2019** https://publications.industry.gov.au/publications/resourcesandenergyquarterlydecember2019/index.html (acceded November 2019)

[90] https://www.motorpasion.com/industria/mina-litio-caceres-podria-abastacer-a-10-millones-coches-electricos-al-ano-sale-adelante (acceded November 2019)

[91] Swain, B. Recovery and Recycling of Lithium: A Review. *Sep. Purif. Technol.* **2017**, *172*, 388–403.

[92] Sverdrup, H. U. Modelling Global Extraction, Supply, Price and Depletion of the Extractable Geological Resources with the LITHIUM Model. *Resour. Conserv. Recycl.* **2016**, *114*, 112–129.

[93] Capellán-Pérez, I.; de Castro, C.; Miguel González, L. J. Dynamic Energy Return on Energy Investment (EROI) and Material Requirements in Scenarios of Global Transition to Renewable Energies. *Energy Strateg. Rev.* **2019**, *26* (September 2018), 100399.

[94] Tarascon, J.-M. Is Lithium the New Gold? *Nat. Chem.* **2010**, *2* (6), 510.

[95] Swiss Resource Capital AG. Lithium Report 2018

https://libertyonelithium.com/pdf/Swiss%20Resource%20Capital%202018%20Lithium%20Report.pdf (acceded November 2019)

[96] Safarian, J.; Engh, T. A. Vacuum Evaporation of Pure Metals. *Metall. Mater. Trans. A Phys. Metall. Mater. Sci.* **2013**, *44A*, 747–753.

[97] Alvatec. Alvasources, Manual. **2015**

[98] Jablonski, A. Evaluation of Procedures for Overlayer Thickness Determination from XPS Intensities. *Surf. Sci.* **2019**, *688*, 14–24.

[99] M.P.Seah; W.A.Dench. Quantitative Electron Spectroscopy of Surface. *Surf. Interface Anal.* **1979**, *1* (1), 2–11.

[100] Tanuma, S.; Powell, C. J.; Penn, D. R. Calculation of Electron Inelastic Mean Free Paths. *Surf. Interf. Anal.* **1993**, *21*, 165–176.

[101] Shinotsuka, H.; Tanuma, S.; Powell, C. J.; Penn, D. R. Calculations of Electron Inelastic Mean Free Paths. X. Data for 41 Elemental Solids over the 50 EV to 200 KeV Range with the Relativistic Full Penn Algorithm. *Surf. Interf. Anal.* **2015**, *47*, 873–888.

[102] Cumpson, P. J.; Seah, M. P. Elastic Scattering Corrections in AES and XPS. II. Estimating Attenuation Lengths and Conditions Required for Their Valid Use in Overlayer/Substrate Experiments. *Surf. Interface Anal.* **1997**, *25* (6), 430–446.

[103] Smekal, W.: Werner, W.; Powell, C. J. Simulation of electron spectra for surface analysis (SESSA): a novel software tool for quantitative Auger-electron spectroscopy and X-ray photoelectron spectroscopy. *Surf. Interface Anal.* **2005**, *37*, 1059–1067.

[104] Maibach, J.; Xu, C.; Eriksson, S. K.; Åhlund, J.; Gustafsson, T.; Siegbahn, H.; Rensmo, H.; Edström, K.; Hahlin, M. A High Pressure X-Ray Photoelectron Spectroscopy Experimental Method for Characterization of Solid-Liquid Interfaces Demonstrated with a Li-ion Battery System. *Rev. Sci. Instrum.* **2015**, *86* (4).

[105] Bluhm, H.; Hävecker, M.; Knop-gericke, A.; Kiskinova, M.; Schlögl, R.; Salmeron, M. In Situ X-Ray Photoelectron Studies of Gas – Solid Interfaces at Near- Ambient Conditions. *MRS Bull.*, **2007**, *32*, 1022–1030.

[106] Favaro, M.; Jeong, B.; Ross, P. N.; Yano, J.; Hussain, Z.; Liu, Z.; Crumlin, E. J.; Zaera, F.; Devanathan, M. A. V.; Tilak, B. V. K.; et al. Unravelling the Electrochemical Double Layer by Direct Probing of the Solid/Liquid Interface., *Nat. Commun.* **2016**, *7*, 12695.

[107] Wu, S. C.; Xiao, T. Q.; Withers, P. J. The Imaging of Failure in Structural Materials by Synchrotron Radiation X-Ray Microtomography. *Eng. Fract. Mech.* **2017**, *182*, 127–156.

[108] Akhtar, K.; Khan, S. A.; Khan, S. B.; Asiri, A. M. Scanning Electron Microscopy: Principle and Applications in Nanomaterials Characterization. *Springer International Publishing AG, part of Springer Nature* **2018**, Chapter 4.

[109] Lee, H.; Lee, D. J.; Kim, Y.-J.; Park, J.-K.; Kim, H.-T. A Simple Composite Protective Layer Coating That Enhances the Cycling Stability of Lithium Metal Batteries. *J. Power Sources* **2015**, *284*, 103–108.

[110] Guntz, M. Sur Une Expérience Simple Montrant La Présence de l'argon Dans l'azote Atmosphérique. *Compt Rend.* **1895**, *120*, 777.

[111] Open Source Systems, Science, Solutions. Atmospheric Composition http://ossfoundation.us/projects/environment/global-warming/atmospheric-composition (acceded August 2019)

[112] North Carolina Climate Office. Composition of the Atmosphere https://climate.ncsu.edu/edu/Composition (acceded August 2019)

[113] Clausing, R. E.; Easton, D. S.; Powell, G. L. Auger Spectra of Lithium Metal and Lithium Oxide. *Surf. Sci.* **1973**, *36* (1), 377–379.

[114] Madden, H. H. KVV Auger Spectrum of Oxidized Lithium. *J. Vac. Sci. Technol.* **1977**, *14* (1), 412.

[115] David, D. J.; Froning, M. H.; Wittberg, T. N.; Moddeman, W. E. Surface Reactions of Lithium with the Environment. *Appl. Surf. Sci.* **1981**, *7* (3), 185–195.

[116] Nebesny, K. W.; Zavadil, K.; Burrow, B.; Armstrong, N. R. Reactions of Clean Lithium Surfaces with SO_2, O_2 and H_2O; Auger Lineshape Analysis and X-Ray Photoelectron Spectroscopic Analysis of the Initial Product Layers. *Surf. Sci.* **1985**, *162* (1–3), 292–297.

[117] Parker, S. D.; Rhead, G. . Oxidation of Lithium Monolayers on Silver (111). A Study by AES, Work Function and Secondary Emission Changes. *Surf. Sci.* **1986**, *167*, 271–284.

[118] Shek, M. L.; Hrbek, J.; Sham, T. K.; Xu, G.-Q. A Soft X-Ray Study of the Interaction of Oxygen with Li. *Surf. Sci.* **1990**, *234*, 324–334.

[119] Schily, U.; Heitbaum, J. Reaction of Clean Lithium with O_2, SO_2 and Liquid $LiAlCl_4 \cdot 3(SO_2)$, an XPS and Auger Analysis. *Vacuum* **1990**, *41* (7–9), 1736–1738.

[120] Schily, U.; Heitbaum, J. Surface Analysis of Freshly Cut Li Samples: Na-Segregation and Film Forming Reaction by O_2, SO_2, and Liquid LiAlCl4· 3(SO_2). *Electrochim. Acta* **1992**, *37* (4), 731–738.

[121] Wang, K.; Ross Jr., P. N.; Kong, F.; McLarnon, F. The Reaction of Clean Li Surfaces with Small Molecules in Ultrahigh Vacuum. I. Dixoygen. *J. Electrochem. Soc.* **1996**, *143* (2), 422–428.

[122] Wulfsberg, S. M.; Koel, B. E.; Bernasek, S. L. The Low Temperature Oxidation of Lithium Thin Films on HOPG by O_2 and H_2O. *Surf. Sci.* **2016**, *652*, 222–229.

[123] Mclean, W.; Schultz, J. A.; Pedersen, L. G.; Jarnagin, R. . Surface Complexes between O_2, H_2O and Lithium. *Surf. Sci.* **1979**, *83*, 354–366.

[124] Qiu, S. L.; Lin, C. L.; Chen, J.; Strongin, M. Photoemission Studies of the Interaction of Li and Solid Molecular Oxygen. *Phys. Rev. B* **1989**, *39* (9), 6194.

[125] Greber, T.; Freihube, K.; Grobecker, R.; Böttcher, A.; Hermann, K.; Ertl, G.; Fick, D. Nonadiabatic Processes during the Oxidation of Li Layers. *Phys. Rev. B* **1994**, *50* (12), 8755–8762.

[126] Hermann, K.; Freihube, K.; Greber, T.; Bröttcher, A.; Grobecker, R.; Fick, D.; Ertl, G. Dynamics of the Interaction of O_2 with Li Surfaces. **1994**, *313*, L806–L810.

[127] Ensling, D.; Thissen, A.; Jaegermann, W. On the Formation of Lithium Oxides and Carbonates on Li Metal Electrodes in Comparison to $LiCoO_2$ Surface Phases Investigated by Photoelectron Spectroscopy. *Appl. Surf. Sci.* **2008**, *255*, 2517–2523.

[128] Kafafi, Z. H.; Hauge, R. H.; Billups, W. E.; Margrave, J. L. Carbon Dioxide Activation by Lithium Metal. 1. Infrared Spectra of Lithium Carbon Dioxide ($Li^+CO_2^-$), Lithium Oxalate ($Li^+C_2O_4^-$), and Lithium Carbon Dioxide ($Li_2^{2+}CO_2^{2-}$) in Inert-Gas Matrices. *J. Am. Chem. Soc.* **1983**, *105* (12), 3886–3893.

[129] Shao, Y.; Paul, J.; Axelsson, O.; Hoffmann, F. M. Identification of Intermediate States Following CO_2 Adsorption on Alkali-Metal Surfaces. *J. Phys. Chem.* **1993**, *97* (29), 7652–7659.

[130] Zavadil, K. R.; N.R., A. Surface Chemistries of Lithium: Detailed

Characterization of the Reactions with O_2 and H_2O Using XPS, EELS, and Microgravimetry. *Surf. Sci.* **1990**, *230*, 47–60.

[131] Hoenigman, J. R.; Keil, R. G. An XPS Study of the Adsorption of Oxygen and Water Vapor on Clean Lithium Films. *Appl. Surf. Sci.* **1984**, *18* (1–2), 207–222.

[132] Fujieda, T.; Yamamoto, N.; Saito, K.; Ishibahsi, T.; Honjo, M.; Koike, S.; Wakabayashi, N.; Higuchi, S. Surface of Lithium Electrodes Prepared in Ar+CO_2 Gas. *J. Power Sources* **1994**, *52* (2), 197–200.

[133] Zhuang, G.; Chen, Y.; Ross, P. N. The Reaction of Lithium with Carbon Dioxide Studied by Photoelectron Spectroscopy. *Surf. Sci.* **1998**, *418*, 139–149.

[134] Momma, T.; Nara, H.; Yamagami, S.; Tatsumi, C.; Osaka, T. Effect of the Atmosphere on Chemical Composition and Electrochemical Properties of Solid Electrolyte Interface on Electrodeposited Li Metal. *J. Power Sources* **2011**, *196* (15), 6483–6487.

[135] Ishiyama, S.; Baba, Y.; Fujii, R.; Nakamura, M.; Imahori, Y. Thermal Stability of BNCT Neutron Production Target Synthesized by In-Situ Lithium Deposition and Ion Implantation. *Phot. Fact. Act. Rep.* **2013**, *30*, 27A/2012G175.

[136] Ishiyama, S.; Baba, Y.; Fujii, R.; Nakamura, M.; Imahori, Y. Low Temperature and Pressure Synthesis of Lithium - Nitride Compound with H_2O Addition on Lithium Target for BNCT. *Mater. Trans.* **2013**, *54* (12), 2233–2237.

[137] Ishitama, S.; Baba, Y.; Fujii, R.; Nakamura, M. Lithium Nitride Synthesized by In-Situ Lithium Deposition and Ion Implantation for Boron Neutron Capture Therapy. *JPS Conf. Proc.* **2014**, *012035*, 1–4.

[138] Wood, K. N.; Teeter, G. XPS on Li Battery Related Compounds: Analysis of Inorganic SEI Phases and a Methodology for Charge Correction. *ACS Appl. Energy Mater.* **2018**, *1*, 4493–4504.

[139] Wu, M.; Wen, Z.; Liu, Y.; Wang, X.; Huang, L. Electrochemical Behaviors of a Li_3N Modified Li Metal Electrode in Secondary Lithium Batteries. *J. Power Sources* **2011**, *196* (19), 8091–8097.

[140] Koch, S. L.; Morgan, B. J.; Passerini, S.; Teobaldi, G. Density Functional Theory Screening of Gas-Treatment Strategies for Stabilization of High Energy-Density Lithium Metal Anodes. *J. Power Sources* **2015**, *296*, 150–161.

[141] Li, Y.; Li, Y.; Sun, Y.; Butz, B.; Yan, K.; Koh, A. L.; Zhao, J.; Pei, A.; Cui, Y. Revealing Nanoscale Passivation and Corrosion Mechanisms of Reactive Battery Materials in Gas Environments. *Nano Lett.* **2017**, *17* (8), 5171–5178.

[142] Guillaume, C. L.; Gregoryanz, E.; Degtyareva, O.; McMahon, M. I.; Hanfland, M.; Evans, S.; Guthrie, M.; Sinogeikin, S. V.; Mao, H.-K. Cold Melting and Solid Structures of Dense Lithium. *Nat. Phys.* **2011**, *7* (3), 211–214.

[143] Zhu, Y.; He, X.; Mo, Y. Strategies Based on Nitride Materials Chemistry to Stabilize Li Metal Anode. *Adv. Sci.* **2017**, 1600517.

[144] Ma, G.; Wen, Z.; Wu, M.; Shen, C.; Wang, Q.; Jin, J.; Wu, X. A Lithium Anode Protection Guided Highly-Stable Lithium-Sulfur Battery. *Chem. Commun.* **2014**, *50* (91), 14209–14212.

[145] Zhang, Y. J.; Wang, W.; Tang, H.; Bai, W. Q.; Ge, X.; Wang, X. L.; Gu, C. D.; Tu, J. P. An Ex-Situ Nitridation Route to Synthesize Li_3N-Modified Li Anodes for Lithium Secondary Batteries. *J. Power Sources* **2015**, *277*, 304–311.

[146] Li, Y.; Sun, Y.; Pei, A.; Chen, K.; Vailionis, A.; Li, Y.; Zheng, G.; Sun, J.; Cui, Y. Robust Pinhole-Free Li_3N Solid Electrolyte Grown from Molten Lithium. *ACS Cent. Sci.* **2018**, *4* (1), 97–104.

[147] Gao, J.; Shi, S.-Q.; Li, H. Brief Overview of Electrochemical Potential in Lithium Ion Batteries. *Chinese Phys. B* **2016**, *25* (1), 018210.

[148] Gerischer, H.; Ekardt, W. Fermi Levels in Electrolytes and the Absolute Scale of Redox Potentials. *Appl. Phys. Lett.* **1983**, *43* (4), 393–395.

[149] Kittel, C.; Kromer, H. Thermal Physics. *W. H. Free. Second Ed.* **1980**.

[150] Trasatti, S. The Absolute Electrode Potential: An Explanatory Note. *J. Electroanal. Chem.,* **1986**, *209*, 417–428.

[151] http://www.casaxps.com/help_manual/line_shapes.htm

(acceded August 2019)

[152] Oswald, S.; Thoss, F.; Zier, M.; Hoffmann, M.; Jaumann, T.; Herklotz, M.; Nikolowski, K.; Scheiba, F.; Kohl, M.; Giebeler, L.; et al. Binding Energy Referencing for XPS in Alkali Metal-Based Battery Materials Research (II): Application to Complex Composite Electrodes. *Batteries* **2018**, *4* (3), 36.

[153] Rendek, L. J.; Chottiner, G. S.; Scherson, D. a. Reactivity of Linear Alkyl Carbonates toward Metallic Lithium: Infrared Reflection−Absorption Spectroscopic Studies in Ultrahigh Vacuum. *Langmuir* **2002**, *18* (17), 6554–

6558.

[154] Kowalczyk, S. P.; Ley, L.; McFeely, F. R.; Pollak, R. A.; Shirley, D. A. X-Ray Photoemission from Sodium and Lithium. *Phys. Rev. B* **1973**, *8* (8), 3583–3585.

[155] Michaelson, H. B. The Work Function of the Elements and Its Periodicity. *J. Appl. Phys.* **1977**, *48* (11), 4729–4733.

[156] Mattheiss, L. F.; Hamann, D. R. Bulk and Surface Electronic Structure of Li_2O. *Phys. Rev. B* **1984**, *30* (4), 1731–1738.

[157] Reuter, K.; Scheffler, M. Composition, Structure, and Stability of RuO_2(110) as a Function of Oxygen Pressure. *Phys. Rev. B - Condens. Matter Mater. Phys.* **2002**, *65* (3).

[158] Böttcher, A.; Grobecker, R.; Greber, T.; Morgante, A.; Ertl, G. Exoelectron Emission during the Oxidation of Na Films. *Surf. Sci.* **1993**, *280* (1–2), 170–178.

[159] Greczynski, G.; Hultman, L. C 1s Peak of Adventitious Carbon Aligns to the Vacuum Level: Dire Consequences for Material's Bonding Assignment by Photoelectron Spectroscopy. *ChemPhysChem* **2017**, *18* (12), 1507–1512.

[160] Taifan, W.; Boily, J. F.; Baltrusaitis, J. Surface Chemistry of Carbon Dioxide Revisited. *Surf. Sci. Rep.* **2016**, *71* (4), 595–671.

[161] Uncertainty Estimates in XPS. Limit of Detection. http://www.casaxps.com/help_manual/casaxps2316_manual/error_estimates_in_casaxps.pdf (acceded August 2019)

[162] Sharma, J.; Gora, T.; Rimstidt, J. D.; Staley, R. X-Ray Photoelectron Spectra of the Alkali Azides. *Chem. physiscs Lett.* **1972**, *15* (2), 232–235.

[163] Aduru, S.; Contarini, S.; Rabalais, J. W. Electron-, X-Ray-, and Ion-Stimulated Decomposition of Nitrate Salts. *J. Phys. Chem.* **1986**, *90*, 1683–1688.

[164] Kumar, S. N.; Bouyssoux, G.; Gaillard, F. Electronic and Structural Characterization of Electrochemically Synthesized Conducting Polyaniline from XPS Studies. *Surf. Interface Anal.* **1990**, *15*, 531–536.

[165] Yue, J.; Epstein, A. J. XPS Study of Self-Doped Conducting Polyaniline and Parent Systems. *Macromolecules* **1991**, *24* (15), 4441–4445.

[166] López-Salas, N.; Gutiérrez, M. C.; Ania, C. O.; Muñoz-Márquez, M. A.; Luisa Ferrer, M.; Monte, F. Del. Nitrogen-Doped Carbons Prepared from Eutectic Mixtures as Metal-Free Oxygen Reduction Catalysts. *J. Mater. Chem. A*

2016, *4* (2), 478–488.

[167] Liu, D. G.; Tu, J. P.; Zhang, H.; Chen, R.; Gu, C. D. Microstructure and Mechanical Properties of Carbon Nitride Multilayer Films Deposited by DC Magnetron Sputtering. *Surf. Coatings Technol.* **2011**, *205* (8–9), 3080–3086.

[168] He, Y.; Ren, X.; Xu, Y.; Engelhard, M. H.; Li, X.; Xiao, J.; Liu, J.; Zhang, J. G.; Xu, W.; Wang, C. Origin of Lithium Whisker Formation and Growth under Stress. *Nat. Nanotechnol.* **2019**, *14*, 1042–1047.

[169] Yu, Y.; Mao, B.; Geller, A.; Chang, R.; Gaskell, K.; Liu, Z.; Eichhorn, B. W. CO_2 Activation and Carbonate Intermediates: An Operando AP-XPS Study of CO_2 Electrolysis Reactions on Solid Oxide Electrochemical Cells. *Phys. Chem. Chem. Phys.* **2014**, *16* (23), 11633–11639.

[170] Favaro, M.; Valero-Vidal, C.; Eichhorn, J.; Toma, F. M.; Ross, P. N.; Yano, J.; Liu, Z.; Crumlin, E. J. Elucidating the Alkaline Oxygen Evolution Reaction Mechanism on Platinum. *J. Mater. Chem. A* **2017**, *5* (23), 11634–11643.

[171] Stoerzinger, K. A.; Hong, W. T.; Crumlin, E. J.; Bluhm, H.; Biegalski, M. D.; Shao-Horn, Y. Water Reactivity on the $LaCoO_3$ (001) Surface: An Ambient Pressure x-Ray Photoelectron Spectroscopy Study. *J. Phys. Chem. C* **2014**, *118* (34), 19733–19741.

[172] Heine, C.; Lechner, B. A. J.; Bluhm, H.; Salmeron, M. Recycling of CO_2: Probing the Chemical State of the Ni(111) Surface during the Methanation Reaction with Ambient-Pressure X-Ray Photoelectron Spectroscopy. *J. Am. Chem. Soc.* **2016**, *138* (40), 13246–13252.

[173] Ye, Y.; Yang, H.; Qian, J.; Su, H.; Lee, K. J.; Cheng, T.; Xiao, H.; Yano, J.; Goddard, W. A.; Crumlin, E. J. Dramatic Differences in Carbon Dioxide Adsorption and Initial Steps of Reduction between Silver and Copper. *Nat. Commun.* **2019**, *10*, 1875.

[174] Qiao, J.; Liu, Y.; Hong, F.; Zhang, J. A Review of Catalysts for the Electroreduction of Carbon Dioxide to Produce Low-Carbon Fuels. *Chem. Soc. Rev.* **2014**, 43, 631-675.

[175] Atomic Calculation of Photoionization Cross-Sections and Asymmetry Parameters https://vuo.elettra.eu/services/elements/WebElements.html (acceded November 2019).

[176] Beamson, G. & Briggs, D. High Resolution XPS of Organic Polymers, Wiley, Chichester, **1992**.

[177] Díaz, J.; Paolicelli, G.; Ferrer, S.; Comin, F. Separation of the sp^3 and sp^2 Components in the C 1s Photoemission Spectra of Amorphous Carbon Films. *Phys. Rev. B* **1996**, *54* (11), 8064–8069.

[178] Oswald, S. Binding Energy Referencing for XPS in Alkali Metal-Based Battery Materials Research (I): Basic Model Investigations. *Appl. Surf. Sci.* **2015**, *351*, 492–503.

[179] Moreno-Castilla, C.; López-Ramón, M. V.; Carrasco-Marín, F. Changes in Surface Chemistry of Activated Carbons by Wet Oxidation. *Carbon* **2000**, *38* (14), 1995–2001.

[180] Bar-Tow, D.; Peled, E.; Burstein, L. Study of Highly Oriented Pyrolytic Graphite as a Model for the Graphite Anode in Li-ion Batteries. *J. Electrochem. Soc.* **1999**, *146* (3), 824–832.

[181] Li, S.; Xu, X.; Shi, X.; Li, B.; Zhao, Y.; Zhang, H.; Li, Y.; Zhao, W.; Cui, X.; Mao, L. Composition Analysis of the Solid Electrolyte Interphase Film on Carbon Electrode of Lithium-Ion Battery Based on Lithium Difluoro(Oxalate)Borate and Sulfolane. *J. Power Sources* **2012**, *217*, 503–508.

[182] Zhao, Q.; Zhang, Y.; Tang, F.; Zhao, J.; Li, S. Mixed Salts of Lithium Difluoro (Oxalate) Borate and Lithium Tetrafluorobotate Electrolyte on Low-Temperature Performance for Lithium-ion Batteries. *J. Electrochem. Soc.* **2017**, *164* (9), A1873–A1880.

[183] Wang, L.; Menakath, A.; Han, F.; Wang, Y.; Zavalij, P. Y.; Gaskell, K. J.; Borodin, O.; Iuga, D.; Brown, S. P.; Wang, C.; et al. Identifying the Components of the Solid–Electrolyte Interphase in Li-ion Batteries. *Nat. Chem.* **2019**, *11* (9), 789–796.

[184] Younesi, R.; Hahlin, M.; Edström, K. Surface Characterization of the Carbon Cathode and the Lithium Anode of Li–O_2 Batteries Using $LiClO_4$ or LiBOB Salts. *ACS Appl. Mater. Interfaces* **2013**, *5* (4), 1333–1341.

[185] Li, J. T.; Swiatowska, J.; Seyeux, A.; Huang, L.; Maurice, V.; Sun, S. G.; Marcus, P. XPS and ToF-SIMS Study of Sn-Co Alloy Thin Films as Anode for Lithium Ion Battery. *J. Power Sources* **2010**, *195* (24), 8251–8257.

[186] Hoffmann, F. M.; Weisel, M. D.; Paul, J. The Activation of CO_2 by Potassium-Promoted Ru(001) I. FT-IRAS and TDMS Study of Oxalate and Carbonate Intermediates. *Surf. Sci.* **1994**, *316* (3), 277–293.

[187] Axelsson, O.; Shao, Y.; Paul, J.; Hoffmann, F. M. A Theoretical and Experimental Study of Reaction Pathways for the Interaction of CO_2 with

Alkali-Modified Surfaces. *J. Phys. Chem.* **1995**, *99* (18), 7028–7035.

[188] Freund, H.-J.; Roberts, M. W. Surface Chemistry of Carbon Dioxide. *Surf. Sci. Rep.* **1996**, *25*, 225–273.

[189] Deal, B. E.; Grove, A. S. General Relationship for the Thermal Oxidation of Silicon. *J. Appl. Phys.* **1965**, *36* (12), 3770–3778.

[190] Bates, J. B.; Dudney, N. J.; Neudecker, B.; Ueda, A.; Evans, C. D. Thin-Film Lithium and Lithium-Ion Batteries. *Solid State Ionics* **2000**, *135* (1–4), 33–45.

[191] Porthault, H.; Decaux, C. Electrodeposition of Lithium Metal Thin Films and Its Application in All-Solid-State Microbatteries. *Electrochim. Acta* **2016**, *194*, 330–337.

[192] Rigaux, C.; Lafort, A.; Bodart, F.; Jongen, Y.; Cambriani, A.; Lucas, S. Analyses of Thick Lithium Coatings Deposited by Sputter-Evaporation and Exposed to Air. *Plasma Process. Polym.* **2009**, *6*, 337–341.

[193] Smith, D. L. Thin-Film Deposition. Principles & Practice. *McGraw-Hill, International Edition* **1995**.

[194] Bunshah, R.F.; Juntz, R.S. Influence of Condensation Temperature on Microstructure and Tensile Properties of Titanium Sheet Produced by High-Rate Physical Vapor Deposition Process. *Metall. Trans.* **1973**, *4*, 21–26.

[195] Pedrosa, P.; Ferreira, A.; Cote, J. M.; Martin, N.; Yazdi, M. A. P.; Billard, A.; Lanceros-Mendez, S.; Vaz, F. Influence of the Sputtering Pressure on the Morphological Features and Electrical Resistivity Anisotropy of Nanostructured Titanium Films. *Appl. Surf. Sci.* **2017**, *420*, 681–690.

[196] https://cordis.europa.eu/project/id/687561 (acceded January 2020)

[197] Agostini, M.; Brutti, S.; Navarra, M. A.; Panero, S.; Reale, P.; Matic, A.; Scrosati, B. A High-Power and Fast Charging Li-ion Battery with Outstanding Cycle-Life. *Sci. Rep.* **2017**, *7*, 1104.

[198] Ma, C.; Cheng, Y.; Yin, K.; Luo, J.; Sharafi, A.; Sakamoto, J.; Li, J.; More, K. L.; Dudney, N. J.; Chi, M. Interfacial Stability of Li Metal-Solid Electrolyte Elucidated via in Situ Electron Microscopy. *Nano Lett.* **2016**, *16* (11), 7030–7036.

[199] Rikarte Oramzabal, J. Surfaces & Interphases in Thin-Film & Conventional Li-ion Batteries. Thesis dissertation, **2019**.

[200] Lang, J.; Qi, L.; Luo, Y.; Wu, H. High Performance Lithium Metal Anode:

Progress and Prospects. *Energy Storage Mater.* **2017**, *7*, 115–129.

[201] Mizuno, S.; Tochihara, H.; Kadowaki, T.; Minagawa, H.; Hayakawa, K.; Toyoshima, I. Formation of a Linear LiOH Compound on Cu (001) : Reaction of H_2O with Li Adatoms at Low Coverages. *Surf. Sci.* **1992**, *264*, 103–113.

[202] Rudolf, P.; Astaldi, C.; Cautero, G.; Modesti, S. Study of Alkali Metal Adsorption on Reconstructed and Unreconstructed Cu Surfaces by HREELS. *Surf. Sci.* **1991**, *251–252*, 127–131.

[203] Dudde, R.; Reihl, B. Electronic Structure of Alkali-Metal Monolayers on Cu (111). *Surf. Sci.* **1993**, *288*, 614–617.

[204] Tochihara, H.; Mizuno, S. Hybrid Surface Structures Formed on Cu (001) and Ag (001) by Alkali-Metal Adsorption. *Surf. Sci.* **1996**, *357–358*, 10–18.

[205] Uhl, B.; Hekmatfar, M.; Buchner, F.; Behm, R. J. Interaction of the Ionic Liquid [BMP][TFSA] with Rutile TiO_2 (110) and Coadsorbed Lithium. *Phys. Chem. Chem. Phys.* **2016**, *18* (9), 6618–6636.

[206] Baggetto, L.; Unocic, R. R.; Dudney, N. J.; Veith, G. M. Fabrication and Characterization of Li-Mn-Ni-O Sputtered Thin Film High Voltage Cathodes for Li-ion Batteries. *J. Power Sources* **2012**, *211*, 108–118.

[207] Bae, S.-Y.; Shin, W.-K.; Kim, D.-W. Protective Organic Additives for High Voltage $LiNi_{0.5}Mn_{1.5}O_4$ Cathode Materials. *Electrochim. Acta* **2014**, *125*, 497–502.

[208] Kim, D.-wook; Uchida, S.; Shiiba, H.; Zettsu, N.; Teshima, K. New Insight for Surface Chemistries in Ultra-Thin Self-Assembled Monolayers Modified High-Voltage Spinel Cathodes. *Sci. Rep.* **2018**, *8*, 11771.

[209] Xue, Z.; He, D.; Xie, X. Poly(Ethylene Oxide)-Based Electrolytes for Lithium-Ion Batteries. *J. Mater. Chem. A* **2015**, *3* (38), 19218–19253.

[210] Xia, S.; Wu, X.; Zhang, Z.; Cui, Y.; Liu, W. Practical Challenges and Future Perspectives of All-Solid-State Lithium-Metal Batteries. *Chem* **2019**, *5* (4), 753–785.

[211] Kelly, T.; Ghadi, B. M.; Berg, S.; Ardebili, H. In Situ Study of Strain-Dependent Ion Conductivity of Stretchable Polyethylene Oxide Electrolyte. *Sci. Rep.* **2016**, *6* (1), 20128.

[212] Yao, P.; Yu, H.; Ding, Z.; Liu, Y.; Lu, J.; Lavorgna, M.; Wu, J.; Liu, X. Review on Polymer-Based Composite Electrolytes for Lithium Batteries. *Front. Chem.* **2019**, *7*, 522.

[213] Zhang, Q.; Liu, K.; Ding, F.; Liu, X. Recent Advances in Solid Polymer Electrolytes for Lithium Batteries.

[214] Bresser, D.; Lyonnard, S.; Iojoiu, C.; Picard, L.; Passerini, S. Decoupling Segmental Relaxation and Ionic Conductivity for Lithium-Ion Polymer Electrolytes. *Mol. Syst. Des. Eng.* **2019**, *4* (4), 779–792.

[215] Rosso, M.; Brissot, C.; Teyssot, A.; Dollé, M.; Sannier, L.; Tarascon, J.-M.; Bouchet, R.; Lascaud, S. Dendrite Short-Circuit and Fuse Effect on Li/Polymer/Li Cells. *Electrochim. Acta* **2006**, *51* (25), 5334–5340.

[216] Barai, P.; Higa, K.; Srinivasan, V. Lithium Dendrite Growth Mechanisms in Polymer Electrolytes and Prevention Strategies. *Phys. Chem. Chem. Phys.* **2017**, *19* (31), 20493–20505.

[217] Armand, M. Polymer Solid Electrolytes - an Overview. *Solid State Ionics* **1983**, *9–10*, 745–754.

[218] Appetecchi, G. B.; Scaccia, S.; Passerini, S. Investigation on the Stability of the Lithium-Polymer Electrolyte Interface. *J. Electrochem. Soc.* **2000**, *147* (12), 4448.

[219] Appetecchi, G. B.; Scaccia, S.; Passerini, S. Investigation on the Stability of the Lithium-Polymer Electrolyte Interface. *J. Electrochem. Soc.* **2000**, *147* (12), 4448.

[220] Nguyen, T. Q.; Breitkopf, C. Determination of Diffusion Coefficients Using Impedance Spectroscopy Data. *J. Electrochem. Soc.* **2018**, *165* (14), E826–E831.

[221] Aldalur, I.; Zhang, H.; Piszcz, M.; Oteo, U.; Rodriguez-Martinez, L. M.; Shanmukaraj, D.; Rojo, T.; Armand, M. Jeffamine® Based Polymers as Highly Conductive Polymer Electrolytes and Cathode Binder Materials for Battery Application. *J. Power Sources* **2017**, *347*, 37–46.

[222] Maibach, J.; Källquist, I.; Andersson, M.; Urpelainen, S.; Edström, K.; Rensmo, H.; Siegbahn, H.; Hahlin, M. Probing a Battery Electrolyte Drop with Ambient Pressure Photoelectron Spectroscopy. *Nat. Commun.* **2019**, *10*, 3080.

APPENDIX

A.1 List of abbreviations

APXPS	Ambient Pressure X-ray Photoelectron Spectroscopy
a.u.	arbitrary units
BE	Binding Energy
CPE	Constant Phase Element
CV	Cyclic Voltammetry
EIS	Electrochemical Impedance Spectroscopy
FIB	Focused Ion Beam
FWHM	Full Width at Half Maximum
KE	Kinetic Energy
LMB	Lithium Metal Battery
PVD	Physical Vapor Deposition
RSD	Residual Standard Deviation
SEI	Solid Electrolyte Interphase
SEM	Scanning Electron Microscopy
UHV	Ultra-High Vacuum
UPS	Ultraviolet Photoelectron Spectroscopy
XPS	X-ray Photoelectron Spectroscopy

A.2 List of contributions

A.2.1 Publications

- Ane Etxebarria, Stephan L. Koch, Oleksandr Bondarchuk, Stefano Passerini, Gilberto Teobaldi, Miguel Ángel Muñoz-Márquez. Work function evolution in Li anode processing. Submitted to *J. Am. Chem. Soc*. (04 February, 2020)
- Yifan Ye, Jin Qian, Hao Yang; Hongyang Su, Kyung-Jae Lee, Ane Etxebarria, Tao Cheng, Hai Xiao, Junko Yano, William Goddard, Ethan Crumlin. Synergy between Silver-Copper Surface Alloy Composition and Carbon Dioxide Adsorption and Activation. Submitted to *ACS Appl. Mater. Interfaces*. (03 February, 2020)
- Ane Etxebarria, Don-Jin Yun, Monika Blum, Yifan Ye, Meiling Sun, Kyung-Jae Lee, Hongyang Su, Miguel Ángel Muñoz-Márquez, Philip N. Ross, Ethan Crumlin. CO_2 interaction with Li metal surface revealed using Ambient Pressure X-ray Photoelectron Spectroscopy. To be submitted to *Nano Lett.* (February, 2020)

A.2.2. Conferences

- Ane Etxebarria, Monika Blum, Pinar Aydogan Gokturk, Don Jen Yun, Miguel Ángel Muñoz-Márquez, Ethan Crumlin. On the way to elucidate reaction mechanisms that involve metallic lithium and atmospheric gases using *in situ* Ambient Pressure X-ray Photoelectron Spectroscopy, 4th International Forum on Progress and Trends in Battery and Capacitor Technologies – Power our future 2019, July 2019, Vitoria-Gasteiz, Spain (**oral**)
- Ane Etxebarria, Monika Blum, Don Jen Yun, Miguel Ángel Muñoz-Márquez, Ethan Crumlin. On the way to elucidate reaction mechanisms that involve metallic lithium and atmospheric gases using *in situ* Ambient Pressure X-ray Photoelectron Spectroscopy, 235th ECS meeting, May 2019, Dallas, USA (**oral**)
- Ane Etxebarria, Oleksandr Bondarchuk, Ethan Crumlin, Miguel Ángel Muñoz-Márquez. Elucidating characteristic effects of atmospheric gases on Lithium surface, ALS User meeting, October 2018, Berkeley, USA (**poster**)

- Ane Etxebarria, Oleksandr Bondarchuk, Miguel Ángel Muñoz-Márquez. Lithium surface evolution under different atmospheres, PhotoElectroCatalysis at the Atomic Scale (PECAS), June 2017, Donostia, Spain (**oral**)
- Ane Etxebarria, Oleksandr Bondarchuk, Miguel Ángel Muñoz-Márquez. Litio metalikoaren gainazalaren egokitzea bateria elektrikoetarako, IkerGazte: Nazioarteko ikerketa euskaraz, May 2017, Iruñea, Spain (**oral**)
- Ane Etxebarria, Oleksandr Bondarchuk, Miguel Ángel Muñoz-Márquez. O_2, N_2 eta CO_2 gasen eragina litio gainazal garbiaren gain: gainazalaren konposizioa eta aln-funtzioaren azterketa. Zientzia eta teknologiaren III kongresua, July 2016, Markina-Xemein, Spain (**poster**)
- Ane Etxebarria, Oleksandr Bondarchuk, Miguel Ángel Muñoz-Márquez. Effect of O_2, CO_2 and N_2 gases on clean lithium surfaces: Surface composition and work function analysis, SIRBATT (Stable Interfaces for Rechargeable Batteries) workshop, May 2016, Orlando, USA (**poster**)
- Ane Etxebarria, Oleksandr Bondarchuk, Miguel Ángel Muñoz-Márquez. Effect of O_2, CO_2 and N_2 gases on clean lithium surfaces: Surface composition and work function analysis, V Jornadas de investigación de la facultad de ciencia y tecnología, April 2016, Leioa, Spain (**poster**)